Palaeoclimate modelling of monsoons during past warm periods

Anni Zhao

A dissertation submitted in partial fulfillment

of the requirements for the degree of

Doctor of Philosophy

of

University College London.

Department of Geography

University College London

March 18, 2023

I, Anni Zhao, confirm that the work presented in this thesis is my own. Where information has been derived from other sources, I confirm that this has been indicated in the work.

Abstract

Three past warm periods were chosen to provide out-of-sample tests for those state-of-the-art climate models by phase 4 of the Palaeoclimate Model Intercomparison Project (PMIP4): the mid-Holocene (6,000 years ago), the Last Interglacial (more precisely 127,000 years ago) and the mid-Pliocene Warm Period (roughly 3.2 million years ago). Experiments were designed for each warm period with improved boundary conditions and protocols; called *midHolocene*, *lig127k* and *midPliocene-eoi400* respectively. This work looks at the monsoon behaviour across the three PMIP4 experiments for the first time, to improve the understanding of palaeomonsoon and to evaluate the performance of current state-of-art models.

Results of this work indicate that both the orbit-induced experiments (*midHolocene* and *lig127k*) show enhanced monsoons in the Northern Hemisphere and weakened monsoons in the Southern Hemisphere as expected. The *lig127k* simulations have stronger response than the *midHolocene*, because of their stronger orbital forcings. Simulated anomalies are generally in good agreement with climate proxy reconstructions, but both experiments underestimate the amplification of the northern African monsoon as well as Arctic warming. The *midPliocene-eoi400* simulations indicate a global warming with a clear pattern of polar amplification, wetter tropics, and enhanced monsoons but with uncertainties. An idealised aerosol experiment highlights the potential importance of uncertainty in the aerosol specifications in the experiment protocol to simulating the mPWP climate. Analyses on the data-model mismatch highlight the source and importance of uncertainties during different time periods.

Despite the existing uncertainties in the simulations, the results of the three experiments are useful for understanding climate response and quantitatively evaluating model performance. The findings from this thesis, combined with future work, improve our understanding of monsoon forced responses and could help to ensure that the next generation of climate models provides more confident projections of future climate change.

Impact Statement

Monsoons are the dominant factors affecting seasonal hydrological cycles and precipitation. These influence local human well-being and socioeconomic development. Future changes in monsoons are important as they will affect the water supply in monsoonal regions and impact more than 60% of the world's human population. However, the temporal and spatial patterns of future monsoon change are strongly dependent on regional characteristics, and the mechanisms behind the changes are not yet well understood. Climate models have been viewed as useful tools to investigate the climate response to different climate forcings, and project future climate change under various scenarios. Palaeoclimate modelling provides the out-of-sample tests to evaluate the performance of the climate models that have been used in future projection, which can therefore raise the confidence in projecting climate changes in the future, benefiting the policy makers when making future decisions.

This work selects three warm periods identified by the the fourth phase of the Model Intercomparison Project (PMIP4) endorsed by the sixth phase of the Coupled Model Intercomparison Project (CMIP6) and provides the latest analysis and evaluation of the results of the experiment for the three periods. The results of the experiments have contributed to the (assessment in the) sixth assessment report of the Intergovernmental Panel on Climate Change (IPCC, 2021). The findings in this work indicate that the PMIP4-CMIP6 *midHolocene*, the PMIP4-CMIP6 *lig127k* and the PlioMIP2 *midPliocene-eoi400* simulations can provide quantitative evaluation and derivation of emergent constraints on the hydrological cycle, and improve the confidence in projecting future changes in monsoons and other climatic variables.

Experiment outputs of the CMIP6 and PMIP4 are now freely available from the

Earth System Grid Federation (ESGF). There are however overheads in analysing this resource that may prove complicated or prohibitive. This work introduces the steps that were used to perform the analyse for several of the initial publications arising from PMIP4. The whole process and the example scripts are reorganised into a software which hope to offer a general analysing process for the CMIP standard outputs. A paper documenting the steps has been submitted to the Geographical Model Development.

Only a few studies have been applied to understanding aerosol effects in the Pliocene, and yet the effect on precipitation has not been analysed. This work also explores the Pliocene climate response under two idealised aerosol scenarios by analysing the simulations produced by a state-of-the-art climate model (CESM1.2). The results indicate that change in aerosol has more impacts on precipitation over tropical regions than the high CO_2 concentration. This highlights the significance of future aerosol emission on monsoons.

Acknowledgements

First and foremost, I would like to give my greatest thanks to my primary supervisor, Prof. Chris Brierley. Thank you for your guidance, supports and patience in the last four years. You were always having your door open to offer help. Your prompt reply was greatly appreciated and extremely helpful when we were not able to meet in person during the lockdown. I could not have completed this thesis without your help. I would also like to thank my secondary supervisor, Prof. Mark Maslin. Thanks you for your help throughout my PhD and your valuable and insightful suggestions on my chapters. Also thanks to Prof. David Thornalley and Prof. Chronis Tzedakis. I have learnt a lot from the lab meeting and the palaeoreading club.

I am also grateful to the modelling groups for producing and donating their model outputs which can be downloaded from the Earth System Grid Federation (ESGF) for free.

Last but not least I want to thank my parents and grandparents for their supports in all aspects.

Contents

List of Figures

List of Tables

Chapter 1

Introduction

The word “monsoon” comes from the Arabic word ”mausim” which means season of winds as the seasonal reversal of the directions of surface winds along the Indian Ocean and its surroundings (the Arabian Sea in particular) and as most of the rains that fall in Southeast Asia occur during the summer. More generally a monsoon is characterised by the seasonal reversal of the surface winds and associated with contrasting precipitation regimes in the tropical and subtropical regions. Understanding changes in monsoon characteristics is important as monsoons are the dominate factors affecting seasonal hydrological cycles and precipitation, which influence local human well-being and socioeconomic development like in Asia where has 60% of the world’s human population and monsoon rainfall is the major water supply. The Sixth Assessment Report (AR6) of the Intergovernmental Panel on Climate Change (IPCC) summarises an enhancement in Asian and northern African monsoons in response to warming induced by emissions of Greenhouse gases (GHGs) which were counteracted by decreases in monsoon precipitation due to the cooling induced by anthropogenic aerosol emissions over the 20^{th} century (Douville et al., 2021; IPCC, 2021d). Models contributed to the phase 6 of the Coupled Model Intercomparison Project (CMIP6) project a precipitation increase over Asian and northern African monsoons while decrease over North American monsoon and monsoons in the Southern Hemisphere (SH) under global warming (IPCC, 2021d).

Monsoonal features in past warm periods were different in location and intensity from today as shown by palaeoenvironmental data (e.g. Kohfeld and Harrison, 2000;

Zhang et al., 2019). For example, the North African Monsoon during the mid-Holocene (6000 years ago) and Last Interglacial (127,000 years ago) was enhanced and expanded further than its modern pattern (e.g. Weldeab et al., 2007; Mohtadi et al., 2016). Analysis of past monsoon changes is useful for understanding how the monsoon responds to external forcings that are outside of their current ranges and improving the knowledge of monsoons which could be helpful for projecting future monsoon changes. Climate models numerically represent the processes in the Earth's system that can play as a useful and powerful tool to simulate monsoon response to prescribed external forcing, understand the mechanisms behind the response, and test new hypothesis. Modelling palaeoclimates allows us to study how climate models produce monsoon response to the forcings in past and evaluate model performance by comparing to proxy data, and therefore assess the confidence in projecting future climate changes by climate models.

Modelling climate changes in the past offers a chance to examine how the state-of-the-art climate models used in future projections could produce the response in climate to the forcing outside of current range. Experimental outputs from the latest Palaeoclimate Modelling Intercomparison Project phase 4 (PMIP4), endorsed by CMIP6, has continuously been released to public in the last three years and they have contributed to the palaeo assessment in several chapters in the IPCC AR6 (Gulev et al., 2021; Eyring et al., 2021; Douville et al., 2021; Fox-Kemper et al., 2021). The primary description papers of the latest PMIP4-CMIP6 experiments have been published (Otto-Bliesner et al., 2021; Brierley et al., 2020; Haywood et al., 2020; Kageyama et al., 2021). The mid-Holocene (MH), Last Interglacial (LIG) and mid-Pliocene Warm Period (mPWP) are the three past warm periods that offer possible systems to simulate future global warming. However, climate models have not been able to fully reproduce the climate change in the past as suggested by proxy data, e.g. underestimation in the North African monsoon expansion during the mid-Holocene (Harrison et al., 2015). Meanwhile, the relationship between large-scale changes and local-scale changes in the past remain unclear, which raises difficulties in interpreting palaeo-environmental data. The latest PMIP4 was designed to deal with these challenges.Analysis of the monsoon response across the PMIP4 experiments has not yet been done. The major aim of this thesis is to analyse the monsoon response in the three warm periods in the PMIP4-CMIP6 simulations. In this chapter, I will introduce the concepts and review the literature relevant to the thesis. Firstly, section 1.1 describes the history of understanding monsoon by reviewing how and why monsoons are treated as a sea-breeze circulation and dynamic components of the atmospheric circulation, and gives the definition of global monsoon domain and regional monsoons. Section 1.2 introduces three climate forcings (orbital forcing, GHGs and aerosols) that affect monsoons, whose effects on monsoons in past warm periods are presented and discussed in chapters 3 to 6. Section 1.3 introduces climate models and the CMIP, and the following section (1.4) introduces PMIP whose outputs are the major simulations analysed in this work. Section 1.5 describes proxy data, monsoon reconstruction and challenge in data-model comparison that are associated with model evaluation. Section 1.6 introduces the findings in monsoon change during the MH, LIG and mPWP. Relationship between this work and published PMIP4-CMIP6 work and aims and outline of this thesis are given in the last section (1.7).

1.1 Monsoon system

1.1.1 Theories

Monsoons have traditionally been viewed as regional sea breeze circulations driven by temperature contrast between land and sea (hereafter referred as to "Sea-breeze" theory). Recently an alternate theory that views monsoons as a global-scale component of the atmospheric circulation has gained prominence (hereafter referred as to "Dynamic" theory), which rises a concept of global monsoon. Regional monsoons are viewed as subsystems in a global monsoon system.

1.1.1.1 'Sea-breeze' theory

The "Sea-breeze" theory (Figure 1.1a) was firstly suggested by E. Hadley in 1686 – viewing a summer monsoon as a gigantic land–sea breeze in which air rises over

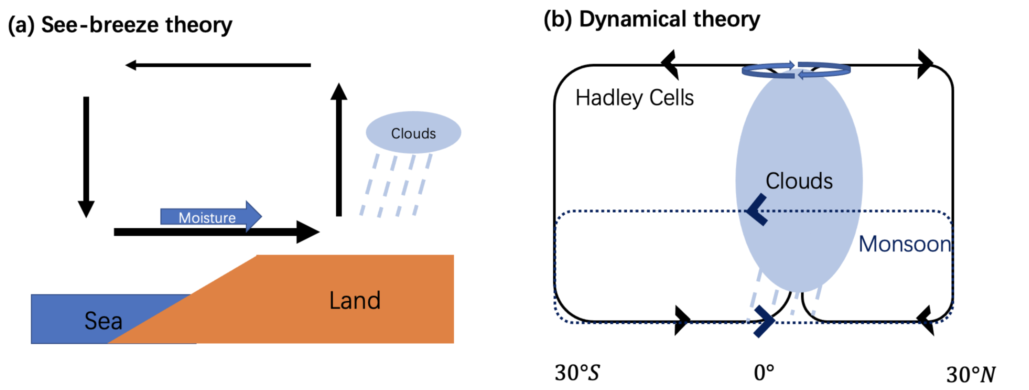

Figure 1.1: Schematic diagrams illustrating (a) the sea breeze theory and (b) the dynamical theory.

the heated land due to the land-sea temperature contrast, and forms clouds and rainfall during ascending (Hadley, 1686). In this view, lands warm more and faster than ocean during the summer and this differential heating drives wind flow blowing from the sea surface (which has high pressure) onshore toward the land (which has lower pressure). The reverse occurs during the winter resulting in dry conditions over land as winds blowing from land to sea. The theory was modified by G. Hadley (1753) to consider the effect of the Coriolis force, and has subsequently been extended further to take account the effects of tropical topographic features (e.g. Meehl, 1992) and elevated diabatic heating from moist convection (e.g. Webster et al., 1998) viewed as global monsoon. The traditional delineation of monsoon regions was only based on winds (e.g. Ramage, 1971), but later recognised the consistent relationship between tropical precipitation, surface pressure, and winds (Webster, 1972; Gill, 1980).

According to this theory, an increased land-sea temperature contrast should result in enhanced precipitation and stronger monsoons. Additionally, the temperature contrast and the precipitation should reach their maximums simultaneously. However, this is not supported by a several analyses of model simulations (e.g. D'Agostino et al., 2019, 2020; Gadgil, 2018; Fasullo, 2012). In reality, in a monsoon region, the land warms and reaches its hottest before the circulation becomes its strongest. This happens in late summer when heavy rainfall and cloudiness in turn have decreased land surface temperature and therefore reduced land-sea temperature contrast.

1.1.1.2 "Dynamic" theory

In 'Dynamic' theory (Figure 1.1b), monsoons are seen as moist energetically direct circulations in the tropics, which are linked to the seasonal swing of the zonal mean Intertropical Convergence Zone (ITCZ) (Schneider et al., 2014; Biasutti et al., 2018). ITCZ is a band of low pressure shifting near the Equator where the trade winds of both hemispheres converge and rise forming deep convective heavy rainfall. The position of the ITCZ is influenced by the shift in the position of subpolar point and the distribution of land and sea. As the sea warms slower than land due to higher heat capacity, the ITCZ tends to move further north or south into land than over sea during the summer. Monsoons and the ITCZ combine to form a planetary energetically direct circulation generating rainfall over land and ocean. Similar to the zonal mean Hadley cells, monsoons export moist static energy (MSE) away from their regions of ascent and produce maximum monsoonal rainfall (shown as the dashed shallow meridional circulation in Figure 1.1b), acting to remove the instability from the atmosphere to bring the free tropospheric temperature in line with the subcloud layer's equivalent potential temperature (Emanuel et al., 1994; Nie et al., 2010). This theory can be used to explain the response in palaeoclimate monsoons to forcings outside of the tropics (e.g. the Eurasian afforestation during the mid-Holocene; Swann et al., 2014a), and to different factors that affect energetically direct circulation (such as the land surface; Broström et al., 1998). D'Agostino et al. (2019, 2020) used this theory to explain the difference in response of simulated monsoons to orbital forcing in the *midHolocene* experiment and to the global warming induced by greenhouse gases in a future scenario, which suggested that the dynamic component drive the monsoon change in response to orbital forcing during the mid-Holocene while thermodynamic component drive the monsoon change in response to atmospheric greenhouse gases increase.

1.1.2 Global monsoon domain

In the last few decades, traditional regional monsoons have begun being viewed as subsystems within a global monsoon system. The global monsoon can be defined as the dominant mode of the annual variation of tropical and subtropical precipitation and circulation (Wang and Ding, 2008), which is consistent with the dynamical theory. Wang and Ding (2008) and Wang et al. (2014b) gave two criteria based on precipitation to delineate monsoon domains: (a) the local annual range of precipitation rate (summer - winter) exceeds 2 mm d^{-1}, and (b) the local summer mean precipitation exceeds 55% of the annual mean precipitation. The local summer season is defined as May-to-September (MJJAS) in the Northern Hemisphere (NH) and November-to-March (NDJFM) in the Southern Hemisphere (SH), and the local winter season as NDJFM in the NH and MJJAS in the SH. Figure 1.2 shows the observed global monsoon domain from the Global Precipitation Climatology Project (GPCP) observational dataset between 1971 and 2000 (Adler et al., 2003) following these two criteria. The decision on the definition of global monsoon and the choice of fixed 5-month window follows the PAGES Working group "Global Monsoon and Low-Latitude Processes: Evolution and Variability" founded in 2007 (Wang et al., 2014b, 2017).

The global monsoon domain covers the traditional major regional monsoons and also incorporates substantial oceanic regions. Affected by local physics, each subsystem (i.e. regional monsoon) has its own features. IPCC AR5 (Christensen et al., 2013) identified seven regional land monsoons (Table 1.1), which was followed by Brierley et al. (2020) and Otto-Bliesner et al. (2021) to compute characteristics of regional monsoons. IPCC AR6 defines regional monsoons differently from the AR5, because though some regional monsoons in the AR5 identified via the global metric, their seasonality in precipitation is not necessarily of monsoon origin (IPCC, 2021b). IPCC AR6 defines six land monsoons and two domains (Table 1.1 IPCC, 2021b), based on published literature, expert judgement and climatological properties of individual regional monsoons.

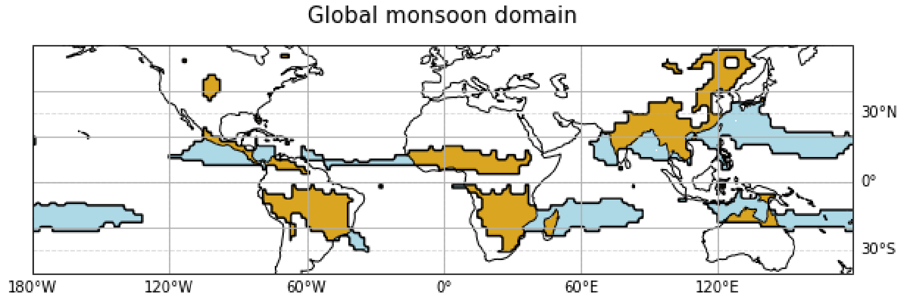

Figure 1.2: Observed (black contour) global monsoon domain following the definition in Wang and Ding (2008) and Wang et al. (2014b). The precipitation data uses the Global Precipitation climatology Project (GPCP) observational dataset between 1971 and 2000 (Adler et al., 2003). Light brown shading shows the major land-based regional monsoons, and light blue represents monsoons over ocean.

Table 1.1: Regional land monsoons and domains identified in IPCC AR5 (Christensen et al., 2013) and AR6 (Douville et al.,2021) and their abbreviations. IPCC AR5 identified seven regional land monsoons. AR6 now has six regional land monsoons and two domains.

Regional land monsoons	IPCC AR5 Christensen et al. (2013)	IPCC AR6
South and Southeast Asian Monsoon	SAS	SAsiaM
East Asian Monsoon	EAS	EAsiaM
West African Monsoon^{+}	NAF	WAfriM
North American Monsoon*	NAMS	NAmerM
Equatorial American Domain*	/	EqAmer
South American Monsoon	SAMS	SAmerM
Australian and Maritime Continent Monsoon	AUSMC	AusMCM
South African Monsoon$^{<}$	SAF	/
South African Domain$^{<}$	/	SAfri

$^{+}$West African Monsoon was called North African Monsoon in IPCC AR5.
* NAMS in AR5 is equivalent to EqAmer in AR6, instead of NmerM which is located north of EqAmer.
$^{<}$ Monsoon SAF in AR5 is defined as a domain SAfri in AR6.

1.2 Climate forcings

Climate forcings are considered to come from outside of the climate system and drive climate changes. This thesis investigates three forcings: orbital forings, atmospheric CO_2 and aerosols. Climate models consider them as external or boundary conditions.

1.2.1 Orbital forcing

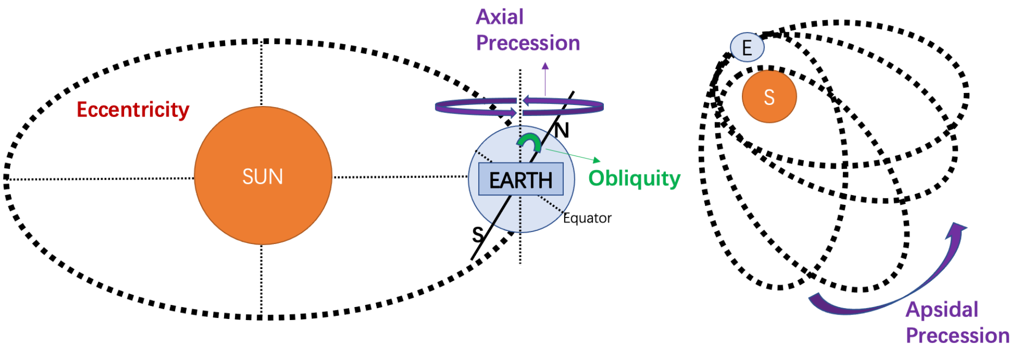

Figure 1.3: Schematic diagram of the Earth's orbital parameters: eccentricity, obliquity and precession (axial and orbital).

According to Milankovitch cycles (Milankovitch, 1941), variations in the Earth's three orbital parameters (eccentricity, obliquity and precession consisting of both axial precession and orbital precession) result in periodic variations in the distribution of solar radiation reaching the Earth. The distribution of insolation (i.e. incoming solar radiation received at the top of the atmosphere (TOA) can be calculated by eccentricity (e), obliquity (ε) and longitude of perihelion ($\overline{\varpi}$) from vernal equinox. Changes in orbits affects the seasonal and latitudinal distribution of the insolation (Berger, 1978). Figure 1.3 shows a sketch of the Earth's orbital parameters and Figure 1.4 shows the time series of orbital variations in the past few million years, focusing on 3.3 - 3.0 million years before present (hereafter referred to as Ma; where present is defined as 1950) and 300 - 0 thousand years before present (ka) that covers the three past warm periods in this thesis. **Eccentricity**, the shape of the Earth's orbit around the Sun, quantified as the deviation of the shape of the orbit from the shape of a circle, varies between 0.00 and 0.06 with a cycle period of 100 kyr and a longer quasi-periodicity at 400 kyr arising from the interactions of Venus and Jupiter. Changes in eccentricity alter the distance between the Earth and the Sun and therefore affecting the total incoming solar radiation but only by a

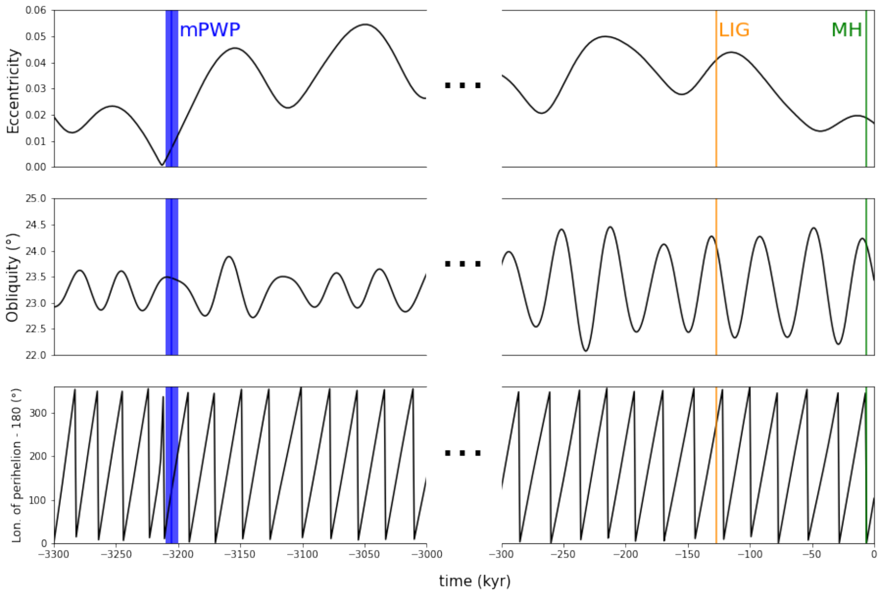

Figure 1.4: Time series of orbital variations in the past few million years from Laskar et al. (2004). The time series are shown over two separate 300,000 year long segments. *mPWP* refers to the mid-Pliocene Warm Period around 3.3 - 3.0 Ma (blue shade), *LIG* to the Last Interglacial at 127 ka (orange line) and *MH* to mid-Holocene at 6 ka (green line). In the PMIP4/PlioMIP2 (see Section 1.4.1.1), the mPWP was focused on KM5c centered on 3.205 Ma (blue line), the warmest phase of marine isotope stage during the mPWP when the orbital configuration was similar to present day (Haywood et al., 2013).

small amount. Though the distance change has limited effects on global and annual mean insolation, it affects the modulation of seasonal and latitudinal distribution of insolation induced by precession and obliquity. **Obliquity** is the axial tilt of the Earth fluctuating between 22° and 24.5° with a cycle period of around 41 kyr. It alters the incoming solar radiation gradient at TOA between low and high latitudes, which generates the atmospheric circulation and the heat transport between the tropics and the poles. Changes in obliquity affect seasonal contrasts by having opposite effects on annual mean insolation in low and high latitudes but no effect on global mean insolation. **Axial precession** is the continuous shift in the orientation of the Earth's rotating axis with a cycle period of around 26 kyr. Besides the rotation of the Earth's axis, the Earth's entire orbit also rotates irregularly due to its interactions with Saturn and Jupiter with a periodicity of 112 kyr, known as **apsidal precession**.

The combination of the two precession components affects the seasonal cycle of insolation with periodicity of about 23 kyr. Combining the eccentricity and axial precession results in a cycle period of 19 kyr. The elliptical orbit rotates with a cycle of 21k year cycle altering the seasons at which aphelion and perihelion occur. Longitude of perihelion is the longitude at which the perihelion would occur if there is no inclination in the Earth's orbit. This parameter is often subtracted by 180° ($\overline{\omega}$ - 180 °) as observed from the Earth rather than the Sun. The position of equinoxes and solstices relative to the perihelion show periodic shifts as the result of the general precession of the equinoxes and the longitude of perihelion. Changes in precession affect the seasons' positions on the orbit and therefore affect the latitudinal and seasonal distribution of insolation. These three orbital parameters together control Earth's incoming solar radiation. Orbital signals have been well recorded in proxy data (Jouzel et al., 2007), and each individual orbital parameter has been calculated (Laskar et al., 2004, 2011) with high degree of confidence.

1.2.2 Greenhouse gases (GHGs)

The greenhouse effect is "the infrared radiative effect of all infrared-absorbing constituents in the atmosphere" (IPCC, 2021c, AVII-28). Greenhouse gases (GHGs) are gases in the atmosphere that produce greenhouse effect by absorbing radiation from the atmosphere and warming the surface. Major GHGs in the Earth's atmosphere include CO_2, CH_4, N_2O and water vapour. Anthropogenic emission of GHGs is the dominant forcing driving global warming since the preindustrial period. Unlike orbital forcing dominantly affecting seasonal variations, forcing induced by GHGs has more effects on annual mean changes. The latest IPCC AR6 WG1 (IPCC, 2021d) assesses that the anthropogenic GMST increase during 2010-2019 relative to 1850-1900 is 1.07°C (0.8 - 1.3), in which CO_2 contributed a warming around 0.6°C and CH_4 contributed to roughly 0.5°C. Climate models simulate polar amplification and reduced E-W Pacific sea surface temperature (SST) gradients that mainly responding to radiative forcing induced by anthropogenic emissions (Forster et al., 2021). At the end of 21^{st} century, global and land monsoons will be likely to change asymmetrically in response to the warming induced by GHGs by increasing more in the

NH than in the SH and increasing over Asia and northern Africa while deceasing over North America though the circulation will likely weaken (Lee et al., 2021). The atmospheric concentration of GHGs varied in past periods (Figure 1.5). For more recent palaeo periods, the concentrations of CO_2, CH_4 and N_2O at have been measured respectively from ice cores from Greenland and Antarctica (e.g. Loulergue et al., 2008; Monnin et al., 2004; Spahni et al., 2005).

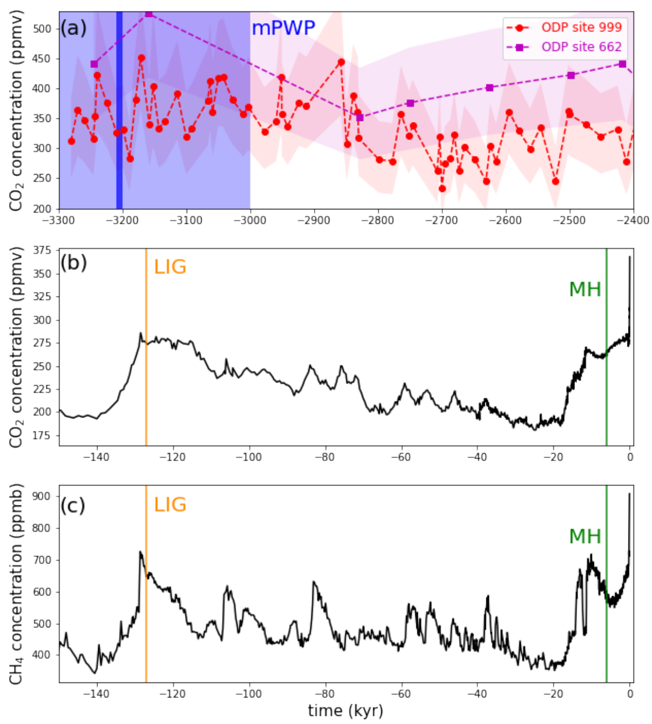

Figure 1.5: GHGs concentrations records in the past. (a) CO_2 record (3.3 - 2.4 Ma) from Martínez-Botí et al. (2015), in which circles represent the minimum estimates and squares represent the maximums. **(b)** Composite CO_2 record from Bereiter et al. (2015) and **(c)** CH_4 from Loulergue et al. (2008) between 150 kyr BP and 1950 CE).

1.2.3 Aerosols

Aerosol is defined as a "suspension of airborne solid or liquid particles, with typical diameters between a few nanometres and a few micrometres and atmospheric lifetimes of up to several days in the troposphere and up to years in the stratosphere."

(IPCC, 2021c, AVII-2). In contrast to GHGs warming the climate, aerosols cool the climate. Currently, human-induced aerosols contributed to a cooling of 0.0°C to 0.8°C between 2010-2019 relative to 1850-1900 (IPCC, 2021d). Most scenarios for future projections in the IPCC AR6 have a decrease in the anthropogenic aerosol forcing, which will contribute to a increase in global mean annual surface temperature and precipitation (Lee et al., 2021).

Aerosols play an important role in climate system through direct effects through aerosol-radiation interactions (ari) and indirect effects through aerosol-cloud interactions (aci). Perturbed aerosols directly affect radiation, known as direct aerosol forcing when the environment remaining unaffected, and have rapid adjustments including changes in cloud (known as semi-direct aerosol effect; Hansen et al., 1997). The aerosol-cloud interactions affect the microphysical properties and evolution of clouds through cloud albedo effects (Twomey, 1977) that increase albedo and cloud optical depth by having a greater number of smaller droplets and cloud lifetime effect (Albrecht, 1989) that increase cloud lifetime by having reduced terminal velocity and less likely to coalesce due to reduced droplet size. Large numbers of studies have been undertaken to investigate aerosol-cloud interactions through observations from both in situ (e.g. Wood et al., 2011), remote sensing (e.g. Cheng et al., 2017), and model simulations (e.g. Reed et al., 2019). They show that clouds and precipitation respond to aerosols in a very complex way. For instance, smoke from vegetation burning could reduce cloud droplet size and delay precipitation (Andreae, 2004), while desert dust could suppress precipitation in thin low-latitude clouds (Rosenfeld et al., 2001). Because of the complexity (source, composition and dispersion etc.), aerosols and their interactions with clouds contribute to the largest uncertainties in understanding aerosol impacts on climate and in climate modelling (Boucher et al., 2013).

1.3 Climate modelling

Climate models are tools to investigate how the climate system would response to various climate forcings, and project future climate change in different sce-

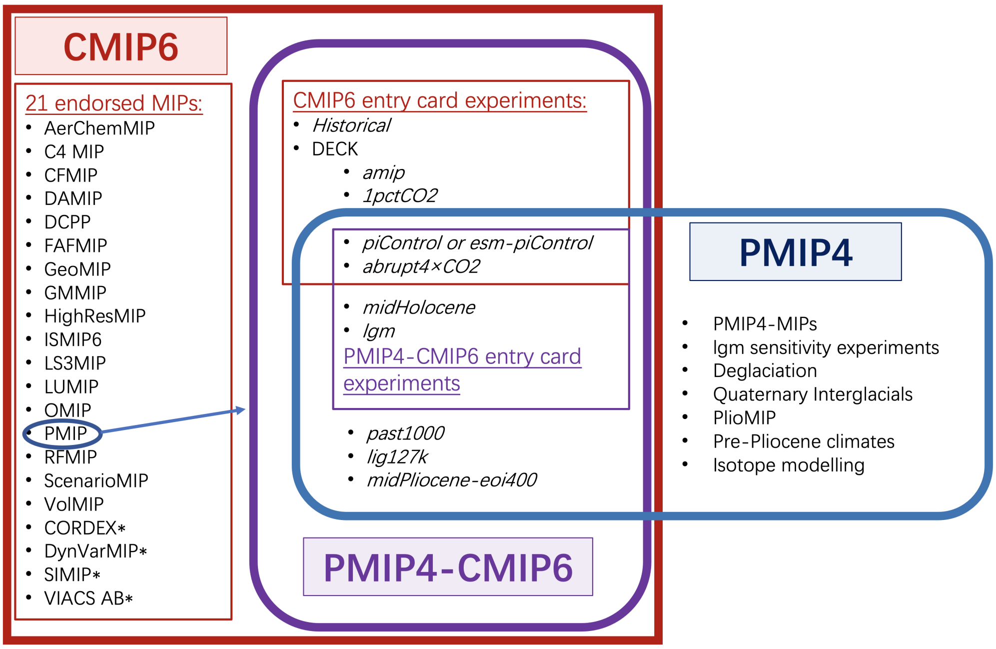

Figure 1.6: Schematic diagram illustrating the PMIP4-CMIP6 experiments and their relationship to CMIP6 and PMIP4, according to Kageyama et al. (2018). Adapted from Zhao et al. (2022) that has been published on the Geoscientific Model Development.)

narios. They represent the climate system through numerical equations based on the physical, chemical and biological properties of the system's components, their interactions and feedbacks, and other known properties. These models work by numerically solving the physical laws and processes in the Earth's system. Any important process at a scale smaller than the model's resolution must be parameterised. In an atmospheric component, cloud macrophysics and microphysics and radiative transfer in sub grid scale is parameterised. Depending on research aims, models range from simple energy balance models that only consider energy budget in zero dimension to complex Earth System Models (see below). A general circulation model (GCM) is one type of complex climate model that provide a numerical solution to Navier-Stokes equations (fluid dynamics) with assumptions. An atmospheric general circulation model (AGCM) simulates the atmosphere dynamically by balancing the large-scale momentum, heat and moisture in the atmosphere with schemes of approximation of small-scale processes like precipitation, cloud formation and the heat exchange between the atmosphere and the surface of land and sea. Coupled atmosphere-ocean general circulation models (AOGCMs) include dynamical physical and chemical processes in the atmosphere, ocean, land and sea ice, and couple them together to represent climate system. A current state-of-art model is an Earth System Model (ESM), expanded on AOGCMs that additionally include representation of biogeochemical cycles and maybe additional components (dynamic vegetation and atmospheric chemistry etc.).

1.3.1 CMIP

Organised by the World Climate Research Programme's (WCRP) Working Group on Coupled Modelling (WGCM) under the auspices of the Climate Variability and Predictability (CLIVAR) project, the CMIP (Meehl et al., 1997), begun in 1996, assesses how the "state-of-the-art" coupled GCMs perform experiments. CMIP has become a major international multi-model research activity and developed over five phases (CMIP1 and CMIP2 Meehl et al. (1997, 2000); CMIP3, Meehl et al. (2007); CMIP5, Taylor et al. (2012); and CMIP6, Eyring et al. (2016)) that contribute to the IPCCs (CMIP3 to AR4 (IPCC, 2007); CMIP5 to AR5 (IPCC, 2013); and CMIP6 to AR6 (IPCC, 2021)). The latest CMIP6 (Figure 1.6) was designed to address three key scientific questions (Eyring et al., 2016):

- "How does the Earth system respond to forcing?"
- "What are the origins and consequences of systematic model biases?"
- "How can we assess future climate changes given internal climate variability, predictability, and uncertainties in scenarios?"

CMIP6 outputs have been gradually uploaded onto the Earth System Grid Federation (ESGF; Balaji et al., 2018) in a standardized format (Juckes et al., 2020). See Section 2.2 in Chapter 2 for details.

1.3.1.1 DECK experiments in the CMIP6

The Diagnostic, Evaluation and Characterization of Klima (DECK; Eyring et al., 2016) include four baseline experiments: *amip*, a historical Atmospheric Model

Intercomparison Project simulation; *piControl*, a pre-industrial control simulation; *abrupt-4xCO2*, a simulation forced by an abrupt quadrupling of CO_2; and *1pctCO2*, a simulation forced by a compound CO_2 increase of 1 percent per year. Detailed description and major purposes of the DECK can be found in Eyring et al. (2016). The DECK combined with the CMIP *historical* experiment serve as the entry cards for model groups to participate in the CMIP phases, and they provide the standards to establish model characteristics (Eyring et al., 2016). In this thesis, I use the DECK *piControl* simulations from the PMIP4-CMIP6 ensemble (see Section 2.1 and Appendix A for model descriptions). The protocol for DECK *piControl* and the biases in the *piControl* simulations as compared to observations are described separately in Section 2.3 and part of Section 6.3.

1.3.2 Equilibrium climate sensitivity

Climate sensitivity is the response in surface temperature to changes in atmospheric CO_2 concentration or other forcings; IPCC AR6 (IPCC, 2021c) clarifies the definitions in climate sensitivity: **Transient climate response (TCR)** is the instant surface temperature response with atmospheric CO_2 increases at a rate of 1% yr^{-1} from the pre-industrial level to the time of a doubling of the concentration; **Equilibrium climate sensitivity (ECS)** is the equilibrium change in surface temperature relative to pre-industrial in response to a doubling of CO_2 relative to pre-industrial level; **Earth system sensitivity (ESS)** is the equilibrium change in surface temperature response in the coupled atmosphere-ocean-cryosphere-vegetation-carbon cycle system to a doubling of the a doubling of CO_2 relative to pre-industrial level. The substantial difference between ECS and ESS is that ESS allows ice sheets to adjust to the external perturbation which contributes to a net positive feedback and causes ESS being larger than ECS.

The very likely range of ECS estimated in the AR6 is 2.5-4.0°C based on multiple lines of evidence (IPCC, 2021d), which is narrower than the estimation at 1.5-4.5°C in AR5 (IPCC, 2013). Zelinka et al. (2020) summarised that there are 27 climate models contributing to CMIP6 and estimate the ECS with a range of 1.8°C to 5.6°C, in which 10 of the 27 models exhibit an ECS exceeding 4.5°C. CMIP6 models estimate the ECS having a higher and wider range than CMIP5 models, as the 28 models provide the estimation of ECS within a range of 2.1°C to 4.7°C and only 2 models have an ECS higher than the upper limit of 4.5°C in AR5. Models and their ECS are given in Section 2.1.

The response in global surface air temperature to perturbed energy imbalance is traditionally treated following a linear relationship as $\Delta N = \Delta F + \alpha\Delta T$, where ΔN is the changes in net energy flux at the top of the atmosphere (TOA); ΔF is the effective radiative forcing that perturbs the TOA net energy flux; α is the net feedback parameter; and ΔT is the change in global surface air temperature. ECS can be estimated by $ECS = -\Delta F_{2xco2}/\alpha$. IPCC AR6 (IPCC, 2021c) gives the definition of an emergent constraint as: 'An attempt to reduce the uncertainty in climate projections, using an ensemble of ESMs to relate a specific feedback or future change to an observation of the past or current climate (typically some trend, variability or change in variability)'. Equilibrium change in palaeoclimate temperature could be used in the emergent constraint by regressing it against the ECS from models, which will get a relationship to translate a palaeoclimate change to ECS. Though with large uncertainties in both palaeoforcing and temperature reconstruction, estimating climate sensitivity from palaeodata benefits from estimating the ECS from archival observations rather than from models; having larger forcings than the instrumental periods as the magnitude is similar or even stronger than a doubling of CO_2; and having nearly equilibrium response as the forcing changed slowing in past (Forster et al., 2021). Currently, only the Last Glacial Maximum (LGM) cooling and the mPWP warming have been used in estimating ECS (Renoult et al., 2020).

1.4 Modelling palaeoclimates

Climate in the past (known as palaeoclimate) was different from the present, and so provides an out-of-sample test. Palaeoclimate modelling provides a chance to test the performance of models that are used to project future climate changes, to study the roles of forcings and their feedbacks that establish the palaeoclimate, and to assess whether the relationship between the palaeo-proxy and palaeo-variable is correct.

1.4.1 PMIP

The PMIP (Joussaume and Taylor, 1995) is one of the CMIP endorsed projects since its beginning in 1990. The aim of PMIP is to analyse how climate responds to past forcings and their major feedbacks, and to assess how credible the climate models can be used to project future climate. The mid-Holocene (hereafter referred to as MH) at 6 ka and the Last Glacial Maximum (LGM) at 21 ka were identified in the first phase of PMIP (PMIP1), with strong contrasting climate states and being able to compare reconstructed data and model simulations from AGCMs (Joussaume et al., 1999; Braconnot et al., 2000). These two periods have been the entry cards in the following phases of PMIP. PMIP has been improved in the subsequent generations, with the introduction of coupled AOGCMs and ocean-atmosphere-vegetation GCMs (OAVGCMs) in PMIP2 (Harrison et al., 2002; Braconnot et al., 2007) and the palaeoclimate simulations being produced by the same models and applied same configurations as the transient 20^{th} century and future simulations in PMIP3 (Braconnot et al., 2011, equivalent to CMIP5), which provided consistency between experiments. In addition to the MH and LGM, PMIP3-CMIP5 also included the Last Millennium between 850 and 1850 CE (past1000).

1.4.1.1 PMIP4

The latest phase of PMIP is PMIP4 (Kageyama et al., 2018, see Figure 1.6), which is equivalent to the CMIP6. In addition to the MH, LGM and past1000 in PMIP3, PMIP4 firstly include for the Last Interglacial (LIG) at 127 ka and the mid-Pliocene Warm Period (mPWP) around 3.3 - 3.0 Ma. PMIP4-CMIP6 experiments now include five periods, which from the most recent to the past are the past1000 (*past1000*; Jungclaus et al., 2017), the MH (*midHolocene*; Otto-Bliesner et al., 2017a), the LGM (*lgm*; Kageyama et al., 2017), the LIG (*lig127k*; Otto-Bliesner et al., 2017a) and the mPWP (*midPliocene-eoi400*; an experiment which also forms part of PlioMIP2 as described in Haywood et al. (2016b)). The *midHolocene* and *lig127k* experiments were designed to examine the response in the climate system to orbital forcings different from present (Otto-Bliesner et al., 2017a). Chapter 3 focuses on analysing the monsoonal changes in the *midHolocene* simulations as compared to the DECK *piControl* simulations, and Chapter 4 on the *lig127k* simulations. The *midPliocene-eoi400* experiment was designed to evaluate the response in climate system to a long-term CO_2 forcing similar to modern level (Haywood et al., 2016b). Chapter 5 provides analysis of the *midPliocene-eoi400* simulations.

1.5 Evaluation of climate model simulations: data-model comparison

Reconstructions and climate models are two contrasting but complementary sources that provide information for climates in the past. Reconstruction develops the profile of past climate and can be used for model evaluation and constraint, while climate models are tools to explore the mechanisms and drivers behind past climate change. Data–model comparison in palaeoclimate studies is useful to assess model performance in reproducing palaeoclimate features (e.g. Braconnot et al., 2012; Harrison et al., 2015).

Reconstruction is an approach to derive the spatial and temporal characteristics of a climate variable in the past from proxy data. A palaeoclimate archive (including ice cores, lake sediments, speleothems, marine sediments, tree rings) preserves evidence of climate change during past periods. A proxy (such as pollen and stable isotopes), contained within archives, is a record interpreted to represent a combination of some climate-related variations in the past by using physical and biophysical principles.

Proxies themselves do not directly show climate variables. Based on the modern relationships between climate properties (e.g. temperature, ice extent and vegetation) and biogeography or the relationship between the variable and proxy obtained in lab work, proxies are treated to reconstruct the climate when they formed through various techniques. A proxy can also be calibrated by comparing to another calibrated proxy (von Gunten et al., 2012). The process of turning a proxy record to a climate variable is called "calibration". Each different kind of proxy has its own way to be calibrated based on different principles (see the following subsections for examples).

Dating methods are used to determine chronologies, which give either the absolute age or relative age of archives and proxies. Estimating age methods (e.g. radiometric dating based on the rate of atomic decay like ^{14}C) directly provide estimations on age. Relative age methods (e.g. palaeomagnetic method based on the reversals of the Earth's magnetic field in the past and marine isotope stages based the cycle of oxygen isotope ratio) provide relative order of age of stratigraphic units. Equivalent age methods set up age-equivalence when separate sedimentary sequences have contemporaneous layers.

1.5.1 Ice cores for air temperature, precipitation and atmospheric composition

Continuous snow accumulation in the past, particularly in polar regions in Greenland and Antarctica, forms ice caps and ice sheets that contain large amount of information about past atmospheric conditions. For examples, ice's deuterium content (δ D$_{ice}$) and oxygen isotopic ratio (δ $^{18}O_{ice}$) can be used to reconstruct local temperature change (e.g. Jouzel et al., 2007). Entrapped air in the ice allows the measurement of atmospheric concentration of CO_2 (e.g. Bereiter et al., 2015) and CH_4 (e.g. Loulergue et al., 2008). Dust records contain the information of desert aerosols and the sodium concentration implies marine aerosols (e.g. Petit et al., 1990).

1.5.2 Marine sediment cores for sea surface temperature

Since 1968, deep sediment cores have been collected by the Deep Sea Drilling Project (DSDP), the Ocean Drilling Program (ODP) and the International Ocean Discovery Program (IODP) from different oceanic sites. Local palaeoSSTs are reconstructed from proxies in these cores. SSTs from marine sediments are commonly reconstructed by applying alkenone unsaturation index ($U_{37}^{K'}$) from phytoplankton algae which alters molecular composition of cell membranes in response to changes in water temperature by increasing the unsaturated alkenone production when temperature decreases (Brassell et al., 1986; Prahl and Wakeham, 1987). Mg/Ca rations from planktonic foraminifera (Mg/Ca; Barker et al., 2005) are also used to reconstruct temperature as the usage of Mg^{2+} or Ca^{2+} during the process of forming biogenic calcium carbonate is temperature dependent. Reconstructing temperature via tetraethers consisting of 86 carbon atoms (TEX_{86}) (Kim et al., 2008) is based on the relative number of cyclopentane rings in the liquid extracts. $\delta^{18}O$ records (e.g. Lisiecki and Raymo, 2005) from the benthic and planktic species precipitated in setiment cores are also used to reconstructed SST (e.g. Rostek et al., 1993).

1.5.3 Pollen records for air temperature and precipitation

The principle behind pollen-based reconstruction is that a taxon has its own bioclimatic limits. For a plant species, its geographic distribution can be estimated by an 'envelope' representing conterminous regions in climate space predominatly related to the seasonality of temperature and the availability of water supply (e.g. Woodward, 1987). Distributions of taxa overlap and constrain the climate space. Pollen-based reconstruction is based on the principle that knowledge of the past vegetation can be used to reconstruct the climate when they formed, based on their modern bioclimatic limits. For expamle, pollen records are converted into biome via the plant functional types (PFTs) method developed by Prentice et al. (1996). Pollen taxa are assigned into one or more PFTs according to the known biology of the species it includes. Affinity scores or each biome are calculated based on the characteristic PFTs it consist of. Pollen records are assigned into the biome with the highest affinity (Prentice et al., 1996). This method reduce the need for specific modern analogue. Biological variables are translated into climatic variables based on the bioclimatic limits of the PFTs. (Peyron et al., 1998) used artificial neural network technique to calibrate the pollen-based reconstructed climatic variables. Artificial neural network uses the PFTs as the inputs and outputs the bioclimatic variables at the pollen sites. The bioclimatic variables are transferred to climatic variables by comparing the bioclimatic variables with the acutal climatic variables to obtain the relationship. To provide greater confidence in the reconstructed changes, a multi-method approach is applied to assess the combined uncertainties of reconstruction and age models on a set of reference pollen records (Bartlein et al., 2011; Brewer et al., 2008).

1.5.4 Reconstructing monsoon climate

The first synthesis paper of the PAGES Global Monsoon Wroking Group (Wang et al., 2014b) summarised the proxy data used to show global and regional monsoons, which is shown here in Figure 1.7. If viewing the global monsoon system as a whole, Wang et al. (2014b) suggested that atmospheric CH_4 and $\delta\ ^{18}O_{atm}$ from ice core air bubbles and marine $\delta\ ^{13}C$ from deep sea sediments could reflect global monsoon intensity across time scales. There are two major types of proxies that have been used to reconstruct palaeomonsoon climate, those ones according to wind strength and the other according to precipitation. Wind-based proxies have long been used to determine the direction, persistence and/or strength of regional monsoon winds, in which aeolian dust (Sarnthein et al., 1981) and monsoon wind-driven upwelling indicators, *e.g. Globigeria bulloides* (Kroon and Ganssen, 1989), in marine sediments are commonly used. Dust from the Loess Plateau in China record the history of East Asian monsoon (e.g. An et al., 2001) by using particle size to estimate wind strength.

As the global monsoon system are more viewed as a hydrological process based on its concept, precipitation-based proxies are more useful to give the information of monsoon precipitation across time scales. Speleothem oxygen isotope records have drawn large attention in the last two decades being used to reconstruct local summer monsoon, because of its high resolution (annual) and precise dating from ^{230}Th (e.g. Cheng et al., 2012). $\delta^{18}O$ is commonly used to reconstruct rainfall amount or variability, as the spatial and temporal variation of $\delta^{18}O$ stored in cores reflects the climatic situation of original evaporation (tropical ocean) and subsequent condensation during the time the core formed. For example, $\delta\ ^{18}O$ from Hulu Cave (Wang et al., 2001; Yuan et al., 2004) and Sanbao Cave (Cheng et al., 2009) in China shows the changes in East Asian Monsoon. According to the concept of monsoon and the definition of global monsoon, the local summer precipitation in monsoon regions dominates local annual precipitation, which means that local annual mean precipitation could reflect monsoon strength. Therefore, reconstructed annual mean precipitation anomalies could be used to indicate changes in monsoon strength. In the following chapters, reconstructed annual mean precipitation anomalies are used in data-model comparison sections to evaluate how well the models can simulate monsoons in the past.

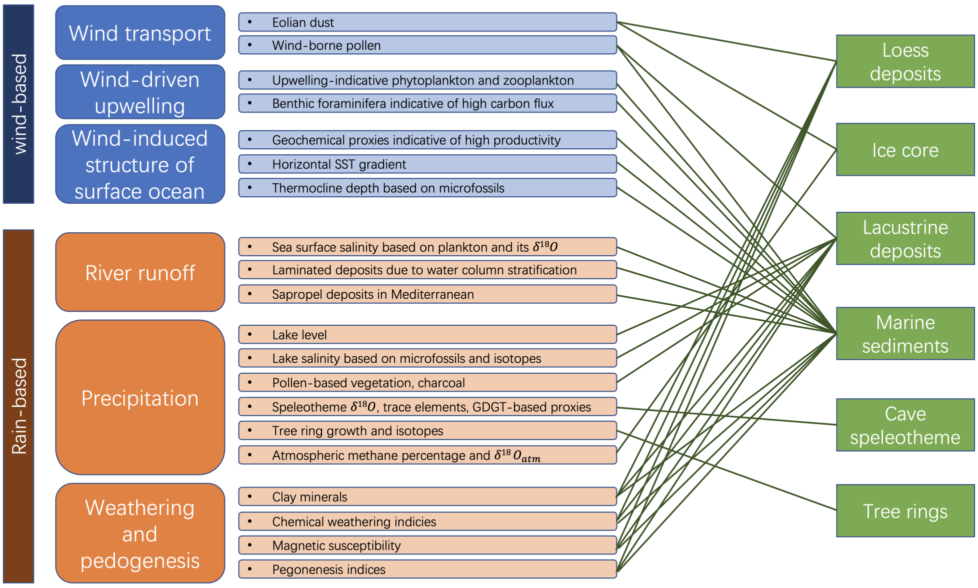

Figure 1.7: Proxies used in reconstructing palaeomonsoon climate (Wang et al., 2014b)).

1.5.5 Challenges in data-model comparison

Evaluating model performance by comparing its results to palaeodata has some important limitations from the insufficient quality of "data" considering variable, dating and spatial coverage. Each reconstruction approach has its own strength and weakness. The assumptions and methodology applied raises uncertainties or bias during reconstruction. Combining multiple proxies (i.e. compilation) reduces uncertainties and provides greater confidence in the reconstructed climate (e.g. Bartlein et al., 2011), but notably it can't entirely eliminate the uncertainties.

The "weight" of dating in uncertainties in climate reconstruction becomes important in mPWP, as it is difficult to determine accurate and precise chronology in deep time. When reconstructing MH and/or LIG climate, proxies are relatively abundant and dating is more accurate. Uncertainties in dating are less important in these two periods' data-model comparison. The coverage of proxy data also limits the comparison. The most recent period in this work, the MH, has relative abundant available proxies than the other two periods, but the coverage of MH reconstructions is still sparse or even missing in some regions with major gaps in tropical regions and in the SH (see Chapter 3). For the mPWP, the proxies are only available over the oceans with sparse coverage (Chapter 5). Challenges from the model side and in data-model comparison in this work are discussed in Chapter 6.

1.6 MH, LIG and mPWP climate and past findings on monsoon change

1.6.1 mid-Holocene

The Holocene is the current interglacial period starting from 11.7 thousand ago (Walker et al., 2009), during which the climate was dominantly affected by changes in orbital forcing and greenhouse gases (GHGs). Reconstructions suggest that global mean surface temperature (GMST) showed a rising trend in the early Holocene, reached its maximum around 7 ka and then followed by a gradual cooling from mid to late Holocene (Marcott et al., 2013; Kaufman et al., 2020a). The cooling is opposite to the warming simulated by models in response to the ice sheets retreat and GHGs increase. Liu et al. (2014) explain that this temperature conundrum was likely caused by the biases in both the seasonality of the proxy reconstruction and the climate sensitivity of current climate models. The MH, about 6 ka, is of great interest of the scientific community by having relatively simple changes in forcing compared to present, because the continental topography, land–sea mask and oceanic bathymetry during the period were similar to their modern conditions. Palaeoevidence shows that the aerosols during the mid-Holocene were less than pre-industrial (e.g. Albani et al., 2015). Ice sheets retreated rapidly though early Holocene and reached their modern condition before 6 ka except in a few places (Carlson and Winsor, 2012). Both proxy data (e.g. Bartlein et al., 2011) and simulations from climate models (Braconnot et al., 2000, 2007) suggest that the surface temperature at the mid-Holocene had stronger seasonality overall showing warmer boreal summer and cooler boreal winter in the Northern Hemisphere (NH) with relatively stronger changes occurring over land than over sea and over high latitudes than over mid to low latitudes as compared to the pre-industrial. The mean annual precipitation during the mid-Holocene was generally increased over the continents in the NH than today, with more increase in the high latitudes while less increase in the low latitudes (Harrison et al., 2015).

Earlier studies have investigated monsoon changes during the mid-Holocene through reconstructions and model simulations (e.g. Haug et al., 2001; Zhao and Harrison, 2012; Liu et al., 2004). Braconnot et al. (2002), Zhao and Harrison (2012) and Liu et al. (2004) provide analysis of simulated monsoon features at the mid-Holocene from PMIP ensembles and conclude that the increased summer insolation enhanced the summer monsoons in the NH with increased monsoon rain rate in western North America, northern Africa and eastern Asia. The SH had an opposite change as the reduced austral summer insolation weakened the summer monsoons with reduced monsoon rain rate in northern South America, southern Africa and northern Australia. Liu et al. (2004) and Zhao and Harrison (2012) suggest that ocean feedbacks amplify the increase in monsoons in the NH while reducing the decrease in monsoons in the SH at the mid-Holocene. Model simulations tend to underestimate the magnitude of changes in monsoonal precipitation and regions as compared to proxy data (Braconnot et al., 2007, 2012; Harrison et al., 2014, 2015). The example of this is the failure to reproduce the amplification of the north African monsoon (Perez-Sanz et al., 2014). More findings on regional monsoons are given in Section 3.3.3.2 in Chapter 3.

1.6.2 Last Interglacial

LIG, 129 to 116 thousand years before 1950CE), corresponding to Marine Isotope Stage 5e (MIS 5e), was characterised by seasonal cycles in insolation in the Northern Hemisphere (NH) stronger than that during the mid-Holocene. This interval was a warm climate state with strong polar warming in the NH and smaller ice sheets that contributed to higher sea level than today (Masson-Delmotte et al., 2013). The continental topography, land–sea mask and oceanic bathymetry during the period are considered similar to their modern conditions (Otto-Bliesner et al., 2017a). The reduction in ice sheets contributed to a rise in sea level of at least 5 m but not exceeding 10 m, with a best estimate at 6 m (Fox-Kemper et al., 2021). LIG has been recognised as an appropriate period to study interactions between climate and ice sheet in warm climate states. Capron et al. (2017) chose the interval of 127 ka as the most appropriate time interval to investigate the effects of a stronger orbital forcing on LIG climate as compared to the preindustrial when GHGs were similar or slightly lower than present day.

The amount of past studies on LIG monsoon changes is relatively less than the MH period. $\delta^{18}O$ records from stalagmites have shown enhanced Asian (e.g. Yuan et al., 2004) and African (e.g. Amies et al., 2019) monsoons. Scussolini et al. (2019) provides a near-global database of proxies for LIG precipitation and compared model simulations to this database. Their results show enhanced LIG monsoon in the NH and weakened monsoon in the SH. Notably, a recent multiproxy study (Wang et al., 2022b) found a weakened South Asian monsoon during the LIG due to higher Indian Ocean SST, which disagrees with the enhancement suggested by models.

1.6.3 mid-Pliocene Warm Period

The Pliocene Epoch spans from 5.33 to 2.58 million years ago (Ma). It was the most recent time in Earth's history when atmospheric CO_2 concentration exceeded 400 ppmv (Bartoli et al., 2011), and Pliocene topography was nearly the same as modern condition. The mPWP, also referred to as the mid-Piacenzian warm period in some studies, is a period roughly 3.3-3.0 Ma (defined as 3.29-2.97 Ma from Dowsett et al. (1999) or 3.26-3.03 Ma from Haywood et al. (2016a)) when the orbital configuration was similar to present. This period is recognised as the last period witih quasi-equilibrium warm climate before Pleistocene when climate had nearly fully responded to the high atmospheric CO_2 concentration (e.g. Haywood et al., 2010).

Under the RCP4.5 scenario, climate reaches equilibrium around the 2040s that is roughly equivalent to stabilizing at Pliocene-like climates. Understanding the environmental process in the mPWP provides a chance to understand how the climate system would respond to a perturbation in its radiative forcing, and evaluate the impacts of climate change caused by emissions (e.g. Haywood et al., 2016b; Pagani et al., 2010). The first study reconstructing regional Pliocene climate was conducted by Zubakov and Borzenkova (1988) based on more than 20 sequences from terrestrial and marine cores. They pointed out that the Pliocene Optimum could be a future analogue; with high CO_2 concentration and climate showing 100-300 kyr cycles with a 4-5 °C amplitude. In the early Pliocene, SST reconstruction shows tropical Pacific warm pool pattern via reduced temperature gradient between western equatorial Pacific (WEP) and eastern equatorial Pacific (EEP) SSTs (Wara, 2005; Dowsett, 2007; Zhang et al., 2014; O'Brien et al., 2014). The Pliocene climate was characterized by reduced temperature gradients (Haywood et al., 2013, 2020; Dowsett et al., 2013; Foley and Dowsett, 2019) from equator to pole e.g.(e.g. Dowsett and Poore, 1991) and from western to eastern Pacific Ocean (e.g. Wara, 2005). The latest PlioMIP2 simulates a warming of 3.2°C (2.1 to 4.8°C) compared to the pre-industrial control runs (Haywood et al., 2020). Based on the estimation of global sea surface temperature (GSST) and the relationship between changes in global mean surface temperature (GMST), proxy data suggested a warming in GMST of 2.5 - 4.0°C during the mPWP than 1850-1900 CE (Gulev et al., 2021).

The studies of mPWP monsoon change based on data were mainly focused on Asian monsoon due to the rare available geological evidence. Records suggest a wetter East Asian monsoon during the mPWP (e.g. Xiong et al., 2010; Nie et al., 2014). Li et al. (2018) analysed mPWP monsoon change at global scale by using the PlioMIP1 simulations and compared the results to the reconstructions that could potentially reflect mPWP monsoon change directly or indirectly. Their findings show that mPWP monsoon was generally enhanced, consistent with the reconstructions (Li et al., 2018).

1.7 Relationship to the PMIP4-CMIP6 publications, research question and outline

The primary description and analysis on the PMIP4-CMIP6 outputs have been published in the last two years (Otto-Bliesner et al., 2021; Brierley et al., 2020; Haywood et al., 2020; Kageyama et al., 2021). Their results have contributed to the assessment in IPCC AR6 (Gulev et al., 2021; Eyring et al., 2021; Forster et al., 2021; Douville et al., 2021). Part of the results written up in this thesis overlap with Brierley et al. (2020) and Otto-Bliesner et al. (2021). The analysis processes, combining contributions from several co-authors, have been published in Geoscientific Model Development as Zhao et al. (2022) under the title 'Analyzing the PMIP4-CMIP6 collection: a workflow and tool (pmip_p2fvar_analyzer v1)'. The usage of simulations and data in this work and the decisions made in analysis are the same as or similar to the papers. Similarity and difference between the publications and this thesis are given in the following chapters.

The PMIP4-CMIP6 *midHolocene* and *lig127k* analysis in Chapter 3 and Chapter 4 is subsequent to Brierley et al. (2020) and Otto-Bliesner et al. (2021), respectively. Chapter 5 uses four *midPliocene-eoi400* simulations that participated in (Haywood et al., 2020) with the reason given in Chapter 2 and 5. The major aim of this thesis is to answer the following two questions:

- 1. How well could the PMIP4 simulations be able to produce the climate patterns, focused on monsoon, in the MH, LIG and mPWP?
- 2. How does the global monsoon system respond to various forcings in the past warm periods outside the range of current limits? Forcings include the orbital focings in the *midHolocene* and *lig127k* simulations and the high atmospheric CO_2 concentration and mPWP boundary conditions in the *midPliocene-eoi400* simulations.

1.7.1 Outline of this thesis

To answer these questions this work is structured as follows:

Chapter 2 describes the methodology used in Chapters 3 to 6. This chapter introduces the models that have completed the simulations; presents the design of the *piControl* simulations and their bias; describes the general computing method for the analysis in this work; and explains the decision on calendar adjustment and the definition of monsoon domain.

Chapter 3 introduces the mid-Holocene climate, describes the protocol of the *mid-Holocene* experiment, and provides an analysis of the PMIP4-CMIP6 *midHolocene* simulations (including temperature, precipitation and monsoon response) aiming to answer: 1) Do PMIP4 models simulate the MH better than PMIP3 models? 2) If a model has a later version contributed to PMIP4, does it preform better than its earlier version contributed to PMIP3?

Chapter 4 provides an analysis of the PMIP4-CMIP6 *lig127k* simulations. This chapter has a similar analysing process as Chapter 3, but trying to deal with: 1) Does equilibrium climate sensitivity (ECS) relate to the quality of model's LIG simulation? 2) Do models with dynamic vegetation perform better?

Chapter 5 analyses the performance of the PlioMIP2 *midPliocene-eoi400* simulations and compares them with if the PlioMIP1 results. Two idealised aerosol experiments are introduced to investigate the potential for aerosols to affect simulating mPWP climate response, raising the potential importance of uncertainty in experimental setup in PlioMIP2.

Chapter 6 discusses the features across chapters. Discussion includes the response to different orbital forcing and different type of forcing. Source of uncertainty causing model-data mismatch and their contribution during different periods are discussed as well. Limitations of the work and suggestions for future works are also given in this chapter.

Chapter 7 gives a conclusion to the findings in this research.

Chapter 2

Methodology

This chapter provides the technical information used in the following Chapters 3 to 6. The contents of this chapter, combined with contributions from co-authors, has been published on Geoscientific Model Development as Zhao et al. (2022) under the title 'Analyzing the PMIP4-CMIP6 collection: a workflow and tool (pmip_p2fvar_analyzer v1)'. Here I will describe the steps taken in order from downloading files to producing the ensemble analysis, as well as the decisions made through the processes. Figure 2.1 shows a sketch of the workflow. At the beginning, I provide an overview of models participating in the CMIP5 and CMIP6 (Section 2.1), whose simulations were downloaded from the Earth System Grid Federation (Section 2.2). Section 2.3 describes the protocol of the CMIP6 DECK *piControl*, used as the control simulations to compute changes in variables, and presents the bias in these simulations. Ideas and effects of calendar adjustment are discussed in Section 2.4. After the adjustment, Section 2.5 describes how to post-process the PMIP4 outputs. Both normal and calendar-adjusted data files are post-processed via the Climate Variability Diagnostics Package (CVDP) to obtain major modes of international climate variability (2.5.1). These CVDP outputs are used as inputs in ensemble analysis (2.5.2) and monsoon analysis (2.5.3). Section 2.6 introduces the method applied to data-model comparison. The last section (2.7) gives a short summary of this chapter.

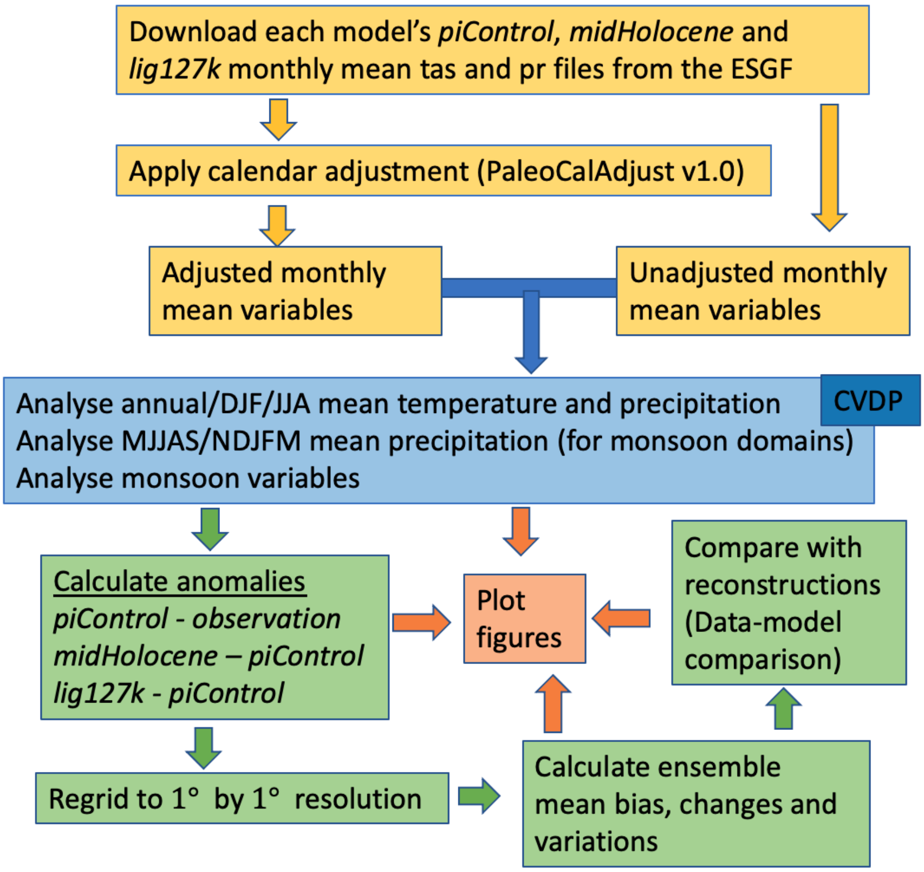

Figure 2.1: Schematic diagram illustrating the analysing processes of the PMIP4-CMIP6 ensemble.

2.1 Model ensembles

Following the description of climate model in Chapter 1 Section 1.3, the complexity of GCMs has increased from only representing dynamic atmospheric physics in mid 1970s to coupling dynamic changes in major components (atmosphere, land surface, ocean, sea ice and ice sheets (i.e. cryosphere) and biogeochemical processes) with better knowledge of climate systems and developments in computing availability. Improvements in models include better descriptions of physical process, improved model resolution and adjusted or tuned model parameters that provide a stable model climate after assembling the components. The CMIP5 models are AOGCMs and ESMs with improvements since CMIP3 contributing to IPCC AR4 (Flato et al., 2013), and the CMIP6 models have further improvements since the CMIP5 generation. Though with continuous improvements in model through generations, an individual model has its own bias and the uncertainty is difficult to quantify. Ensemble modeling is a process that uses multiple models to predict an outcome in order to increase the robustness of the prediction (see Section 2.5.2 for choices and challenges).

In this section, I will provide an overview of models involved in the ensemble analysis in Chapters 3 to 6. Model descriptions are given in Appendix A. Chapter 3 presents PMIP4-CMIP6 *midHolocene* simulations completed by 16 models. A similar number of models have performed the equivalent PMIP3-CMIP5 *midHolocene* simulations, which will also be included in Chapter 3 for comparison between the two phases of PMIP. Chapter 4 includes PMIP4-CMIP6 *lig127k* simulations completed by 17 models and Chapter 5 includes PlioMIP2 *midPliocene-eoi400* simulations completed by 4 models.

2.1.1 PMIP3-CMIP5 models

As briefly mentioned in Section 1.3.1, CMIP5 is the previous phase of CMIP and contributed to the IPCC AR5 (IPCC, 2013). PMIP3 is the corresponding phase of PMIP contributing to the palaeoclimate assessment in the IPCC AR5 (Christensen et al., 2013; Flato et al., 2013). PMIP3-CMIP5 models (Table 2.1) here are defined as the models that have participated in CMIP5 and completed *midHolocene* simulations, and only the PMIP3-CMIP5 *midHolocene* analysis is included in this thesis. The *midHolocene* experiment is one of endorsed CMIP5 experiment that also included in PMIP3 (Braconnot et al., 2011). Some of them are the previous generation of PMIP4-CMIP6 models. The involvement of the PMIP3-CMIP5 *midHolocene* simulations helps to evaluate if there is improvements between PMIP generations and between model generations. See Chapter 3 for more information about the PMIP3 *midHolocene* experiment.

2.1.2 PMIP4-CMIP6 models

CMIP6 is the latest phase of CMIP and supports the IPCC AR6 and has recently been released to public (IPCC, 2021a, see Sections 1.3.1 and 1.4.1 in Chapter 1 for more information). Since the publication of AR5 in 2013, model groups had

Table 2.1: Models contributing to the *midHolocene* simulations under CMIP5. The effective climate sensitivity (ECS) is preferentially taken from Andrews et al. (2012).

Model Name	ECS(K)	Key reference
BCC-CSM1-1	3.1	Xin et al. (2013)
CCSM4	2.9	Gent et al. (2011)
CNRM-CM5	3.3	Voldoire et al. (2013)
CSIRO-MK3-6-0	4.1	Rotstayn et al. (2011)
CSIRO-MK3L-1-2	3.1	Phipps et al. (2012)
EC-Earth-2-2	4.2	Hazeleger et al. (2012)
FGOALS-G2	3.7	Li et al. (2013a)
FGOALS-S2	4.5	Bao et al. (2013)
GISS-E2-R	2.1	Schmidt et al. (2014b)
HadGEM2-CC	4.5	Collins et al. (2011)
HadGEM2-ES	4.6	Collins et al. (2011)
IPSL-CM5A-LR	4.1	Dufresne et al. (2013)
MIROC-ESM	4.7	Sueyoshi et al. (2013)
MPI-ESM-P	3.5	Giorgetta et al. (2013)
MRI-CGCM3	2.6	Yukimoto et al. (2012)

put large efforts into model development. Climate models have been improved to their current versions participating in CMIP6. Table 2.2 lists the models that have completed the simulations of PMIP4 experiments that I analyse in Chapters 3 to 6. If a model has completed the DECK and historical simulations and uploaded to the ESGF, it would be recognised as a CMIP6 model. The rationale for the choice of the *midHolocene* and *lig127k* ensembles was whether the model had completed the simulations and been able to provide them before the two PMIP papers (Brierley et al., 2020; Otto-Bliesner et al., 2021) were published, respectively. Notably, AWI-ESM-2-1-LR has completed the PMIP4 *lig127k* experiment and and UofT-CCSM-4 has completed the PMIP4 *midHolocene*, but they are not included in CMIP6. Their simulations are used here, because they were included in the analysis of Otto-Bliesner et al. (2021) and Brierley et al. (2020), and I will not distinguish them as non-CMIP models following the decision in these two papers. Hereafter all of these models are referred to as PMIP4-CMIP6 models. AWI-ESM-1-1-LR, AWI-ESM-2-1-LR, MPI-ESM1-2-LR and NESM3 include interactive vegetation. 10 of these models have earlier versions that contributed to PMIP3-CMIP5 *midHolocene* emsemble, in which 6 of them show higher ECS than their earlier versions of CMIP5 models. For

Table 2.2: Models contributing to the *midHolocene* (MH), *lig127k* (LIG) and/or *midPliocene-eoi400* (mPWP) simulations under CMIP6.

Model	ECS (K)	Ref	Participation MH	LIG	mPWP
ACCESS-ESM1-5	3.9	Ziehn et al. (2020)		Y	
AWI-ESM-1-1-LR	3.6	Sidorenko et al. (2015)	Y	Y	
AWI-ESM-2-1-LR*	3.6	Sidorenko et al. (2015)		Y	
CESM2+	5.3	Gettelman et al. (2019)	Y	Y	Y
CNRM-CM6-1	5.1	Craig et al. (2017)		Y	
EC-EARTH-3-3+	4.3	Döscher et al. (2021)	Y	Y	
FGOALS-f3-L+	3	He et al. (2020)	Y	Y	
FGOALS-g3+	2.9	Li et al. (2020)	Y	Y	
GISS-E2-1-G+	2.7	Kelley et al. (2020)	Y	Y	Y
HadGEM3-GC31-LL+	5.4	Williams et al. (2018)	Y	Y	
INM-CM4-8	2.1	Volodin et al. (2018)	Y	Y	
IPSL-CM6A-LR+	4.5	Boucher et al. (2020)	Y	Y	Y
MIROC-ES2L+	2.7	Hajima et al. (2020)	Y	Y	
MPI-ESM1-2-LR+	2.8	Mauritsen et al. (2019)	Y	Y	
MRI-ESM2-0+	3.1	Yukimoto et al. (2019)	Y		
NESM3	3.7	Cao et al. (2018)	Y	Y	
NorESM1-F	2.3	Guo et al. (2019)	Y	Y	Y
NorESM2-LM	2.5	Seland et al. (2020)	Y	Y	
UofT-CCSM-4*	3.2	Chandan and Peltier (2017)	Y		

* Models that have completed PMIP4 protocols but do not participate in CMIP6.
+ Models that have earlier versions that contributed to PMIP3-CMIP5 *midHolocene*.

the *midPliocene-eoi400* simulations used in Chapter 5, only 4 models had done that and uploaded the simulation to the ESGF before I started writing my thesis.

2.2 Data availability

Each CMIP6 model was required to complete the DECK and historical simulations (and endorsed MIPs simulations if available) and wrote the outputs to netCDF files with one variable stored per file in standard format following the CMIP6 Data Request (DREQ; Juckes et al., 2020). Model groups have uploaded their files onto the Earth System Grid Federation (ESGF; Balaji et al., 2018, available at https://esgf-node.llnl.gov/search/cmip6/). Searching results on the ESGF can be restricted by selecting appropriate search constraints (e.g. Variable, Experiment ID and Frequency). PMIP4 monsoon changes in Chapters 3 to 6 are analysed by using monthly

Table 2.3: List of constrains and variables that were downloaded from the ESGF.

Experiment ID	*piControl, midHolocene, lig127k*	and *midPliocene-eoi400*
Variant label	r1i1p1f1	
Table ID	Amon	
Long name of variables	Near-Surface Air Temperature	Precipitation
Variable ID	tas	pr
Unit	K	kg m^{-2} s^{-1}
Descrption	near-surface (usually, 2 meter) air temperature	at surface; includes both liquid and solid phases from all types of clouds (both large-scale and convective)

near-surface air temperature and precipitation as initial inputs. Table 2.3 lists the constraints and the relevant information of the two variables that were downloaded from the ESGF. If not mentioned, all temperature analysis in this thesis is near-surface air temperature. Data used in this thesis was acquired for the *piControl* in the DECK and *midHolocene, lig127k* and *midPliocene-eoi400* in the PMIP4 if available. The variant ID of CMIP metadata is defined in a format of 'r1i1p1f1', where r is realisation, i is initialisation, p is physics, f is forcing and each number is the index for the corresponding configuration. Only a single variant that related to the design of PMIP4 Tier 1 experiments was selected for each experiment. r1i1p1f1 was selected if the model has multiple runs in that experiment: only r1i1p1f1 has been selected from the multiple FGOALS-g3 *midHolocene* runs; and only the r1i1p1f1 variant has been selected from the IPSL-CM6A-LR *midHolocene* which has four different forcings available (Braconnot et al., 2019b), as it related to the protocol of the Tier 1 *midHolocene*. Simulations completed by AWI-ESM-2-1-LR and UofT-CCSM4 have not been upload to ESGF, so the files were directly asked and collected from the corresponding model groups.

2.3 piControl simulations

The CMIP6 DECK *piControl* simulations are used as the control simulations in this thesis, i.e. changes in variables are referenced to the *piControl* by *experiment* - *piControl*. Following the description of CMIP6 DECK experiments in Section 1.3.1.1, the DECK *piControl* experiment uses coupled atmosphere–ocean with prescribed or calculated atmospheric CO_2 concentration for evaluation and unforced variability (Eyring et al., 2016). Table 2.4 lists the design of the *piControl* experiment. The CO_2 concentration is prescribed at 284.3 ppm, and the other two GHGs, methane and nitrous oxide, are at 808.2 ppb and 273 ppb. The concentrations are more realistic than the those in the CMIP5 prescribing CO_2 at 280 ppm, CH_4 at 760 ppb and N_2O at 270 ppb (Taylor et al., 2012). The solar constant used in the *piControl* is 1360.747 Wm^{-2}, which is slightly lower than the 1365 Wm^{-2} prescribed in CMIP5. According to Laskar et al. (2011), the orbital parameters are set to 1850 CE condition that was used in CMIP5, i.e. eccentricity at 0.016764, obliquity at 23.459°, and perihelion-180 at 100.33°. The vernal equinox is fixed to the noon on March 21st. Aerosol, vegetation and ice sheets are either interactive or prescribed as modern condition depending on individual model design. Model groups run their *piControl* simulations for a few hundred to a few thousand model years to reach an equilibrium state.

2.3.1 Bias in the *piControl* simulations

As the CMIP6 models that have completed the experiments are different, results in this section are shown separately for the *piControl* ensembles used to as the control for the three PMIP4-CMIP6 experiments. Because the temperature variables presented in following chapters are calculated from surface air temperatures and there are few spatially-explicit observations for the pre-industrial, this section compares the spatial pattern of the surface air temperature in the *piControl* with the C20-Reanalysis mean surface temperatures between 1851-1900 CE (Compo et al., 2011), which is available at https://psl.noaa.gov/data/gridded/data.20thC_ReanV2c.html [last assessed on 31 July 2021]. The zonal averages are compared to the averages of observed temperature for the period 1850-1900 CE from the HadCRUT4 dataset

Table 2.4: *piControl* experimental design

	CMIP6	CMIP5
Time period	1850 CE	1850 CE
Orbital parameters		
Eccentricity	0.016764	0.016764
Obliquity (°)	23.459	23.459
Perihelion – 180 (°)	100.33	100.33
Vernal equinox	Fixed to noon on 21 March	Fixed to noon on 21 March
GHGs		
Carbon dioxide (ppm)	284.3	280
Methane (ppb)	808.2	760
Nitrous oxide (ppb)	273	270
Other GHGs	CMIP DECK piControl	0
Solar constant (W m^{-2})	1360.747	1365
Paleogeography	Modern	Modern
Ice sheets	Modern	Modern
Vegetation	CMIP DECK piControl	Prescribed
Aerosols: dust, volcanic, etc.	CMIP DECK piControl	Prescribed

(Morice et al., 2012; Ilyas et al., 2017). The annual and seasonal mean precipitation rates in the *piControl* are compared to a modern climatology of 1971-2000 from the Global Precipitation Climatology Project (GPCP; Adler et al., 2003), due to the lack of sufficiently complete early observations. The bias in the *piControl* simulations reveals the problems in model components, which requires further improvements in models and the understanding of the processes in climate. This section only describes the bias patterns. Their effects on simulating monsoon response are discussed in corresponding sections in following chapters.

2.3.1.1 Bias in temperature

Multi-model means of zonal-average temperature bias (Figure 2.3) shows that models contributed to PMIP4-CMIP6 *midHolocene* and/or *lig127k* produce slightly cooler than observations at NH high latitudes while warmer at SH high latitudes. Spreads across the ensemble are large at high latitudes. The warmer SH high latitudes bias is affected by the large warm bias produced by MIROC-ES2L and EC-Earth3-LR. MIROC-ES2L's warm bias over SH high latitudes is associated

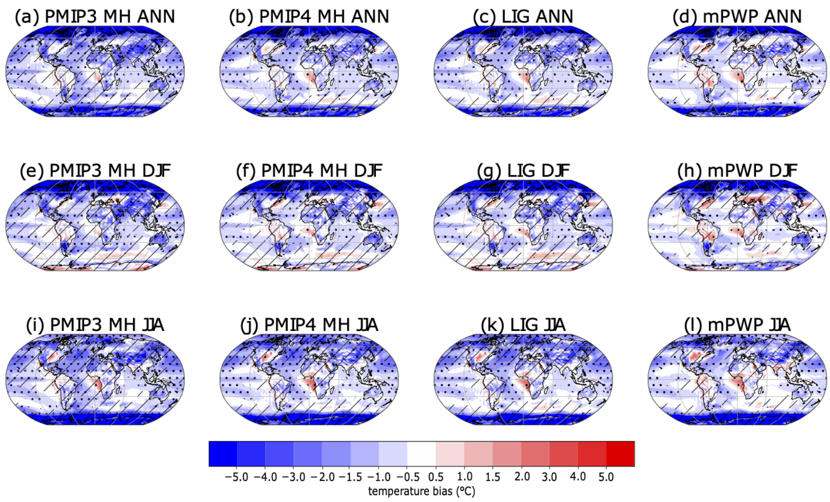

Figure 2.2: Comparison of the CMIP6 ensemble used in *midHolocene*, *lig127k* and *midPliocene-eoi400* to observations – surface air temperature in °C. Dots mark the region where at least 80% of the models agree on the sign of MMM. Dash lines mark the region where the standard deviation is larger than 1.0 °C. Bias in the individual simulations are given in Appendix A3.

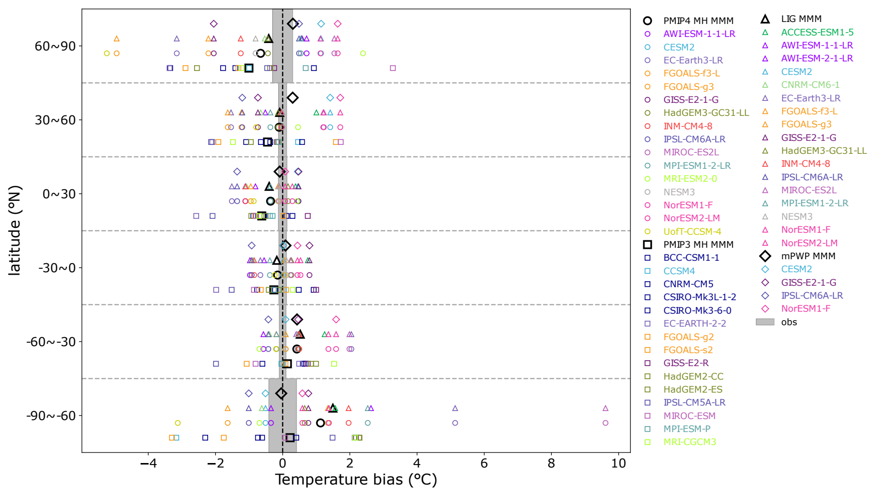

Figure 2.3: Comparison of the pre-industrial zonal mean temperature profile of individual climate models and MMM to the 1850-1900 observations. The area-averaged, annual mean surface air temperature for 30° latitude bands in the CMIP6 models and a spatially complete compilation of instrumental observations over 1850-1900 (grey shading, Morice et al., 2012; Ilyas et al., 2017).

with the cloud radiative processes represented by the model (Hajima et al., 2020). The bias has been reduced in some of the models since the PMIP3-CMIP5 generation except the SH mid and high latitudes (Figure 2.3), and the spread across the ensemble has been reduced. Figure 2.2 shows the observation and the ensemble mean bias (referred to as the mean difference between the pre-industrial climatology of each model and observation). Dots in panels mark the region where at least 80% of the models agree on the sign of MMM and dash lines mark the region where the standard deviation is larger than 1.0 °C. PMIP4-CMIP6 models in general show cooler bias than the observations, most noticeably in the poles, over land (except the southeastern region of the North America due to the warmer gulf stream), the NH oceans and the Labrador Current. The seasonal panels show that models simulate colder winter than expected from the observations. Though the match in annual mean temperature between models and the observations/reanalysis appears satisfactory in the tropics, the north polar region is noticeably too cold in both the annual and seasonal mean. The eastern boundary ocean upwelling regions, Atlantic and Indian Ocean sectors of the Southern Ocean are too warm in models. The Antarctica, the Gulfstream, the Kuroshio Current and the Indian Ocean sectors of the Southern Ocean are warmer in DJF than in JJA, while the South Atlantic and the land over the southeastern region of the North America show the opposite trend. The mismatches indicate a difficulty in sufficiently resolving the regional ocean circulation features. The PMIP4-CMIP6 generation also includes simulations with dynamic vegetation, for example. The associated vegetation-snow albedo feedback would tend to reduce the simulated cooling (e.g. O'ishi and Abe-Ouchi, 2011), but can introduce a larger cooling bias in the *piControl* simulations (Braconnot et al., 2019b). However, changes in the treatment of aerosols in the PMIP4-CMIP6 ensemble could enhance the simulated cooling (Pausata et al., 2016; Hopcroft and Valdes, 2019).

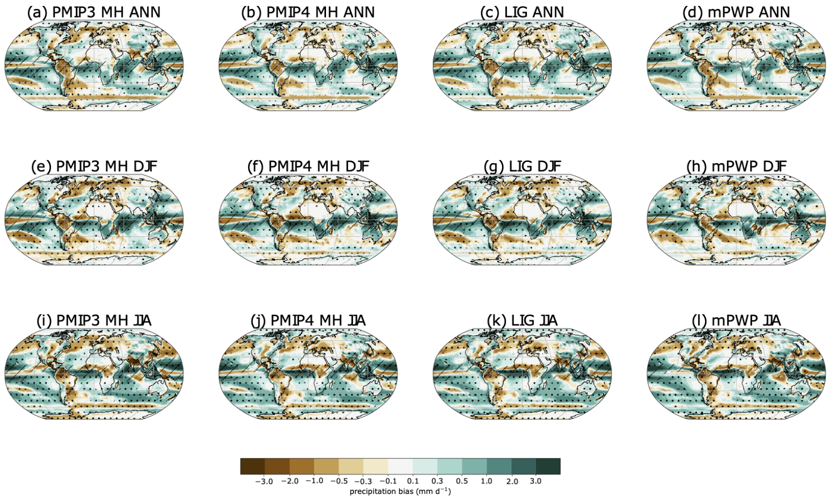

Figure 2.4: Same as Figure 2.2 but for precipitation in mm d^{-1}. The *piControl* simulations are compared to the GPCP (Adler et al., 2003).

2.3.1.2 Bias in precipitation

Figure 2.4 shows that models fail to sufficiently capture the precipitation's magnitude and distribution. Individual models still show complex bias in simulating annual and seasonal precipitations. The bias has been reduced as compared to CMIP5-PMIP3. The precipitation in the ITCZ is generally underestimated, while that over the adjacent ocean regions is overestimated. The southern portion of the SPCZ is too zonal, due to the poor representation of the meridional SST gradient between the Equator and 10°S in the west Pacific (Brown et al., 2013). CMIP6-PMIP4 models underestimate the precipitation over the ocean region, the Europe and the western Eurasia in mid-to-high latitudes. Models also exhibit a dry bias over the upwelling regions in the Southern Ocean and the Antarctica.

The domain-averaged rain rates over eastern Asia, South America, southern Africa and the Australian–Maritime Continent are likely to be overestimated in the *piControl* simulations (Figure 2.5a). The areal extent in the *piControl* simulations is underestimated over the NH monsoons except southern Asia and overestimated over the Australian–Maritime Continent (Figure 2.5b). The largest bias in monsoonal variables is the underestimation in the areal extent over northern Africa. Discussion

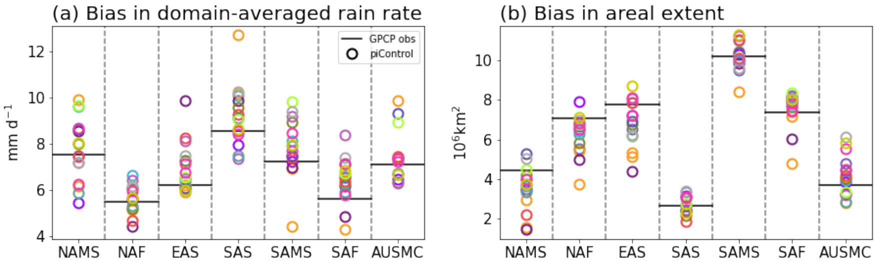

Figure 2.5: Bias in the domain-averaged and areal extent of regional land monsoons.

in Chapters 3 and 4 show that the North African monsoon poleward extension in the *midHolocene* simulations only remove the bias in *piControl*, which could be a explanation to the underestimation compared to the reconstruction (Harrison et al., 2015; Brierley et al., 2020).

2.4 Calendar adjustments

2.4.1 Calendar effects and adjustments

As shown in Section 1.2.1, the orbital configurations at the MH and the LIG were different from those at 1850 CE, which means that aggregating up daily output to monthly averages using a 'fixed-length' (fixed number of days in months) calendar to define the number of days in each month could incorporate the palaeo simulations of a particular month from a different position along the Earth's orbit. Instead, a 'fixed-angular' (fixed angle degrees in the Earth's orbit for months) calendar to define the length of each month should be considered, as this method alters number of days in months based on the variations in the orbit. Kepler's equation could be used to calculate the fixed-angular length of months varying over time (Curtis, 2014). As discussed in Joussaume and Braconnot (1997), the vernal equinox is the fixed starting point for orbital calculations. Matches in model-model or data-model comparisons that are actually caused by palaeo calendar effects may lead to misunderstanding in climate mechanisms in the past. As when comparing palaeo experiments with pre-industrial simulations or observations to obtain the change in monthly or seasonal climate patterns, inappropriate incorporation of monthly data may produce simulated changes similar to those observed climate changes.

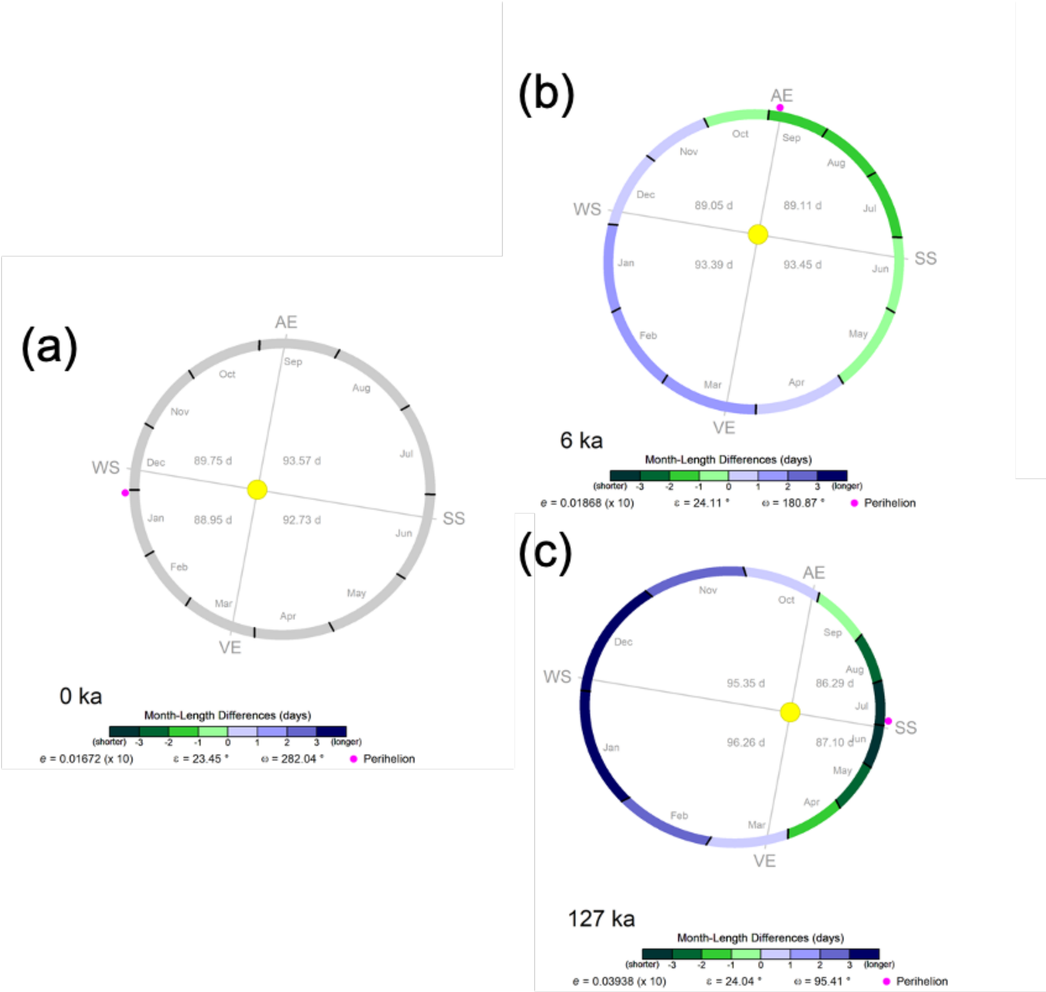

Figure 2.6: Calendar effects at 6 ka and 127 ka. The adjusted start date, end date and number of days of each month at (b) 6ka and (c)127ka as compared to (a) 0ka. Note that the vernal equinox (VE) remains fixed as 21st March. Figures are adapted from https://github.com/pjbartlein/PaleoCalAdjust; Bartlein and Shafer (2019).

Bartlein and Shafer (2019) provide a calendar adjustment method to solve palaeo-calendar effects in the latest PMIP4-CMIP6 simulations that are produced and stored in the format adopted by CMIP. The approach includes three major steps: (1) determine the appropriate lengths of months by fixed-angle for a PMIP4 palaeo experiment; (2) if the input file is monthly means, interpolate the monthly data to daily averages via mean-preserving method; and finally (3) interpolate daily data back to monthly data by accumulating or averaging according to the start and end days from the first step (Bartlein and Shafer, 2019). This method has been written into a set of Fortran 90 programs and modules (PaleoCalAdjust v1.0), and a detailed description of the software and usage can be found in Bartlein and Shafer (2019). Figure 2.6 shows the shifts in month characteristics at 6 ka and 127 ka referenced to the present-day (1850 CE). Shifting in the start and end days of months shows the climatic precession, while variations in number of days reflect changes in perihelion.

Month lengths were shorter in the MH than the present-day from May to October with greatest decrease in August, and the perihelion occurred in September. Differences between the mid-month day and June solstice reduced from April to December, with greatest differences occurring in November at 5 days closer (Bartlein and Shafer, 2019). In the LIG, month lengths were shorter than the present-day from April to September with greatest decrease in July, and the perihelion occurred in July. Differences between the mid-month day and June solstice were closer from July through December, with greatest differences occurring in September and October at 12.80 days and 12.70 days closer (Bartlein and Shafer, 2019). Both two past warm periods had relative longer boreal winter months that started and ended earlier than the present-day and relatively shorter boreal summer months. These calendar effects alter the mid-month insolation at different latitudes both in short-term and long-term.

2.4.2 Evaluation on the effects of calendar adjustments

According to the mechanism described above (Section 2.4.1), calendar adjustment would affect the start/end date and the number of days of each month but would not alter the total number of days of a year. Logically, annual mean temperature and precipitation would not be affected by calendar adjustment. Annual mean variables used in this work are not adjusted. Bartlein and Shafer (2019) evaluate the effects of calendar adjustment on the several variables by using PMIP3-CMIP5 simulations. For monthly mean temperature, calendar effects are generally consistent with the effects on insolation. Calendar effects on monthly precipitation are more complex as they are associated with spatial movements in the ITCZ and monsoon patterns. Results in Bartlein and Shafer (2019) show that adjusting the calendar affects the spatial pattern of monthly temperature and precipitation at 6 ka and 127 ka. This implies that seasonal temperature and precipitation at 6 ka and 127 ka has calendar effects. Therefore, calendar adjustment is applied in calculating seasonal (JJA and DJF) mean *midHolocene* and *lig127k* temperature and precipitation.

For variables that change abruptly (monsoon variables in this work), the calendar adjustment tool may not be an appropriate method to correct calendar effects if using monthly averaged files as inputs. To investigate how the PaleoCalAdjust software could impact the accuracy of abruptly changing variables, averaged summer rain rate during the monsoon season in global monsoon domain regions in the IPSL-CM6A-LR *midHolocene* simulations is analysed here by comparing the rain rate computed from daily and monthly mean precipitation. The definition of monsoon domain and monsoon summer rain rate are described in section 2.5. Months during the monsoon season are assumed to have the same number of days in averaging, which means that the monsoon summer rain rate is taken as the average monthly precipitaion rate of the five months instead of the weighted average taking the difference in the number of days of the months into account. This is the approach advised in CVDP.

As shown in Figure 2.6, calendar adjustment affects the start date, length (total number of days) and end date of monsoon season in both hemispheres. Overall, the summer rain rate calculated from the unadjusted monthly mean precipitation rate (here after referred to as unadjusted monsoon summer rain rate) shows wetter bias in monsoon regions as compared to the accurate monsoon summer rain rate calculated from daily-resolution precipitation (referred to as accurate monsoon summer rain rate) as shown in Figure 2.7a, except in the East Asian Monsoon region where shows a slight drier bias instead. Figure 2.7b shows the difference between the summer rain rate calculated from adjusted monthly mean precipitation rate (referred to as adjusted monsoon summer rain rate respectively) and the accurate monsoon summer rain rate. Calendar adjustment causes a drier bias in all monsoon regions (Figure 2.7b), and the magnitude is larger than the wetter bias shown in panel a. Therefore, the monsoon analysis in the following chapters uses unadjusted monthly mean precipitation.

The Southern American Monsoon System (SAMS; Figure 2.7) is selected as an example to look into a single monsoon domain, as it is isolated from the other regional monsoons. The summer monsoon rate is underestimated after the adjustment, and the magnitude is larger than unadjusted one that shows a slight overestimation. The bias (i.e. the difference in SAMS summer rain rate between that calculated from adjusted/unadjusted monthly precipitation rate and from daily rate) is -0.33 mm d^{-1} (-5.14% relative to the daily one) from the adjusted monsoon summer rain rate, whose magnitude is greater than the wetter bias (0.12 mm d^{-1}, 1.8%) from the unadjusted monsoon summer rain rate. Figure 2.7d shows the temporal changes in averaged precipitation rate over SAMS and the effects of calendar adjustment on it. The precipitation rate in the SAMS increases sharply from November and then reaches its maximum at the end of January, which means that in this period the monthly mean rate of each month is lower than the daily rate at the end of the month. The beginning date of November at 6 ka is 5 days earlier than the date in 0 ka. The start date and end date of each month in NDJFM in mid-Holocene are both earlier than those in the 1850 CE, except the end date of March which is the same. When adjusting the calendar effects from November to January, the new adjusted monthly mean precipitation rate accumulates a few days' daily rate estimated from the earlier month's old unadjusted monthly rate which is lower than the daily rate at the end of the month that should actually be accumulated. In opposite, the adjustments on the monthly mean precipitation in February and March result in a wetter bias, but the magnitude is less than the drier bias from November to January (Figure 2.7d). The wetter bias in the unadjusted monthly mean precipitation rate is caused by the fact that the rate is calculated over a slight afterward shifting period that misses a few days at the beginning with less rain but covers more days at the end with more rain. Overall, the adjustment brings a drier bias in monsoon summer rain rate and its magnitude is larger than the wetter bias from the unadjusted monthly mean precipitation. According to the magnitude of bias, calendar adjustment is not carried out on monsoon variables in this thesis.

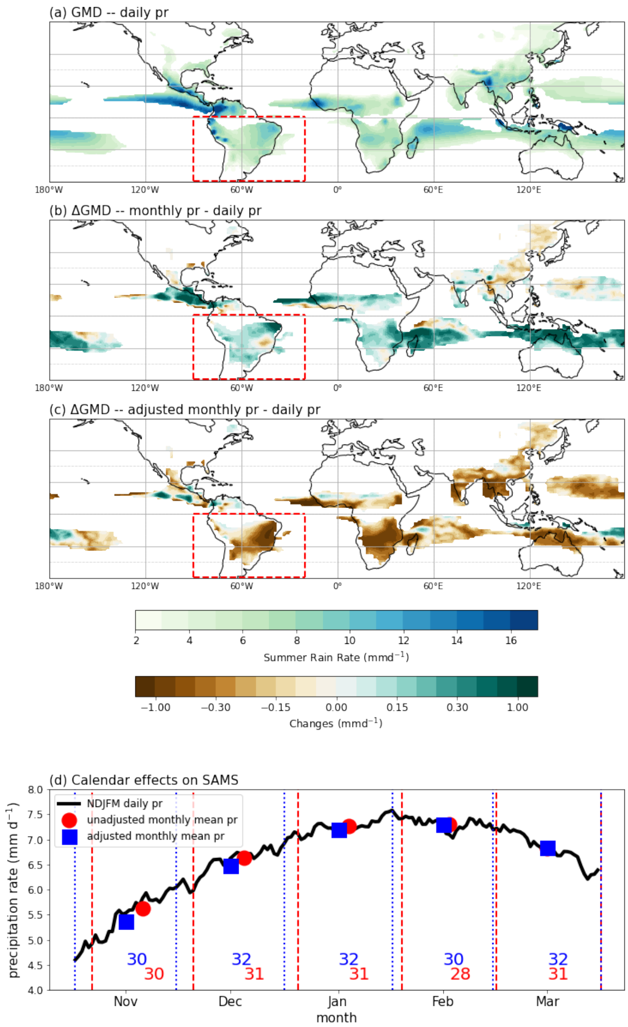

Figure 2.7: Effects of calendar adjustment on global monsoon domain (GMD). (a) The MH GMD calculated from IPSL-CM6A-LR *midHolocene* daily precipitation rate (GMD_{daily}). (b) The difference between the GMD calculated from unadjusted IPSL-CM6A-LR *midHolocene* monthly mean precipitation ($\mathrm{GMD}_{unadjusted}$) and panel (a), i.e. $\mathrm{GMD}_{unadjusted}$ - GMD_{daily}. (c) same as panel (b) but for the difference between the GMD from adjusted monthly precipitation and panel (a) ($\mathrm{GMD}_{adjusted}$ - GMD_{daily}). (d) Effects of calendar adjustment on the Southern American Monsoon System (SAMS; marked as red dashed boxes in panels a to c). Area averaged adjusted (blue squares) and unadjusted (red circles) monthly mean precipitation over SAMS are compared to daily precipitation (thick black line). Blue dotted (red dashed) lines in the figure are the adjusted (unadjusted) begin dates of each month. The numbers at the bottom are the number of days in each month, blue for adjusted and red for unadjusted.

2.5 Processing PMIP4 outputs

NetCDF files of monthly time series are used as inputs of the Climate Variability Diagnostics Package (CVDP; Phillips et al., 2014) to provide the spatial patterns of annual and seasonal mean surface air temperature and precipitation rate. CVDP also computes spatial patterns of monsoon intensity and summer rain rate and time series of rain rate and areal extent of regional monsoons (see Section 2.5.3 for definitions of these monsoonal variables). These CVDP outputs are then used as inputs in the ensemble analysis as described in Section 2.5.2.

2.5.1 CVDP

The CVDP was developed by the National Center for Atmospheric Research (NCAR)'s Climate Analysis Section to improve and facilitate the evaluation of major modes of international climate variability, like ENSO and AMO, in models and observations. This package computes spatial patterns, standard deviation and trend maps, climatological fields, power spectra and time series of climate variability in any user-specified model simulations whose files fit CMIP5/CMIP6 output standards. Analysis results of each model are presented via web pages including a summary table that contains model performance for key metrics of international variability shown as pattern correlations and RMSE compared to the chosen observations. Outputs are saved as a single netCDF file containing the information for each variable. This package has been adapted for palaeoclimate purposes (Brierley and Wainer, 2018). Scripts of this palaeo version are available from `https://github.com/pmip4/CVDP-ncl`. The orginal CVDP code is available at `https://www.cesm.ucar.edu/working_groups/CVC/cvdp/`

The CVDP package is written in NCL, which requires the installation of NCL. Driving scripts are named by the calculations, e.g. tas.mean_stddev.ncl computes and returns the global means and standard deviations of 2m air temperature. There are 4 steps to run the package:

- 1: Set the namelist that contains the information of simulation files being used as the input, in a format of "`Model_name experiment_name | path | start_year | end_year`".
- 2 (optional): If observation is used, set the namelist_obs file that contains the information of observational dataset.
- 3: Modify and run driver.ncl. User-adjustable options are located at the top of the script. There's no need to change the rest of the code.
- 4: Examine the CVDP output. CVDP outputs are saved as netCDF files. Analysis results of each model are presented via webpages, which also include a summary table comparing model performance against any chosen observations.

2.5.2 Ensemble analysis

The purpose of using ensembles is to explore the uncertainty in model simulations arising from different aspects from climatic internal variability to model physics (Knutti et al., 2013; Tebaldi and Knutti, 2007), however it has also been used in projecting climate change and evaluating model performance. A multi-model ensemble samples internal variability and structural uncertainty. Unweighted multi-model means is commonly used to characterise multi-model ensemble results, based on the assumptions that all models are independent, each model contributes same number of simulations, and each model has fared no difference in objective evaluation. Although multi-model ensembles have limitations (Masson and Knutti, 2011), the climate variables in this methods are broadly reliable on global scale as compared to observations (Yokohata et al., 2012). IPCCs (e.g. Flato et al., 2013; Eyring et al., 2021) have used multi-model mean in model evaluation. The ensemble analysis in this thesis uses this approach of equal-weighted multi-model means.

The initial analysis of changes in annual and seasonal mean temperature and precipitation in this thesis are applied by using CVDP (Phillips et al., 2014; Brierley and Wainer, 2018). According to the evaluation of the calendar effects on monthly mean temperature and precipitation in 6 ka and 127 ka as described in Bartlein and Shafer (2019), analysis of seasonal (JJA and DJF) changes in temperature and precipitation uses the adjusted monthly mean "tas" and "pr", while other analysis uses the unadjusted variables instead. Changes in each CMIP-PMIP generation are shown as the ensemble mean changes, i.e. the average of the change (*experiment - piControl*) produced by individual models. As each model uses a different resolution, anomalies in each model are firstly regridded to 1° x 1° resolution using a bilinear interpolation before calculating the ensemble mean changes and variations. The regridded coordinates of latitude (°N; hereafter referred to as regridded lat) are -89.5, -88.5,..., 88.5, 89.5. The regridded coordinates of longitude (°E; hereafter referred to as regridded lon) are -179.5, -178.5,..., 178.5, 179.5. The ensemble mean is calculated as the average of the regridded anomalies in each model within the group. The ensemble variation is the standard deviation of the regridded changes in all available PMIP3-CMIP5/PMIP4-CMIP6 models. Difference between the two CMIP-PMIP generations is calculated as changes in the ensemble-mean of PMIP4-CMIP6 minus the ensemble-mean of PMIP3-CMIP6.

2.5.3 Monsoon analysis

In palaeoclimate, as the monsoon domain varies through time, it is not appropriate to use fixed monsoon domain boundary for the present-day here. Following Section 1.1.2, the definition of monsoon domain in Wang and Ding (2008) and Wang et al. (2014b) is used here to apply on the ensemble mean summer rainfall and monsoon intensity. A local summer is defined as May-September (MJJAS) in the Northern Hemisphere (NH) or November-March (NDJFM) in the Southern Hemisphere (SH). A local winter is defined as NDJFM in the NH and MJJAS in the SH. Averaged summer rain rate is the averaged daily rain rate in the summer. Monsoon intensity is the difference in averaged daily precipitation rate between local summer and local winter. The definition of the monsoon is that at least of 55% of the annual total rainfall comes from summer, and the monsoon intensity is no less than 2 mm d^{-1}. Global monsoon domain maps are contoured as monsoon summer rain rate.

As mentioned in Section 1.1.2 in Chapter 1, the definition of regional land monsoon in IPCC AR6 (Douville et al., 2021) differs from those in IPCC AR5 (Christensen et al., 2013). In order to staying consistent with Brierley et al. (2020) and Otto-Bliesner et al. (2021), I will keep using the definition by Christensen et al. (2013) to compute and analyse regional monsoons. Seven regional monsoons are North American Monsoon System (NAMS), North African monsoon (NAF), South Asia monsoon (SAS), and East Asia summer monsoon (EAS) in the NH and South American Monsoon System (SAMS), South African monsoon (SAF), and Australian–Maritime Continent monsoon (AUSMC) in the SH. The south Asian monsoon and east Asian monsoon. SAS and EAS separate along the longitude at 105°E and the latitude at 20°N. Five diagnostics for each individual monsoon are defined as:

- the change in the area-averaged monsoon summer rain rate (hereafter referred as to “pav”), which is the change in monsoon summer rain rate averaged over the monsoon domain;
- the standard deviation of interannual variability in the area-averaged summer rain rate (hereafter referred as to “psd”), which is change in the standard deviation of the 1D time series of area-averaged summer rain rate;
- the change in the areal extent of the monsoon domain (hereafter referred as to “aav”), which is the change in averaged area of monsoon domain;
- the change in standard deviation of the year-to-year variations in the areal extent of the regional monsoon domain (hereafter referred as to “asd”), which is the change in standard deviation of the 1D time series of domain area;
- and the change in total amount of precipitated water (hereafter referred as to “totwater”), which is the change in cumulative monsoonal rainfall over the domain as area-averaged summer rain rate x domain area (i.e. totwater = pav x aav).

These monsoon diagnostics are calculated as percentage changes by (*experiment*

-*piControl*) x 100% / *piControl*). Results are shown as unfilled coloured shapes (see figure captions) which colours are chosen according to the colour guidelines provided by IPCC-WG1 (available at https://github.com/IPCC-WG1/colormaps; last assessed on 17th May 2021). PMIP3-CMIP5 models are coloured same as their updated versions of PMIP4-CMIP6 models if available, otherwise they are coloured by dark blue.

2.6 Data model comparison

As introduced in Section 1.5, comparing simulated features to reconstructions allows to evaluate how climate models can reproduce the climate. In the following chapters, data model comparison is conducted by comparing the similarities and mismatches between simulated anomalies and observational evidence of past climates. Detailed description of proxy compilations are provided in corresponding chapters. For spatial maps, reconstructed data points are directly overlapped at sites on the regridded ensemble mean anomalies obtained from Section 2.5.2, and are coloured by using the same color map and magnitude scale as that applied to the map of simulated anomalies. For the points of single sites, the latitude (longitude) of each data point is rounded to its nearest regridded lat (regridded lat). Simulated anomalies are collected at these regridded coordinates as the site-level points produced by individual models. For the points of global (regional) spatial coverage, the model simulations are sampled only at grid points (regridded coordinates) where there are reconstructions available due to the poor global coverage of available reconstructions. Averages are taken as equal-weighted means of sampled points regardless of where the data points are, which means ignoring the latitudinal weight. This means that site-level data-model comparison is site-level averaged difference between data and simulations with a global/regional spatial coverage.

2.7 Summary

This thesis uses the PMIP3-CMIP5 and the PMIP4-CMIP6 simulations that have contributed to the relevant assessment in the IPCC AR6 (Gulev et al., 2021; Eyring et al., 2021; Douville et al., 2021). There are currently 19 PMIP4-CMIP6 models that have completed the PMIP4 *midHolocene* (16), PMIP4 *lig127k* (17) and/or PlioMIP2 *midPliocene-eoi400* (4) simulations (Table 2.2), and 15 PMIP3-CMIP5 climate models produced PMIP3 *midHolocene* simulations (Table 2.1). The *pi-Control* simulations are used as the control simulations to compute changes. This chapter introduced the ensembles, describes the general computing method for the analysis in the following chapters, presents the decision on calendar adjustment, and the definition of monsoon domain.

Monthly mean variables involved in this thesis were downloaded from the ESGF and applied calendar adjustment on those gradually changed variables like seasonal mean surface air temperature and precipitation, and not applied on those changing abruptly like monsoon domains as the adjustment would bring drying bias. The files are the inputs of the CVDP, a package to improve and facilitate the evaluation of major modes of international climate variability, to compute the spatial patterns of annual and seasonal surface temperature and precipitation monsoon variables (summer rain rate and intensity) and the time series of regional monsoon variables. These outputs are the initial files to compute ensemble analysis. Because the simulations have differing spatial resolution, they have been regridded to 1° by 1° before applying the ensemble analysis. The definition of global monsoon domain follows Wang and Ding (2008) and Wang et al. (2014b), in order to staying consistent with Brierley et al. (2020) and Otto-Bliesner et al. (2021). The whole process from downloading files from the ESGF to plotting the final analysis and relevant scripts have been published in the peer-reviewed journal Geoscientific Model Development as (Zhao et al., 2022).

Chapter 3

Monsoon response to the orbital forcing in the CMIP6-PMIP4 *midHolocene* simulations

As mentioned in Chapter 1, the mid-Holocene has long been included in the PMIP since its beginning (Joussaume et al., 1999; Braconnot et al., 2007, 2012) to contribute to understanding the climate change responding to a change in the seasonal and latitudinal distribution in insolation induced by orbital forcing (Berger and Loutre, 1991) and to evaluate model performance in the last three major assessments of the IPCC (Jansen et al., 2007; Flato et al., 2013; Eyring et al., 2021). Relatively abundant reconstructions available for this period (e.g. Bartlein et al., 2011; Kaufman et al., 2020a) provide good opportunities to examine how climate responds to orbital forcing and to evaluate how climate models simulate the responses (e.g. Hargreaves et al., 2013; Jiang et al., 2015; Harrison et al., 2014, 2015; Bartlein et al., 2017). Brierley et al. (2020) provides the preliminary analysis of the latest PMIP4-CMIP6 *midHolocene* simulations that have been published in last two years and contributed to the CMIP6 involved in the IPCC AR6 (Eyring et al., 2021; Forster et al., 2021).

In this chapter, I will mainly analyse the PMIP4-CMIP6 *midHolocene* monsoon following the analysis I contributed to Brierley et al. (2020), and evaluate model performance through data-model comparison. As the mid-Holocene has been included since the beginning of PMIP, the *midHolocene* simulations offer a good opportunity to investigate the improvement between PMIP generations. This chapter will try to anwser the following two questions:

- Do PMIP4 models simulate the *midHolocene* better than PMIP3 models?
- Do later versions of a same model family give better results than earlier versions in simulating the mid-Holocene?

Section 3.1 introduces the difference between the mid-Holocene and pre-industrial including changes in orbital parameters, temperature, precipitation and regional monsoon. Section 3.2 describes the protocol of the PMIP4 *midHolocene* and the models that have performed the PMIP4-CMIP6 *midHolocene* simulations. The following section analyses the response in temperature (3.3.1), precipitation (3.3.2) and monsoon (3.3.3). Simulated changes by individual models are also analysed, which aims to answer the second question. Section 3.4.2 evaluates model performance via data-model comparison. Section 3.5 summarises the comparison between two PMIP generations. A conclusion is provided at the end of this chapter as Section 3.6.

3.1 mid-Holocene climate change

3.1.1 Orbital forcing at 6 ka

The mid-Holocene had very different seasonal and latitudinal distribution of incoming solar radiation than today due to altered orbital configuration (Figure 3.1), while other configurations were similar to their modern conditions. At the mid-Holocene, obliquity was larger than today and perihelion occurred near the boreal autumn equinox instead of close to the boreal winter solstice in 1850 CE (Bartlein and Shafer, 2019, Figure 3.1). Compared to 1850 CE, the different orbital configurations at the mid-Holocene induced altered seasonal and latitudinal distribution of top-of-atmosphere (TOA) insolation (Figure 3.2a) by showing large positive insolation anomalies during boreal summer and large negative insolation during austral

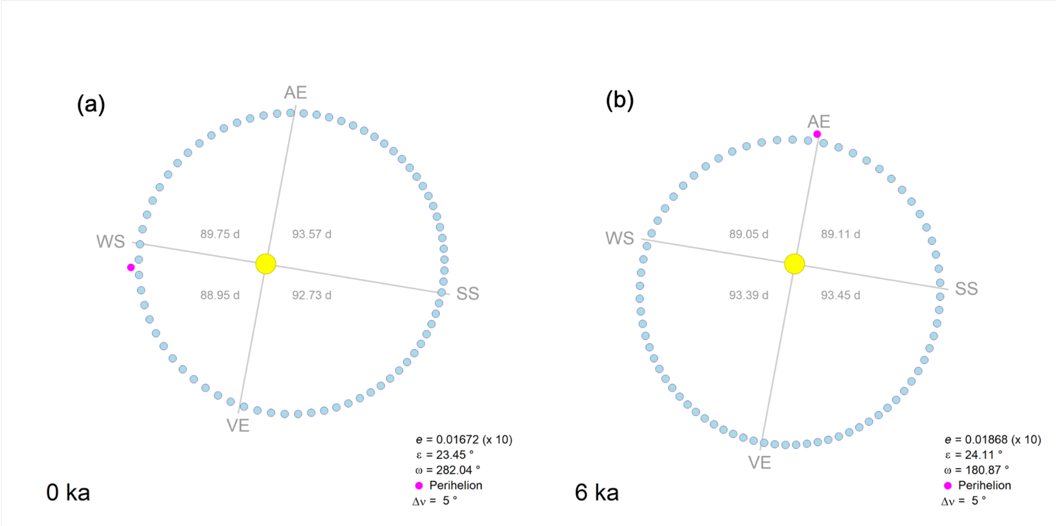

Figure 3.1: Orbital configuration at 0 ka and 6 ka. (Adapted from Bartlein and Shafer, 2019).

summer. The annual insolation anomaly (Figure 3.2b) shows a slight increase in high latitudes in both hemispheres and a decrease in the tropics, but no change in global mean insolation. PaleoCalAdjust software (Bartlein and Shafer, 2019, see Section 2.4) was applied to remove the effects of altered month lengths due to changes in orbital configuration on seasonal variables.

3.1.2 Temperature

As suggested by both pollen proxy data (e.g. Bartlein et al., 2011) and PMIP1 and PMIP2 *midHolocene* simulations (Braconnot et al., 2000, 2007), the surface temperature at the mid-Holocene had stronger seasonality overall showing warmer boreal summer and cooler boreal winter in the Northern Hemisphere (NH) with relatively stronger changes occurred over land than over sea and over high latitudes than over mid to low latitudes as compared to the pre-industrial. Exceptions include: a colder boreal summer in the southern Europe; a warmer boreal winter in the North America and the North Pacific due to the sea ice loss in Arctic (Park et al., 2018, through idealized climate model perturbation experiments), and a colder boreal summer in the monsoon-affected regions in northern Africa and southern Asia due to increased cloud cover and higher evaporation brought by a northward shift

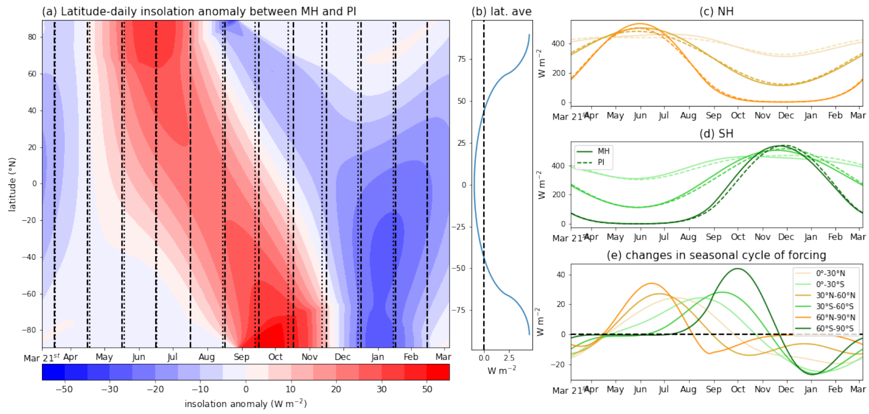

Figure 3.2: Latitude-daily insolation anomaly between 6 ka and 1850 CE. (a) The difference in the seasonal cycle insolation at the top of the atmosphere (W m^{-2}) between the mid-Holocene at 6 ka and pre-industrial at 1850 CE. Date starts from March 21st, i.e. the vernal equinox,to remove the uncertainties in calendar correction. The black dashed lines show the start day of each month at 1850 CE and the dotted lines show that at 6 ka, which illustrate the effect of orbital changes on calendar. (b) The change in mean annual forcing (W m^{-2}) by latitude. The seasonal cycle of incoming solar radiation in W m^{-2} for mid-Holocene and pre-industrial in low and mid latitudes in the (c) NH and (d) SH, and (e) the changes in the changes in the cycles. (*Insolation was computed via a python package "climlab.radiation.insolation"*.)

and intensification of the monsoons. Proxy data (Bartlein et al., 2011; Kaufman et al., 2020a, see below for more information) also suggest colder southern Europe while warmer central Europe in both seasons. The temperature features in previous PMIP experiments are generally consistent with the proxy data, as the models were able to reproduce the warming in high latitudes in simulations (Joussaume et al., 1999; Braconnot et al., 2007), but often failed to produce the correct magnitude (Braconnot et al., 2012; Harrison et al., 2015).

3.1.3 Precipitation

The mean annual precipitation during the mid-Holocene was generally increased over the continents in the NH than today, with more increase in the high latitudes while less increase in the low latitudes (Harrison et al., 2015). The mean annual precipitation was increased by less than 100 mm over the Europe, by 100 to 500 mm over the Mediterranean, and by 200 to 500 mm across the northern Africa. Precipitation was also increased over southern and eastern Asia, the most southern and western regions of North America and the South America. A reduction occurred along the equator and near the south coast of southern Africa (Bartlein et al., 2011). The previous three PMIP ensembles (Joussaume et al., 1999; Braconnot et al., 2007; Harrison et al., 2014) were not able to reproduce the magnitude of precipitation increase over western Africa and produced too much continental drying (Harrison et al., 2015).

3.1.4 Monsoon

As mentioned in Section 1.6, global monsoon enhancement is the most important change in the hydrological cycle at the mid-Holocene in response to changes in seasonal insolation by showing strengthened NH monsoon and weakened SH monsoon (Jiang et al., 2015). Most of the earlier studies investigating mid-Holocene regional monsoons agree with the change in global scale. For example, continental and marine palaeo records (Metcalfe et al., 2015) show that North American Monsoon (NAMS) began to strengthen after the Last Glacial Maximum and reached its peak extent around mid-Holocene, which is in response to orbital forcing and ice sheet retreat suggested by deglacial records of monsoon strength from isotopic analysis of leaf wax biomarkers in marine sediment cores (Bhattacharya et al., 2018). The expansion was constrained by regional changes in SST as both suggested by multiple reconstructions (Barron et al., 2012) and model simulations (Liu et al., 2004; Zhao and Harrison, 2012). The North African Monsoon (NAF), referred to as West African monsoon in some studies (e.g. Gaetani et al., 2017) and IPCC AR6 (Douville et al., 2021; IPCC, 2021b), was strengthened during the early-to-mid Holocene as suggested by both proxy (Weldeab et al., 2007; Mohtadi et al., 2016) and simulations (Braconnot et al., 2019b), which then followed by continuous drying to modern condition (Masson-Delmotte et al., 2013). Sahara and Sahel was covered by vegetation during the mid-Holocene (e.g. Prentice and Webb III, 1998; Prentice et al., 2000; Bigelow et al., 2003; Qin et al., 1998), which had large effects on monsoon systems (see Section 3.4.2.2 for a discussion of its effect on reproducing NAF). Paleo records suggest a strengthened and expanded East Asian Summer Monsoon (EAS) during the mid-Holocene (Liu et al., 2015; Wang et al., 2014a; Goldsmith et al., 2017), which was also simulated by climate models (Zhao and Harrison, 2012; Jiang et al., 2013; Piao et al., 2020). The enhancement of EAS during the mid-Holocene was mainly driven by changes in orbital forcing with modulated land-sea contrast by summer solar radiation (Wang et al., 2014a; Jin et al., 2014; Selvaraj et al., 2007). Both climate models (Prado et al., 2013a) and reconstructions (Bird et al., 2011; Mollier-Vogel et al., 2013; Prado et al., 2013b) suggest that the South American Monsoon (SAMS) was weaker during the mid-Holocene than modern in response to orbital forcings. IPCC AR6 (Douville et al., 2021) has defined the South African Monsoon (SAF) used in AR5 (Christensen et al., 2013) to a land domain instead of a monsoon system. As analysed by Chevalier et al. (2017), PMIP3 simulations show a weakened SAF during the mid-Holocene, which is consistent with reconstructions (e.g. Chevalier and Chase, 2015). Paleo records suggest the Australian–Maritime Continent Monsoon (AUSMC) during the mid-Holocene was weaker than current (Steinke et al., 2014), due to a weaker dynamic component and reduced net energy input as suggested by model simulations (D'Agostino et al., 2020). According to Eroglu et al. (2016), AUSMC and EAS had an antiphase relationship over the last 9 thousand years.

3.2 PMIP4-CMIP6 *midHolocene*

3.2.1 Experimental design

The protocol of the CMIP6-PMIP4 *midHolocene* experiment is described in detail in Otto-Bliesner et al. (2017a) (also see Table 3.1). Orbital parameters use the orbital configuration at 6 ka (Figure 3.1; Berger, 1978; Berger and Loutre, 1991). The eccentricity is set to 0.018682, which is 0.001918 higher than that described in the *piControl*. The obliquity is 24.105°, increased by 0.646° than the *piControl*. The perihelion-180 in the *midHolocene* is changed from 100.33° in the *piControl* to

0.87°. The prescribed concentrations of GHGs in the PMIP4-CMIP6 *midHolocene* use more realistic concentrations derived from ice cores and observations (Otto-Bliesner et al., 2017a) as compared to the PMIP3-CMIP5 generation. The atmospheric CO_2 is specified at 264.4 ppm, reduced by 15.6 ppm from PMIP3-CMIP5, which is now 19.9 ppm lower than the *piControl*. CH_4 is specified at 597 ppb, which is 56 ppb lower than the PMIP3-CMIP5 set-up and is reduced by 211.2 ppb than the *piControl*. N_2O is specified at 262 ppb, as 8 ppb lower than in the PMIP3-CMIP5 set-up and 11 ppb lower than the *piControl*. The changes in these prescribed concentrations of GHGs lead to a reduction of 0.3 W m^{-2} in effective radiative forcing (Otto-Bliesner et al., 2017a). Other boundary conditions remain the same as the *piControl*, with an exception of CESM2 which used potential vegetation that removed crops and urban areas in its CMIP6 simulations (Otto-Bliesner et al., 2020).

3.2.2 Models

The PMIP4-CMIP6 *midHolocene* ensemble includes simulations made by 16 of the models described in Appendix A, in which AWI-ESM-1-1-LR, MPI-ESM1-2-LR and NESM3 include interactive vegetation. Notably, NorESM1-f and UofT-CCSM-4 have run the PMIP4 *midHolocene* protocol and performed the PMIP4-CMIP6 *midHolocene* simulations, but they are not members of CMIP6. A similar number (15) of models have performed the equivalent PMIP3-CMIP5 *midHolocene* simulations, which also have been described in Appendix A. 9 of the 16 PMIP4-CMIP6 *midHolocene* simulations were completed by updated versions of the models that contributed to PMIP3-CMIP5.

3.3 Features in the PMIP4-CMIP6 ensmeble

3.3.1 Temperature response

Changes in obliquity bring an increase in the annual mean insolation in high latitudes and a decrease at low latitudes during mid-Holocene that leads to an increase in annual mean insolation in high latitudes at roughly 4.3 W m^{-2} greater than at

Table 3.1: Experimental design, according to Otto-Bliesner et al. (2017a).

	CMIP6 *piControl*	PMIP4 *midHolocene*	CMIP5 *piControl*	PMIP3 *midHolocene*
Orbital parameters				
Eccentricity	0.016764	0.018682	0.016764	0.018682
Obliquity (°)	23.459	24.105	23.459	24.105
Perihelion – 180 (°)	100.33	0.87	100.33	0.87
Vernal equinox	Fixed to noon on 21 March	Fixed to noon on 21 March	Fixed to noon on 21 March	Fixed to noon on 21 March
GHGs				
Carbon dioxide (ppm)	284.3	264.4	280	280
Methane (ppb)	808.2	597	760	650
Nitrous oxide (ppb)	273	262	270	270
Other GHGs	CMIP DECK *piControl*	0	0	0
Solar constant (W m^{-2})	1360.747	Same as *piControl*	1365	Same as *piControl*
Paleogeography	Modern	Same as *piControl*	Modern	Same as *piControl*
Ice sheets	Modern	Same as *piControl*	Modern	Same as *piControl*
Vegetation	CMIP DECK *piControl*	prescribed or interactive as in *piControl*	Prescribed	Prescribed or interactive as in *piControl*
Aerosols: dust, volcanic, etc.	CMIP DECK *piControl*	Prescribed or interactive as in *piControl*	Prescribed	Same as *piControl*

0 ka and a decrease in the tropics at -1.0 W m^{-2}. The pattern of mean annual temperature change in the PMIP4-CMIP6 ensemble between the *midHolocene* and the *piControl* simulations follows the expectation from the orbital forcing at 6 ka. The character of annual insolation forcing (Figure 3.2) results in an increase in annual mean surface temperature over the Arctic and Europe as compared to the *piControl* simulations (Figure 3.3a). A decrease is simulated in the tropics and extratropical regions, in particular over India and northern and central Africa which is associated with stronger precipitation during summer that cools the region. Across the ensemble, at least 80% (i.e. 13 out of 16) of the models produce *midHolocene*

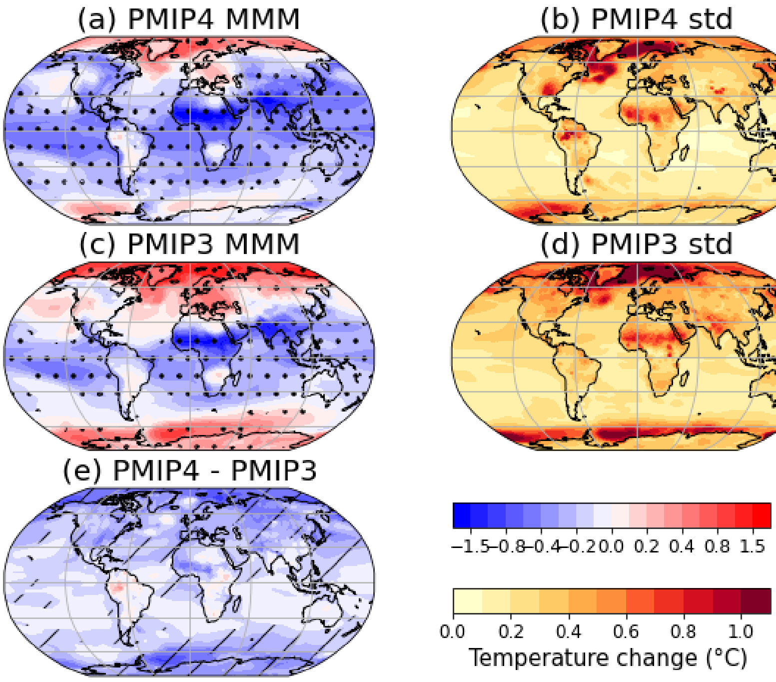

Figure 3.3: Annual mean temperature changes in the *midHolocene* simulations in °C. The multi-model mean of annual mean temperature changes (*midHolocene* – *piControl*) and the inter-model spread, defined as the across-ensemble standard deviation, across (a,b) PMIP4-CMIP6 and (c,d) PMIP3-CMIP5 simulations. Dot-shaded region reflects where at least 80% (i.e. 13 out of 16) of the models agree the sign of MMM. Panel (e) shows the difference between PMIP4-CMIP6 and PMIP3-CMIP5 (PMIP4 - PMIP3). Slash marks the region showing signigicant difference ($p < 0.05$). Simulated changes by individual models are shown in Appendix B.

cooling in low to mid latitudes, while large variance in simulated anomalies occurs over the northern Africa and in the high latitudes in both hemispheres, particularly over the Arctic ocean (Figure 3.3b). In line with the story, both hemispheres had less incoming solar radiation during DJF reaching at the TOA at 6 ka than 0 ka with a relative large reduction in the SH. These seasonal changes in inslolation result in cooling over land in DJF (particularly in the NH) and over the tropical oceans (Figure 3.5a) in the *midHolocene* simulations as compared to the *piControl*. Disagreement and large variance occurs on simulated DJF Arctic warming (Figure 3.5b). The Arctic warming during boreal winter could be explained by the

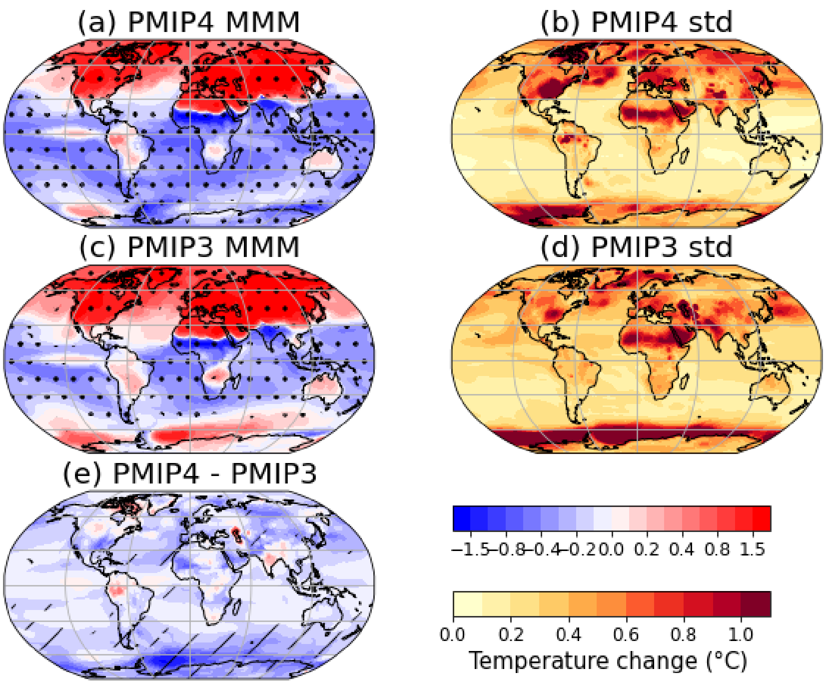

Figure 3.4: Same as Figure 3.3 but for JJA. Simulated changes by individual models are shown in Appendix B.

maintenance of positive DJF surface temperature anomalies in Arctic as the result of the memory of cryosphere and ocean feedbacks (Serreze and Barry, 2011), as well as the warming in the Southern Ocean. The increased insolation in the NH during boreal summer (JJA) warms the NH mid to high latitudes is warmer than the *piControl*, in particular over land (Figure 3.4a). Most models simulate these warming, though with large variance (Figure 3.4b). This increased land-sea and interhemispheric temperature gradient shifts the monsoons northward and leads to an intensification of the NH monsoons (see Section 3.3.3). The enhanced monsoon over northern Africa and southern Asia in turn cools the monsoon-affected regions, as shown in Figure 3.4a).

Comparing to the PMIP3-CMIP5 ensemble, the geographical pattern of temperature anomalies in the PMIP4-CMIP6 is similar to that shown in PMIP3-CMIP5 (Panel c of Figures 3.3, 3.4 and 3.5). Simulated temperature change in both ensem-

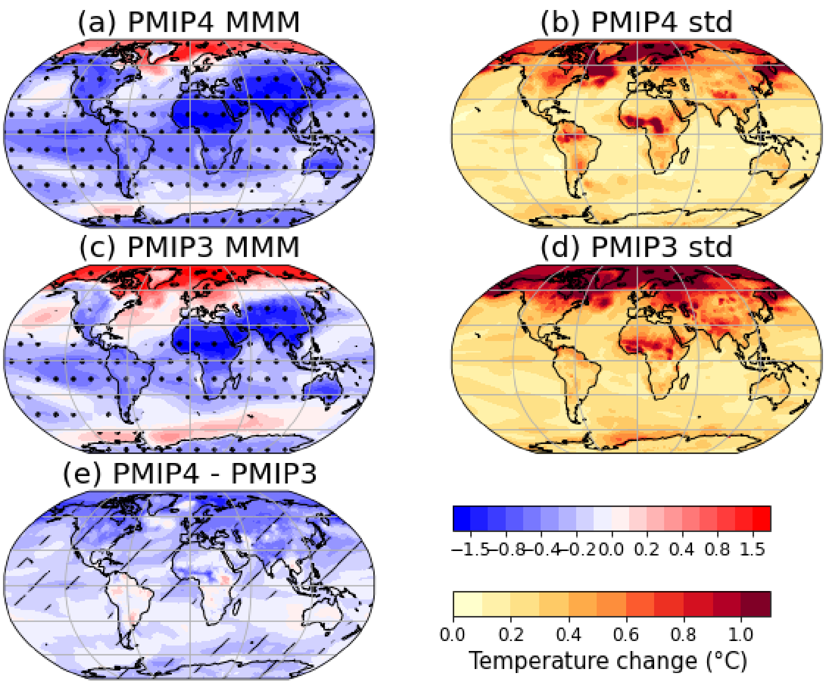

Figure 3.5: Same as Figure 3.3 but for DJF. Simulated changes by individual models are shown in Appendix B.

bles are in agreement with earlier PMIP results (Braconnot et al., 2000; Harrison et al., 2002, 2015), and the underestimation of Arctic warming still exists (see Section 3.4.2 for a discussion). Both generations show large variance occurring in the high latitudes and northern Africa but the magnitude in the PMIP4-CMIP6 *midHolocene* ensemble has been reduced than that in the PMIP3-CMIP5 ensemble (Panel d), implying a better consistency across the PMIP4-CMIP6 simulations. The PMIP4-CMIP6 ensemble is slightly colder than the PMIP3-CMIP5, as shown in Panels e of Figures 3.3, 3.4 and 3.5 and Figure 3.6. A statistical t test is applied to detect changes between the two ensembles. Dashed lines in panels e of Figures 3.3, 3.4 and 3.5 mark the regions where the difference is significant (i.e. $p < 0.05$) that the null hypothesis that there is no difference between PMIP4-CMIP6 and PMIP3-CMIP6 ensemble is rejected. The t test results show that the PMIP4-CMIP6 ensemble is significantly cooler in mid to high latitudes, especially during

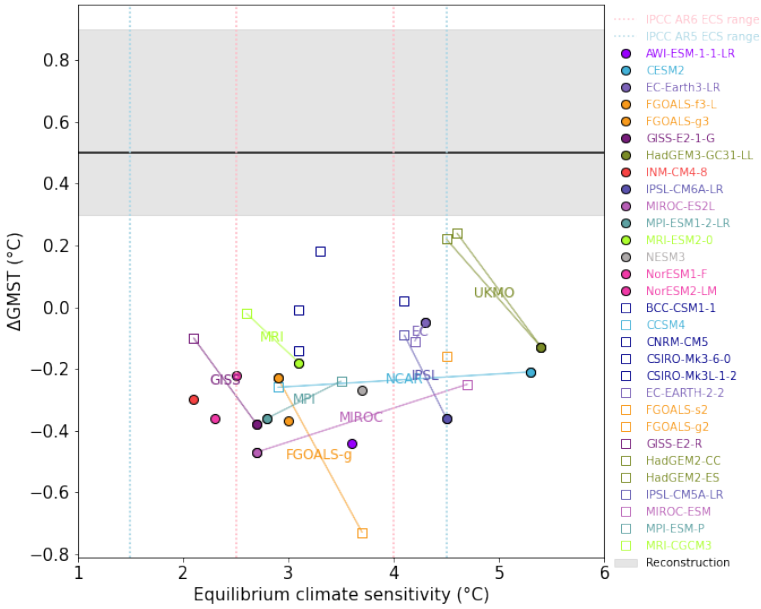

Figure 3.6: Equilibrium climate sensitivity (ECS) vs. change in mean annual surface air temperature (GMST) in the *midHolocene* simulations between the PMIP3 and PMIP4 generations. The shifts between different generations of models are indicated and labelled after their modelling group, if available. Black line represents the change in GMST extimated by Kaufman et al. (2020a) with the grey shading showing 80% CI.

local winter.

The prescribed GHGs in the PMIP4-CMIP6 is lower than that in the PMIP3-CMIP5 (Section 3.2.1), which lead to a reduction of 0.3 W m^{-2} in effective radiative forcing (Otto-Bliesner et al., 2017a). The reduced forcing leads to a cooler PMIP4-CMIP6 ensemble than PMIP3-CMIP5. Moreover, Brierley et al. (2020) has examined the response in annual mean temperature to the change in CO_2 concentration by using the *abrupt4xCO2* simulations. The response gives a similar pattern shown in Figure 3.3e. Large proportion of CMIP6 models have an higher equilibrium climate sensitivity (ECS, definied as the equilibrium change in surface temperature relative to pre-industrial in response to a doubling of CO_2 relative to pre-industrial level) than their earlier versions contributing to CMIP5 (Section 2.1 and Appendix A). The higher ECS is linked to improvement in cloud feedbacks and aerosol-

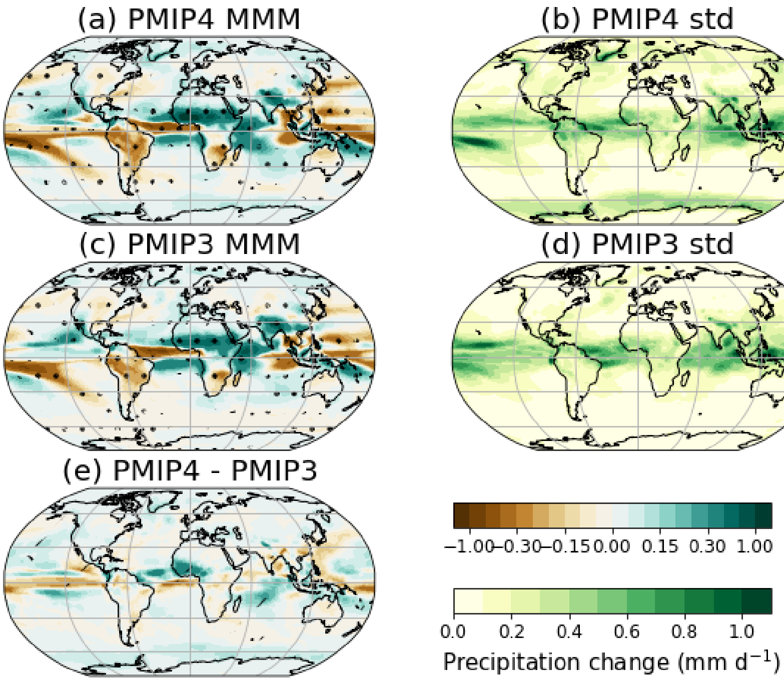

Figure 3.7: Same as Figure 3.3 but for annual mean precipitation change in the *mid-Holocene* simulations in mm d^{-1}.

cloud interactions (Meehl et al., 2020; Zelinka et al., 2020), as developments in the physical representation of clouds lead to stronger positive feedback via decreasing extratropical low cloud coverage and albedo (Zelinka et al., 2020). However, as shown in Figure 3.6, those PMIP4-CMIP6 models with a higher ECS do not necessarily produce cooler mid-Holocene GMST than the rest PMIP4-CMIP6 models with relative lower ECS. Those PMIP4-CMIP6 models having higher ECS than the earlier PMIP3-CMIP5 generation do not always produce colder mid-Holocene as well. These indicate that the difference between the two generations is more likely caused by responding to the GHGs concentration reductions in the PMIP4 protocol rather than relating to the improvements between model generations.

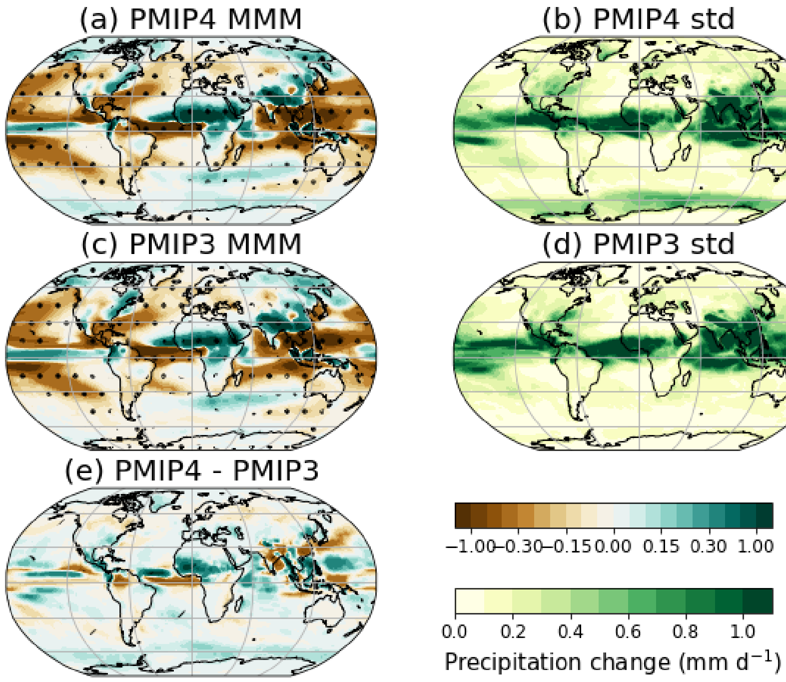

Figure 3.8: Same as Figure 3.7 but for JJA. Simulated changes by individual models are shown in Appendix B.

3.3.2 Tropical precipitation response

Changes in ensemble averaged annual mean precipitation (*midHolocene - piControl*) show a large-scale redistribution of moisture throughout the year (Figure 3.7a), in particular over tropics and extratropics. There is a reduction of annual mean precipitation over South America, over northwest Pacific and along the Equator in the Pacific and Atlantic oceans while an increase occurring over the adjacent seas and over northern Africa extending into Saudi Arabia and accumulating along the Himalayas. Large spread of simulated precipitation anomalies across models is seen in the tropics in the SH. The large spread in the SH high latitudes in the PMIP4-CMIP6 ensemble mean is caused by the strong increase precipitation simulated by NorESM2-LM, which results in a slight increase in precipitation shown in the ensemble mean while all other 15 models simulate a slight decrease (see Appendix B for annual mean anomalies produced by individual models). This also happens

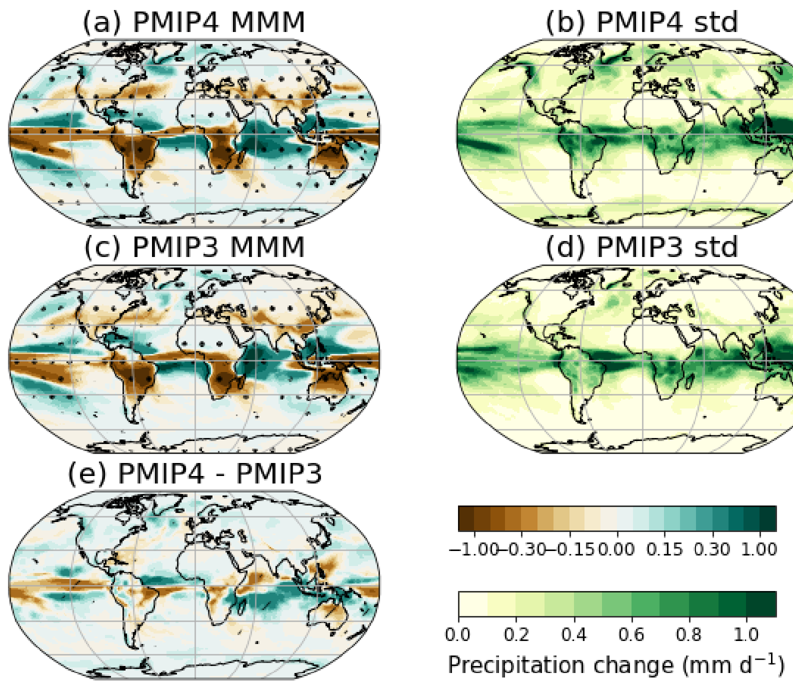

Figure 3.9: Same as Figure 3.7 but for DJF. Simulated changes by individual models are shown in Appendix B.

in both JJA and DJF mean precipitation changes (Figures 3.9a and 3.8a).

Strong seasonal insolation changes have more effects on seasonal precipitation. Figures 3.9a and 3.8a show that the seasonal changes in precipitation have large shifts in the Intertropical Convergence Zone (ITCZ) in the *midHolocene* simulations as compared to the *piControl*, and the largest model spread occurs over the ITCZ (Panel b in both figures). During DJF, the ITCZ has reduced precipitation over the tropical Pacific Ocean but with more rainfall over the Indian Ocean. The tropical Atlantic ITCZ shows a southward shift during DJF. Precipitation reduces over SH lands during austral summer as well, indicating weakened and narrowed monsoons in the SH. During JJA, the ensemble mean indicates a northward shift in the tropical Atlantic ITCZ. The precipitation over southern and eastern Asia and northern Africa increases during boreal summer. Except these regions and the Pacific rain belt, the JJA precipitation reduces elsewhere.

The spatial pattern of annual mean precipitation in the PMIP4-CMIP6 ensemble is close to that seen in the PMIP3-CMIP5 (Figure 3.7c), and the difference between the two generations is not significant (Figure 3.7e). Comparing to the seasonal shifts in ITCZ in the PMIP3-CMIP5 ensemble (panels c in Figure 3.9 and 3.8), the PMIP4-CMIP6 ensemble simulates a larger northward shift of the tropical Atlantic ITCZ, a wetter Indian Ocean and a widening of the Pacific rain belt though the difference is not significant (panel e in both figures). This northward shift is due to the stronger interhemispheric and land-sea temperature gradient in the PMIP4-CMIP6 ensemble (see Section 3.3.1) caused by difference in protocols. All individual models contributed to the two ensemble produce changes in seasonal precipitation in the tropics and extratropics, but the spread across each ensemble is large (panel b and d of the figures). For model generations, PMIP4-CMIP6 models do not perform differently to PMIP3-CMIP5 modeling in producing precipitation anomalies.

3.3.3 Monsoon response

3.3.3.1 Changes in monsoon domain

In general, the pattern of global monsoon domain patterns simulated by each individual model agrees on the sign of ensemble mean respectively (Figure 3.10a and Appendix), but the variations in magnitude across models are large (Figure 3.10b).Multi-model mean of the global monsoon domain and monsoon summer rain rate (for the definition, see Chapter 2) changes (PMIP4-CMIP6 *midHolocene* - *piControl*) shows that the NH monsoons are strengthened and the SH monsoons are weakened (Figure 3.10a). Monsoons over land and over ocean give opposite change, as the NH monsoon domain expands over land and reduces over oceans, and the SH monsoon domain reduces over land and expands over oceans. The NAF rainfall increases mostly below 15°N (Figure 3.10a) and extends northward (Figure 3.11) than the *piControl*, but there are large variations across models (Figure 3.10b). Underestimation in NAF has existed since the beginning of PMIP (Braconnot et al., 2000; Harrison et al., 2002, 2015), and still exists in the PMIP4-CMIP6 ensemble. Potential explanations are discussed in Section 3.4.2.2. There is no obvious rela-

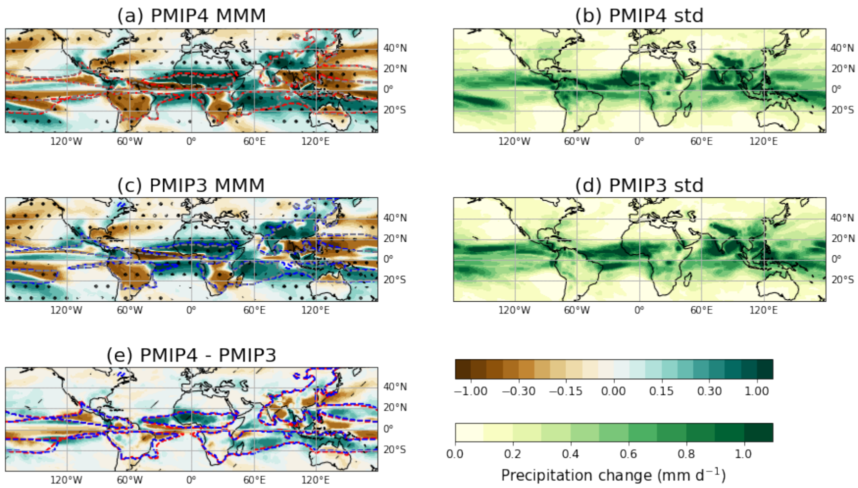

Figure 3.10: Same as Figure 3.3 but for mean global monsoon domain (contour) and changes in monsoon summer rain rate (shading) in mm d^{-1}) in the *mid-Holocene* simulations The red, blue and grey contour in the left column shows the boundary of multi-model mean global monsoon domain computed for the PMIP4-CMIP6 *midHolocene*, PMIP3-CMIP5 *midHolocene* and the *piControl* simulations, respectively. The identification of the monsoon domain follows the description in Chapter 2. Simulated changes by individual models are shown in Appendix B.

tionship between the change in monsoon rainfall and the shift in domain boundary, i.e. strong *midHolocene* monsoon rainfall changes do not accompany large domain boundary shift between the *midHolocene* and the *piControl*. The enhanced NH monsoons and weakened SH monsoons are in good agreement with previous studies (e.g. Zhao and Harrison, 2012; Jiang et al., 2015). Generally the monsoon response follows the expectation from changes in insolation. D'Agostino et al. (2019, 2020) analyse the CMIP5 *midHolocene* simulations and state that changes in mid-Holocene global monsoon are primarily driven by changes in atmospheric circulation.

The pattern of global monsoon in the PMIP4-CMIP6 *midHolocene* simulations is very similar to that in the PMIP3-CMIP5 (Figure 3.10c,d). However, PMIP4-CMIP6 models simulate more increase of monsoon summer rain rate over western Africa and less increase over southern China than the PMIP3-CMIP5 ensemble,

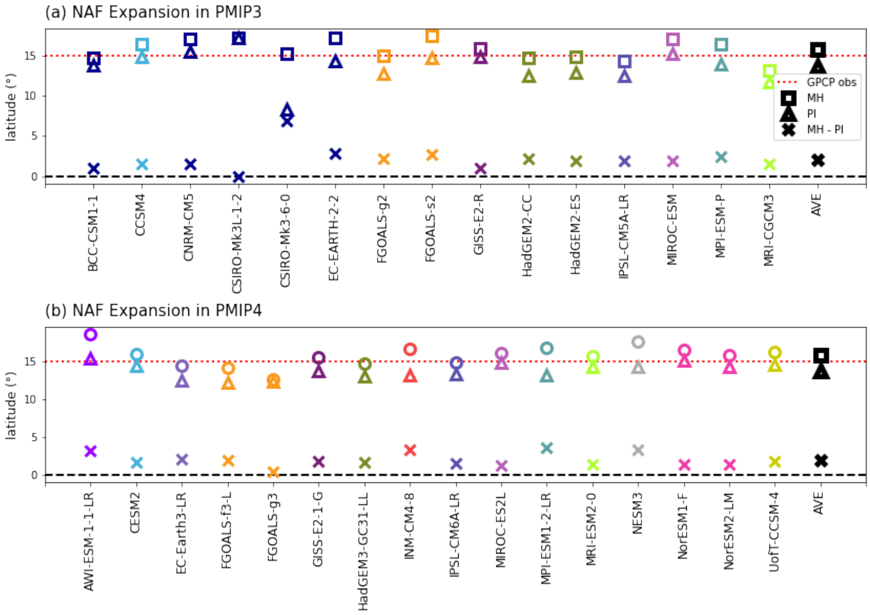

Figure 3.11: NAF expansion in the PMIP3-CMIP5 and PMIP4-CMIP6 ensembles. The northward monsoon expansion is calculated by determining the change in latitude where the zonal mean summer (MJJAS) rain rate equals to 2 mm d^{-1} over the North Africa (15°W – 30°E).

though the difference is not significant (Figure 3.10e).

3.3.3.2 Changes in regional monsoons

Besides the influence of insolation on global monsoon, regional monsoons are also affected by local topography, land-sea distribution and oceanic circulations that cause the differences among regional monsoons (Wang et al., 2017). Christensen et al. (2013) identifies seven regional land monsoons, which are North American Monsoon System (NAMS), northern Africa (NAF), southern Asia (SAS), and East Asia summer (EAS) in the Northern Hemisphere and South American Monsoon System (SAMS), southern Africa (SAF), and Australian–Maritime Continent (AUSMC) in the Southern Hemisphere. Paragraphs below give the detailed description of changes in each regional monsoon.

North American Monsoon (NAMS) is wetter and expanded in the PMIP4-CMIP6

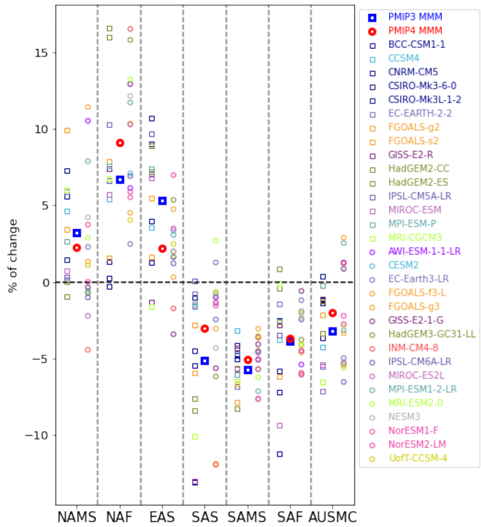

Figure 3.12: Relative change in domain averaged rain rate of regional monsoons in the *midHolocene* simulations relative to the *piControl*. See Section 2.5.3 for a description of the diagnostic.

midHolocene simulations as compared to the *piControl*. The enhancement agrees with earlier studies based on both simulations (Liu et al., 2004; Zhao and Harrison, 2012) and proxies (Metcalfe et al., 2015), in response to orbital forcing and ice sheet retreat (Bhattacharya et al., 2018). The enhancement was constrained by regional changes in SST (Barron et al., 2012). The relative changes are small, as the multi-model mean area-averaged monsoonal precipitation rate is only 2.3% (-4.4% to 11.5%) larger than in the *piControl* (Figure 3.12) and the averaged areal extent increases by 4.5% (-11.3% to 21.1%) (Figure 3.14). The total amount of precipitated water, computed as the precipitation rate multiplied by the areal extent, is 7.0% (-10.4% to 33.9%) more than the *piControl* simulations (Figure 3.16). The *midHolocene* NAMS has more stable precipitation rate but more changeable areal extent, as shown by the changes in standard deviation of interannual variability in the area-averaged precipitation rate (Figure 3.13) and in the areal extent (Figure 3.15) respectively.

Comparing to the PMIP3-CMIP5 ensemble, the PMIP4-CMIP6 ensemble simulates stronger internal variability in the NAMS and has smaller increase in the areal

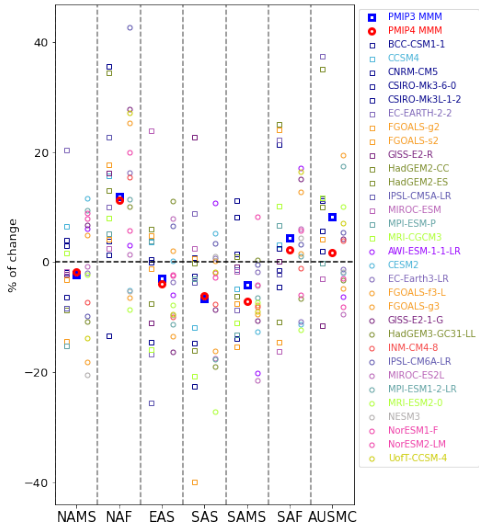

Figure 3.13: Same as Figure 3.12 but for the relative change in the standard deviation of interannual variability in the area-averaged monsoon summer rain rate of regional monsoons.

extent (a 4.5% relative increase compared to the 10.2% in the PMIP3-CMIP5), and therefore simulates smaller increase in cumulative precipitated water (about half) than the PMIP3-CMIP5. Though simulating smaller changes than the PMIP3-CMIP5, the difference between the two ensembles is not significant.

North African Monsoon (NAF) was strengthened during the early-to-mid Holocene as suggested by both proxy (Weldeab et al., 2007; Mohtadi et al., 2016) and simulations (Braconnot et al., 2019b), which then followed by continuous drying to modern condition (Masson-Delmotte et al., 2013). Sahara and Sahel was covered by vegetation during the mid-Holocene (Prentice and Webb III, 1998; Prentice et al., 2000; Bigelow et al., 2003; Qin et al., 1998), which suggests wetter northern Africa during the mid-Holocene and it had large effects on monsoon systems (see Section 3.4.2.2 for a discussion of its effect on reproducing NAF). The PMIP4-CMIP6 ensemble shows a wetter and wider NAF in the *midHolocene* simulations, which is in line with early studies (Jiang et al., 2015; Zhao and Harrison, 2012). As shown in Figure 3.12, the averaged rain rate of the NAF in the *midHolocene* simulations is 9.1% (2.5% to 16.6%) higher than in the *piControl*. The areal extent

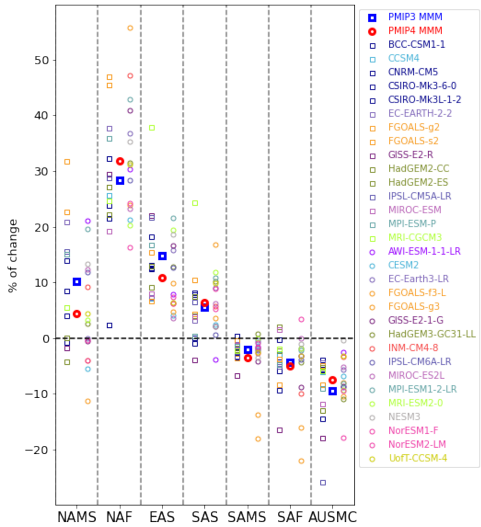

Figure 3.14: Same as Figure 3.12 but for the relative change in areal extent of regional monsoons.

increases by 31.8% on average with a range of 16.2% to 55.7% (Figure 3.14). The total amount of rainfall over the area accumulates to 48.3% (22.8% to 71.2%) more than the *piControl* simulations (Figure 3.16). As shown by the percent changes in the standard deviation of interannual variability in area-averaged precipitation (Figure 3.13b) and areal extent (Figure 3.15), the *midHolocene* simulations have larger internal variability of both monsoon rain rate and monsoon domain area. On average, the PMIP4-CMIP6 ensemble simulates changes in precipitation rates similar to the PMIP3-CMIP5 ensemble, but the NAF expands larger in PMIP4-CMIP6.

Paleo records suggest a strengthened and expanded East Asian Summer Monsoon (EAS) during the mid-Holocene (Liu et al., 2015; Wang et al., 2014a; Goldsmith et al., 2017), which was also simulated by climate models (Zhao and Harrison, 2012; Jiang et al., 2013; Piao et al., 2020). The PMIP4-CMIP6 ensemble agree with the enhancement suggested by previous studies by producing a consistent precipitation increase (*midHolocene* - *piControl*) over eastern Asia (Figure 3.12), as 14 out of the 16 models simulate expanded EAS, though the changes are small. Figures 3.12 shows an averaged increase of 2.2% than the *piControl* simulations.

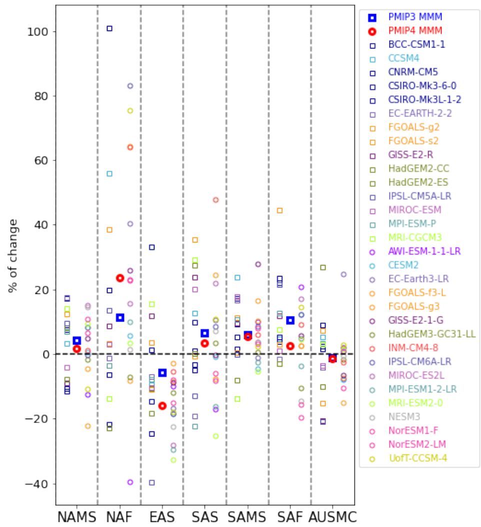

Figure 3.15: Same as Figure 3.12 but for the relative change in the standard deviation of interannual variability in the areal extent of regional monsoons.

All models produce an increase in areal extent by 10.9% on average ranging from 3.6% to 21.6% (Figure 3.14). The change in the total amount of water precipitated in each monsoon season is 13.3% (4.5 to 23.4%) more in the *midHolocene* simulations than *piControl* (Figure 3.16). The wetter and wider EAS shown in the PMIP4-CMIP6 simulations were present in the PMIP3-CMIP5 generation, but the magnitude of precipitation increase and areal extension have been reduced (Figures 3.13 and 3.15). Relative changes in the standard deviation of interannual variability in the area-averaged precipitation rate and the areal extent are -4.0% (-16.3% to 11.2%) and -15.9% (-32.8% to -2.8%) respectively in the PMIP4-CMIP6 generation, which are more negative but with smaller variations across models than the PMIP3-CMIP5.

South Asian Summer Monsoon (SAS) is drier but wider in the PMIP4-CMIP6 *midHolocene* simulations than the *piControl* (Figures 3.12 and 3.14). The precipitation rate is -3.1% on average less than the *piControl* ranging from -12.0% to 2.7% (Figure 3.12). Comparing to the *piControl* simulations, the SAS areal extent in the *midHolocene* simulations increases by 6.4% (-3.7% to 16.9%) as shown in

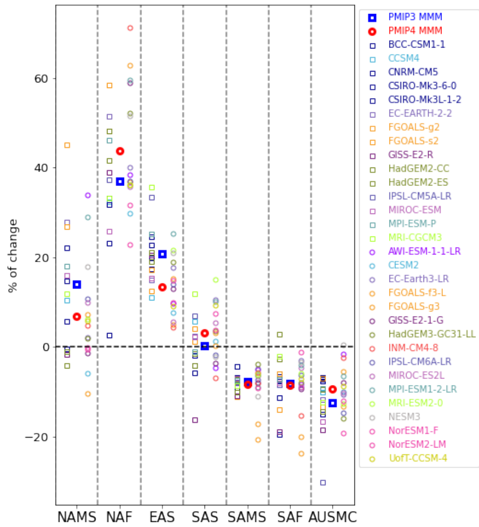

Figure 3.16: Same as Figure 3.12 but for the relative change in cumulative rainfall over domain of regional monsoons.

Figure 3.14. Though the change in standard deviation of the year-to-year variations in the areal extent of SAS is only 3.3% on average, it varies from -25.2% (simulated by MPI-ESM1-2-LR) to 47.7% (simulated by INM-CM4-8) across models (Figure 3.15). Change in cumulative rainfall (Figure 3.16) is less consistent among models ranging from -7.0% to 15.1%, but on average it shows an increase by 3.2%, which is higher than the 0.23% (-16.2% to 12.0%) presented in the PMIP3-CMIP5 generation which had a reduction of precipitation rate by -5.1% (-13.1% to 0.1%) (Figure 3.12) and an expansion of areal extent by 5.6% ranging from -3.8% to 24.3% (Figure 3.14).

Both climate models (Prado et al., 2013a) and reconstructions (Bird et al., 2011; Mollier-Vogel et al., 2013; Prado et al., 2013b) suggest that South American Monsoon (SAMS) was weaker during the mid-Holocene than modern in response to orbital forcings. In agreement with earlier studies (Bird et al., 2011; Mollier-Vogel et al., 2013; Prado et al., 2013b), the PMIP4-CMIP6 ensemble shows a drier and constricted SAMS in the *midHolocene* simulations. The ensemble mean change (*midHolocene* - *piControl*) in monsoonal precipitation rate of the SAMS shows consistent reduction by -5.1% (-7.7% to -3.0%) (Figure 3.12) with a decreased internal climate variability around -7.2% (-21.5% to 8.2%) (Figure 3.13). The areal extent of the *midHolocene* SAMS is -3.4% (-18.1% to 0.7%) smaller than the *piControl* simulations (Figure 3.14), while the internal variability increases by 5.4% (-5.4% to 27.9%) and less consistent across the ensemble (Figure 3.15). The cumulative rainfall therefore shows a reduction by -8.4% (-20.6% to -3.8%) compared to the *piControl* (Figure 3.16). In general, characteristics of the SAMS in the PMIP4-CMIP6 ensemble were similar to those in the PMIP3-CMIP5. The ensemble mean changes in areal extent and cumulative rainfall are affected by FGOALS-f3-L and FGOALS-g3 which produce much more decrease than other PMIP4-CMIP6 models, though they simulate the two smallest precipitation reduction.

The PMIP4-CMIP5 *midHolocene* simulations also show a drier South African Monsoon (SAF) with reduced areal extent than the *piControl*. The mean decrease in precipitation rate is -3.7% ranging from -6.0% to -0.6% as shown in Figure 3.12). 15 out of 16 models simulate reduced areal extent ranging from -22.0% to -0.1%, except NorESM1-F produces the only expansion in the ensemble at 3.5% (Figure 3.14). On average, the areal extent in the *midHolocene* simulations decrease by -5.1% than the *piControl* simulations. Though the change in internal variability of areal extent is small (2.6%) on average (Figure 3.15), the variation is large across the PMIP4-CMIP6 ensemble (-19.5% to 20.7%). The *midHolocene* cumulative rainfall decreases by -8.6% (-23.8% to -1.1%), with 13 models concentrating on a range between -9.4% and -1.1% (Figure 3.16). The PMIP4-CMIP6 ensemble shows similar changes in SAF as the PMIP3-CMIP5 ensemble but has reduced mean internal variability of precipitation rate and areal extent respectively, meanwhile the variation in the changes in internal variability of areal extent across models has been enlarged.

The PMIP4-CMIP6 ensemble shows a decrease in the Australian–Maritime Continent (AUSMC) both in precipitation (Figure 3.12) and areal extent (Figure 3.14) in the *midHolocene* simulations as compared to the *piControl*. The change in area-averaged precipitation is -2.0% less than the *piControl* simulations on average

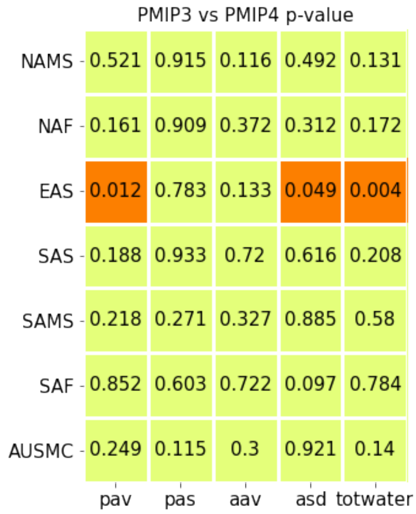

Figure 3.17: Evaluation of the significance of difference in monsoon change between PMIP4-CMIP6 and PMIP3-CMIP5 *midHolocene*. Red boxes highlight the variables that show significant difference between the PMIP4-CMIP6 and the PMIP3-CMIP5 simulations, while the rest means no significance.

ranging from-6.5% to 2.9%. Majority of the models produce small changes in the internal variability of precipitation rate as less than +/-10%, except MPI-ESM1-2-LR and FGOALS-g3 that simulate an increase by around 20% (Figure 3.13). The mean decrease in areal extent is -7.4% with a range of -17.8% to -0.4% wiyh most models having the reduction less than -11% (Figure 3.14). The mean change in the standard deviation of year-to-year areal extent of the AUSMC is -1.6%, affected by the 24% more extension produced by EC-Earth3-LR (Figure 3.15). The PMIP4-CMIP6 AUSMC results are similar to the PMIP3-CMIP5, but the magnitude in reduction have been slightly reduced in this generation. Changes in cumulative rainfall is small (-9.4%, -19.2% to 0.5%) across the PMIP4-CMIP6 ensemble (Figure 3.16), in which NESM3 provides the only increased *midHolocene* cumulative rainfall at 0.5% by having a slight precipitation enhancement and the least constriction in areal extent.

In line with the changes in global monsoon domain, regional monsoons in the NH are enhanced, especially for the NAF that shows greatest change, and in the SH are weakened, especially for the AUSMC (Figures 3.12, 3.14 and 3.16). Changes in mean atmospheric circulation bring more precipitation over land than over ocean in the *midHolocene* simulations. Therefore, the increased insolation during the boreal summer in the NH leads to an expansion and intensification in the NAF, and also in the EAS and NAMS though in which the enhancement is small and less consistent across the ensemble. SH shows opposite change in the SAMS, SAF and AUSMC. Changes in internal climate variability within the monsoon systems (Figures 3.13 and 3.15) are not consistent across the PMIP4-CMIP6 ensemble. Models producing large variability in one region does not always produce large variability in other regions, which suggests that this variability is also linked with regional feedbacks rather than being an inherent characteristic of a model. The regional monsoon diagnostics have been introduced in Section 2.5.3.

Changes in regional monsoons agree with the findings in previous PMIPs (Braconnot et al., 2000, 2007; Zhao and Harrison, 2012; Liu et al., 2004). PMIP3-CMIP5 models in general also simulate enhanced NH monsoons and weakened SH monsoons (Figures 3.12 to 3.16), and the difference between the two generations are not significant except in simulating EAS monsoon rain rate change (Figure 3.17). For those PMIP4-CMIP6 models that have earlier versions participating in the PMIP3-CMIP5 *midHolocene*, there is no clear trend between the versions, i.e. a PMIP4-CMIP6 model not always produce larger/smaller change than its earlier version both in monsoon response and internal climate variability (Figures 3.12 to 3.16), which suggests that improvements in model physics of a model have complicated effects on simulating monsoon change.

3.4 Data-model comparison

3.4.1 Proxy data used in this chapter

3.4.1.1 Bartlein et al. (2011)

Bartlein et al. (2011) provides a compilation of quantitative pollen-based reconstructions of six land climate variables from a number of sources, which are mean annual temperature (MAT), mean temperature of the coldest month (MTCO), mean temperature of the warmest month (MTWA), growing season temperature (GDD5), mean annual precipitation (MAP), and the ratio of actual to potential evaporation (α). All variables were estimated for 2° x 2° grids by combining the reconstructions at individual pollen sites and using modern-analogue, regression and model-inversion techniques at sites (Bartlein et al., 2011). The uncertainties are available at grid level, estimated as a pooled estimate of the standard errors of the original reconstructions for all sites in each grid cell. The Bartlein et al. (2011) data set shows a fair coverage over the Europe and North America, a sparse coverage over the Mid-continental Eurasia and eastern Asia, and has large data gaps especially in the tropics and SH. This dataset was extended by adding some speleothem and ice core temperature reconstructions to evaluate the PMIP3-CMIP5 simulations by Harrison et al. (2014). The following sections in this chapter use the extended version of MAT and MAP (shown as the color filled triangles in Figure 3.18d and Figure 3.20 respectively).

3.4.1.2 Temperature 12k (Kaufman et al., 2020b)

The Temperature 12k database (Kaufman et al., 2020b) is a compilation of temperature proxy records throughout the Holocene, which has 1319 published time series data derived from lake sediment, marine sediment, peat, glacier ice and other natural archives. Mean annual, summer, and winter temperatures are available in this database. The mean annual and seasonal temperatures at the mid-Holocene have been extracted and then compared to the last millennium interval (from 6.0 +/- 0.5 to 0.6 +/- 0.5 ka) to obtain site-level mid-Holocene temperature anomalies (shown as the color filled circles in Figure 3.18a, b and c for annual, summer and winter respectively). The dataset used in following sections has been estimated to 1° x 1° grids resolution by firstly taking the average at sites where have multiple proxy data to obtain site-level data and then taking the mean of all site-level data points within each grid box.

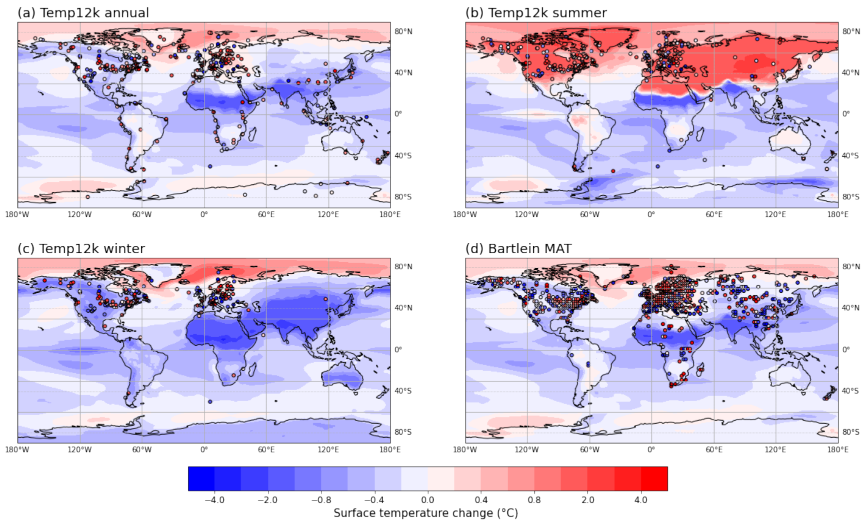

Figure 3.18: Comparison between simulated changes in the midHolocene simulations and reconstructions. Panels (a) (b) and (c) show the reconstructed anomalies from the Temperature 12k compilation (filled circles; Kaufman et al., 2020b) of annual, winter and summer, respectively overlapping on surface temperature changes from PMIP4-CMIP6 simulations (same as the panel (a) in Figures 3.7, 3.5 and 3.4). Panel (d) compares simulated annual mean temperature change (same as the panel (a) in Figure 3.3) with pollen-based reconstructions (marked as filled triangles from Bartlein et al. (2011).

3.4.2 Comparing to reconstructions

3.4.2.1 Temperature

Figure 3.6 shows that the annual mean temperature change in the PMIP4-CMIP6 *midHolocene* ensemble shows a global cooling of -0.28°C (-0.47°C to -0.05°C), lower than the estimation from Kaufman et al. (2020b) of a warming at 0.5°C (0.3°C - 0.9°C with 80%CI). The underestimation in mid-Holocene temperatue also happens to the PMIP3-CMIP5 ensemble. Both PMIP4-CMIP6 and PMIP3-CMIP5 generations produce cooling in the tropics, subtropics and mid-latitudes, and PMIP4-CMIP6 *midholocene* is significantly colder by having more reliable prescribed GHGs concentrations (see Section 3.2.1 and 3.3.1) except 30°S to 0° (Figure 3.19). However, the simulated cooling is not consistent with the warmer zonal mean annual mean temperature changes (6 ka - 0 ka) at most latitudes estimated from Temperature 12k compilation (shown by the error bars in Figure 3.19;

Kaufman et al., 2020b), whereas the Bartlein et al. (2011) compilation demonstrates the heterogeneity within these estimates (box plots in Figure 3.19). The tropical cooling simulated by all of the PMIP4-CMIP6 models is outside the confidence intervals of Temp12k. The mismatch is caused by models failing to reproduce the regional warming in low to mid latitudes and in the North America and underestimate the warming in Europe by producing more cooling during boreal winter over Europe and North America (Figure 3.18). Though failing to simulate the regional boreal summer cooling in the NH, model simulations at some degree reproduce the warming during boreal summer in the NH. The underestimated mid-Holocene Arctic warming in the PMIP4-CMIP6 has existed in the earlier PMIP3-CMIP5 (Harrison et al., 2015; Yoshimori and Suzuki, 2019). The regional temperature bias in the CMIP5 *midHolocene*, *piControl* and *historical* are similar (Ackerley et al., 2017; Harrison et al., 2015). This indicates the persistent errors in representing the climate system.

3.4.2.2 Precipitation

The Bartlein et al. (2011) dataset provides pollen-based reconstructed mean precipitation anomalies at 6 ka (dots in Figure 3.20) that allows to quantitatively evaluate how the *midHolocene* simulations could reproduce the MH precipitation anomalies. Figure 3.20 shows that the mismatch between simulated precipitation change and the Bartlein et al. (2011) dataset is complicated. The PMIP4-CMIP6 *midHolocene* ensemble shows little change in the *midHolocene* mean annual precipitation over Europe where there are relatively abundant reconstruction data, and fails to capture the modest precipitation increases over northern Europe, increases in central Europe, and much wetter conditions in the Mediterranean during the mid-Holocene that were suggested by the pollen-based reconstructions of annual mean precipitation. The ensemble fails to capture the complex precipitation response over the North America, suggested by the mixture of increase and decrease in reconstructed precipitated anomalies over this region.

Over the monsoon regions, though the mean annual precipitation change does not

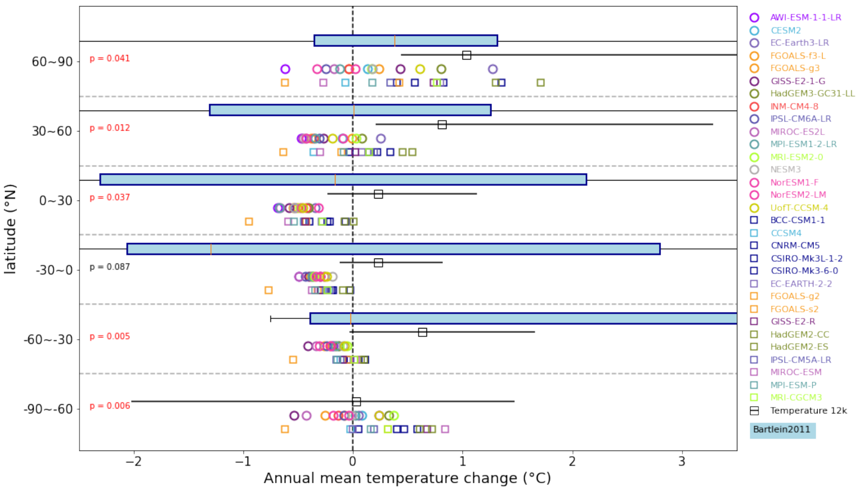

Figure 3.19: Comparison between simulated zonal averaged temperatures and reconstructions. The simulated annual mean temperature change averaged over 30° zonal bands for each of the individual PMIP4-CMIP6 and PMIP3-CMIP5 models. The equivalent changes estimated from the Temperature 12k compilation (Kaufman et al., 2020a) via a multi-method approach are shown along with their 80 % confidence interval. Box plots represent the distribution of Bartlein et al. (2011) reconstructed temperatures within each latitude bands.

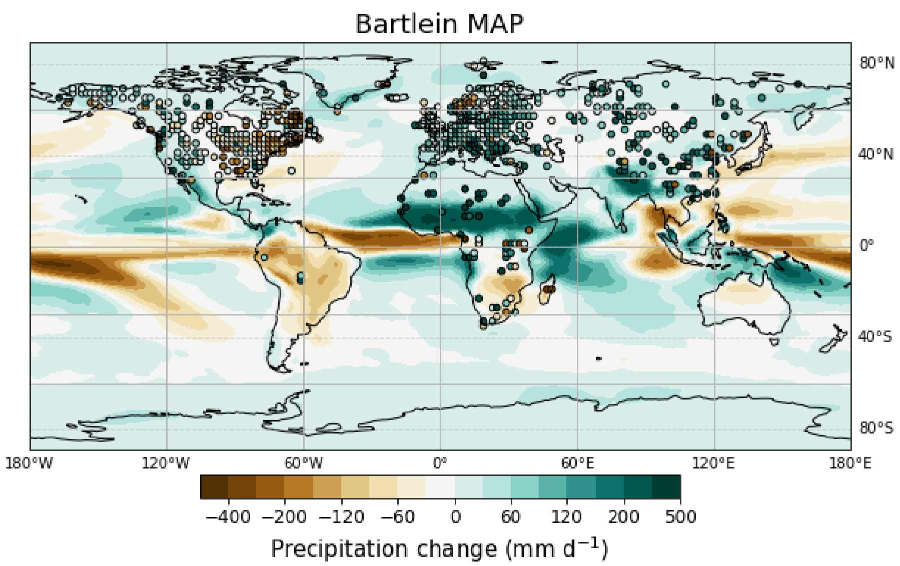

Figure 3.20: Comparison between PMIP4-CMIP6 simulated annual precipitation changes and pollen-based reconstructions from Bartlein et al. (2011).

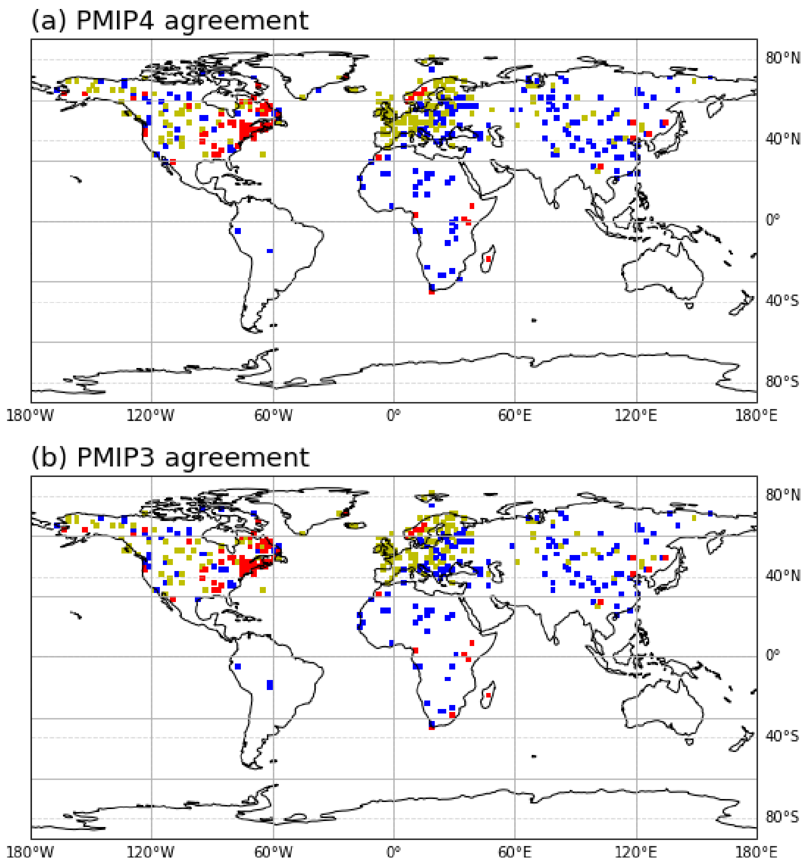

Figure 3.21: Agreement between (a) PMIP4-CMIP6 and (b) PMIP3-CMIP5 *mid-Holocene* annual precipitation changes (δpr) and pollen-based reconstructions (*anm*) from Bartlein et al. (2011). Yellow means at least 80% of models produce the precipitation change within the range of reconstruction with the consideration of the standard error at site (*anm +/- 1se*). Red means at least 80% of models produce more precipitation than reconstruction (i.e. $\delta pr > anm + 1se$), and blue means less (i.e. $\delta pr < anm - 1se$).

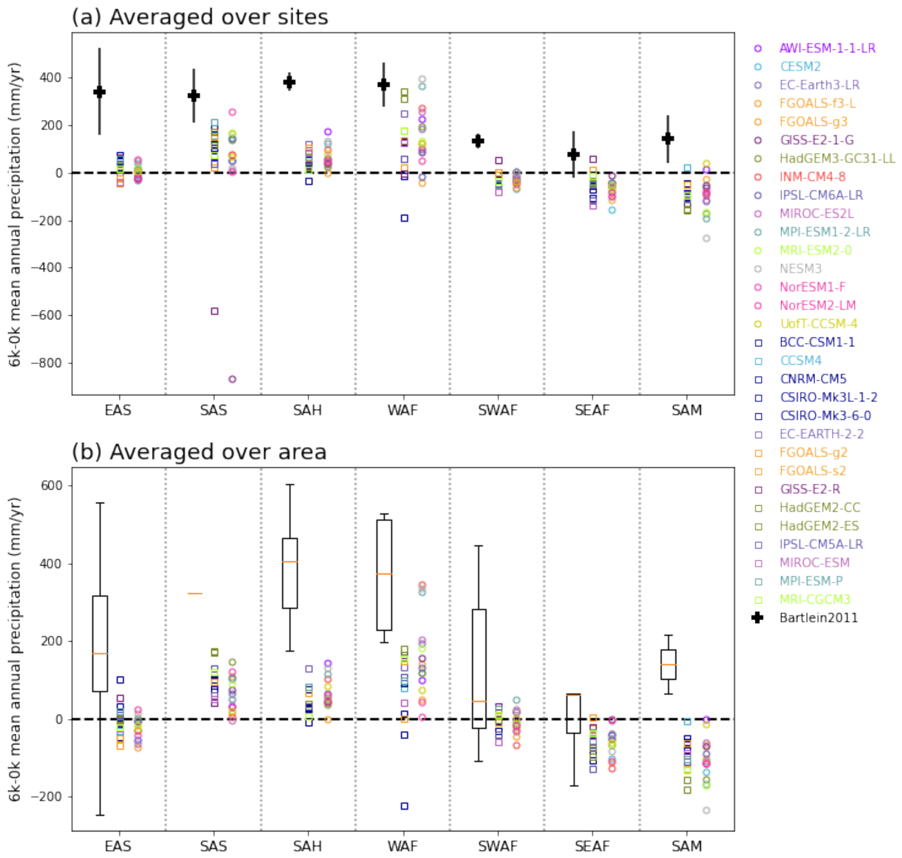

Figure 3.22: Comparison between simulated annual precipitation changes and pollen-based reconstructions from Bartlein et al. (2011). (a) Simulations are sampled only at grids where reconstruction points are available and applied area-weighted. (b) Simulated annual mean precipitation change is averaged over the region with the consideration of area-weight. Seven regions following the definition in the IPCC AR6, because part of the dataset plotting in panel (b) has contributed to Fig3.11 in IPCC AR6 Chapter 3 (Eyring et al., 2021). Regions (abbreviation; number of proxy data within the region) are E. Asia (EAS; 34), S. Asia (SAS; 1), Sahara (SAH; 15), West-Africa (WAF; 4), South-West-Africa (SWAF; 5), South-East-Africa (SEAF; 7) and South-American-Monsoon (SAM; 2). Simulations are sampled only at grids where reconstruction points are available.

directly shows the change in monsoon, it can in some way reflects the strength of monsoons. According to the definition of global monsoon and the characteristics of regional monsoons, majority of precipitation over monsoon-affected regions falls during monsoon seasons and very less during local winter. Therefore, using reconstructed annual mean precipitation should be able to reflect monsoon property. Over the NH monsoon regions, models produce expected precipitation increase in the *midHolocene* simulations (Figure 3.20) but likely underestimate the magnitude and outside the range of the reconstructions with a consideration of proxy uncertainties (Figure 3.21). Reconstructions suggest a precipitation increase over the SAMS during the mid-Holocene while models simulate a reduction (SAM column in Figure 3.22). In the South-East-Africa and South-West-Africa (SEAF and SWAF in Figure 3.22), reconstructions estimate a wetter southern Africa during the mid-Holocene, which the estimations from the models simulations in both PMIP4-CMIP6 and PMIP3-CMIP5 ensemble are not consistent with.

The Sahara (SAH) and West-Africa (WAF) columns in Figure 3.22 indicate that models show a smaller response in precipitation than the proxy data. This underestimation has been presented in previous generations (Joussaume et al., 1999; Braconnot et al., 2007, 2012; Perez-Sanz et al., 2014) and unchanged in AR4 (Jansen et al., 2007) and AR5 (Christensen et al., 2013). Harrison et al. (2015) suggests that the mismatch arises from biases in the *piControl*. As shown by Figure 3.10a, the NAF monsoon domain in PMIP4-CMIP6 *piControl* simulations is less northward than the observations, particularly over the ocean. The NAF expansion in the *midHolocene* simulations only removes the underestimation in the *piControl* as compared to the GPCP observation (Figure 3.11), which has also been displayed in the supplement of Brierley et al. (2020). Meanwhile, reconstructions suggest that Sahara was covered by vegetation during the wetter mid-Holocene (Prentice and Webb III, 1998; Prentice et al., 2000; Bigelow et al., 2003; Qin et al., 1998), but this has not been included in the *midHolocene* protocol (Otto-Bliesner et al., 2017a). Some studies have investigated the importance of considering vegetation over Sahara during mid-Holocene, and they suggest that simulated precipitation changes at the mid-Holocene show better agreement with reconstructions if the models have interactive vegetation or use more realistic vegetation cover over the Sahara (e.g. Lu et al., 2018; Swann et al., 2014b; Pausata et al., 2016; Gaetani et al., 2017; Messori et al., 2019) by leading to a cyclonic water vapour flux anomaly over North Africa with a strengthened westerly flow that brings large amounts of moisture into the Sahel from the Atlantic Ocean (Messori et al., 2019), though the mismatch between simulations and reconstructions still exists. Moreover, greening Sahara during the mid-Holocene could result in increased precipitation in all regional monsoons in the NH (Sun et al., 2019). However, the increase of *midHolocene* NAF rainfall simulated by those PMIP4-CMIP6 models that include schemes of dynamic vegetation (Section 3.2.2) do not perform better than the rest of models (Figures 3.12 and 3.14). This may be caused by climate models having climatological bias (Harrison et al., 2015) or too weak feedbacks between vegetation and water cycle (Hopcroft et al., 2017). Tierney et al. (2017) found that climate models are not able to reproduce the Green Sahara if not including strong vegetation and dust feedbacks. The effects of dust on mid-Holocene precipitation over Sahara and Sahel have also been pointed out by Thompson et al. (2019). However, the importance of dust has been rejected by Hopcroft and Valdes (2019) as reducing MH dust only leads to limited precipitation enhancement. AWI-ESM-1-1-LR, MPI-ESM1-2-LR and NESM3 in PMIP4 include interactive vegetation, but they perform no significant difference in the *midHolocene* simulations than other models. Appropriate dynamic vegetation and dusts schemes therefore should be considered in future studies.

This section compares PMIP4-CMIP6 and PMIP3-CMIP5 ensembles with the two compilations described above. Temperature and precipitation are compared separately. Taylor diagram (Figure 3.23) shows that both PMIP4-CMIP6 and PMIP3-CMIP5 models have nearly no skill in predicting mid-Holocene temperature and precipitation change. There is no strong correlation between site-level simulated anomalies here and reconstructed anomalies in (Kaufman et al., 2020b) and (Bartlein et al., 2011).

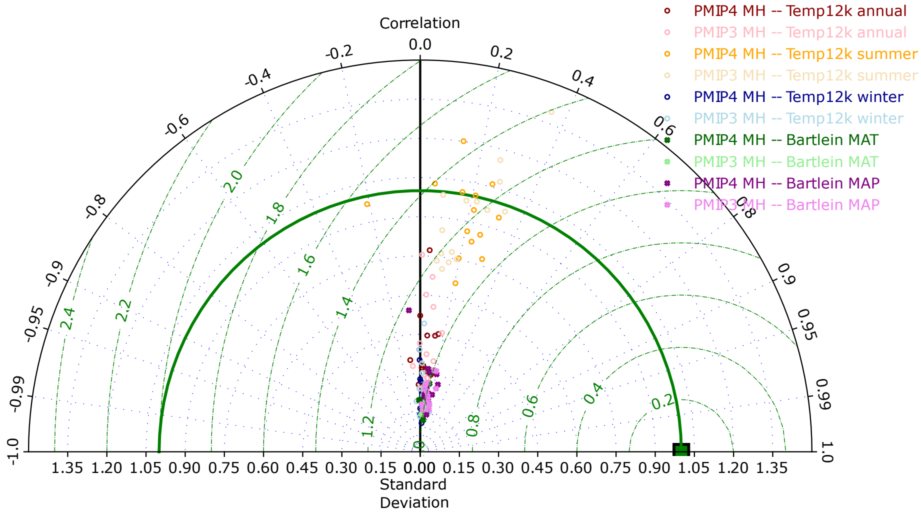

Figure 3.23: Taylor diagram for the *midHolocene* temperature and precipitation anomalies. The distance of any point from the origin point (0) gives the standard deviation of field, from the green reference point (1.0) gives the centered root mean square difference between model and data. Pattern correlation between model and data is given by the azimuthal coordinate. Model points are sampled at sites where data are available, as shown in Figure 3.18 and 3.20. Model statistics are corrected to account for observational uncertainties, by subtracting the estimated contributions made by reconstructed errors of the two proxy compilation described in Section 3.4. A similar analysis has been published in Brierley et al. (2020) by analysing seasonality (summer - winter and MTWA - MTCO) instead of seasonal temperature change presented here.

3.5 PMIP4-CMIP6 vs PMIP3-CMIP5

Different to the other two past warm periods discussed in this thesis, the *mid-Holocene* has been involved in the PMIP since its beginning, which offers an opportunity to evaluate improvements between generations of PMIP as well as individual models. Results and discussion in previous sections show that the PMIP4-CMIP6 *midHolocene* ensemble is in general colder than PMIP3-CMIP5, but the difference is caused by changes in prescribed atmospheric GHGs concentration rather than developments in models. Hotelling's T^2 test (Wilks, 2011) has been used to evaluate differences between model simulations. It tests the hypothesis of equality of multivariate ensemble means . This approach has been used to evaluate the difference between PMIP generations (Harrison et al., 2014, 2015; Brierley

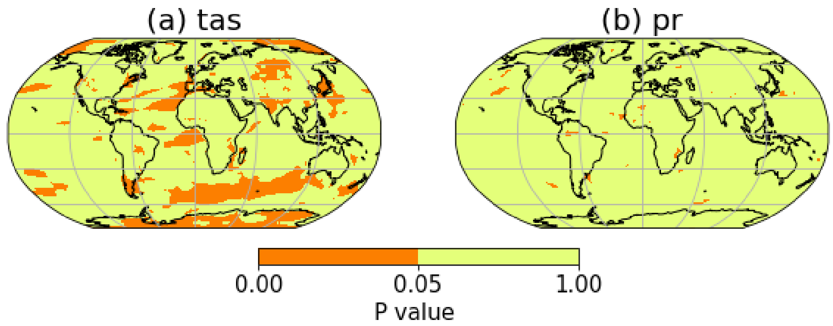

Figure 3.24: Results of p values of Hotelling's T2 test (Wilks, 2011) comparing the PMIP4-CMIP6 and PMIP3-CMIP5 ensembles. Values less are than 0.05 (orange) reject the hypothesis of equality of the multivariate ensemble means the two ensemble, i.e. where would be considered sigficiant. Values include ANN, DJF and JJA mean temperature (panel a: tas ANN, DJF, JJA) and precipitation (panel b: pr ANN, DJF, JJA). Brierley et al. (2020) presents similar analysing comparing more variables.

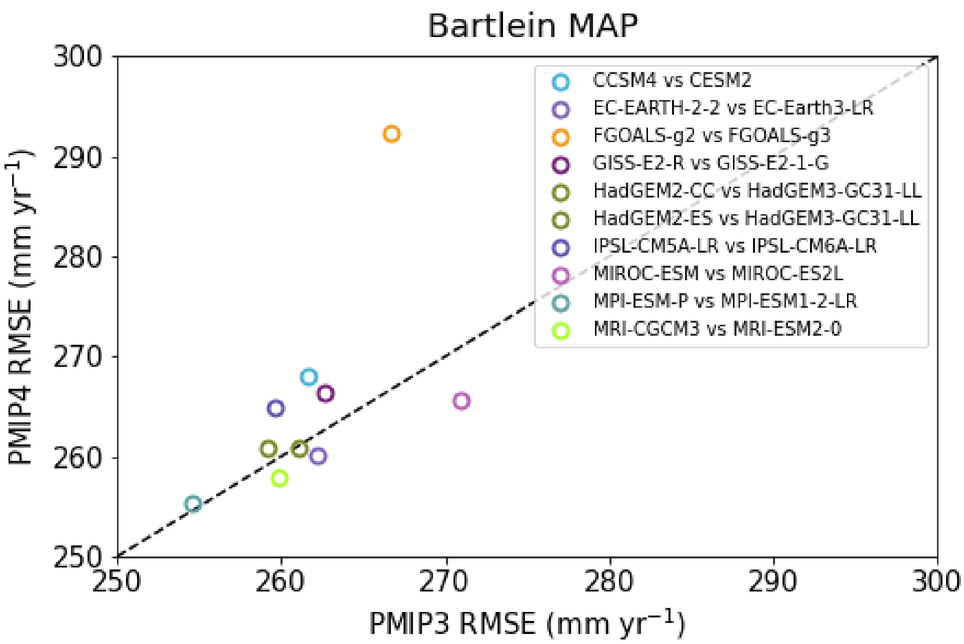

Figure 3.25: Comparison between RMSE values between MAP from Bartlein et al. (2011) and simulated *midHolocene* annual mean precipitation change from PMIP4-CMIP6 models and their earlier generations contributing to the PMIP3-CMIP5.

et al., 2020). Figure 3.24 shows the maps of the p values for testing the hypothesis of equality of the multivariate ensemble means of anomalies of *midHolocene* annual, DJF and JJA mean temperature and precipitation, respectively. There are nearly no regions to be considered to be significant in simulating precipitation anomalies. Though some regions show significance in simulating temperatures, the total number of grid cells with $p > 0.05$ does not exceed the false discovery rate (Wilks, 2006). Results here agrees with the findings in Brierley et al. (2020) by involving different and/or more variables. Harrison et al. (2015) presents a similar analysis comparing PMIP2-CMIP3 with PMIP3-CMIP5, suggesting that there's little difference between PMIP2-CMIP3 with PMIP3-CMIP5. This suggests that PMIP2-CMIP3, PMIP3-CMIP5 and PMIP4-CMIP6 are not significantly different. It would be appropriate to include the simulations of the three generations as a single ensemble for other analysis (e.g. D'Agostino et al., 2019, 2020; Yoshimori and Suzuki, 2019) to increase the power of statistical analysis.

9 of the 16 PMIP4-CMIP6 models participating in the *midHolocene* have earlier versions contributing to the PMIP3-CMIP6 *midHolocene* ensemble, allowing to evaluate if later versions of a same model family perform better than the earlier generations. Root mean square error (RMSE) between proxy data and simulated change by PMIP4-CMIP6 and PMIP3-CMIP5 models are conducted to evaluate the agreement between reconstructions and simulations. Comparing to MAP from Bartlein et al. (2011), the improvements in simulating the mid-Holocene precipitation are regionally dependant as a PMIP4-CMIP6 model producing better global precipitation (Figure 3.25) does not always perform better over monsoon affected regions (Figure 3.22). Comparison between the RMSE values shows that there are no uniform improvements between model generations as those PMIP4-CMIP6 models are not simulating better MH temperature change than their PMIP3-CMIP5 versions (Figure 3.26). For example, FGOALS-g3 agrees less with reconstructed Arctic warming than FGOALS-g2, but it is better simulating winter temperature change. HadGEM3-GC31-LL captures the Arctic warming than its earlier versions HadGEM2-CC and HadGEM2-ES, agreeing with the improvement stated by the

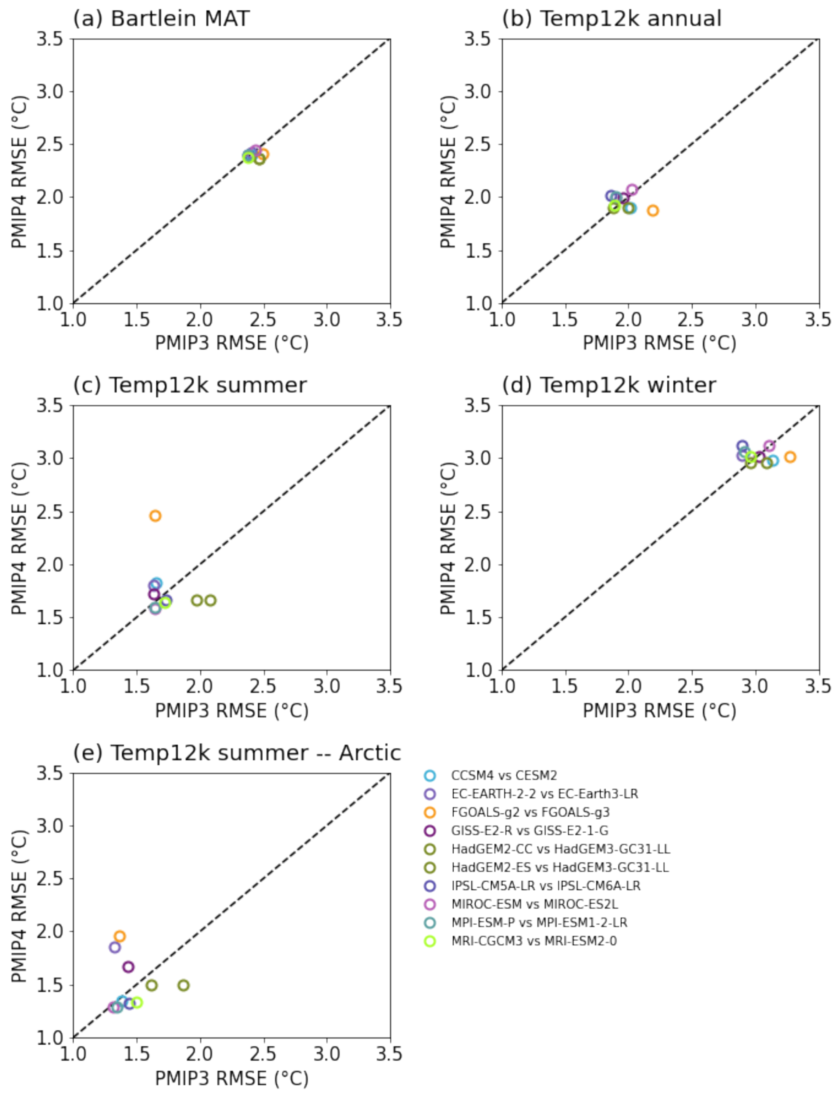

Figure 3.26: Same as Figure 3.25 bur for temperature. (a) Simulated annual mean temperature change versus pollen reconstructed MAT from Bartlein et al. (2011). (b) Annual, (c) summer and (d) winter mean temperature change versus proxy data from Temp12k dataset (Kaufman et al., 2020b). Panel (e) enlarges north to 60°N of panel (c) reflecting the Arctic warming.

model group UK Met Office (Williams et al., 2020).

3.6 Conclusion

This chapter analyses the PMIP4-CMIP4 *midHolocene* simulations and compares its results to its earlier version PMIP3-CMIP5 and proxy reconstructions to investigate if the PMIP4-CMIP6 ensemble is different to the PMIP3-CMIP5 and if it has been improved. Results in Section 3.3 show that the mean seasonal changes in temperature and precipitation in the PMIP4-CMIP6 ensemble follow the theoretical response to changes in insolation forciing. During JJA, the increased insolation in the NH results in a summer warming that enhances the interhemispheric temperature gradient and more warming over land that enhances the gradient between land and sea. The ITCZ in the *midHolocene* simulations shows a northward shift than the *piControl*. Changes in mean atmospheric circulation bring more precipitation over land than over ocean in the *midHolocene* simulations. Therefore, the increased insolation during the boreal summer in the NH leads to an expansion and intensification in the NAF, and also in the EAS and NAMS though in which the enhancement is small and less consistent across the ensemble. The reduced precipitation rate in the *midHolocene* SAS is due to the decreased precipitation in the Philippines and Southeast Asia that counteracts the intensification of precipitation on the southern flank of the Himalayas (here and in Brierley et al., 2020). The increased precipitation over northern Africa and India in turn reduces local temperature which is cooler than the *piControl* condition. During the DJF, the decreased insolation in the SH results in more precipitation occurring over ocean while less over land, showing weakened and constricted SAMS, SAF and AUSMC as expected. These changes in monsoons in the PMIP4-CMIP6 *midHolocene* simulations in general agree with the earlier studies (e.g. Braconnot et al., 1999; Liu et al., 2004; Zhao et al., 2005; Zhao and Harrison, 2012; Joussaume et al., 1999; Braconnot et al., 2002). D'Agostino et al. (2019, 2020) suggest that changes in monsoon at the mid-Holocene are dominantly caused by changes in net energy input and the mean atmospheric circulation flow, as the monsoon enhancement in the NH is driven by the strengthened mean atmospheric flow that brings more rainfall over land than over ocean (D'Agostino et al., 2019) while the weakened monsoon in the SH is associated with weakened local atmospheric circulation over land and strengthened flow over ocean (D'Agostino et al., 2020).

The most pronounced and robust changes occur in the NAF with large spread across models, but its magnitude of northward extension and precipitation increase in the *midHolocene* is still underestimated compared to the suggestions from reconstructions (Braconnot et al., 1999, 2002; Harrison et al., 2015). Possible explanations could be the climatological bias in GCMs (Harrison et al., 2015), not prescribing mid-Holocene vegetation (Otto-Bliesner et al., 2017a), or the missing of strong feedbacks between vegetation and water cycles (Hopcroft et al., 2017). The mechanism behind the mean atmospheric circulation suggested by D'Agostino et al. (2019) and dynamic vegetation should be considered in future studies.

The PMIP4-CMIP6 *midHolocene* simulations show similar temperature patterns to those were present in the PMIP3-CMIP5 ensemble, as well as in PMIP2 (Harrison et al., 2014). The slight cooler global mean temperature change in the PMIP4-CMIP6 compared to the PMIP3-CMIP5 is caused by using more realistic prescribed greenhouse gas concentrations instead of improvements in model physics. The agreement in large scale changes in precipitation between the two ensembles indicates that the broad-scale precipitation patterns in the PMIP4-CMIP6 ensemble are similar to the PMIP3-CMIP5, which were also presented in the previous generations (Braconnot et al., 2007, 2000). Previous findings (Harrison et al., 2015; Brierley et al., 2020) and T test results (statistical t test and Hotelling's T^2 test) in this chapter suggest no significant difference between PMIP generations. This implies that PMIP simulations could be considered as a single ensemble for analysis (D'Agostino et al., 2019, 2020; Yoshimori and Suzuki, 2019) to increase the power of statistical analysis.

Chapter 4

Monsoon response to the orbital forcing in the CMIP6-PMIP4 *lig127k* simulations

Last Interglacial (LIG) had been discussed in IPCC since its first phase (Folland et al., 1990), but little modelling evidence has been discussed until AR4 (Jansen et al., 2007) and AR5 (Masson-Delmotte et al., 2013). The LIG ensemble in the AR5 suggested changes in regional temperatures (Masson-Delmotte et al., 2013), but as models using various protocols, it was difficult to examine whether the difference was caused by difference in cryosphere feedback strength (Otto-Bliesner et al., 2013) or the variation between experimental designs across the ensemble. Meanwhile, the LIG simulations were produced by models that were the earlier and/or lower-resolution version being used to make future projections, which made the assessment of model reliability difficult (Lunt et al., 2013). In PMIP4, the *lig127k* experiment is included in the first time as an endorsed experiment (Kageyama et al., 2018). All models have completed the *lig127k* simulations by applying the same protocol that is described in Otto-Bliesner et al. (2017a). Its Tier 1 simulation was designed to examine the response in climate to an orbital forcing stronger than the mid-Holocene (MH) with the GHGs similar to their pre-industrial levels (Kageyama et al., 2018; Otto-Bliesner et al., 2017a). Including both *midHolocene* and *lig127k* offers a chance to quantify the effect of orbital forcing, which will be discussed in

Chapter 6.

In this chapter, I will analyse the PMIP4-CMIP6 *lig127k* monsoon, following the analysis in Otto-Bliesner et al. (2021). Models that could simulate a better LIG climate might imply they can produce better future projection. This chapter will also try to evaluate model perform via investigating two questions:

- **Does equilibrium climate sensitivity (ECS) relate to the quality of model's LIG simulation?** If so, it may imply that LIG climate could be used to constrain ECS (see Chapter 1 Section 1.3.2).

- **Do models with dynamic vegetation perform better?** As discussed in Section 3.4.2.2, earlier studies focused on MH monsoon have suggested that models with more realistic MH vegetation cover like including "Green Sahara" simulate better MH monsoon response. The LIG also responded to orbital forcing but having stronger magnitude, which implies that models with dynamic vegetation may be able to perform better monsoon response in *lig127k* simulations.

Section 4.1 describes the orbital parameters at 127 ka, the protocol of the PMIP4 *lig127k* experiment and the models that have performed the PMIP4-CMIP6 *lig127k* simulations. Following sections include the response in temperature (Section 4.2) and monsoon (Section 4.3) to the orbital forcing. Comparison between simulated changes and proxy reconstructions also goes into these two sections to evaluate model performance. The discussion section (Section 4.4) attempts to answer the two questions above in light of the results. A brief conclusion is provided at the end of this chapter (Section 4.5).

4.1 The PMIP4-CMIP6 *lig127k* experiment

4.1.1 Orbital forcing at 127 ka

the Last Interglacial was characterised by larger eccentricity than present-day. At 127 ka, eccentricity and obliquity was larger than today and perihelion occurred near the boreal summer solstice instead of close to the boreal winter solstice in 1850

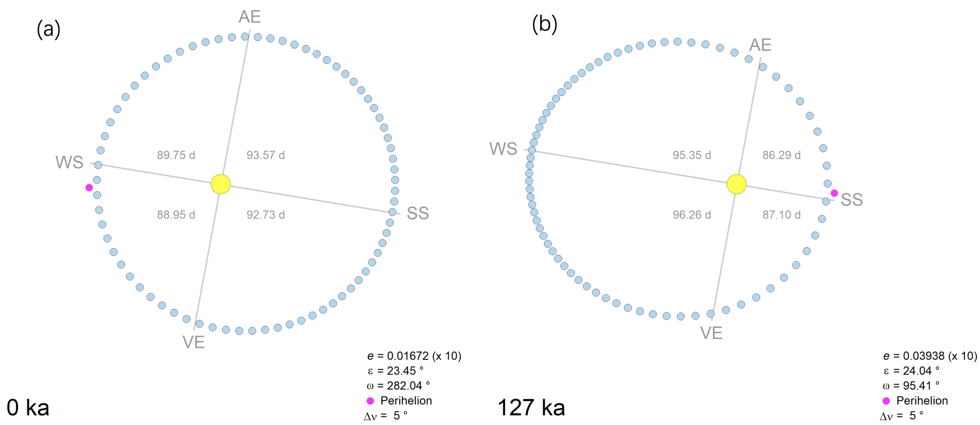

Figure 4.1: Orbital forcing at (a) 0 ka and (b) 127 ka. e stands for eccentricity, ε for obliquity and ω for longitude of perihelion from from vernal equinox (VE). AE shows the position of autumnal equinox, WS shows that of winter solstice and SS of summer solstice (Adapted from Bartlein and Shafer, 2019).

CE (Figure 4.1). Compared to 1850 CE, the different orbital configurations at the LIG induced altered seasonal and latitudinal distribution of top-of-atmosphere insolation (Figure 4.2a) by showing large positive insolation anomalies during boreal summer and large negative insolation during austral summer. The annual insolation anomaly (Figure 4.2b) shows a slight increase in high latitudes in both hemispheres and a decrease in the tropics, but no change in global mean insolation.

4.1.2 Experimental design

Otto-Bliesner et al. (2017a) provided detailed description of the protocol of the *lig127k* experiment in the PMIP4-CMIP6. Table 4.1 lists the settings. Three orbital parameters are prescribed using the configuration at 127 ka (Figure 4.1) following Berger and Loutre (1991). The *lig127k* experiment prescribes less GHGs concentrations than the *piControl* (Table 4.1). The prescribed concentrations of greenhouse gases in the PMIP4-CMIP6 *lig127k* use realistic concentrations derived from ice cores (Otto-Bliesner et al., 2017a). Other boundary conditions (including solar constant, palaeogeography, ice sheets, vegetation and aerosols) remain the same as those prescribed in the *piControl* (Table 4.1), unless the model has its own specific setup. Vegetation in each model is treated same as the *piControl*, as either to be

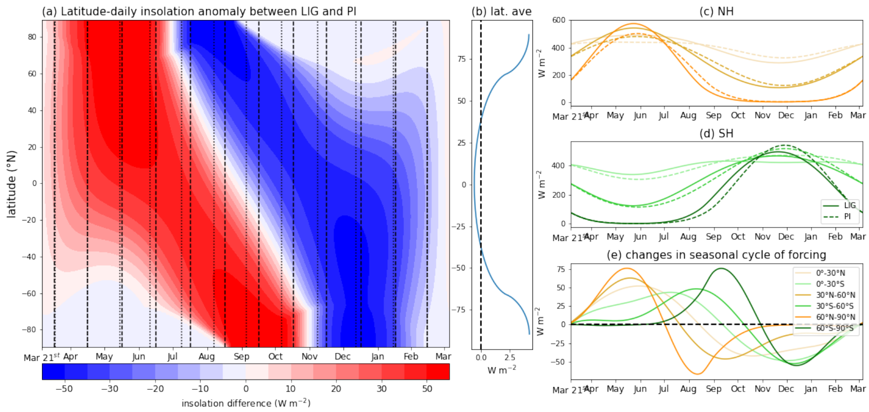

Figure 4.2: Latitude-daily insolation anomaly between 127 ka and 1850 CE. (a) The difference in the seasonal cycle insolation at the top of the atmosphere (W m^{-2}) between the last Interglacial at 127 ka and pre-industrial at 1850 CE. Date starts from March 21^{st}, i.e. the vernal equinox,to remove the uncertainties in calendar correction. The black dashed lines show the start day of each month at 1850 CE and the dotted lines show that at 127 ka, which illustrate the effect of orbital changes on calendar. (b) The change in mean annual forcing (W m^{-2}) by latitude. The seasonal cycle of incoming solar radiation in W m^{-2} for mid-Holocene and pre-industrial in low and mid latitudes in the (c) NH and (d) SH, and (e) the changes in the changes in the cycles. (*Insolation was computed via a python package "climlab.radiation.insolation"*.)

prescribed the same vegetation as in the *piControl* or predicted dynamically with the vegetation interacting with other components. See the next section for implementations in the models.

4.1.3 Models

The PMIP4-CMIP6 *lig127k* ensemble includes 17 models as described in Section 2.1.2. 15 out of the 17 models have completed the DECK experiments and uploaded their simulations on the ESGF (see Appendix A). AWI-ESM-2-1-LR has completed the PMIP4 *lig127k* simulations but had not run all the DECK experiments nor uploaded the simulations on the ESGF at the time of writing, so its simulations were directly asked from the model group. Across the ensemble, AWI-ESM-1-1-LR, AWI-ESM-2-1-LR, MPI-ESM1-2-LR and NESM3 equip with interactive vegetation.

Table 4.1: *lig127k* experimental design, according to Otto-Bliesner et al. (2017a).

	piControl	*lig127k*
Orbital parameter		
Eccentricity	0.016764	0.039378
Obliquity (°)	23.459	24.04
Perihelion – 180 (°)	100.33	275.41
Vernal equinox	Fixed to noon on 21 March	Fixed to noon on 21 March
GHGs		
Carbon dioxide (ppm)	284.3	275
Methane (ppb)	808.2	655
Nitrous oxide (ppb)	273	255
Other GHGs	CMIP DECK *piControl*	0
Solar constant (W m^{-2})	1360.747	Same as *piControl*
Paleogeography	Modern	Same as *piControl*
Ice sheets	Modern	Same as *piControl*
Vegetation	CMIP DECK *piControl*	Same as *piControl*
Aerosols: dust, volcanic, etc.	CMIP DECK *piControl*	Same as *piControl*

4.1.4 Proxy reconstructions

4.1.4.1 Temperature compilations

Though reconstructed LIG temperature anomalies do not direct reflect monsoon change during the LIG, comparison between simulated and reconstructed temperature is discussed because temperature proxy data is more abundant than the precipitation evidence and it provide quantitative estimates that could be useful in model evaluation. The compilation (Hoffman et al., 2017) has 186 site-level reconstructed sea surface temperature (SST) anomalies (86 annual, 59 summer and 41 winter) derived from different reconstruction methods (see Section 1.5.1 for details). The distribution of the dataset is shown by the circles in Figure 4.5. For each site, the anomaly is computed at the difference between the SST estimation taken at 127 ka relative to the local estimation from 1870-1889 CE HadISST dataset (Raymo and Nisancioglu, 2003). 41 out of the 86 reconstructed annual SST anomalies at sites were calculated as the average between the summer and winter SSTs and used HadISST dataset to correct the local seasonal bias. This compilation used Monte Carlo approaches to propagate uncertainties in relative dating and temperature re-

Table 4.2: Models and simulated mean annual (ΔT_{ANN}), DJF (ΔT_{DJF}) and JJA (ΔT_{ANN}) temperature change in the PMIP4-CMIP6 *lig127k* simulations (*lig127k* - *piControl*). Models are split into three categories according to the relationship between their ECS and the ECS range (2.5°C to 4.0 °C given by the IPCC AR6 (IPCC, 2021d). Models with the ECS lower than 2.5°C are here after referred as to low-ECS model, within the IPCC suggested range referred as to IPCCrange-ECS model, and higher than 4.0°C referred as to high-ECS model.

Model	ECS (°C)	ΔT_{ANN} (°C)	ΔT_{DJF} (°C)	ΔT_{JJA} (°C)	Ref
low-ECS models					
INM-CM4-8	2.1	-0.2	-1.0	0.9	Volodin et al. (2018)
NorESM1-F	2.3	-0.2	-1.2	1.0	Guo et al. (2019)
IPCCrange-ECS models					
NorESM2-LM	2.5	-0.1	-1.1	1.2	Seland et al. (2020)
GISS-E2-1-G	2.7	-0.1	-0.9	1.0	Kelley et al. (2020)
MIROC-ES2L	2.7	-0.4	-1.2	0.7	Hajima et al. (2020)
MPI-ESM1-2-LR	2.8	-0.1	-1.1	1.1	Mauritsen et al. (2019)
FGOALS-g3	2.9	0.4	-0.4	1.6	Li et al. (2020)
FGOALS-f3-L	3.0	-0.5	-1.3	0.7	He et al. (2020)
AWI-ESM-1-1-LR	3.6	-0.3	-1.4	0.8	Sidorenko et al. (2015)
AWI-ESM-2-1-LR	3.6	-0.2	-1.0	0.9	Sidorenko et al. (2015)
NESM3	3.7	0.1	-0.9	1.4	Cao et al. (2018)
ACCESS-ESM1-5	3.9	0.3	-0.5	1.5	Ziehn et al. (2020)
high-ECS models					
EC-EARTH-3-3	4.3	0.5	-0.5	1.6	Döscher et al. (2021)
IPSL-CM6A-LR	4.5	-0.3	-1.3	1.0	Boucher et al. (2020)
CNRM-CM6-1	5.1	0.4	-0.7	1.8	Craig et al. (2017)
CESM2	5.3	-0.1	-1.0	1.1	Gettelman et al. (2019)
HadGEM3-GC31-LL	5.4	0.6	-0.3	1.7	Williams et al. (2018)
Ensemble average		-0.0	-0.9	1.2	Otto-Bliesner et al. (2021)

constructing, and gave 2 standard deviations as the integrated uncertainties (Hoffman et al., 2017).

Capron et al. (2014, 2017) compilations include 41 reconstructed high-latitude SST changes (3 annual, 23 summer and 15 winter) at sites in the North Atlantic Ocean and Southern Ocean (squares in Figure 4.5), one surface air temperature (SAT) record from the Greenland ice sheet and four from the Antarctic ice sheet (diamonds in Figure 4.5). SSTs were derived from different reconstruction methods, and SATs were deduced from ice core water isotopic profiles. The 127 ka SSTs and SATs at all sites are estimated as the the median temperature averaged over the

128–126 ka period. The SST anomalies are referenced to 1870–1899 CE SSTs in the HadISST dataset (Raymo and Nisancioglu, 2003). For the SAT anomalies, the reconstruction from Greenland is referenced to borehole temperature measurements and those from the Antarctica are referenced to the water isotopic profiles between 1870 and 1899 CE (Capron et al., 2017). This compilation used Monte Carlo approaches to propagate uncertainties in relative dating and temperature calibration, and gave 2 standard deviations (2σ) as the integrated uncertainties (Capron et al., 2017).

Otto-Bliesner et al. (2021) further include two compilations of continental air temperature reconstructions. They are not used here as the two datasets show Arctic MTWAs and European MTWAs and MTCOs instead of seasonal mean change and can cause conflicts when comparing to JJA and DJF mean temperature response.

4.1.4.2 Precipitation

Unlike reconstructed MH precipitation data that are quantitative and are abundant over Europe and eastern North America (Section 3.4.2.2), reconstructed LIG precipitation is limited by proxy quantity, coverage and quality. Though it is difficult to have quantitative evidence, Scussolini et al. (2019) provide a near-global coverage of precipitation evidence derived from pollen, speleothem, lacustrine sediment composition and multi-proxy reconstructions to show the signal of precipitation change. The compilation includes 138 proxy sites and selects proxy signals approximately corresponding to 127 ka. Proxy signals are defined as much drier, drier, no noticeable anomaly, wetter and much wetter, shown by different markers in Figure 4.11. Besides the signals, 11 sites have quantitative reconstructed mean annual precipitation (MAP).

4.2 Temperature response

The LIG was characterised by larger eccentricity and obliquity than modern and the position of perihelion is nearly 180° opposite, close to the boreal summer solstice. The annual mean surface temperature in the *lig127k* ensemble mean (Figure 4.3a

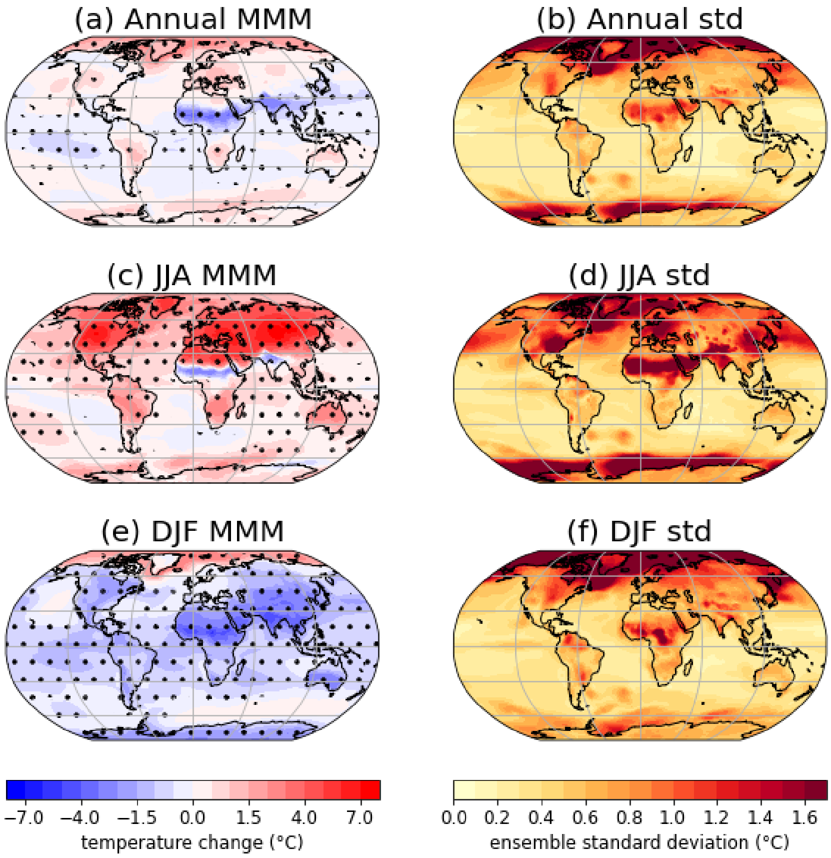

Figure 4.3: Multi-model mean of (a) annual, (c) JJA and (e) DJF temperature change (°C) and ensemble standard deviation (b,d and f) in the PMIP4-CMIP6 *lig127k* ensemble as compared to the *piControl*. Dot-shaded regions reflect where at least 80% (i.e. 14 out of 17) of the models agree the sign of MMM.

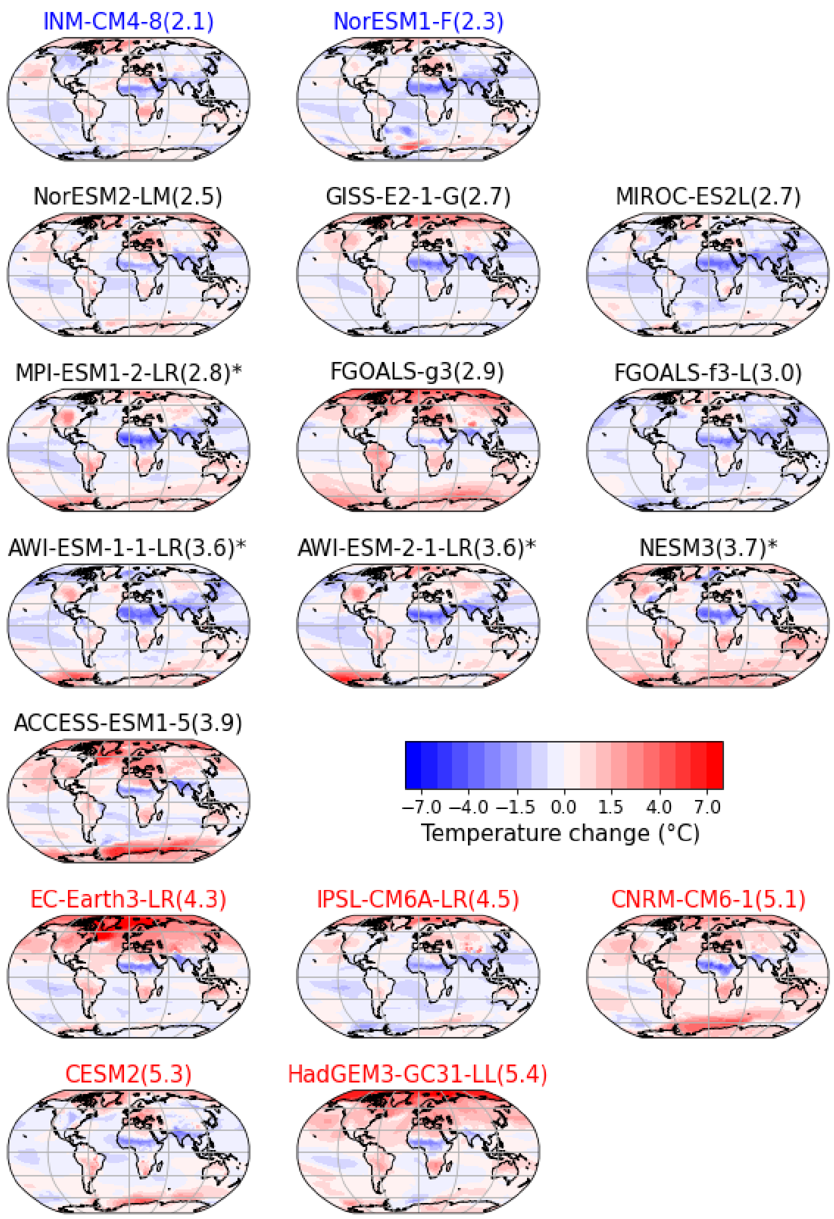

Figure 4.4: Annual mean temperature (°C) change performed by individual models. Each panel title is named as the model name (ECS) and colored according to the ECS (blue for ECS < 2.5°C, black for 2.5°C $<$ ECS < 4.0°C and red for ECS > 4.0°C.) $*$ marks the models including dynamic vegetation.

and 4.4; as compared to the *piControl*) shows warming in high latitudes in both hemispheres and especially over the continents and cooling in low to mid latitudes. This is expected from the response to the insolation anomalies at 127 ka by annually receiving more insolation in high latitudes while less in tropics (Figure 4.2b). Monsoon affected regions in the northern Africa, India and southeast Asia show stronger annual cooling than surroundings, which is related to the summer cooling caused by greater cloud cover and higher evaporation brought by a northward shift of strengthened monsoons. However, the magnitude of the annual mean temperature changes is less than 1°C, except the Arctic warming and the cooling in the North Africa and India, and the multi-model mean of global mean annual mean surface air temperature is negative but nearly 0°C (Table 4.2), which is weaker than that in *midHolocene* (see Chapter 6 for a comparison and discussion). The simulated *lig127k* temperature change is lower and even shows a different sign than the LIG GMST warming of 0.5 - 1.5 °C assessed in AR6 (Gulev et al., 2021). Panels a and b in Figure 4.5 show the comparison between the simulated changes in annual mean surface temperature (*lig127k* - *piControl*) and reconstructed anomalies from Hoffman et al. (2017) and Capron et al. (2017). Over high latitudes, majority of the reconstructions at sites show warmer LIG and a few sites in the North Atlantic show cooling. The PMIP4-CMIP6 *lig127k* ensemble shows warmer high latitudes than the *piControl*, which match the reconstructed warming over the Antarctica, Greenland and Arctic Ocean but fail to reproduce the magnitude. The temperature mismatch over ice sheets could be explained by models using the same Greenland and Antarctic ice sheets as in the *picontrol* instead of allowing the ice sheets to evolve to smaller and lower condition of the LIG climate (Otto-Bliesner et al., 2021). This can be supported by Holloway et al. (2018), who suggest the importance of ice sheet melting the LIG missing heat problem in simulations. Over lower latitudes (40°N - 40°S), simulations and reconstructions are in good agreements in the cooling over tropical Atlantic and the warming around New Zealand and in the upwelling region off the west coast of North America, though underestimate the magnitude of warming. Models produce slight cooling or no change in annual mean temperature anomalies over the South Atlantic near southern Africa, which fail to produce the warming suggested by reconstructions and are outside of 2σ uncertainties (Figure 4.5b). Across the ensemble, AWI-ESM-1-1-LR, AWI-ESM-2-1-LR, MPI-ESM1-2-LR and NESM3, those applied dynamic vegetation scheme do not produce smaller mismatch between model and data than other models, which suggests that models with dynamic vegetation do not necessarily be better in simulating LIG climate response.

Unlike the small change in annual temperature, *lig127k* produces stronger warming during JJA and cooling during DJF. Both hemispheres received more incoming solar radiation during JJA in particular in NH high latitudes while a reduction during DJF especially in the SH (Figure 4.2). As expected, *lig127k* shows warming across the globe during JJA especially in North America and central Eurasia by having the greatest *lig127k* warming at least 6°C warmer than the *piControl*. The exceptions occur in the monsoon regions in the northern Africa and India due to increased cloud cover and higher evaporation brought by a northward shift and intensification of the monsoons. Cooling also shows over part of the ocean surface in the SH, but this is less than 0.5°C. During DJF, the *lig127k* simulations simulate cooling nearly everywhere except the Arctic Ocean and Southern Ocean. The Arctic warming could be related to ocean memory (Serreze and Barry, 2011; Marino et al., 2015; Govin et al., 2012) and presumably considered with sea ice change discussed in Otto-Bliesner et al. (2021). Large spread across the ensemble occurs in simulating warming in the Arctic and Southern Ocean and cooling in the monsoon region in the northern Africa throughout the year (Figure 4.3b, d and f). Compared to the earlier LIG ensemble, patterns of annual and seasonal temperature changes in the PMIP4-CMIP6 *lig127k* ensemble are similar to those found in Lunt et al. (2013), but the warming in the PMIP4-CMIP6 ensemble is larger. However, it is difficult to compare the PMIP4-CMIP6 *lig127k* ensemble with the earlier LIG ensemble as the simulations involved in Lunt et al. (2013) did not apply a uniform protocol: the orbits and greenhouse gas concentrations varied between ensemble members. The four models with dynamic vegetation scheme do not produce better in JJA

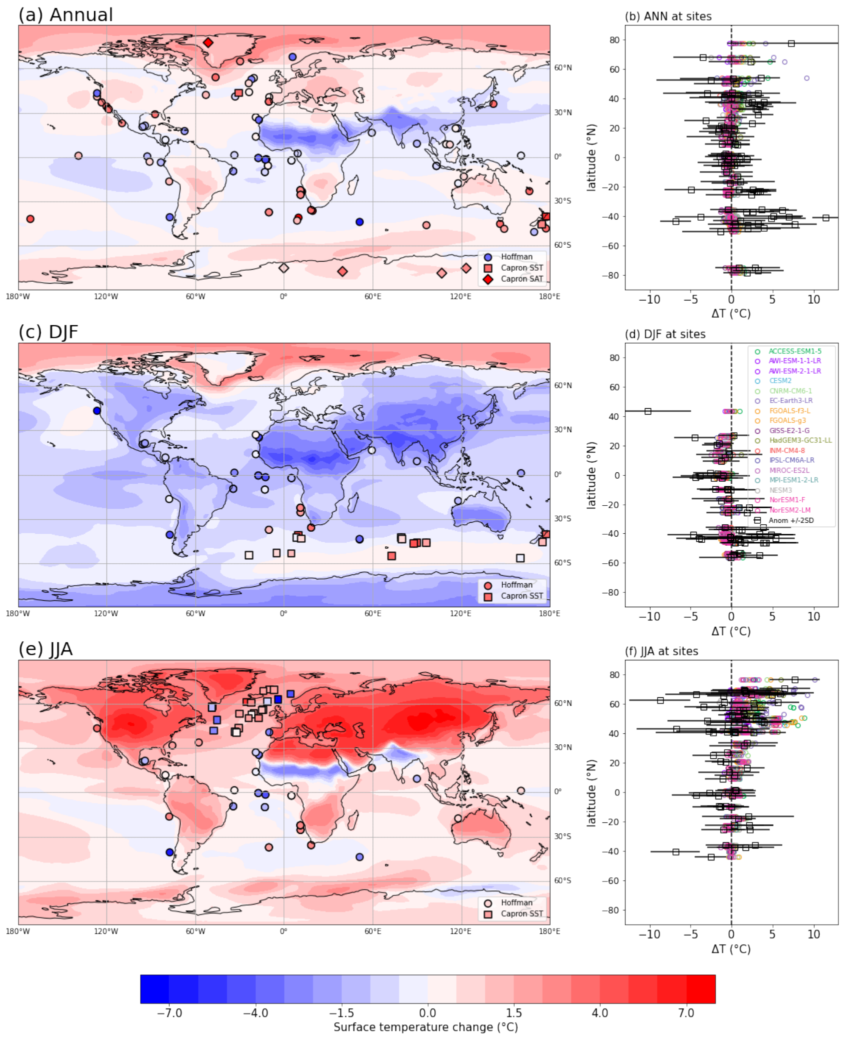

Figure 4.5: Comparison in (a) annual, (c) JJA and (e) DJF mean surface temperature anomaly (°C) between the PMIP4-CMIP6 ensembles (*lig127k* - *piControl*) and estimations from proxy reconstructions (Hoffman et al., 2017; Capron et al., 2014, 2017). Panels (b), (d) and (f) compare the reconstructed anomalies shown in the left column with the simulated anomalies at sites by individual models.

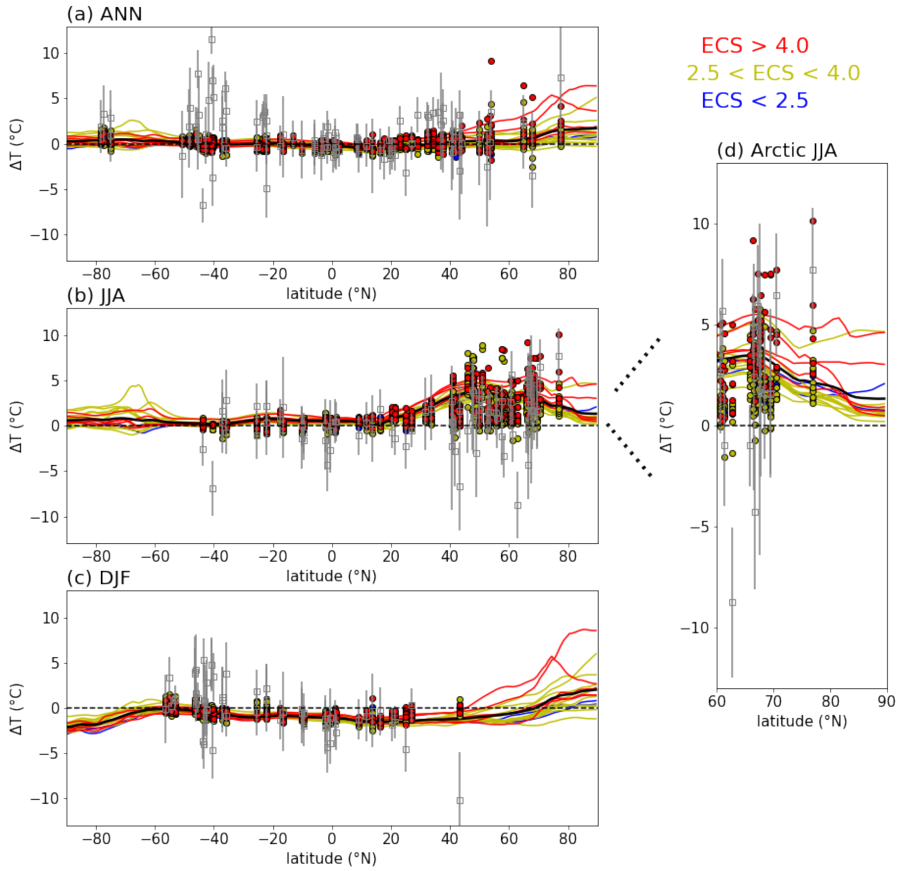

Figure 4.6: Zonal temperature anomaly (°C). Panels a, b and c are the same as panels b, d and f in Figure 4.5 but are colored according to the ECS (i.e. red for ECS > 4.0°C, yellow for 2.5°C < ECS < 4.0°C and blue for ECS < 2.5°C). Panel d enlarges the JJA Arctic (60°N to 90°N) warming in panel b

temperature response than others, which also happen to DJF.

In DJF, model simulations provide cooling over the tropical Atlantic, along the eastern coast of Mexico and along the western coast of South America, which match the sign of DJF cooling suggested by proxy reconstructions (Figure 4.5c and d). Over the Southern Ocean, SSTs by Capron et al. (2017) suggest warming during austral summer, at sites where slight cooling/warming or no change is produced across the ensemble outside of 2σ uncertainties (Figure 4.5d). The Capron et al. (2017) compilation provides reconstructed boreal summer SSTs over

Table 4.3: Multi-model mean and standard deviation of RMSEs between simulations from different ECS categories (low, IPCCrange and high) and proxy data. Due to the data availability and distribution, tropical annual mean temperature change (°C) uses the reconstructed annual mean SST anomalies between 23.5°S to 23.5°N from Hoffman et al. (2017), Arctic warming (°C) uses summer temperature anomalies north to 60°N from Capron et al. (2017), and MAP (mm yr^{-1}) uses all of the quantitative values from Scussolini et al. (2019).

		low-ECS	IPCCrenge-ECS	high-ECS	whole ensemble
	No. of models	2	10	5	17
	No. of data points	MMM (std)			
Tropical annual mean temperature change (°C)	36	1.70 (0.01)	1.68 (0.07)	1.70 (0.03)	1.69 (0.06)
Arctic warming (°C)	8	4.29 (0.04)	4.36 (0.41)	5.33 (1.11)	4.64 (0.81)
MAP (mm yr^{-1})	12	367.4 (6.8)	366.3 (16.2)	372.4 (9.8)	368.2 (14.0)

the North Atlantic Ocean, which suggest cooling over the Nordic Seas and three sites in the northeastern North Atlantic and warming else where between 40°N and 70°N (Figure 4.5e and f). However, models simulate consistent warming over the whole North Atlantic Ocean. Over lower latitudes, models do not produce the reconstructed cooling over the tropical Atlantic and the warming in the upwelling region off the west coast of southern Africa. The mismatch between simulations and the Capron et al. (2017) compilation could come from that the *lig127k* simulations have not incorporated potentially remnant ice sheets over Scandinavia and Canada that produce meltwater discharging (Otto-Bliesner et al., 2021; Barlow et al., 2018) and included the memory in the ocean of the H11 event (Marino et al., 2015; Govin et al., 2012) that lead to Southern Ocean warming and North Atlantic Ocean warming (Stone et al., 2016; Holloway et al., 2018). Unresolved changes in regional ocean circulations could be another factor.

HadGEM3-GC31-LL produces the largest LIG warming, and is the only one within the range of LIG warming estimation given in AR6 (Figure 4.7). Notably, it has the highest ECS across the ensemble, which is 1.4°C higher than the upper limit given

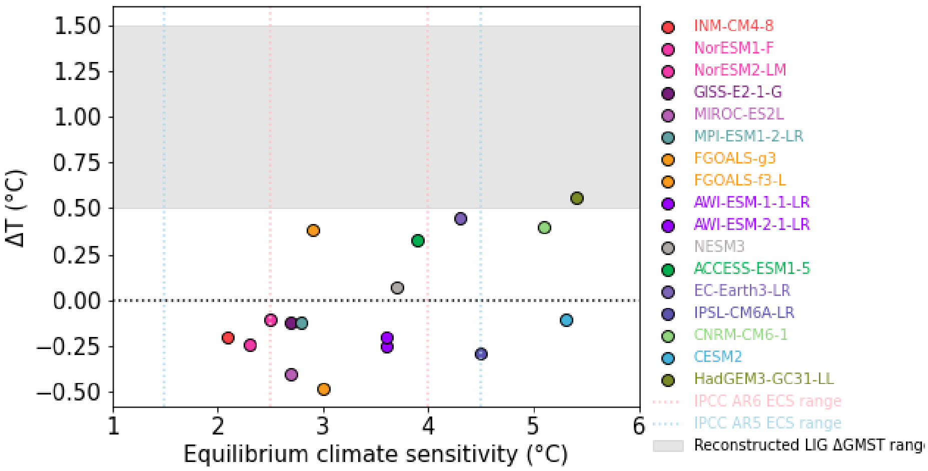

Figure 4.7: Comparison between ECS (°C) and simulated global mean surface temperature (°C) in *lig127k* simulations. Grey shading shows the range of LIG GMST anomaly given in IPCC AR6 Chapter 2 (Gulev et al., 2021).

by IPCC AR6 (IPCC, 2021d). However, models with higher ECS do not necessary produce warmer LIG than those with lower ECS, and there is no clear relationship between ECS and simulated LIG annual mean temperature change.

Root mean square errors (RMSEs) between proxy reconstructions vs simulations from different categories of ECS are calculated to investigate if models with low, IPCCrange or high ECS perform differently (Table 4.3). T-tests are conducted on these RMSE values to detect the significance of the difference, testing the hypothesis that there is no significant difference between RMSE values between the simulations from different ECS categories (low, IPCCrange and high) and proxy data. Models with high ECS are not doing better than others in simulating the tropical (23.5°S to 23.5°N) annual mean temperature change (Table 4.3), confirmed by all of the t-tests that show no significant difference in RMSE (p-values are not shown here). This suggests that it is difficult to discriminate the performance of models having different ECS in simulating tropical temperature change. One high-ECS model (IPSL-CM6A-LR) and one IPCCrange-ECS model (FGOALS-g3) capture the JJA Arctic warming better than the rest of models (Figure 4.6d), but they do not perform better in other latitudes. Yoshimori and Suzuki (2019) studied the contribution of the individual components to the mid-Holocene Arctic surface temperature change and their results suggest that the simulated Arctic temperature change are largely affected by change in sea ice surface temperature and sea ice concentration with the warming peak occurring in October. It could imply that the PMIP4-CMIP6 *lig127k* simulations underestimate the Arctic warming due to the response to sea ice rather than GHGs. This could explain why a model's estimated ECS has less effect on the capture of the LIG Arctic warming. RMSE results (Table 4.3) support this as models with high ECS agree less with the proxy data. T-test results (not shown here) suggest no significant difference in simulating Arctic warming between models with different ECS. These indicate that it is difficult to discriminate model performance across the three ECS category of models. There is also no clear relationship between models' ECS and their simulated seasonal temperature change. Those models with higher ECS do not simulate stronger seasonal change in temperature than those with low ECS. These suggest that models with higher ECS are not more sensitive to *lig127k* forcings and they do not perform better in simulating LIG temperature change, which imply that a model's estimated ECS is affected by its sensitivity to GHGs forcing instead of orbital ones.

The four models (AWI-ESM-1-1-LR, AWI-ESM-2-1-LR, MPI-ESM1-2-LR and NESM3) applied dynamic vegetation scheme do not produce smaller mismatch between model and data than other models. However, the proxy data compared here are SSTs, which could be unable to detect terrestrial signal and miss local response related to the inclusion of interactive vegetation. Otto-Bliesner et al. (2021) further compare continental air temperature reconstructions These suggest that models with dynamic vegetation do not necessarily preform better in simulating LIG temperature change.

4.3 Monsoon response

The *lig127k* global monsoon shows enhanced and expanded NH land monsoons and weakened and narrowed SH land monsoons as compared to the *piControl* (Figure 4.8). In contrast to the changes in land monsoons, the *lig127k* monsoon

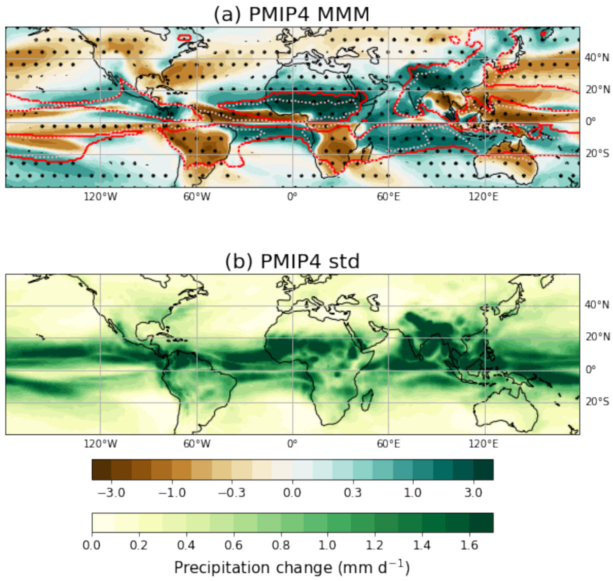

Figure 4.8: Mean global monsoon domain (mm d^{-1}) in the PMIP4-CMIP6 *lig127k* ensemble. Same as Figure 4.4 but for mean global monsoon domain (contour) and changes in monsoon summer rain rate (shading) in mm d^{-1}) in the *lig127k* simulations. The red solid and pink dotted contour shows the boundary of multi-model mean global monsoon domain computed for PMIP4-CMIP6 *lig127k* and *piControl* simulations, respectively. The identification of the monsoon domain follows the description in Section 2.5.3.

domain over the oceans weakens in the NH and strengthens in the SH. In general, the global monsoon domain patterns simulated by each individual model agree on the sign of ensemble mean respectively, but the variations in magnitude among models are large (Figure 4.8). Changes in monsoon follow the expectation of response to changes in orbital forcing. The seasonal changes in precipitation (*lig127k* - *piControl*) show large shifts in the Intertropical Convergence Zone (ITCZ) and a redistribution of precipitation between land and ocean (Figure 4.9), simulated by all models. Notably, NorESM2-LM simulates strong *lig127k* precipitation increase in the high latitudes in both hemispheres and over the continents in the NH, which has a disproportionate effect on the magnitude of precipitation change in the ensemble mean.

The JJA ensemble mean precipitation change (Figure 4.9c) indicates a northward

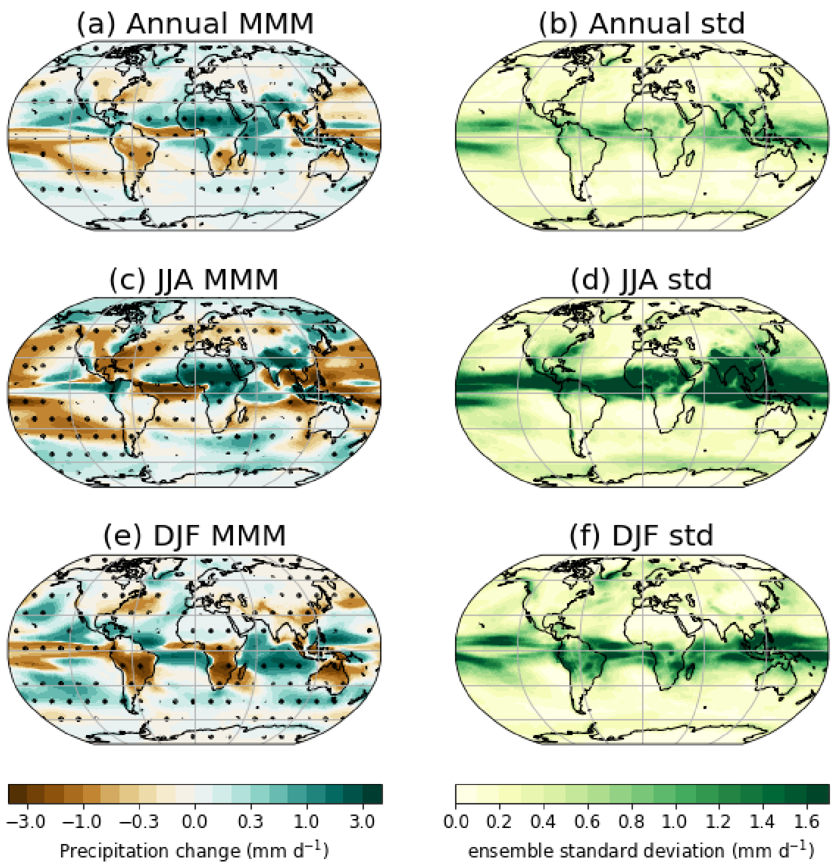

Figure 4.9: Same as Figure 4.3 but for annual mean precipitation change in mm d^{-1}.

shift in the tropical Atlantic ITCZ. The precipitation over northern Africa shows a strong increase in the *lig127k* simulations during boreal summer compared to the *piControl*. The enhanced precipitation over northern Africa extends into Arabian Peninsula and the Indian Ocean. Changes in precipitation over African monsoon-affected region lead to the strongest monsoon rainfall increase and the largest shift in the poleward boundary of the monsoon domain across regional monsoons, as shown in Figure 4.10. The *lig127k* domain-averaged monsoon summer rain rate over the North African monsoon (NAF) is 21.0% (8.2% - 38.5%) higher than the *piControl*, and the areal extent expands by 80.5% on average than the *piControl* with a range of 39.0% to 167.4%. The total amount of rainfall over NAF, thereby, accumulates to 117.7% (69.7% - 202.0%) more than the *piControl* (Figure 4.10). African increased freshwater runoff during last interglacial sapropel suggested by Amies et al. (2019) via planktic foraminiferal calcite $\delta^{18}O$ indicates enhanced LIG African monsoon. Reconstructions suggest that the northern boundary of NAF during the LIG expanded into the Middle East as far north as Israel (Orland et al., 2019). The *lig127k* simulations capture the increase in NAF precipitation and area, but are likely to underestimate the magnitude. As both *lig127k* and *midHolocene* Tier 1 experiments were designed to examine climate responses to strong orbital forcing, the possible explanations to mid-Holocene mismatch (see Section 3.4.2.2) might be able to explain the mismatch here as well, most notably dynamic vegetation (Messori et al., 2019; Pausata et al., 2016). Levis et al. (2004), based on model simulations, suggest the importance of soil feedback on the northward expansion of African monsoon during interglacials. It implies the importance of vegetation, which would affect local soil feedback. The four models with dynamic vegetation do not produce greater enhancement in NAF. Further investment on local vegetation is needed. The rain rate over the North American monsoon (NAMS) increases by 11.9% (-1.2% – 27.8%) falling into two groups with 6 out of the 17 models producing changes larger than 23% while the rest less than 11%, and the areal extent increases by 5.7% ranging from -15.9% to 27.7%. Outside of these regions and the Pacific rain belt, JJA precipitation reduces elsewhere in the tropics and extratropics (Figure 4.9c). The extended precipitation accumulates along the Himalayas, i.e. enhanced precipitation over southern Asia, but precipitation over Southeast Asia is reduced (Figures 4.8 and 4.9). The compensation leads to nearly no change in South Asian monsoon (SAS) monsoon rain rate (at -0.5% on average) with less consistency across the ensemble. Though with less monsoon rain rate change over SAS, the areal extent shows a consistent increase by 20.1% on average with a range of 2.6% to 47.1% relative to *piControl*. The enhanced SAS agrees with earlier reconstruction (e.g. $\delta^{18}O$ suggesting enhanced Indian summer monsoon Magiera et al., 2019). Notably, a recent multiproxy study (Wang et al., 2022b) found a weakened South Asian monsoon during the LIG due to higher Indian Ocean SST that disagrees the enhancement suggested by models. Results here still produce SAS enhancement like earlier model studies (Otto-Bliesner et al., 2021), disagree with Wang et al. (2022b). Precipitation over eastern Asia also shows strong increase in its monsoon region. The *lig127k* EAS shows an averaged increase of 9.9% in monsoon rain rate and an expansion in areal extent by 22.2% (Figure 4.8). The enhancement agrees with the intensified EAS as suggested by monsoon evidence, e.g. Chinese loess (Chen et al., 2003) and oxygen isotope ratios of stalagmites (Yuan et al., 2004). Over northern Asia, the only proxy reconstructed precipitation indicates a higher precipitation during the LIG, while the simulated changes in annual mean precipitation between *lig127k* and *piControl* show overall drier condition across the ensemble, except NorESM2-LM which reproduces the higher precipitation in the LIG (see Appendix C. Overall, evidence suggests enhanced EAS, SAS and NAF in the NH. *lig127k* NH monsoons agree with enhancement suggested by proxies.

During DJF, the ITCZ shows reduced precipitation over the tropical Pacific Ocean and having more rainfall over the Indian Ocean (Figure 4.9e). The tropical Atlantic ITCZ shows a southward shift in the *lig127k* during DJF. In the SH, precipitation reduces over the continents during austral summer while it increases over the adjacent oceans. This indicates a redistribution of precipitation between land and ocean that results in weakened and narrowed SH monsoons. The South American Monsoon System (SAMS) shows consistent reduction by -12.2% (-17.7% to -4.8%) in monsoon rain rate and by -7.7% (-34.5% - 2.1%) in areal extent (Figure 4.10). South African monsoon (SAF) rain rate decreases by -9.2% (NorESM1-F produced the only increase by 8.1% while the rest of the models in the ensemble simulate relative changes in precipitation rate concentrating on -16.9% - -5.0%). Its area reduces by -17.2% on average ranging from -61.9% to -1.4%. The monsoon rain rate of Australian–Maritime Continent (AUSMC) is -4.8% less than *piControl* and are less consistent across the ensemble. Its areal extent reduces by -31.4% ranging from -48.2% to -9.6%.

There are fewer studies on LIG monsoon changes than on the mid-Holocene, and

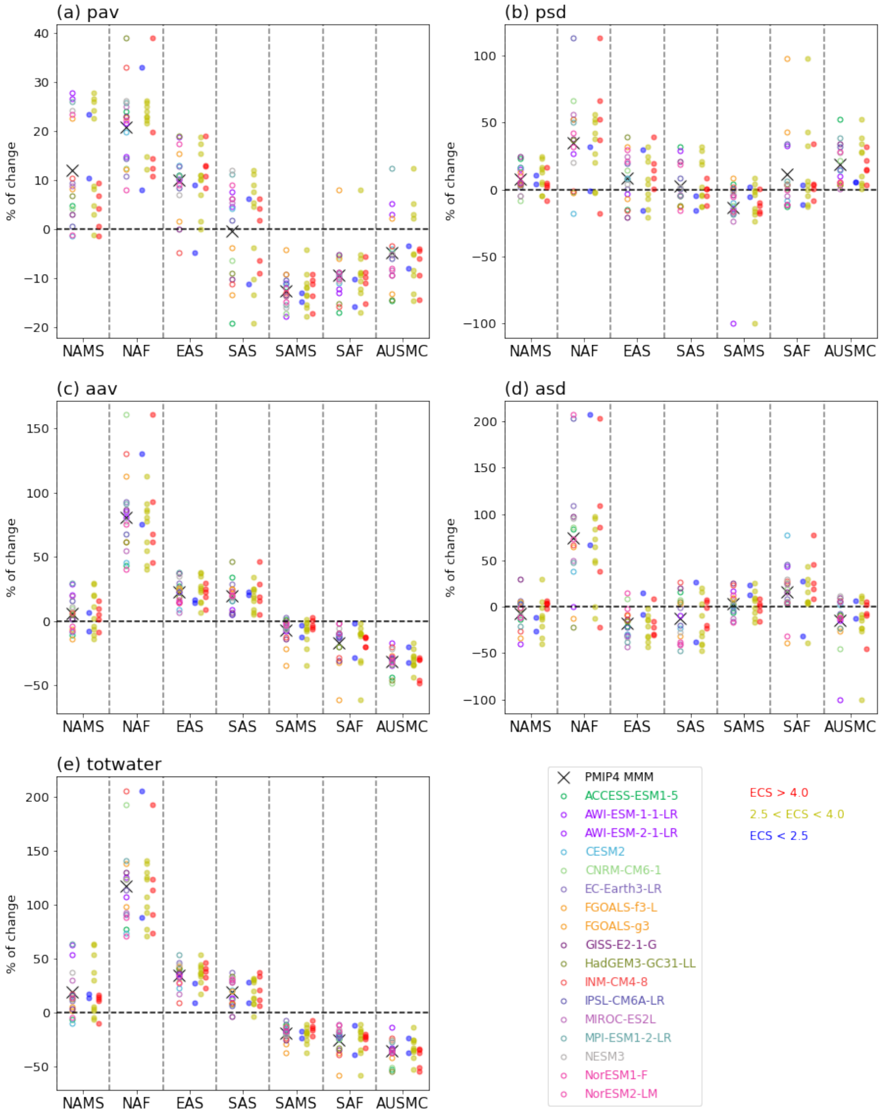

Figure 4.10: Relative change in regional monsoon diagnostics See Section 2.5.3 for a description of the diagnostic. The circles in each left shows are colored according to models, and the dots in each right column are colored by ECS (i.e. red for ECS > 4.0°C, yellow for 2.5°C $<$ ECS < 4.0°C and blue for ECS $<$ 2.5°C.)

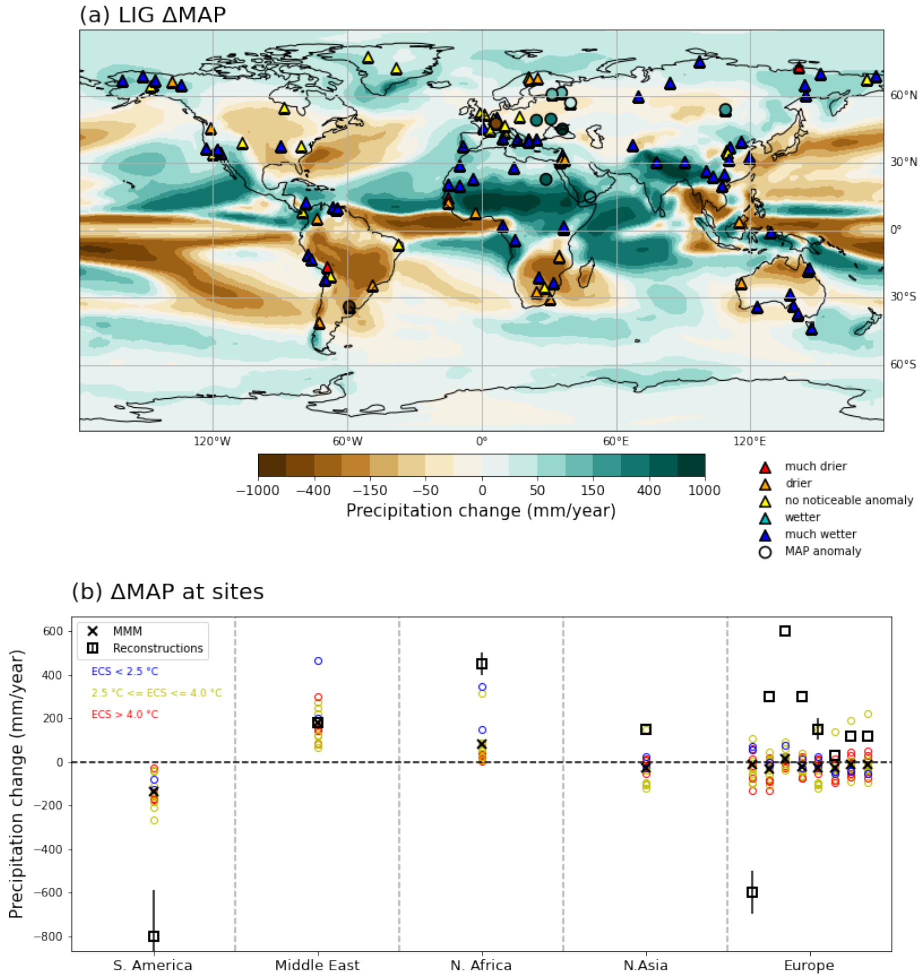

Figure 4.11: Comparison in mean annual precipitation (MAP) change in mm/year between the PMIP4-CMIP6 ensembles (*lig127k* - *piControl*) and proxy reconstruction from Scussolini et al. (2019). Triangles in panel (a) show the precipitation change on a semi-quantitative scale following Scussolini et al. (2019) and circles show the quantitative reconstructed precipitation change in mm/year. Panel (b) shows the comparison between the with reconstructed precipitation change (circles in panel (a)) with the simulated changes at sites by individual models, coloured by model's ECS: red for ECS > 4.0°C, yellow for 2.5°C $<$ ECS $<$ 4.0°C and blue for ECS $<$ 2.5°C.

most of them focus on NH monsoons especially Asian monsoon and Indian monsoon (e.g. Chen et al., 2003; Wang et al., 2022b). Monsoon reconstruction is limited by data availability and poor coverage (Scussolini et al., 2019). Like the analysis in Chapter 3, reconstructed mean annual precipitation anomaly is used to evaluate change in monsoons as the major proportion of the annual precipitation within the monsoon region falls during the monsoon season. Though it is difficult to have quantitative evidence, Scussolini et al. (2019) provide a near-global coverage of precipitation evidence showing the signal in mean annual precipitation change, and a few sites have quantitative estimates. Figure 4.11 shows the comparison between simulated annual mean precipitation change (*lig127k* - *piControl*) and the proxy signals and reconstructed anomalies available from Scussolini et al. (2019). Over the NH, the proxy signals show higher annual precipitation during the LIG than the pre-industrial or recent past (Figure 4.11a). Comparing to the NH signals, the ensemble averaged annual mean precipitation change (*lig127k* - *piControl*) agrees on the sign of change over the northern coastal region of North America, western and northern Africa, Middle East, southern Asia and Alaska, and disagrees over central and eastern North America, Europe, and central and part of eastern Asia where simulations produce drier *lig127k* than the reconstructions (Figure 4.11b). Simulations match the reconstructed higher precipitation over Middle East. The MMM of the simulated mean annual precipitation change at the site in the Middle East that has quantitative evidence (Scussolini et al., 2019) is very close to the reconstructed anomaly at the site. Models catch the wetter signal over northern Africa though fail to reproduce the magnitude. Across the ensemble, NorESM2-LM simulates more precipitation increase at the sites and therefore its simulated site-level mean annual precipitation change better matches the reconstructed anomaly. However, it is likely to simulate too much precipitation increase in other regions than the rest of the models as shown in Figure 4.9.

Over the SH, the proxy signals are irregular by showing combination of (much) drier, (much) wetter and no noticeable signals in precipitation over western South America and southern Africa (Scussolini et al., 2019), where the simulations produce weakened precipitation in the *lig127k* as compared to the *piControl* (Figure 4.11a). The only available reconstruction in the southeast of Southern America shows that the MAP during the LIG was -800 mm/year lower than pre-industrial (Scussolini et al., 2019). Model simulations catch the drier *lig127k* conditions, but fail to reproduce that magnitude (Figure 4.11b). Over Australia, the proxy signals show much wetter conditions during the LIG, while simulations show disagreement by producing drier *lig127k* than *piControl*.

There is no clear relationship between changes in rain rate and areal extent in regional monsoons (Figure 4.10). Those models producing greater rain rate change do not necessarily produce greater change in areal extent. A model's ECS does not affect its simulated monsoon response, as there is no trend between model ECS and simulated monsoon diagnostics (right columns in Figure 4.10) and models having high ECS do not simulate better LIG precipitation change shown by proxy data (Figure 4.11, Table 4.3). Models producing large variability in one region do not always produce large variability in other regions, which suggest that this variability is linked with regional feedbacks rather than being an inherent characteristic of a model.

4.4 Discussion

According to the definition given in Chapter 1, ECS reflects a model's sensitivity to a doubling of CO_2 relative to pre-industrial level. Those models with a high ECS are more sensitive to GHG forcing than those estimating low ECS. However, this may not apply to the response to orbital forcing. Logically, increased GHG forcing warms the climate by increasing net energy input while orbital forcing change the seasonal and latitudial distribution of insolation throughout a calendar year and therefore has more affect on seasonal temperature change. Analysis in above sections indicates that there is no clear relationship between ECS and climate response in the *lig127k* simulations. Generally, models with high ECS do not perform better in simulating LIG climate better than those having low ECS. Those models having ECS within the range given by IPCC AR6 do not obviously simulate better LIG climate. The lack of an obvious trend between a model's estimated ECS and its simulated climate response to *lig127k* prescribed orbital forcing indicates that the mechanisms behind climate response to orbital forcing are different to those behind to GHGs forcing. D'Agostino et al. (2019, 2020) analyse the driving component contributing to the monsoon response in the CMIP5 *midHolocene* and RCP85 simulations, which are dominantly responding to orbital forcing and CO_2 forcing respectively. Their results suggest that the dynamic component drives the strengthened NH monsoon (D'Agostino et al., 2019) and weakened SH monsoon (D'Agostino et al., 2020) in the *midHolocene* simulations while the thermodynamic component drives the monsoon increase in the RCP85 simulations. It implies that the change in dynamic component of monsoon also drives the monsoon change in *lig127k* simulations as both experiments are driven by orbital forcing. How climate responds to CO_2 forcing will be discussed in Chapter 5 via analysing the response during mPWP.

Comparing to proxy data, simulations are inconsistent in some regions where the absence or use of inappropriate factors like vegetation, ocean circulation or melting water. As discussed in Chapter 3, using more realistic mid-Holocene vegetation cover, e.g. applying "Green Sahara", could improve the simulation of the monsoon response especially over West Africa during the mid-Holocene (Messori et al., 2019; Pausata et al., 2016). It implies that the monsoon response in the *lig127k* simulations could also be improved if including appropriate LIG vegetation cover as both periods were affected by orbital forcing. In this PMIP generation, the majority of models applied the prescribed 1850 CE vegetation cover same as in the *piControl* instead of a realistic vegetation, with an exception of CESM2 which used potential vegetation that removed crops and urban areas in its CMIP6 simulations (Otto-Bliesner et al., 2020). Four of the models (AWI-ESM-1-1-LR, AWI-ESM-2-1-LR, MPI-ESM1-2-LR and NESM3) participating in the *lig127k* ensemble include a dynamic vegetation scheme. Logically, models applying dynamic vegetation scheme could perform better than those using fixed prescribed PI vegetation as their vegetation responds to with local climate changes. However, the four models do not perform better than the others in simulating LIG climate as shown by the results in above sections.

This does not prove that including dynamic vegetation could not improve simulating LIG climate. As the comparison is conduced across the results from independent models, the benefit of including dynamic vegetation could also be counteracted by other inappropriate schemes within the model and/or those models not including dynamic vegetation have other better design that improve the quality of simulations. MIROC model group run the *lig127k* simulation with the inclusion of dynamic vegetation in another version of MIROC model, MIROC4m-LPJ and compared the results of different versions with reconstructed LIG climate (O'ishi et al., 2021). Their comparison indicates the importance of including dynamic vegetation to reproduce the Arctic warming and the warming over NH land, though the warming still can not be fully reproduced. Therefore, further study on the usage and improvement on dynamic vegetation should be conduced to improve the analysis in the next PMIP generation.

4.5 Conclusion

The PMIP4-CMIP6 *midHolocene* and *lig127k* simulations show strong seasonal changes in seasonal temperatures and precipitation, in line with the theoretical response to changes in insolation forcing which increased during boreal summer and decreased during boreal winter. The *lig127k* experiment was designed to have stronger orbital forcing than the *midHolocene*. The responses are similar but stronger than the *midHolocene* as expected (see Chapter 6 for the comparison). The *lig127k* experiment is characterised by strong NH warming especially over land during JJA in response to the increased boreal summer insolation in the NH. Monsoons are enhanced in the NH during boreal summer and weakened in the SH during austral summer. Comparing to the reconstruction from proxy data, the *lig127k* ensemble captures the warming and the enhanced NH monsoons, but fails to fully reproduce the magnitude.

Simulations have been split into three subsets based on the model's ECS and are compared with proxy data to investigate if the ECS relate to the quality of model's LIG simulation. Results (tropical annual mean temperature change, Arctic warming and MAP) show that there is no significant difference in simulated response by models with different ECS, which suggest that those models with high ECS do not perform better than those estimating low ECS. The mechanism behind the response to orbital forcing being different to that behind responding to GHG forcing can explain the lack of clear trend between a model's ECS and its simulated climate response. However, it is still worth for further investigation, as the models with ECS higher than 4°C produce greater Arctic warming than others though the difference is not significant.

The analyses of data-model mismatch in this chapter point out the importance of vegetation. Four of the models participating in the *lig127k* ensemble include dynamic vegetation, but they do not simulate the LIG climate better than those without it. The reason might be that other inappropriate schemes counteract the improvements by dynamic vegetation and/or those models not including dynamic vegetation have other better schemes that improve the results. Further investigation into the role of dynamic vegetation schemes should be considered.

Chapter 5

Monsoon response in the *midPliocene-eoi400* simulations and aerosol uncertainties in monsoon changes for mid-Pliocene Warm Period climate

The previous chapters discuss the effects of changes in orbital forcing on climate in the Last Interglacial (LIG) and mid-Holocene (MH) periods. The third warm climate experiment included in CMIP6 is *midPliocene-eoi400*, which represents the mid-Pliocene warm period (mPWP) centered on 3.205 Ma, the warmest phase of marine isotope stage during the mPWP when the orbital configuration was similar to present day (Haywood et al., 2013). While LIG and MH climate change was predominately driven by orbital forcing, climate change during the mPWP was dominated by elevated atmospheric CO_2 concentrations that were similar to the present-day level. Climate models have been used to understand mPWP climate for approximately three decades (Chandler et al., 1994). The purpose of using models in palaeoclimate research is to investigate the drivers and mechanisms behind the climate changes shown in proxy reconstructions. Understanding climate change during the mPWP offers a window into future global warming as it was the most recent time in Earth's history when atmospheric CO_2 concentration exceeded 400 ppmv (Bartoli et al., 2011). Additionally the continental configuration was similar to present-day, and of course proxy data exists to ground truth the experiment. Comparing the simulated mPWP climate change with MH and LIG climate change would help to evaluate how climate models could simulate climate change in response to different forcings, which will be discussed in the next chapter. As described in Chapter 1, the Pliocene Model Intercomparison Project (PlioMIP; Haywood et al., 2010) is a coordinated international climate modelling project initiative aimed of understanding the climate and environments of mPWP, exploring model uncertainties and evaluating the potential relevance to future climate change. Its first phase (PlioMIP1; Haywood et al., 2010, 2011) proposed a single set of model boundary conditions aligned with the PRISM3D reconstruction (Dowsett et al., 2010), and prescribed the atmospheric CO_2 at 405 ppmv. Haywood et al. (2013) provides a preliminary description of large features in PlioMIP1, which showed strong polar amplification as suggested by proxy data, though potentially underestimated its magnitude.

The mPWP around 3.2 Ma has been included in PMIP4-CMIP6 with the chosen experiment being the Tier 1 experiment identified by PlioMIP2 (Haywood et al., 2016b). PlioMIP2 applied various CO_2 levels aligned with PRISM4 reconstructions (Dowsett et al., 2016), in which the chosen experiment (*midPliocene-eoi400*) set the CO_2 concentration at 400 ppmv. Additional sensitivity simulations in PlioMIP2 include those to understand climate changes in future ("Pliocene4Future") and in the past ("Pliocene4Pliocene"). New boundary conditions are used to improve boundary condition uncertainty pointed out in PlioMIP1, which include updated topography and ocean bathymetry, ice sheets, sea levels, soil and lakes data sets while land cover remained as in PRISM3 (Haywood et al., 2016b). Latest PlioMIP2 simulations have been published and contributed to PlioMIP2 analysis (Haywood et al., 2020) and assessment in IPCC AR6 chapters (Gulev et al., 2021; Eyring et al., 2021; Douville et al., 2021; Fox-Kemper et al., 2021). In this chapter, I provide an analysis of the *midPliocene-eoi400* simulations that had been uploaded to ESGF (see Chapter 2) at the point of writing, which include simulations performed with 4 models. The ensemble here is different to the PlioMIP2 ensemble described in Haywood et al. (2020), which contains additional 12 non-CMIP simulations. The first half of this chapter aims to address if the *midPliocene-eoi400* simulations are able to reproduce the mPWP cliamte and if they are doing better than the PlioMIP1 results published in Haywood et al. (2013).

Section 5.1 describes the protocol of *midPliocene-eoi400*, the 4 models whose simulations are used in this chapter, proxy data used in data model comparison and the assessment of similarity and difference between the *midPliocene-eoi400* ensemble here and Haywood et al. (2020). In order to distinguish ensemble results, the analysis based on the subset of 4 simulations analysed in this work, hereafter I refer to them as to "*midPliocene-eoi400*" and results of Haywood et al. (2020) are referred as to "PlioMIP2". Section 5.2 gives the analysis of temperature, precipitation and monsoon response in *midPliocene-eoi400* simulations and compare them with the PlioMIP2 results (Haywood et al., 2020) to see if they capture the mPWP climate change.

Increased atmospheric CO_2 concentration results in a radiative forcing warmed mPWP of 1.9 W m^{-2} during the period (Haywood and Valdes, 2004). Sensitivity studies (e.g. Lunt et al., 2012b) found that CO_2 dominates 36-61 % of the mPWP warming, whilst vegetation change contribute to 21-27 %, orography contributing to 0-26 % and ice sheets contributing to 9-13 %. However, GCMs cannot accurately simulate the reduced temperature gradients (Dowsett et al., 2013; Haywood et al., 2020) as the mechanism is not fully understood and recognized (Fedorov et al., 2013). Increased CO_2 concentration is clearly one factor, but needs to combine with other mechanisms (Crowley, 1996).

Previous studies suggested the effect of seaways (e.g. Karas et al., 2017; Dowsett et al., 2019) on Pliocene climate confirmed by pollen evidence (Khan et al., 2022), but Otto-Bliesner et al. (2017b) found that changes in inter-ocean gateways could not maintain the warm pool, therefore a comprehensive analysis of the impacts of palaeogeographic changes is required. Brierley and Fedorov (2016) used a single model to analyse the impact of Miocene–Pliocene changes in three inter-ocean gateways, and they found the compensating impacts between the closing of the Central American Seaway and the opening of the Bering Strait and suggested the overestimation of cooling in previous studies with the closure of the Central American Seaway. The mechanisms behind the warm pool could also involve enhanced vertical ocean mixing by tropical cyclones (Fedorov et al., 2013), but this mechanism does not reproduce the warming completely in models. Reduced cloud albedo gradient (Burls and Fedorov, 2014) could be involved in the mechanisms as well, but the causes of changes in cloud albedo remain unclear. Cloud properties (cloud effective radius and cloud condensation nuclei) may be important (Kiehl and Shields, 2013). Unger and Yue (2014) used Pliocene vegetation and found the importance of aerosol and chemistry-climate feedback in modelling Pliocene climate as the aerosol cooling effect masks 15-100 % of the CO_2 effects while chemistry-climate feedback warms climate about 30-250 % of CO_2 effects. Aerosol forcing could be an important factor causing uncertainties in modelling mPWP climate. Mismatches between simulations and proxy estimations occur and aerosol effects could be a possible explanation to explain the mismatch, as recent studies have suggested that the mismatch has been reduced by including explicit aerosol–cloud interactions in models (Sagoo and Storelvmo, 2017; Feng et al., 2019).

Applying aerosol forcing to mPWP, as an example, offers a chance to examine climate response under high CO_2 condition. The second half of this chapter tries to investigate the potential for aerosols to affect simulating mPWP climate response, raising the potential importance of uncertainty in experimental setup in PlioMIP2. The investigation will be conducted by analysing the simulations of an experiment with idealised aerosol scenarios, which were performed by Dr. Ran Feng. In section 5.3, two existing Pliocene simulations with different aerosol scenarios are analysed, one with pre-industrial aerosol concentrations and one with present-day aerosol concentrations (Lamarque et al., 2010). The changes caused by removing anthropogenic concentrations in the Pliocene are compared, in order to understand the importance of considering aerosol effects in modelling Pliocene climate. This

Table 5.1: *midPliocene-eoi400* experimental design

	piControl	*midPlioceneEoi400*
Orbital parameters		
Eccentricity	0.016764	Same as piControl
Obliquity (degrees)	23.459	Same as piControl
Perihelion – 180	100.33	Same as piControl
Vernal equinox	21^{st} March at noon	Same as piControl
Greenhouse gases		
Carbon dioxide (ppm)	284.3	400
Methane (ppb)	808.2	Same as piControl
Nitrous oxide (ppb)	273	Same as piControl
Other GHGs	CMIP DECK piControl	Same as piControl
Solar constant (W m^2)	TSI: 1360.747	Same as piControl
Paleogeography	Modern	PRISM4 reconstruction
Ice sheets	Modern	PRISM4 reconstruction
Vegetation	CMIP DECK piControl	Dynamic, or PRISM4
Aerosols	CMIP DECK piControl	Same as piControl
Citation	Eyring et al. (2016)	Haywood et al. (2016)

chapter focuses on changes in tropical precipitation, because precipitation varies much more than other near-uniform variables like temperature and irradiation in tropics, and it is important in predicting future tropical agriculture condition.

5.1 *midPliocene-eoi400*

5.1.1 Experimental design

Haywood et al. (2016b) described the design of the Tier 1 *midPliocene-eoi400* experiment in the PMIP4-CMIP6 that is equivalent to PlioMIP2 (Table 5.1). The atmospheric CO_2 concentration was prescribed at 400 ppmv, which is slightly lower than the 405 ppmv prescribed in the PlioMIP1 (Haywood et al., 2010). According to Haywood et al. (2016b), prescribed boundary conditions were aligned with PRISM4 reconstructions (Dowsett et al., 2016), with modelling groups able to choose between “standard” or “enhanced” versions. Vegetation cover is either prescribed using the PRISM4 vegetation (Salzmann et al., 2008; Haywood et al., 2016b) or determined by model’s scheme of dynamic vegetation.

5.1.2 Models

This chapter only includes those simulations that had been uploaded to ESGF before writing this thesis to maintain consistency with the methods described in Chapter 2. This therefore only includes simulations performed with 4 models: CESM2, GISS-E2-1-G, IPSL-CM6A-LR and NorESM1-F (further information on the models can be found in Appendix A). Notably, the ensemble here is only a small subset of PlioMIP2 (Haywood et al., 2020) which itself includes 16 models. Comparison between *midPliocene-eoi400* ensemble and PlioMIP2 is given in Section 5.2.3.

5.1.3 Proxy reconstruction

In order to being consistent with Haywood et al. (2020), data-model comparison in annual mean temperature anomalies (mPWP - pre-industrial) throughout this chapter use the same proxy dataset, i.e. reconstructed mPWP SSTs in PRISM4 (Foley and Dowsett, 2019) which use an interval of 30,000 years. The pre-industrial SSTs uses the observed 1870-1988 SSTs from the NOAA Extended Reconstructed Sea Surface Temperature (ERSST) version 5 dataset (Huang et al., 2017). Salzmann et al. (2008) compared 28 present-day mean annual precipitation anomalies (mid-Pliocene - present-day) from literature for selected regions. Only 10 anomalies were chosen for data-model comparison in this chapter as their precise coordinates and anomalies could be found in literature. The 10 points have been regenerated into 6 points as the 3 sites in western coast of USA and 3 in Yunnan, China are within a single model grid. Therefore each three have been reorganised into a single point by taking their average.

5.2 Results from *midPliocene-eoi400* simulations

5.2.1 Temperature response

Mean annual temperature change in PlioMIP2 is warmer than that estimated in PlioMIP1 (Haywood et al., 2020). The PlioMIP1 estimates a global warming of 2.7 °C during the mPWP in model simulations (Haywood et al., 2013) that fills into

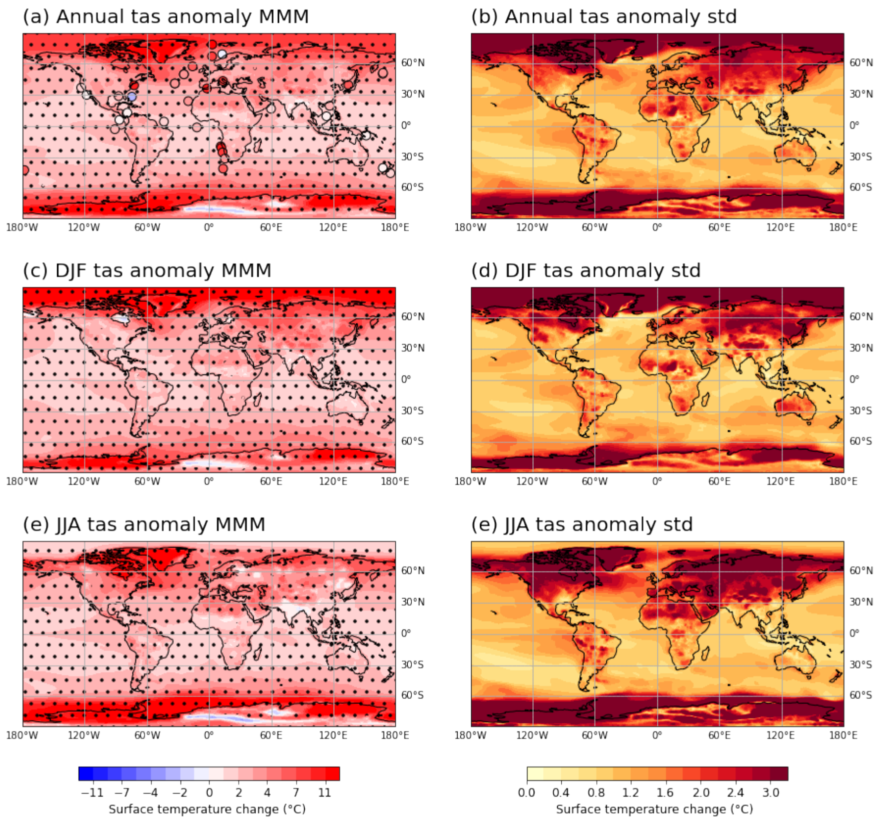

Figure 5.1: Annual and seasonal surface air temperature change (°C) in the *midPliocene-eoi400* simulations. (a, c, e) are annual, DJF and JJA ensemble mean temperature change (*midPliocene-eoi400* - *piControl*). Points in (a) are reconstructed SST anomalies (see Section 5.1.3). Dotted regions mark where all models agree the sign of multi-model mean anomaly. (b, d, f) are the standard deviations of annual, DJF and JJA temperature changes across the ensemble.

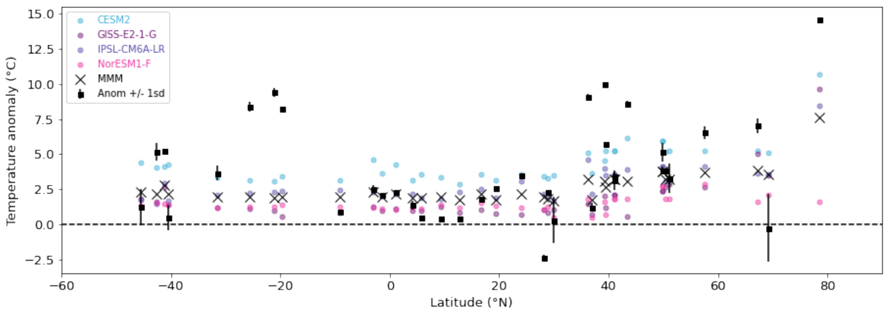

Figure 5.2: Comparison between proxy estimated change in annual mean temeprature (°C) shown in Figure 5.1a with modelled temperature change at the locations of the proxy data.

two bands at 1.8–2.2°C and 3.2–3.6°C (Haywood et al., 2013). Simulated warming is concentrated at high latitudes, which was dominated by greenhouse gases emission and clear sky albedo (Hill et al., 2014). Haywood et al. (2020) states that the warmer PlioMIP2 is caused by the addition of new and more sensitive models instead of the modifications in boundary conditions between the two PlioMIPs.

Across the *midPliocene-eoi400* ensemble, simulations show good agreement in simulating the mPWP warming over the tropics and oceans between 60°N and 60°S while show large spread over the Arctic and the Southern Ocean and most of the Antarctica (Figure 5.1). Overall, the warming in the tropical NH is stronger than in the tropical SH, which causes an interhemispheric temperature gradient. The relatively stronger warming over the Greenland Sea and Baffin Bay than the rest of the Arctic may be the result of prescribed boundary conditions including the closed ocean gateways of the Canadian Archipelago and Bering Strait (Haywood et al., 2020). The warming may also be explained by the simulated reduction in NH sea ice cover (de Nooijer et al., 2020) and the smaller prescribed Greenland Ice Sheet. Similarly in the SH, there is a strong warming over the east and west Antarctica. The interior of east Antarctica shows cooling in contrast to its surroundings, though with large variations across the ensemble (Figure 5.1a,b). This is a consequence of the prescribed topography of East Antarctic Ice Sheet that exceeds in some regions in the *midPliocene-eoi400* that prescribed in the *piControl*. Simulated *midPliocene-eoi400* annual mean temperature change overall fails to reproduce

Table 5.2: Reconstructed and modelled precipitation change (mPWP - PI) in mm yr^{-1} at sites.

lat	42	36.35	11.06	26	-22	-35
lon	-118	-76.22	40.35	99.5	150	150
CESM2	155	-204	486	748	123	168
GISS-E2-1-G	-36	-119	-18	1246	-39	60
IPSL-CM6A-LR	40	-184	255	91	-58	-357
NorESM1-F	109	-78	337	322	168	110
MMM	67	-146	265	602	49	-5
Recon.*	234	250	308	-351+	898	1482

*Regions, sites and reconstructed anomalies were taken from Salzmann et al. (2008);
+ Site in Yunnan combines the three sites described in Kou et al. (2006).

the magnitude of reconstructed temperature change at proxy sites (Figure 5.1 and Figure 5.2). Sites in the tropical oceans show relative better agreement between model and data. However, models underestimate the warming in high latitudes and especially in upwelling region along the western coastline of southern Africa. The underestimation in the reduction of temperature gradients shown by proxy data in *midPliocene-eoi400* has persisted since PlioMIP1. Ensemble mean changes in surface air temperature (*midPlioccene-eoi400 - piControl*) and spreads across the ensemble in DJF (Figure 5.1c,d) are similar to those shown in annual ones. During JJA, Arctic amplification is weaker than annual and DJF and more consistent across the ensemble, while the SH polar amplification is stronger with larger variation across the simulations (Figure 5.1e,f).

5.2.2 Precipitation response

Changes in annual and seasonal mean precipitation rate in PlioMIP2 (Figure 5.3a,c,e) show a redistribution of precipitation, although the change varies in each simulation (Figure 5.3b,d,f). Figures 5.3 and 5.4 show that the *midPliocene-eoi400* precipitation is stronger over high latitudes, tropical Pacific Ocean, Asia and North Africa extending to North Atlantic Ocean and Indian Ocean in the NH. mPWP precipitation is reduced over subtropical oceans, tropical North America and subtropical southern Africa as compared to the *piControl*. The drier tropical and subtropical

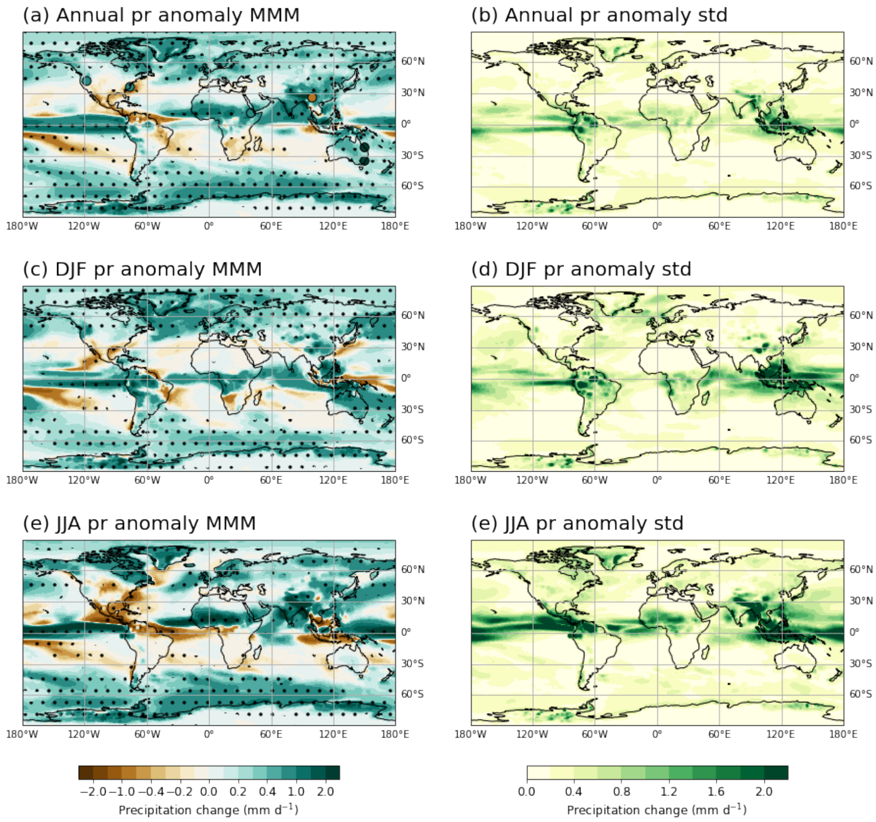

Figure 5.3: Annual and seasonal mean precipitation change (mm d^{-1} in the *midPliocene-eoi400* simulations. Same as Figure 5.1 but for precipitation. Shaded circles in panel (a) are reconstructed mean annual precipitation anomalies chosen from Salzmann et al. (2008). See Section 5.1.3 for details.

SH agrees with the finding in Pontes et al. (2020), which states that warming induced interhemispheric temperature gradient intensifies energy flux across the equator that shifts the ITCZ northward and weakens and displaces the STCZ in the SH polewards. The spatial pattern (Figure 5.3) indicates changes in the Hadley circulation that are influenced by the reduced meridional temperature gradient. Changes in precipitation over the tropical Atlantic Ocean and monsoon regions varies throughout the year depending on the shift in the ITCZ (although these are considerble spread across the ensemble.

Comparing to reconstructed mean annual anomalies at sites (Salzmann et al., 2008), both PlioMIP1 and PlioMIP2 fail to reproduce the magnitude of mPWP precipitation anomalies or even simulate opposite change. None of the *midPliocene-eoi400* simulations captures the much wetter Australia suggested by proxy data suggest that Australia was wetter in the mPWP. Proxy data suggest drier Yunnan, china that was shown in PlioMIP1, while the four PlioMIP2 simulations all show precipitation increase over the region. Simulations also fail to reproduce the precipitation increase over East USA and they all even simulate a decrease instead. Meanwhile, though both responding to high CO_2 forcing, future precipitation change is projected to be wetter getting wetter and drier getting drier (Lee et al., 2021) instead of becoming wetter as during the mPWP, which can be explained by the weaker atmospheric circulation and moisture transport during mPWP induced by the decreased equator-to-pole temperature gradient than in future projections (Burls et al., 2017).

During DJF, precipitation is stronger over Australia, middle Africa and South America except Borborema Plateau and eastern Asia, and is weaker over southern Africa and Borborema, tropical North America, Arabian Peninsula and India (Figure 5.3b). The largest spread across the ensemble occurs over Maritime Continent (Figure 5.3d). During JJA, *midPliocene-eoi400* precipitation over tropical Americas and Maritime Continent (Figure 5.3b) is less than the *piControl*. Precipitation over northern Africa, southern and eastern Asia and tropical Atlantic Ocean in the NH increases during boreal summer in the *midPliocene-eoi400* simulations (Figure 5.3e), though with significant differences over the tropical across the ensemble (Figure

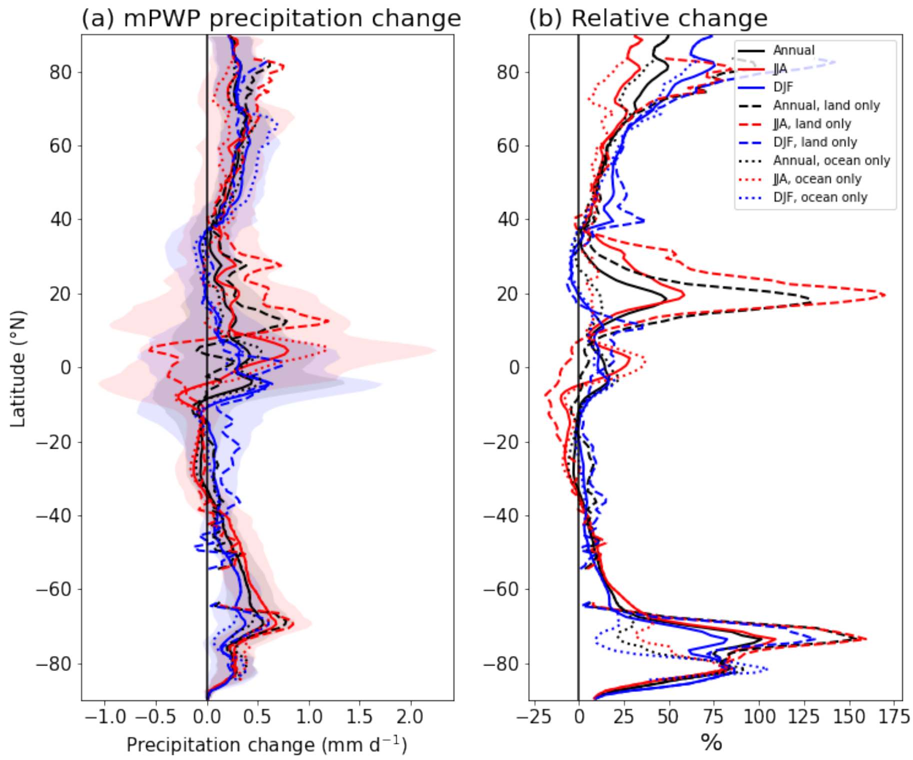

Figure 5.4: *midPliocene-eoi400* zonal mean precipitation change in (a) mm d^{-1} and (b) percent change relative to the *piControl*.

5.3f).

5.2.3 *midPliocene-eoi400* vs PlioMIP2

The PlioMIP2 ensemble includes results of 16 models (Haywood et al., 2020). Here only includes results of 4 models due to the availability on the ESGF, having a size being merely one fourth of PlioMIP2. The main features of the *midPliocene-eoi400* ensemble in this work are similar to PlioMIP2 (Figure 5.5). Both ensembles show similar spatial patterns and magnitude of multi-model mean change and multi-model spread in temperature and precipitation. The PlioMIP2 ensemble estimates that the GMST of *midPliocene-eoi400* is 3.18 °C, ranging from 1.73 to 5.17 °C with a standard deviation of 1.08°C, warmer than the *piControl* (Haywood et al., 2020). Though only 4 simulations are analysed here, they show a warming of 3.01 °C with

Table 5.3: Comparison of change in mPWP global mean annual mean surface temperature and annual mean precipitation between *midPliocene-eoi400* ensemble and PlioMIP2 ensemble published by Haywood et al. (2020)

Ensemble Size	*midPliocene-eoi400* 4 models	PlioMIP2 (Haywood et al., 2020) 16 models
Temperature (°C)	p = 0.80	
MMM	3.01	3.18
stddev	1.45	1.08
max	4.95 (CESM2)	5.17 (CESM2)
min	1.73 (NorESM1-f)	1.73 (NorESM1-f)
Precipitation (mm d^{-1})	p = 0.78	
MMM	0.18	0.19
stddev	0.10	0.08
max	0.31 (CESM2)	0.37 (CCSM4-Utr)
min	0.07 (GISS-E2-1-G)	0.07 (GISS-E2-1-G)

a range of 1.73 to 4.95 °C with a standard deviation of 1.45°C (Table 5.3), which have similar average and range as the PlioMIP2 and the difference is not significant ($p = 0.80$). Furthermore, the model that simulates the largest warming (CESM2) and that which simulates the smallest (NorESM1-f) are the same in the two ensembles. The difference in standard deviation here is due to the size of PlioMIP2 ensemble is larger than here. Zonal averaged temperature change at 1° latitude band gives similar trend as p values fall within a range of 0.51 to 0.99, which gives no significant difference. As for change in precipitation, all models produce an increase in global mean annual mean precipitation. GISS-E2-1-G simulates the smallest change in both ensembles at 0.07 mm d^{-1}. The *midPliocene-eoi400* produces an increase in precipitation at 0.18 mm d^{-1} with a standard deviation at 0.10 mm d^{-1}, which is 0.01 mm d^{-1} lower PlioMIP2 (stddev = 0.08 mm d^{-1}) and the difference is not significant ($p = 0.78$) between the two ensembles. Therefore, though the *midPliocene-eoi400* ensemble has a smaller size than PlioMIP2, it can in some way reflects the features shown in PlioMIP2.

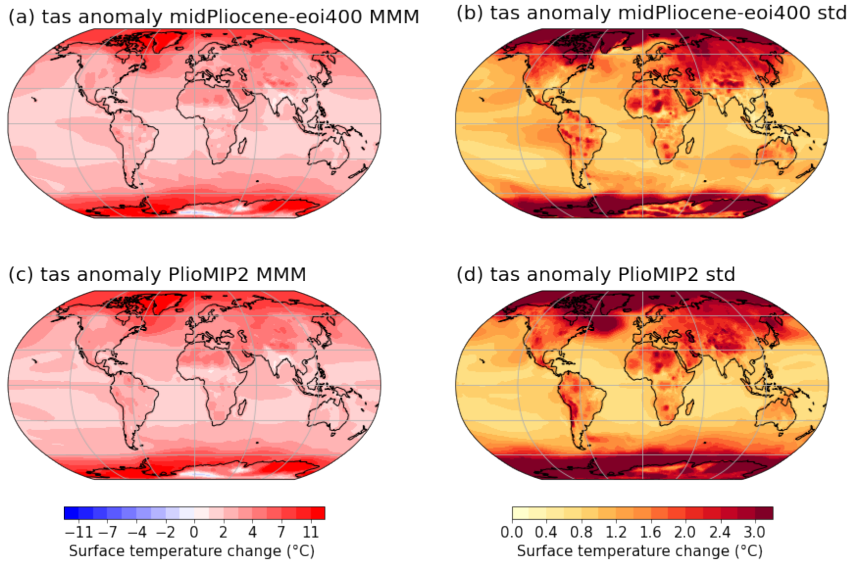

Figure 5.5: Comparison between *midPliocene-eoi400* annual mean surface temperature anomaly (°C) and PlioMIP2 published in Haywood et al. (2020). (a) multi-model mean anomaly computed from *midPliocene-eoi400* simulations and (b) multi-model spread shown as standard deviation. (c,d) Corresponding anomaly and spread published in Haywood et al. (2020).

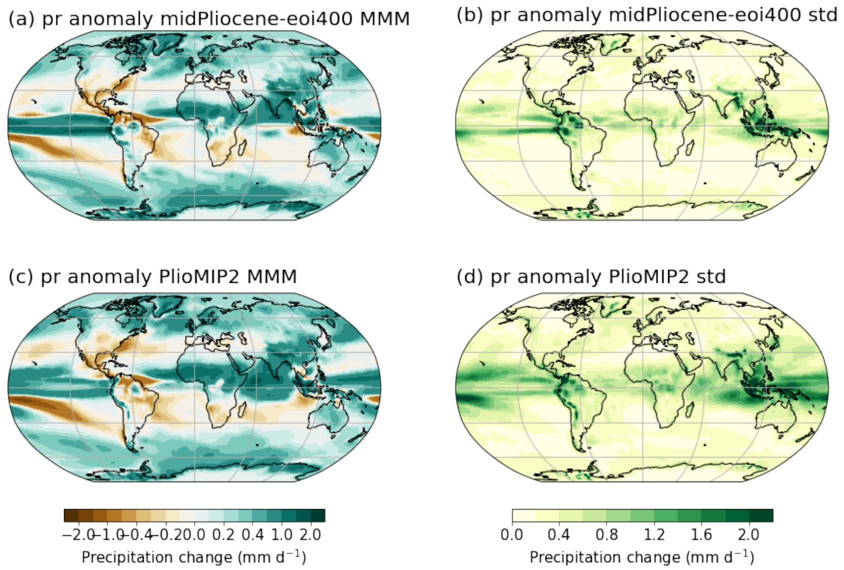

Figure 5.6: Same as Figure 5.5 but for annual mean precipitation anomaly (mm d^{-1}).

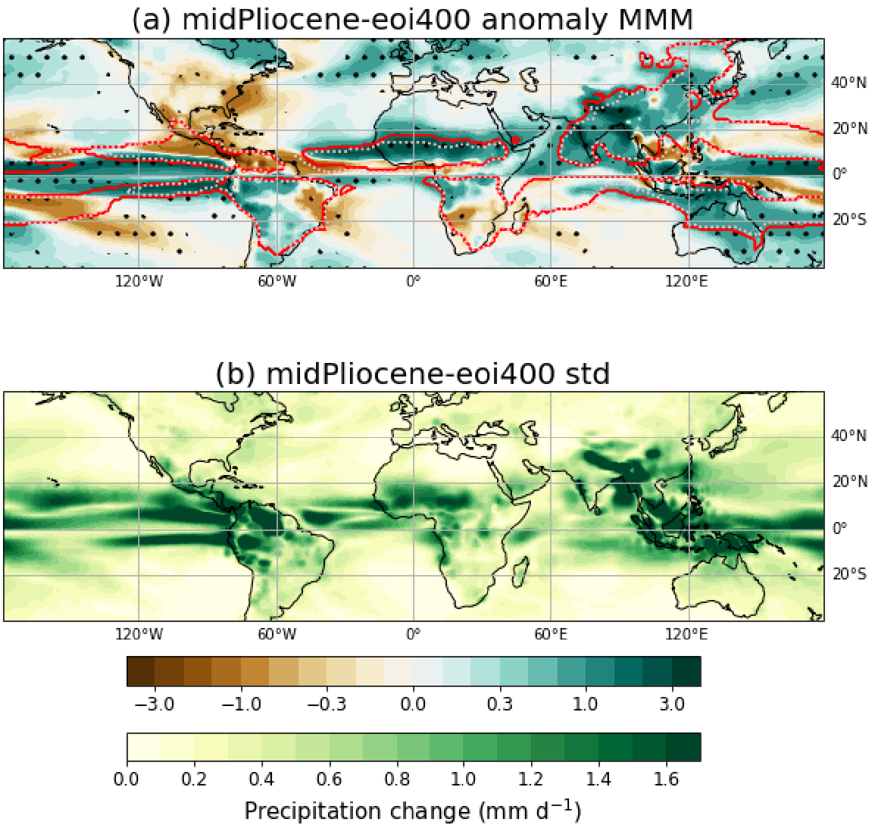

Figure 5.7: Mean global monsoon domain (contour) and changes in monsoon summer rain rate (shading) in mm d^{-1} in the PMIP4-CMIP6 *midPliocene-eoi400* ensemble. The red solid and pink dotted contour shows the boundary of multi-model mean global monsoon domain computed for PMIP4-CMIP6 *midPliocene-eoi400* and *piControl* simulations, respectively. The identification of the monsoon domain follows the description in Section 2.5.3.

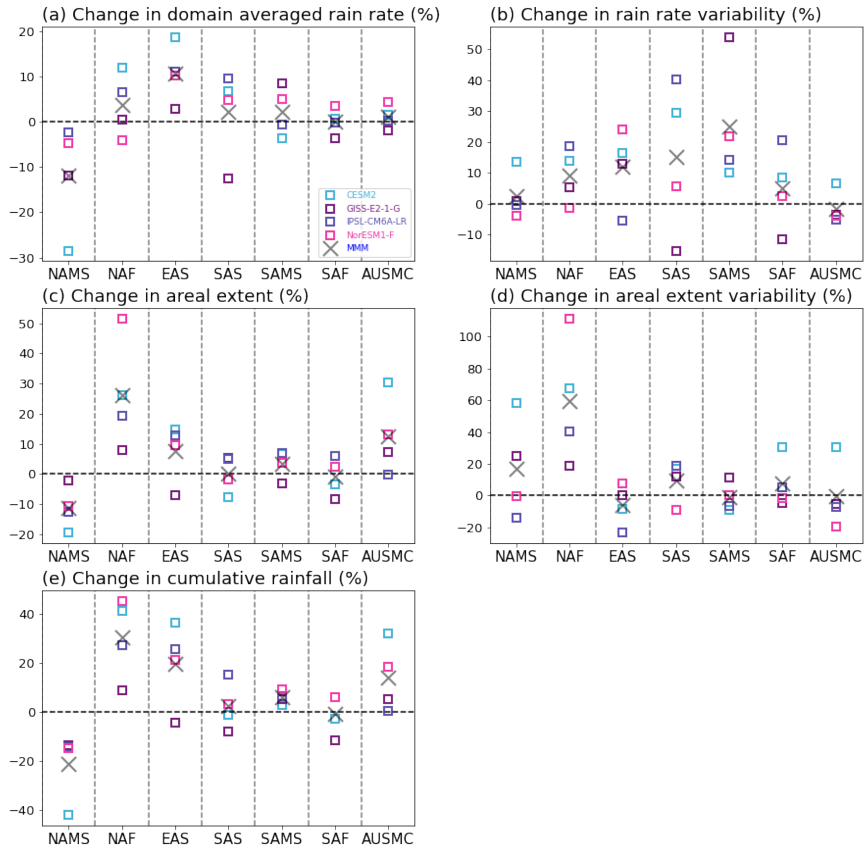

Figure 5.8: Relative change in regional monsoon diagnostics See Section 2.5.3 for a description of the diagnostic.

5.2.4 Monsoon response

In the *midPliocene-eoi400* simulations, the monsoon is changed in response to global warming forced by higher atmospheric CO_2. The higher warming in the NH than SH alters temperature gradients (Section 5.2.1) and shifts the ITCZ northward leading to an influence over monsoon affected regions. As shown in Figure 5.3a, the annual mean mPWP precipitation enhances over some monsoon regions (including western and northern Africa, India, East and Southeast Asia and Australia) and weakens over others (including northern and southern America and southern Africa). Monsoons are enhanced and expanded over North Africa, South Asia, East

Asia, Australia in the *midPliocene-eoi400* simulations as compared to the *piControl* (Figure 5.7). The enhancement agree with the finding in earlier studies based on PlioMIP1 simulations (e.g. Li et al., 2018). Loess in China provides abundant data for an intensified EAS via carbon isotope (Wang et al., 2022a) and particle size and its composition (Xiong et al., 2010; Ding et al., 2005). The largest relative increase in precipitation occurs in EAS with an ensemble increase of 10.76% (Figure 5.8). Wang et al. (2019b) conclude enhanced EAS during mPWP via $\delta^{13}C$ and C_4 grass pollen. They point out the influence of the location of the ITCZ on monsoon precipitation, supported by Section 5.2.2. NAF shows that largest ensemble mean expansion at 26.16%, which contributes to the largest increase in cumulative rainfall at 30.47% (Figure 5.8). Lake records from the US showing wetter-than-modern condition during mPWP (Ibarra et al., 2018), but all four models show reduction in the NAMS. The precipitation changes over SAF show a dipole pattern as increased over northern part while decreased in the south (Figure 5.7). This compensation results in nearly no change in SAF (Figure 5.8). Compensation also occurs over SAMS (Figure 5.7), but the reduction is limited to a small region in the east and there is a overall increase in cumulative rainfall (Figure 5.8). The strengthening in SAMS here conflicts with the conclusion of weakened SAMS from earlier studies (e.g. Li et al., 2018). All PlioMIP1 models produce weakened SAMS while only 55% of PlioMIP2 models show weakening (Pontes et al., 2020) due to change in boundary condition of soil in which PlioMIP1 applied modern soil distribution and that had changed to reconstructed mPWP distribution. 2 out of 4 models in the *midPliocene-eoi400* ensemble produce reduced precipitation in SAMS but only 1 model (GISS-E2-1-G) simulates contraction and it simulates the largest increase in precipitation. The results of SAMS here may be limited by the size of the ensemble and the choice of the members. However it must be ruled that these are generally the more sophisticated climate medels.

5.3 Effects of idealised aerosol scenarios on mPWP climate

s Both PlioMIP1 and PlioMIP2 have failed to reproduce the mean annual temperature and precipitation change shown by reconstructions (Section 5.2.1), which implies that models might not include some important mechanisms or the protocols might fail to prescribe some important boundary conditions. The effect of prescribed soil distribution on SAMS response mentioned in above (Pontes et al., 2020) reveals the importance of correct boundary condition. Prescribed forcing could be a source of uncertainty in simulating climate response (Feng et al., 2019). Currently, mPWP simulations use modern-day or pre-industrial aerosol concentration that may differ from the conditions during mPWP. This implies that aerosol effects may be one of the possible explanation for the mismatch between reconstructions and simulations. However, little research has tried to understand aerosol effects in Pliocene (e.g. Unger and Yue, 2014). More attention in palaeoclimate studies relevant to aerosols has been paid to the Last Glacial Maximum (LGM) period when the global dust cycle was enhanced (Lambert and Albani, 2021). Mineral dust could alter the radiation budget and amplify polar temperature when dispersing in the atmosphere (Lambert et al., 2013) and could affect the oceanic biogeochemical cycle with soluble Fe aerosol entering the Southern Ocean (Conway et al., 2015). Unger and Yue (2014) found the importance of aerosol and chemistry-climate feedbacks in modelling Pliocene climate, as the aerosol cooling compensates 15-100 % of the warming induced by high CO_2 while chemistry-climate feedback warms the climate with the magnitude of 30-250% of the CO_2 induced warming. Sagoo and Storelvmo (2017) found that dust indirect effects could explain some of the mismatch between model and data for LGM and mPWP. They used a new empirical parameterisation for ice nucleation on dust particles to investigate radiative forcing RF induced by different dust loading from low to high. Results showed that increased dust reduces the size of ice crystals in clouds while increasing their number. This increases the shortwave cloud RF, thus, cooling surface temperature and amplifying polar warmth (Sagoo and Storelvmo, 2017).

Due to the lack of reconstructions of aerosol loadings, most modelling studies set aerosol concentration same as present-day condition (e.g. Yan et al., 2016) or pre-industrial levels (Zheng et al., 2019), or use idealised aerosol scenarios (Sagoo and Storelvmo, 2017). In order to further investigating the potential effect of aerosol on mPWP climate, here I analyse two Pliocene simulations with different aerosol scenarios (Feng et al., 2019), one with pre-industrial aerosol concentrations and one with present-day aerosol concentrations (Lamarque et al., 2010). The simulations were performed by Dr. Ran Feng on the Cheyenne and Yellowstone provided by NCAR's Computational and Information Systems Laboratory in Boulder, Colorado in the USA. They have been used to analyse the effects of aerosol-cloud interactions on mPWP seasonally sea ice-free Arctic (Feng et al., 2019).

5.3.1 Methods

The simulations were performed by Dr. Ran Feng, which have been used to analyse the effects of aerosol-cloud interactions on mPWP seasonally sea ice-free Arctic (Feng et al., 2019). Simulations were performed with the Community Earth System Model version 1.2 (CESM1.2; Hurrell et al., 2013) composed of Community Atmospheric Model version 5.3 (CAM5.3; Martinez, 2012), Parallel Ocean Program version 2 (POP2; Danabasoglu et al., 2012), Community Land Model version 4 (CLM4; Oleson, 2010) and Community Ice Code version 4 (CICE4; Holland et al., 2012). Atmosphere and land components have $0.9°$ x $1.25°$ resolution, and ocean and sea ice components have a $\sim 1°$ resolution. CAM5.3 includes more aerosol-cloud interactions and a more reasonable aerosol distribution as compared to other models. Compared to observations, CAM5.3 simulates too strong response in cloud radiative to aerosol changes (Martinez, 2012). Meanwhile, freezing on soot and insoluble aerosols in mixed phase clouds and cloud-borne aerosols in convective clouds is not simulated heterogeneously. The 3-mode version of modal aerosol module (MAM3; Liu et al., 2012b) is used as the aerosol micro-physical scheme for long-term climate simulations in this study, which uses Aiken, accumulation and coarse modes to solve number and size concentration of internal condensation and coagulation of different species among modes. Assumptions and limitations of MAM3 are described in Liu et al. (2012b).

The experiments were branched from an existing CCSM4-PlioMIP1 simulation at model year 500 (Rosenbloom et al., 2013). Differences and similarities between CESM1 and CCSM4 are summarised in Meehl et al. (2013). The key differences occur in CAM5 which has new aerosol scheme, inclusion of aerosol-cloud-interactions, and more realistic boundary layer and radiation (Meehl et al., 2013; Martinez, 2012). Boundary condition were set up based on PlioMIP1 (Haywood et al., 2011, see Section 5.1).

Two pollutant scenarios were applied to CESM1.2. One is a pre-industrial pollutant scenario (hereafter referred as to Plio_Pristine, which can be treated as equivalent to a PlioMIP1 simulation) Lamarque et al. (2010) provided an gridded (0.5° x 0.5°) emission dataset, including reactive gases and aerosols, that covers the historical period from 1850 to 2000. The aim of this dataset is to provide consistent gridded emissions for CMIP5 models to use in running chemistry model simulations that would contributed to the assessment in IPCC AR5. The other aerosol scenario is an industrial pollutant scenario (hereafter referred as to Plio_Polluted) that added 2000s emissions from Lamarque et al. (2010) to the pre-industrial pollutants.

Each experiment runs for another 300 model years from the CCSM4-PlioMIP1 simulation. The final 100 model year runs show a quasi-equilibrium state. Results are shown as the difference between the averaged annual means of the last 100 years. Effects of removing pollutants are conducted by compare the Plio_Pristine to the Plio_Polluted, i.e. Plio_Pristine - Plio_Polluted.

5.3.1.1 Evaluating Plio_Pristine

Figure 5.9 shows the changes in surface temperature and precipitation between mPWP and pre-industrial (hereafter referred as to PI). CESM results capture both reduced meridional and zonal temperature gradients, as Figure 5.9a shows greater positive temperature change occurring in eastern Pacific Ocean and in high latitudes shown in the PlioMIPs. However, CESM simulations underestimate the magnitude

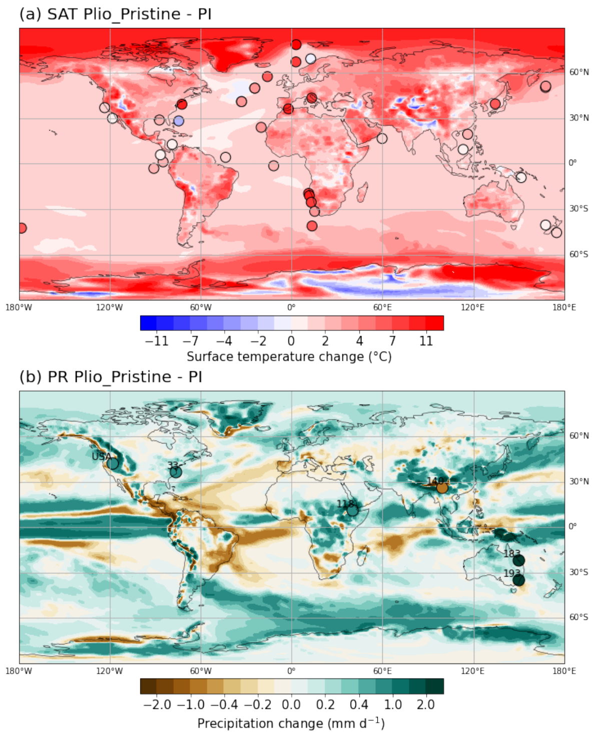

Figure 5.9: Mean annual (a) surface air temperature (SAT) in °C and (b) precipitation (PR) in mm d^{-1} change (Plio_Pristine - PI). Shaded circles are reconstructed SST anomalies (see Section 5.1.3).

of reduction in both SST gradients during the mPWP as compared with reconstructed SST changes (Figure 5.9a), which is also underestimated in the PlioMIP2 and simulations (Haywood et al., 2020) but the difference is smaller than that in the CESM simulations. Reconstructed SST anomalies show much higher warming by 5°C and 6°C warmer than CESM simulation in high latitudes (40 - 80 °N) in North Atlantic Ocean and along the western coastline of South Africa. Overall, the results from this experiment generally agree with the annual mean SAT anomalies from PlioMIP1, PlioMIP2 and *midPliocene-eoi400* (Section 5.2.1). However, PlioMIPs produce higher warming in the mPWP, particularly in higher latitudes in Northern Hemisphere that show better match with proxy reconstructions than the single CESM simulation.

Comparing to the PI, the Plio_Pristine annual mean precipitation increases over tropical Pacific Ocean and decreases over the adjacent latitudes (Figure 5.9b). Over the Atlantic Ocean, precipitation reduces in most regions except a narrow band near West Africa along the Equator. Opposite changes occur in the Indian Ocean on the either side of Equator. CESM simulations capture the right trends shown by reconstructed data, but in general underestimate the magnitudes, particularly in Australian sites (Figure 5.9). The precipitation anomalies from this experiment simulate the overall increase within the tropics and the decrease in the sub-tropics, unlike the multi-model means from PlioMIP1 (Haywood et al., 2013) and PlioMIP2 (Haywood et al., 2020). The CESM simulations generally underestimate both the magnitude and the area range of precipitation anomalies within the Atlantic Ocean. Over the Pacific Ocean, this experiment simulates a narrow band with negative precipitation anomaly, which is not shown by the two PlioMIPs. Over the Indian Ocean, the experiment simulates increase precipitation in the southern tropics, which is opposite to the *midPliocene-eoi400* results (Section 5.2.1).

The following results may be model-dependent, as the experiments used idealised aerosol scenarios and runs were branched from an earlier CCSM4-PlioMIP1 simulation. CCSM4 overestimates SST anomalies in the SH, but underestimates that in the Northern Hemisphere (Rosenbloom et al., 2013), as compared to PRISM3 reconstructed data. So, the CESM1 runs started from a less warm Northern Hemisphere. The underestimated warming in the Northern Hemisphere may be able to explain that the positive SAT anomalies in this study is weaker than the multi-model means from PlioMIP1. The atmospheric model, CAM, had been updated to include aerosol-cloud interactions from CAM4 to CAM5 (Meehl et al., 2013) from CCSM4 to CESM1. CAM4 only includes aerosol direct effects (Gent et al., 2011), while CAM5 includes both direct and indirect aerosol effects (Hurrell et al., 2013). However, according to an earlier comparison (Meehl et al., 2013), CESM1 has higher equilibrium climate sensitivity (0.9 °C higher) and transient climate response (0.6 °C higher) than CCSM4 (Meehl et al., 2013), which requires greater climate system response to forcings and feedbacks from aerosols. These differences could also affect our results in this study. Further work is required to analyse these problems.

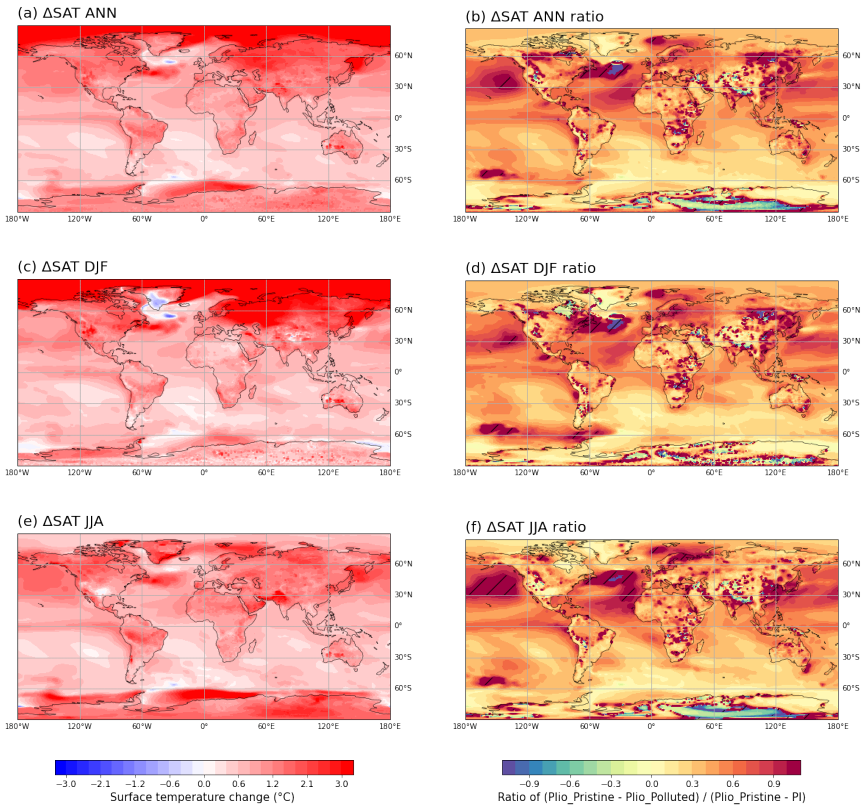

Figure 5.10: Annual and seasonal surface air temperature change in °C. (a, c, e) are annual, DJF and JJA temperature change (Plio_Pristine - Plio_Polluted). (b, d, f) are the ratio of annual, DJF and JJA temperature changes by removing anthropogenic aerosols to by applying PlioMIP1 boundary conditions, i.e. (Plio_Pristine - Plio_Polluted) / (Plio_Pristine - PI). Shading (dashed lines) marks where the ratio is greater than 1 or smaller than -1, i.e. where removing anthropogenic emissions is more important than changes in boundary conditions on affecting local temperature.

5.3.2 Effects of removing anthropogenic aerosols on temperature

Aerosol effects contribute a negative forcing on climate (see Section 1.2.3). Therefore, reducing atmospheric aerosols are expected to warm the climate. By removing present-day anthropogenic aerosols from atmosphere (i.e. Plio_Pristine - Plio_Polluted), annual mean temperature increases globally by 0.84 °C (Feng et al., 2019), which is close to the estimated modern cooling contributed by aerosols at 0 - 0.8 °C in IPCC AR6 (IPCC, 2021d). The impact is strongest in high latitudes and over NH continents where aerosol concentration are higher (Figure 5.10a). The spatial pattern of change in annual mean temperature shows that temperature rises about 0.4 - 1.0 °C in tropical Pacific Ocean and causes more warming by increasing 1.0 - 1.4 °C in subtropical Pacific and the upwelling region in eastern Pacific (Figure 5.10a), which therefore reduces both meridional and zonal temperature gradients in Pacific Ocean.In future, global warming (particularly in the NH) would be enhanced by removing emitted aerosols. However, though removing aerosols could bring further warming, mPWP warming is dominantly induced by changes in boundary conditions rather than aerosols (Figure 5.10b) as removing anthropogenic aerosols only causes more warming than the mPWP boundary conditions over Northeastern Pacific and high-latitude North Atlantic Ocean. Similarly, changes in boundary conditions are relative more important than aerosol effects in mPWP warming during DJF and JJA (Figure 5.10c to f).

5.3.3 Effects of removing anthropogenic aerosols on the hydrological cycle

Precipitation responds to the removal of aerosols in a more complex manner, but most changes occur in regions of deep convection (Figures 5.11). By removing industrial pollutants, precipitation increases near the Equator (dominant in NH) and decreases in subtropics, indicating northward, narrower and stronger convection. Some of the changes in precipitation over Asia are a direct consequence of the high anthropogenic emissions in the region, and so would likely not occur in the Pliocene through uncertainty in natural aerosols. Anthropogenic aerosols causes southward shift of ITCZ (Ridley et al., 2015; Voigt et al., 2017), thus, removing human induced aerosols should lead to a more northward shift ITCZ, which is shown in results in this study. CMIP5 model simulations show that future ITCZ would become narrower and weaker under global warming (Byrne and Schneider, 2016). Figures 5.11 agrees that the warmer climate would have a narrower ITCZ. The pattern of changes in precipitation strength matches the temperature change, which agrees with Berg et al. (2013) as higher temperatures cause stronger convective precipitation. In northern tropics, anthropogenic aerosols have caused a reduction of rainfall through twentieth century (Ridley et al., 2015), so precipitation should increase after removing aerosols from the atmosphere. However, CMIP5 model simulations show that future ITCZ would become weaker through this century as responding to further warming (Byrne et al., 2018). Actual changes in the strength of ITCZ need further discussion through analysis of additional variables. In DJF, precipitation increases in South Africa, most of the equatorial Asian-Pacific region, and the eastern equatorial Pacific (Figure 5.11c). Precipitation in JJA increases along equator, in E and SE Asia, and in North America while decreases in Pacific Ocean adjacent to precipitation increased region (Figure 5.11e). Large reduction in JJA precipitation also shows in southern Indian Ocean, South Atlantic Ocean, and along the coastline of West Africa and eastern coastline of South America.

Removal of human-induced aerosol emissions causes more precipitation change than the applied mPWP boundary condition over subtropical Pacific Ocean and South Atlantic Ocean, Indian Ocean and Southeast Asia (Figures 5.11b, d and f). Figure 5.12 shows the relative importance of removing anthropogenic aerosols and mPWP boundary conditions on mPWP zonal mean precipitation change. The ratio indicates that aerosol forcing is more important than the mPWP boundary conditions (including high CO_2) affecting the precipitation in the tropics, which could imply the importance of aerosol scenario in future projection about tropical precipitation. Studies suggest that anthropogenic aerosols cause the southward shift of the ITCZ, weaken the Hadley circulation and reduce the precipitation in deep convective areas in response to the NH cooling induced by aerosols (Hwang et al., 2013; Wang et al., 2019a).

The overall uniform warming over tropical and subtropical regions (Plio_Pristine - PI and Plio_Pristine - Plio_Polluted) result in general increase in sea level pressure

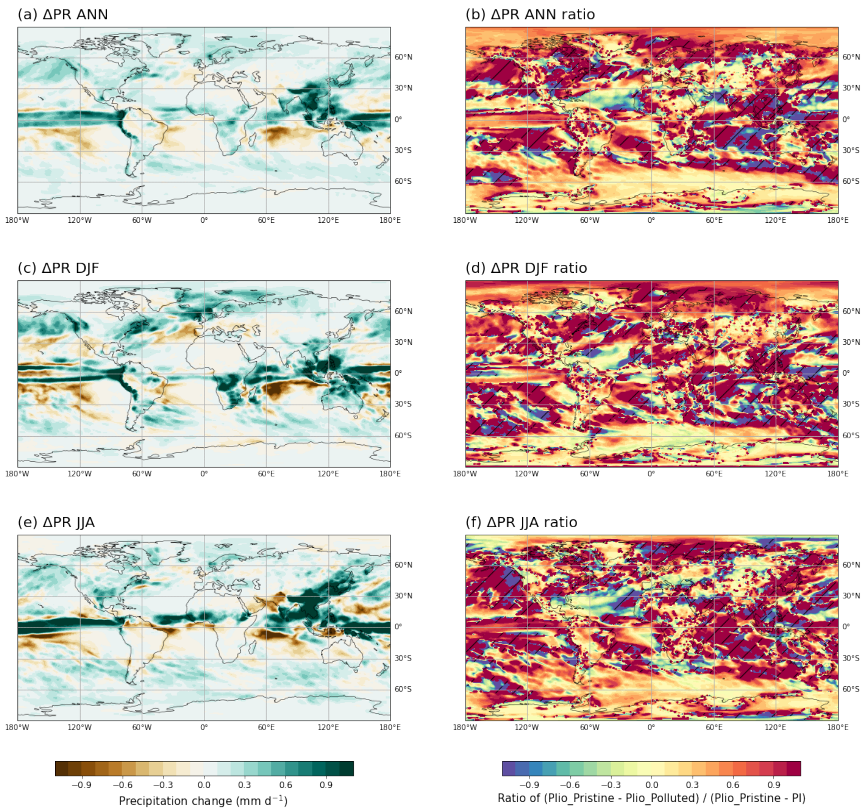

Figure 5.11: Annual and seasonal precipitation change (mm d^{-1}). Same as Figure 5.10 but for precipitation.

and have relatively small effects on surface wind, while removing anthropogenic aerosols rises the sea level pressure and have much stronger effects on surface wind that shows seasonal variances (Figure 5.13).

5.3.4 Effects of removing anthropogenic aerosols on monsoon

Results from the above show that the idealised removal of anthropogenic aerosols from mPWP climate makes little difference to temperature, but it clearly affects tropical precipitation where most of the monsoon-affected regions are located in. This implies that the choice of prescribed aerosol scenario could affect mPWP

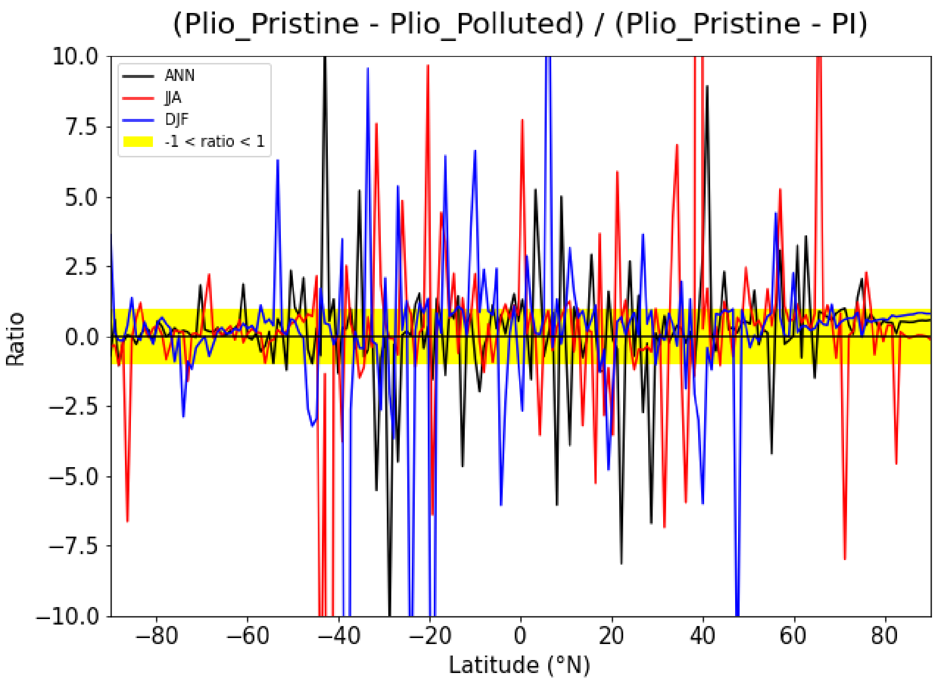

Figure 5.12: Relative importance of removing anthropogenic aerosols and mPWP boundary conditions on mPWP zonal mean precipitation change. The ratio is computed as ((Plio_Pristine - Plio_Polluted) / (Plio_Pristine - PI)).

monsoon response.

Figure 5.14 shows changes in the global monsoon domain and summer rain rate during the mPWP (Plio_Pristine - PI) and effects of removing anthropogenic aerosols (Plio_Pristine - Plio_Polluted). The boundary of global monsoon domain in the Plio_Pristine simulation (red contour in Figure 5.14) is similar to that in PI (black), as well as in Plio_Polluted (blue). Less change in these boundaries implies that removal of anthropogenic aerosols has little effect on the location of monsoon domain boundary. Though not affecting the boundaries, removing anthropogenic aerosols changes the spatial land monsoon precipitation. IPCC AR6 Chapter 8 (Douville et al., 2021) states that anthropogenic aerosol emission in the NH partly caused the global land monsoon precipitation reduction during 1950s to 1980s. At regional scale, aerosol emissions induced by human caused decreases in monsoon precipitation over western Africa and eastern and southern Asia by cooling the climate over the 20th century. In contrast, removing aerosol emissions is expected

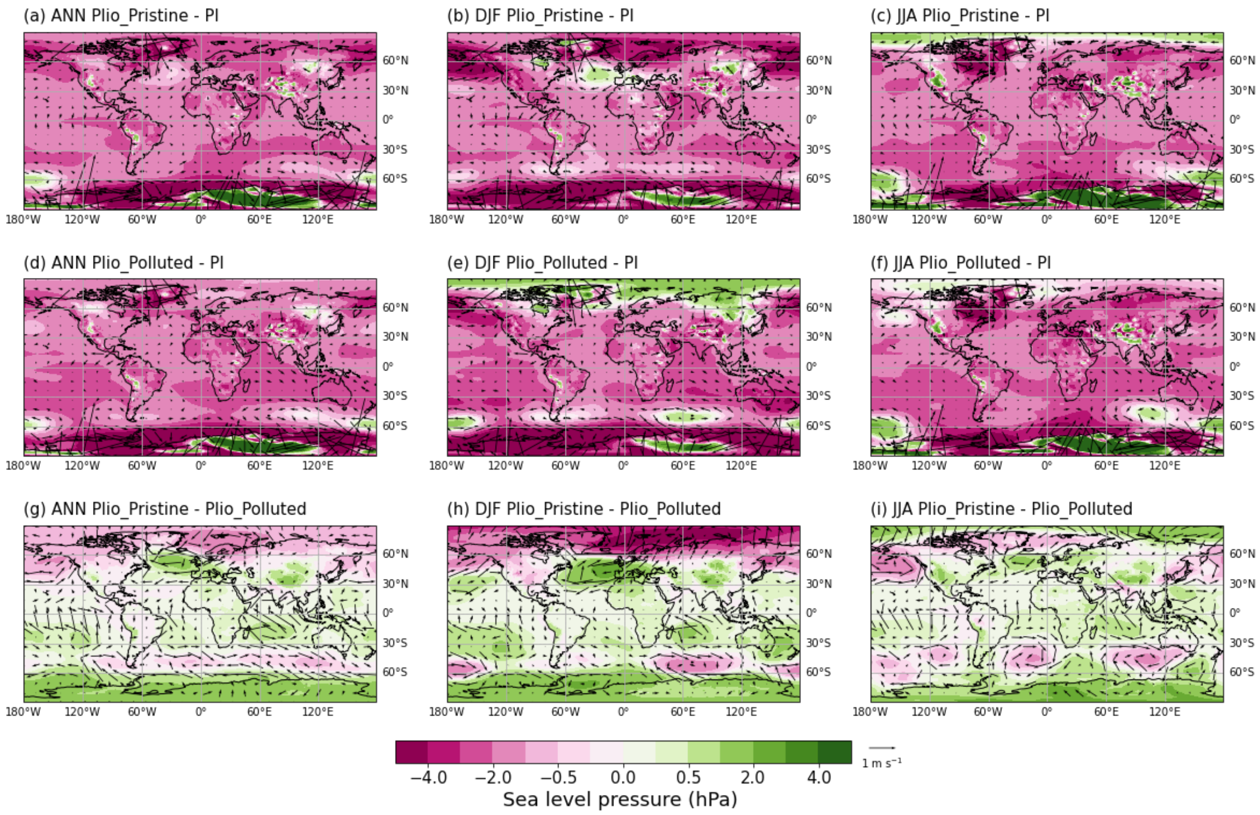

Figure 5.13: Changes in annual and seasonal sea level pressure (hPa) and surface wind (m s^{-1}) in Plio_Pristine (a,b,c) and Plio_Polluted (d,e,f) relative to PI, and by removing aerosols (Plio_Pristine - Plio_Polluted; g,h,i).

to reduce the cooling effect induced by the aerosol emissions and increase the precipitation over western Africa and eastern and southern Asia during local monsoon seasons. Figure 5.14b shows the increase in monsoon summer rain rate over the three regions agreeing with the logic. The result here is consistent with projected future monsoon enhancement, as global and Asian summer monsoon precipitation is likely to increase by 2050s due to the expected reductions in anthropogenic aerosol emissions (Wilcox et al., 2020). Though this study used idealised aerosol scenario that could not occur during mPWP, it reveals the importance of prescribed aerosol scenario on simulating mPWP monsoon response.

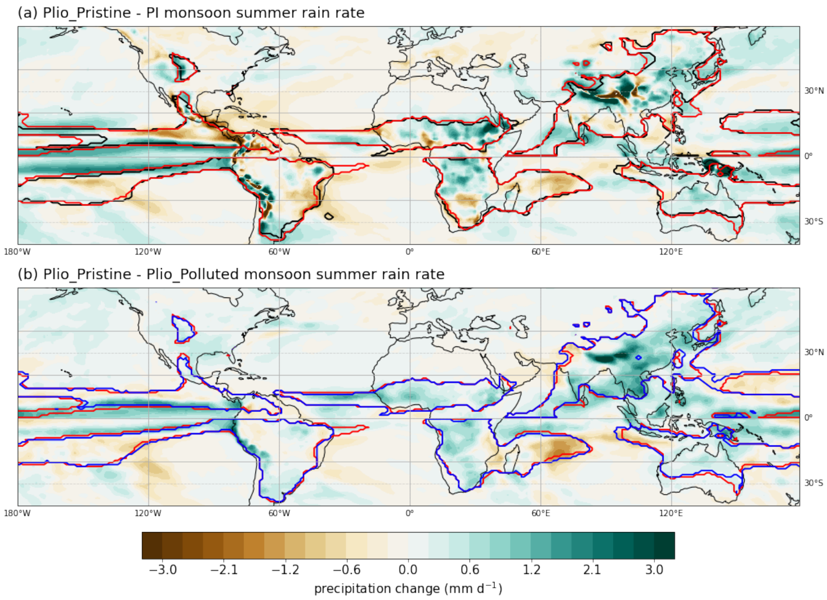

Figure 5.14: Changes in monsoon summer rain rate (mm d^{-1} (a) during the mPWP (Plio_Pristine - PI) and by removing anthropogenic from the atmosphere (Plio_Pristine - Plio_Polluted). Black, red and blue contours represent the boundary of the global monsoon domain following Wang et al. (2014b) in PI, Plio_Pristine and Plio_Polluted respectively.

5.4 Conclusion

PlioMIPs provide realistic mPWP boundary conditions with CO_2 level at about 400 ppmv. Available reconstructed data from PRISM4 allow to test and evaluate possible scenarios with high CO_2 concentration. Temperature response shows the warming, polar amplification and reduced temperature gradients similar to precious PlioMIP1 (Haywood et al., 2020). Changes in the spatial pattern of surface temperature have impacts on precipitation. As expected, the *midPliocene-eoi400* simulations show increase in mean annual and seasonal precipitation in the tropics and high latitudes and a decrease in the subtropics relative to the *piControl*. The large increase in JJA precipitation over NH continents comes from stronger NH monsoons over Aisa and Africa. The monsoon in northern Australia is also stronger in the *midPliocene-eoi400* simulations. However, both PlioMIP1 and PlioMIP2 fail to reproduce the magnitude of reduction in temperature gradients as suggested by reconstructions. They are also unable to reproduce the changes in mean annual precipitation, although the data quality and quantity is not as good as for temperature.

Using unrealistic prescribed forcing could be a source of uncertainty. The protocol of *midPliocene-eoi400* prescribed pre-industrial aerosols, which might be a possible explanation to the mismatch between model and data. A set of existing simulations with two idealised aerosol scenarios (Feng et al., 2019) are analysed to the effect of aerosol on mPWP climate response. In contrast to GHGs warming the climate, aerosols cool the climate. The idealised experiments introduced in this chapter are used to analyse the effect of removing anthropogenic aerosols from the mPWP climate, though they have some limitations. As expected, mean annual temperature increases globally and and particularly in the NH due to asymmetrical emissions concentrating in the NH, agreeing with the findings from an earlier studies (e.g. Samset et al., 2018), in which several models have been applied to test removing all anthropogenic emission under present-day conditions. Removal of industrial polluting effects also causes asymmetric changes in precipitation. Aerosols have more impacts on annual and seasonal precipitation over the tropics and subtropics than the mPWP boundaries. Precipitation increases over eastern and southern Asia and western Africa during monsoon seasons after removing the aerosols. Though not affecting the location of monsoon domain boundary, removal of anthropogenic aerosol change the precipitation within the domain. Though the aerosol scenarios are ideal that could not occur during mPWP, it reveals the importance of prescribed aerosol scenario on simulating mPWP monsoon response.

Chapter 6

Discussion

So far, previous chapters have analysed the climate response to various forcings in three past warm periods. In this chapter, I will bring the results from the previous chapters together to compare and contrast the climate response to different forcings. Additional discussion about the aerosol effects on the mPWP climate will not be presented here, as the idealised experiments are specific to the analysis in Chapter 5.

First two sections compare the climate response between experiments. Section 6.1 firstly compares the climate response in the *midHolocene* ensemble with those in the *lig127k* ensemble, because both experiments were designed to examine the climate change in response to different orbital forcing. In order to reduce the impacts of using different model members and different control simulations, here I use the subset of 14 models that have performed the both experiments (see Table 2.2 for the member list). Section 6.2 then compares the climate response to orbital forcing in the two ensembles with the response to increased atmospheric CO_2, by just the 4 models that have performed the *midPliocene-eoi400* simulations. All the three experiments show mismatches between the simulated anomalies and these reconstructed from proxy data. Section 6.3 discusses the possible reasons causing the mismatches in this PMIP generation. Section 6.4 focuses on the limitation in this work and discusses the potential improvements in next PMIP generation. A brief conclusion is given at the end as Section 6.5.

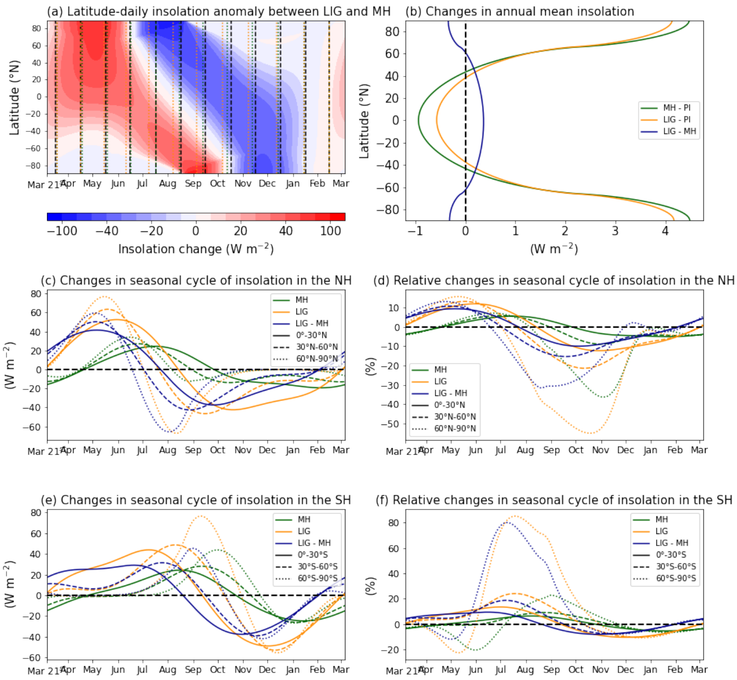

Figure 6.1: Comparison between the latutide-daily insolation anomaly at 6 ka (MH) and 127 ka (LIG) relative to 1850CE (PI), and the difference between the two periods. (a) Change in insolation between LIG and MH. Date starts from March 21st, i.e. the vernal equinox,to remove the uncertainties in calendar correction. The black dashed lines show the start day of each month at 1850 CE and the green and orange dotted lines show that at 6 ka and 127 ka respectively, which illustrate the effect of orbital changes on calendar. (b) Change in zonal averaged annual mean insolation; changes and relative changes in 30° zonal bands in the (e,f) NH and (g,h) SH.

6.1 Climate change response to orbital forcing

The Last Interglacial (LIG at 127 ka) and mid-Holocene (MH at 6 ka) were characterized by orbital configuration different to that at 1850 CE. The orbit at 6 ka was characterised by larger obliquity and its perihelion occurred near the boreal autumn equinox rather than near the boreal winter solstice at PI. The eccentricity at 6 ka was similar to PI. The orbit at 127 ka was characterised by larger eccentricity than the PI and its perihelion occurred close to the boreal summer solstice. The obliquity at 127 ka was also larger than at PI but the increase was slightly smaller than at 6

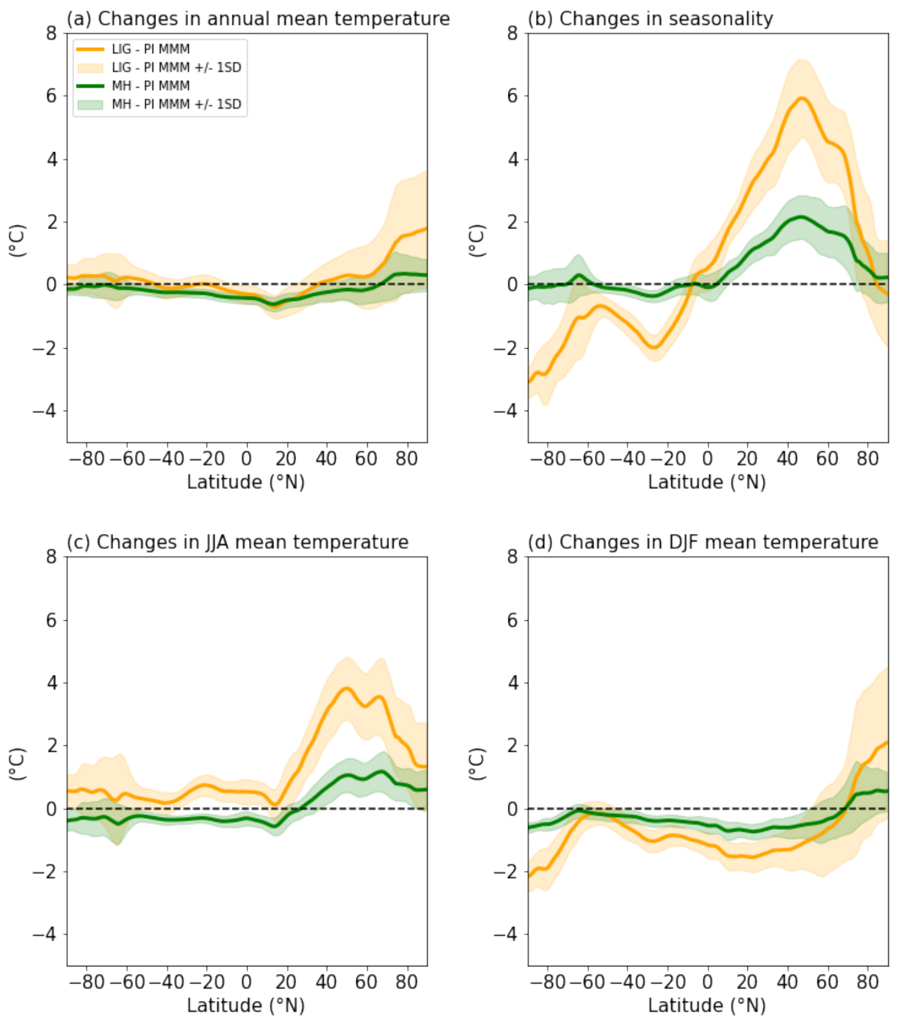

Figure 6.2: Zonal mean temperature change in the *midHolocene* (green) and *lig127k* (orange) simulations of (a) annual, (b) seasonality, (c) JJA, and (d) DJF. Solid lines are multi-model means with shading showing standard deviation. The seasonality is computed as the difference in mean temperature between the warmest month and the coldest month (MTWA - MTCO).

ka. Both periods were characterised by receiving more insolation at the top of the atmosphere (TOA) in the NH (less in the SH at 6 ka) during JJA and less incoming solar radiation in both hemispheres during DJF as compared to 1850 CE (Figure 6.1).

The major difference between the protocols of the *midHolocene* and *lig127k* experiments comes from their prescribed orbital parameters (Otto-Bliesner et al., 2017a). A comparison between the climate change in the *midHolocene* and *lig127k* simulations provides a chance to examine the sensitivity of climate to these parameters.

Changes in obliquity bring an increase in the annual mean insolation in high latitudes and a decrease at low latitudes in both periods (Figure 6.1b). The change in annual mean insolation was greater at 6 ka, as it had a larger obliquity than at 127ka. The MH insolation increase at high latitudes was roughly 4.3 W m^{-2} greater than at 0 ka and 0.3 W m^{-2} greater than at 127 ka. The tropical decrease in the annual mean insolation at 6 ka was -1.0 W m^{-2}, while the decrease at 127 ka was -0.6 W m^{-2} relative to that at 0 ka (Figure 6.1). Though annual mean insolation anomaly at 6 ka was stronger than at 127 ka, changes in annual mean surface temperature in the *midHolocene* simulations are weaker than the *lig127k* simulations (Figure 6.2a). This interesting contrast suggests that there must be other important processes besides direct response to insolation anomalies, for example, the ocean memory (Marino et al., 2015; Govin et al., 2012) and polar amplification with smaller and thinner sea ice in the Arctic (Serreze and Barry, 2011). Previous studies suggest the memory in the ocean of the H11 event (Marino et al., 2015; Govin et al., 2012) led Southern Ocean warming and North Atlantic Ocean warming at the time (Stone et al., 2016; Holloway et al., 2018), although such memory is unlikely to be captured by the timeslice experimental design used here.

In contrast to the stronger annual mean insolation anomalies, the seasonal cycle of changes in insolation induced by orbital forcing at 127 ka was stronger than that at 6 ka (Figure 6.1) as a result of a larger eccentricity and the position of perihelion near boreal summer solstice. Comparing to 1850 CE, the NH summer insolation anomalies was 5-10% greater at 6 ka and roughly 10-15% greater at 127 ka. Both periods saw the greatest seasonal changes in high latitudes in both hemispheres. In the SH, the magnitude of insolation change at 6 ka was again weaker than at 127 ka, and the anomalous insolation anomalies were shifted to austral spring. In response to the prescribed orbital forcing, both *midHolocene* and *lig127k* ensembles show strong seasonal variations in surface temperature as compared to the *piControl* (Figure 6.2), with a larger temperature change in the *lig127k* simulations. Both ensembles show an increase in seasonality in the NH and the greatest change occurring at about 40–55°N, but the change is significantly greater in the *lig127k* ensemble at 5.7°C than the 2.1°C in *midHolocene* (Figure 6.2b). There appears to be an important threshold of 27°C. South of 27°N, the zonal mean JJA temperature change is positive in the *lig127k* simulations but negative in the *midHolocene*, though the change in both ensembles is smaller than 0.5°C. However above 27°N, both ensembles show positive change in zonal mean JJA temperature, with the *lig127k* (at 2.75°C) being warmer than the *midHolocene* (at 0.80°C). The greatest *lig127k* JJA warming occurs near 50°N at 3.85°C, which is higher than the maximum temperature increase in the *midHolocene* at 1.21°C occurring around 65 to 68°N. The ensemble mean DJF zonal-averaged temperature change relative to *piControl* is negative south of 69°N for both *lig127k* and *midHolocene* and the anomaly is stronger in the *lig127k*. Though the insolation anomalies are negative in high latitudes in the NH in both periods (Figure 6.1c,d), both ensembles provide positive temperature change (*lig127k* at 1.31°C and *midHolocene* at 0.48°C). The Arctic warming during boreal winter could be explained by the maintenance of positive DJF surface temperature anomalies in Arctic as the result of the memory of cryosphere and ocean feedbacks (Serreze and Barry, 2011).

The seasonal cycle in insolation anomaly and the consistency in temperature change in both the *midHolocene* and *lig127k* simulations indicate that CMIP6 models can produce temperature response to insolation anomalies induced by various orbital forcings, which was a purpose of the design of the two experiments (Otto-Bliesner et al., 2017a; Kageyama et al., 2018). Proxy data suggest that the GMST (129-125 ka) was 1.0-1.5°C higher than the PI, which overlaps with the low end of the temperature range projected under SSP1-2.6 for the end of of 23^{rd} century (Gulev et al., 2021). The possibility of simulating LIG climate change could test the models used for future projections, though the major forcing are different. However, both the *midHolocene* and *lig127k* ensembles cannot fully reproduce the magnitude of warming suggested by proxy data (see Sections 3.6 and 4.5 in earlier chapters). This mismatch in both ensembles implies that there must be some important processes, at global and/or regional scales, that have not been included in the experimental design or that are missed or poorly presented in the physical schemes of models. For instance, both experiments prescribed ice sheets as being same as the *piControl* (Otto-Bliesner et al., 2017a). Under Arctic amplification, the Greenland Ice Sheet is likely to retreat and becomes thinner, which will effect local albedo and meltwater discharge and therefore affects temperature, sea level, ocean circulation etc. The reconstructed LIG cooling in the Nordic Seas and south of Greenland was likely associated meltwater from ice sheets over Scandinavia and Canada (Barlow et al., 2018; Otto-Bliesner et al., 2021), which the *lig127k* simulations did not incorporate this meting and show warming in the region.

Though the response in precipitation to orbital forcing is complex (Sections 3.3.2, 3.3.3 and 4.3), both the *midHolocene* and *lig127k* simulations produce enhanced and expanded NH monsoons and weakened and constricted SH monsoons (Figure 6.3). Nonetheless the direction of the changes are the same across both experiments. The magnitude of most monsoon change in the *lig127k* is more than twice larger than that in the *midHolocene* and the difference is significant in most of the regional monsoons (Figure 6.3f). The only exception is that the *lig127k* ensemble produces a smaller reduction in domain averaged rain rate (Figure 6.3b) over southern Asia monsoon than the *midHolocene*, but the difference is not significant and are less consistent across the simulations. Relative changes in the inter-annual variability of domain-averaged rain rate (Figure 6.3b) and areal extent (Figure 6.3d) are less consistent across the ensembles, but the *lig127k* simulations generally produce a stronger signal than the *midHolocene* simulations. Those models that produce large variability in one regional *midHolocene* monsoon does not necessarily pro-

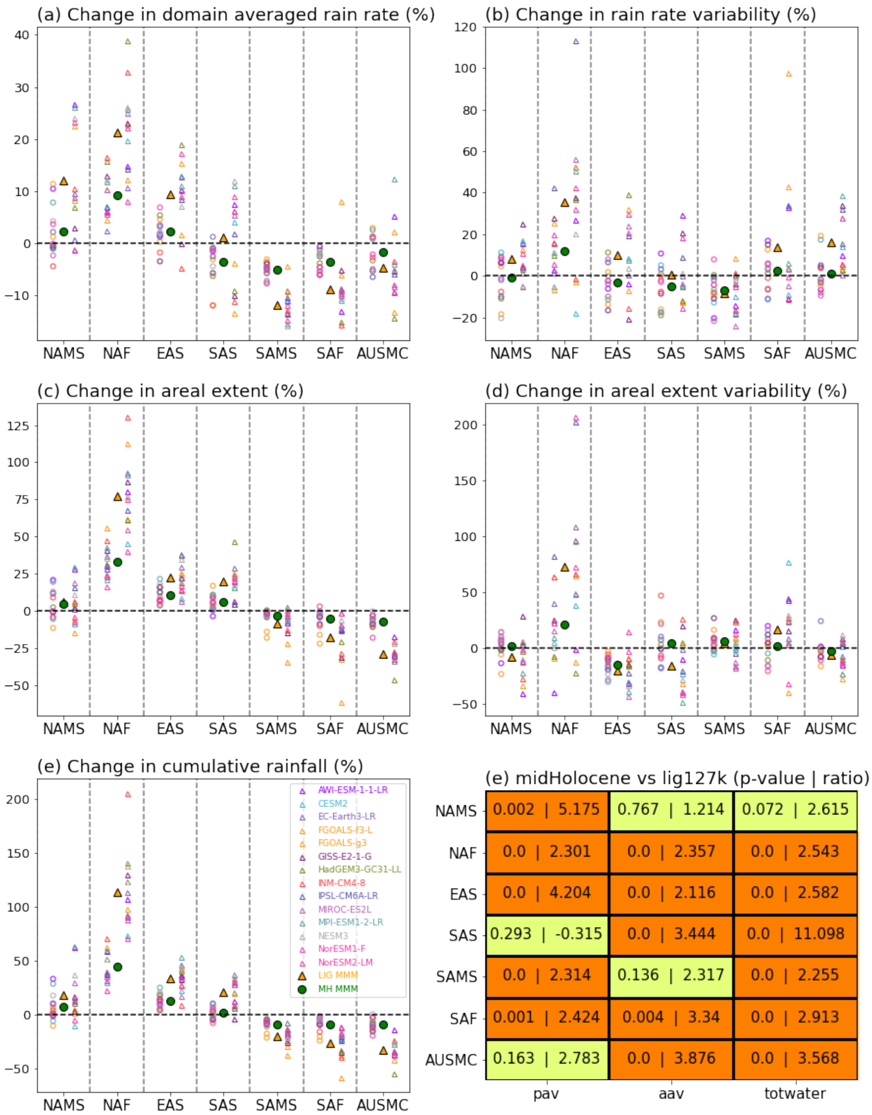

Figure 6.3: Relative changes in *midHolocene* and *lig127k* regional land monsoons. (a) The change in area-averaged precipitation rate during the monsoon season. (b) Change in the standard deviation of interannual variability in the area-averaged precipitation rate.(c) The change in the areal extent of the regional monsoon domains. (d) Change in the standard deviation of interannual variability in the areal extent. (e) The percentage change in the total amount of water precipitated in each monsoon season computed as (a) x (c). Panel (f) shows the comparison between PMIP4 *midHolocene* and *lig127k*. For each grid box, the number before "|" is p-value and the number after "|" is the ratio of the diagnostic computed by PMIP4 LIG / PMIP4 MH.

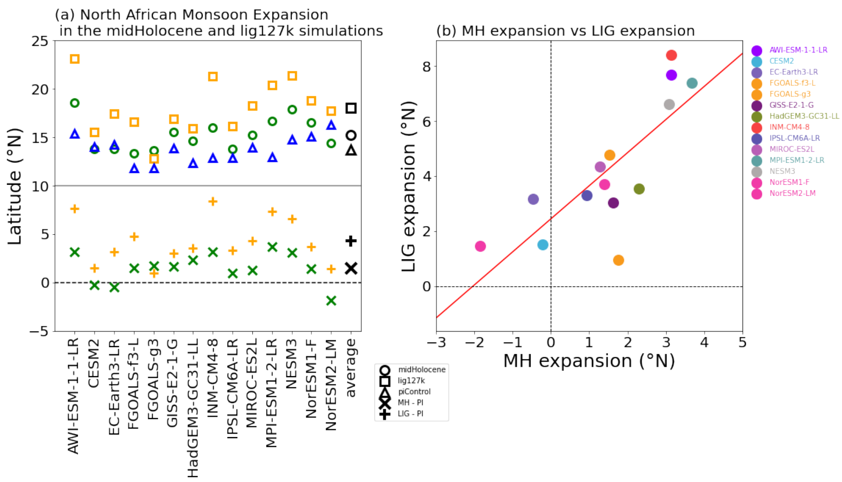

Figure 6.4: NAF expansion in the PMIP4-CMIP6 *midHolocene* and *lig127k* ensembles. (a) The poleward boundary of NAF in the *midHolocene*, *lig127k* and *piControl* simulations and the expansions. (b) Relationship between the northward shift of the poleward boundary in the two ensembles. Red line shows the linear regression. The poleward boundary of NAF is calculated by determining the change in latitude where the zonal mean summer (MJJAS) rain rate equals 2 mm d^{-1} over the North Africa (15°W–30°E).

duce large variability in other monsoons, but there is large chance that they do produce large variability in that same monsoon in *lig127k*. In summary, both ensembles are able to produce enhanced monsoons in the NH and weakened monsoons in the SH and the signal is larger in the *lig127k*, which agrees with the monsoon theory response to the insolation-driven changes in seasonal temperature (Schneider et al., 2014). This indicates that all models produce the same large-scale redistribution of moisture by the atmospheric circulation, though they still fail to reproduce the magnitude of changes (Sections 3.4.2 and 4.3). Changes in mid-Holocene global monsoon are primarily driven by changes in atmospheric circulation (D'Agostino et al., 2019, 2020), which could imply that the *lig127k* monsoon changes are also associated with atmospheric dynamics.

The most pronounced changes in both ensembles occur over North African monsoon (NAF). All *lig127k* and *midHolocene* simulations show increased rain rate, areal extent and cumulative rainfall than the *piControl* simulations (Figure 6.3a). There is a significant relationship (p = 0.001, R^2 = 0.61) between the NAF expansion (relative to the *piControl*) in the *midHolocene* and the *lig127k* simulations (Figure 6.4b), with best fit of the *lig127k* experiment being 1.2 x the *midHolocene* with an offset of 2.45°. This relationship could potentially help to estimate the NAF expansion during the LIG from the MH reconstructed precipitation anomalies, due to the lack of proxy data at the LIG. Figures 6.4 and 6.3 show that the ensemble averaged enhancement and expansion in the *lig127k* ensemble are outside of the range of rain rate and areal extent changes in the *midHolocene*. There are 14 models that have completed both *lig127k* and *midHolocene* simulations, and on average both *lig127k* and *midHolocene* ensembles produce NAF northward extension (Figure 6.4). All *lig127k* simulations and 11 out of the 14 *midHolocene* simulations provide NAF northward expansion relative to the *piControl*. Only CESM2, EC-Earth3-LR and NorESM2-LM simulate MH NAF retreat rather than expansion. 13 out of the 14 models simulate greater NAF expansion in the *lig127k* simulations than the *midHolocene* simulations, with FGOALS-g3 being the only model with a larger NAF expansion during the MH.

Both the *midHolocene* and the *lig127k* simulations usually show a large underestimation in the experiments as compared to reconstructions (Sections 3.4.2.2 and 4.3) and this mismatch has existed since the beginning of PMIP (e.g. Joussaume et al., 1999; Harrison et al., 2015). Both protocols applied prescribed modern vegetation cover (Otto-Bliesner et al., 2017a) and most models did not turn on dynamic vegetation scheme through running simulations. The mismatch implies the importance of including schemes of dynamic vegetation or using prescribed MH/LIG vegetation cover. Earlier studies suggested that simulated precipitation changes at the mid-Holocene show better agreement with reconstructions if the models have interactive vegetation or use more realistic vegetation cover over the Sahara (e.g. Lu et al., 2018; Swann et al., 2014b; Pausata et al., 2016; Gaetani et al., 2017; Messori et al., 2019), though the mismatch between simulations and reconstructions still exists. Vegetation schemes of the PMIP4-CMIP6 models and importance of dynamic vegetation should be further investigated.

6.2 Climate change responding to different types of forcings

The mPWP, LIG and MH were three past warm periods that offers possible systems to simulate future global warming. Unlike the strong seasonal variations with small annual means change in the *midHolocene* and *lig127k* simulations in response to orbital forcings, the *midPliocene-eoi400* simulations produce more change in annual mean variables mainly responding to high CO_2 forcing, and the patterns of seasonal changes are similar to those in annual changes (Figures 6.5). The *midPliocene-eoi400* simulations see strong polar amplifications in both hemispheres. This contrasts to the SH polar cooling during DJF in the *midHolocene* and *lig127k* simulations. Meanwhile, there is nearly no change in seasonality in the *midPliocene-eoi400* between 60°S and 70°N and significant reduction in polar latitudes (Figure 6.5). The magnitude of annual mean surface temperature change over land is greater than over the ocean in all three ensembles (Figures 3.3, 4.3 and 5.1). Changes in land-sea temperature contrast and polar amplification result in changes in precipitation and monsoons.

The response of monsoons in the *midPliocene-eoi400* simulations are different to those in the other two ensembles (Figure 6.6). All the three periods show enhanced monsoons over northern Africa and eastern Asia. The decreased North American monsoon (NAMS) in the *midPliocene-eoi400* shows opposite signal to the NAMS enhancement shown in the *midHolocene* and *lig127k*. In the SH, changes are less robust than in the NH. The *midPliocene-eoi400* simulations produce enhanced regional monsoons, while the *midHolocene* and *lig127k* simulate weakened monsoons. The mechanism behind monsoon changes during the three periods are different as well. D'Agostino et al. (2019, 2020) state that monsoon changes under RCP8.5 are likely driven by thermodynamics and net energy input. As the high CO_2 concentration is also a major forcing in the *midPliocene-eoi400*, it implies that is different to the mechanisms are operating than in the *midHolocene* and *lig127k* (which monsoon change is mainly driven by dynamic component D'Agostino et al., 2019, 2020). As discussed in Chapters 3 to 5, all *midHolocene*,

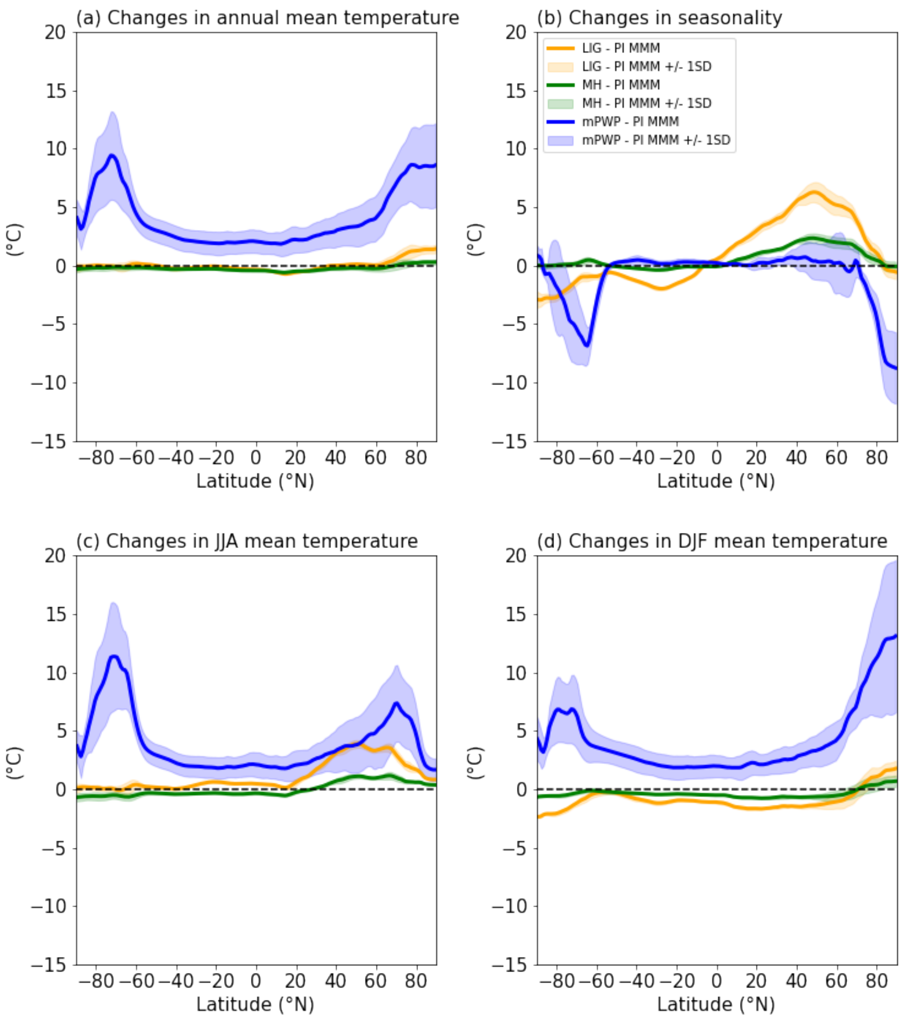

Figure 6.5: Similar to Figure 6.2 but also includes *midPliocene-eoi400* simulations.

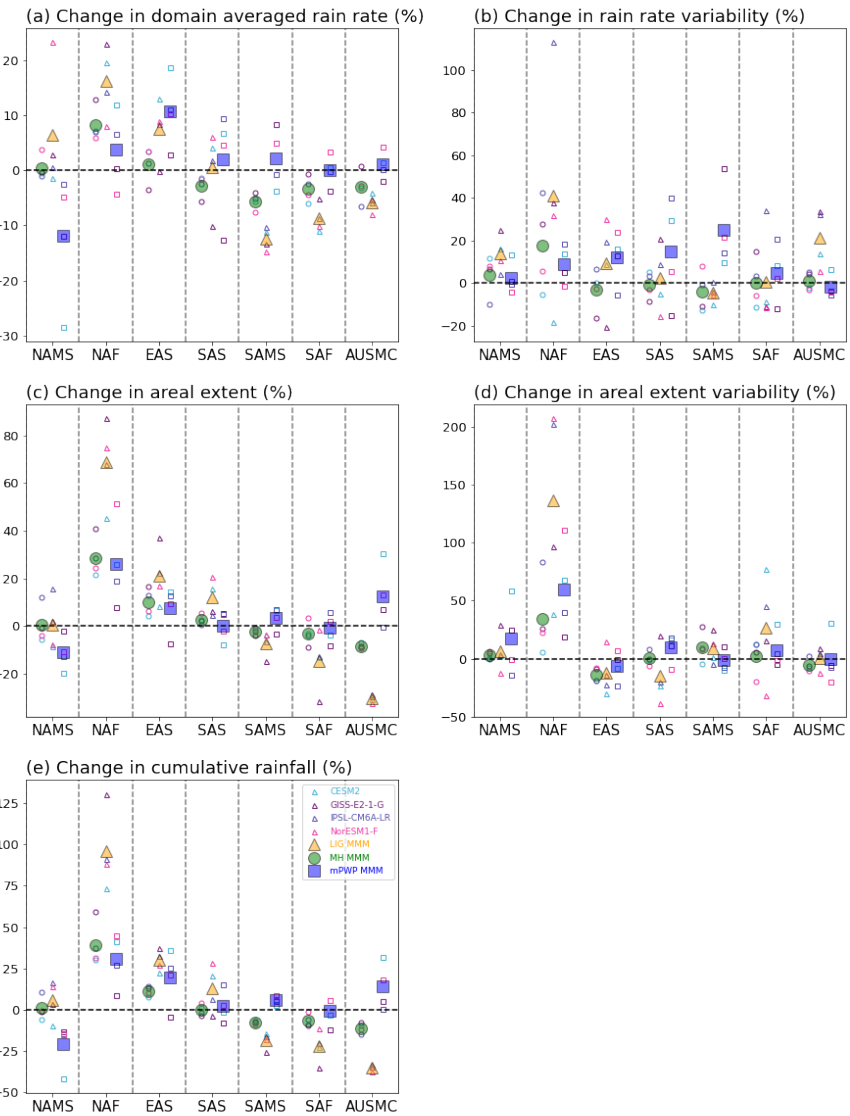

Figure 6.6: Similar to Figure 6.3 but also includes *midPliocene-eoi400* simulations.

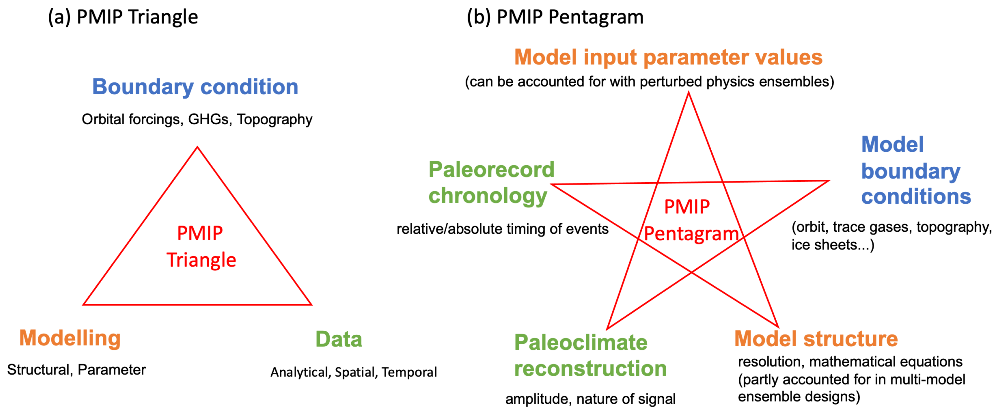

Figure 6.7: Sources of uncertainty to address the mismatch between model and data. The PMIP triangle (Haywood et al., 2013) was established to assess the causes of disagreement between model and data. It has been reformulated into a pentagram as being suitable for transient simulations to examine major long-term and abrupt climate transitions (Ivanovic et al., 2021).

lig127k and *midPliocene-eoi400* simulations cannot fully reproduce the magnitude of change suggested by proxy data. These mismatches indicate that the models used in future projections cannot produce the climate response to various types of forcing correctly. Further improvements are required.

6.3 Data-model mismatch in PMIP simulations and potential improvements

All the ensembles in this work show some mismatches between models and data. Simulated anomalies cannot always reproduce the magnitude of the reconstructed anomalies or may even show an opposite change. The cause of the mismatch is rarely obvious and can be difficult to quantitatively attribute. Haywood et al. (2013) summarise the key findings in PlioMIP1 and highlight the complexity of understanding data–model mismatch via the PMIP triangle (as shown in Figure 6.7a). The PMIP triangle illustrates the possible uncertainties in modelling (from model structure and parameter), proxy data (from analysing, and temporal and spatial) and boundary conditions (from prescribed forcings like orbital parameters, GHGs, topography and aerosols etc.). To understand the cause of mismatch between model and data and reduce the disagreement requires the balance of the three sources of uncertainty. This has subsequently been developed to subdivide both the model and data uncertainty (Ivanovic et al., 2021). As the ensembles here do not look at perturbed physics, it is not possible to consider structural uncertainty separately.

Among the three palaeo warm periods, mid-Holocene is closest to modern. The dominant forcing during this period came from orbit parameters, which can be computed quite accurately and precisely from equations (Berger, 1978; Laskar et al., 2004, 2011). The topography during the mid-Holocene was very similar to its present-day conditions. Therefore, using PI topography as prescribed boundary conditions should lead to relative small contribution to uncertainty. However, the *midHolocene* set the vegetation and aerosols prescribed same as *piControl* in Tier 1 simulations (Otto-Bliesner et al., 2017a) instead of mid-Holocene condition or using dynamic vegetation scheme. This set-up misses the 'Green Sahara' (e.g. Pausata et al., 2016) and real dust (e.g. Messori et al., 2019) that have significant effects on climate during the periods, which would produce further northward extension of the NAF if included in simulations, and reduce the underestimation in NAF expansion. There is substantially more proxy data available during the mid-Holocene than at earlier times. Prescribed GHGs used realistic values reconstructed from ice cores. Temporal and spatial uncertainty in proxy data is small in reconstructions of mid-Holocene climate. Nonetheless the coverage of MH reconstructions are concentrated in Europe while sparse or even missing in other regions especially in tropic and the SH (e.g. Bartlein et al., 2011). This means that the reconstruction could miss some important regional changes leading to biases in reconstructing global properties. The *midHolocene* ensemble cannot fully reproduce the magnitude of warming suggested by proxy data (see Chapter 3). This mismatch implies that there must be some important processes, at global and/or regional scales, that have not been included in the experimental design or that are missed or poorly presented in the physical schemes of models. The agreement in precipitation between model and data is complex, and *midHolocene* simulations are likely to underestimate the enhancement in North African monsoon (Harrison et al., 2015; Brierley et al., 2020), which is a longstanding issue in the development of the PMIP (Liu et al., 2021). Palaeoclimate simulations are usually performed with a low on resolution in order to reduce computing cost, which might fail to represent sub-grid scale features that are important in climate processes. Decision on prescribed boundary conditions in protocols could have impacts on the accuracy of producing palaeo climate (Ivanovic et al., 2021). Besides the limitation in resolution, biases in the *piControl* (in Chapter 2) suggest that models miss or poorly describe some key aspects of climate dynamics.

The Last Interglacial is a period similar to the mid-Holocene though with stronger orbital forcing (Figure 6.1). The design of *lig127k* protocol is similar to *mid-Holocene* as setting the orbital forcing and GHGs to 127 ka condition and prescribing other boundary conditions same as *piControl*. Therefore many uncertainties in the boundary conditions for the *midHoloce* experiment also apply to the *lig127k* experiment. The magnitude of uncertainties in those conditions set same as the *piControl* might even be larger than the *midHolocene*, as logically the difference between 127 ka and present should be larger than 6 ka. The availability of LIG proxy data is less than the MH and comes with large chronological uncertainty. Reconstructed LIG temperate anomalies are mainly SSTs, yet with large gaps in tropical Pacific Ocean. Temperature proxy data are missing over land. The coverage of reconstructed temperature is poor and misses many important regional features shown in the simulations. Meanwhile, though there is a new LIG precipitation compilation (Scussolini et al., 2019), large proportion of the data only qualitatively reflects the magnitude of precipitation change by category (strong, weak or no change) instead of giving quantitative change that could be used to evaluate the magnitude of mismatch.

Studies suggest that biases in the control simulation affect the climate change in response orbital forcing during the LIG and MH (e.g. Harrison et al., 2014; Ohgaito and Abe-Ouchi, 2009). This implies that bias in the CMIP6 *piControl* should also influence the response to the PMIP4-CMIP6 *midHolocene* and *lig127k* orbital forc-

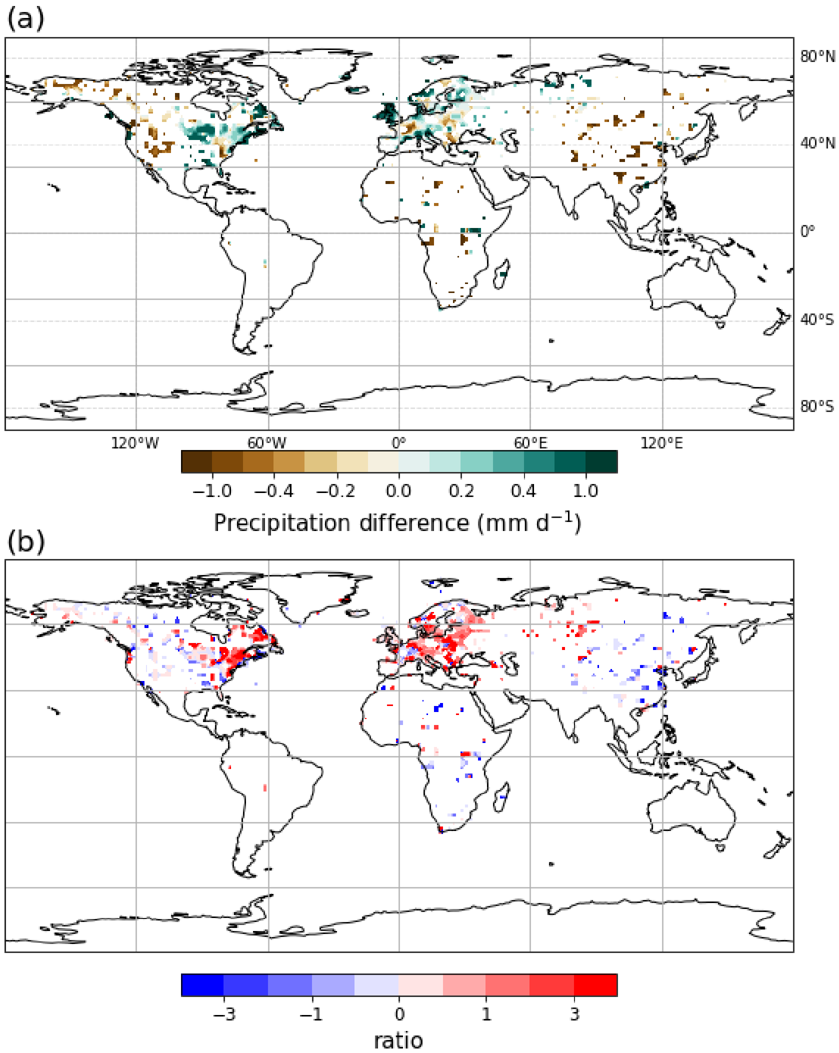

Figure 6.8: Comparison between the mismatch between the simulated and reconstructed anomalies (mismatch = (*midHolocene* - *piControl*) - reconstruction) and the bias in *piControl* simulations as compared to the observation (bias = *piControl* - GPCP observation) during the mid-Holocene. (a) The difference between the mismatch and the bias (mismatch - bias). (b) The ratio between the mismatch and the bias (mismatch / bias). See Chapter 2 for the details of the observation. See Chapter 3 for the details of the reconstruction.

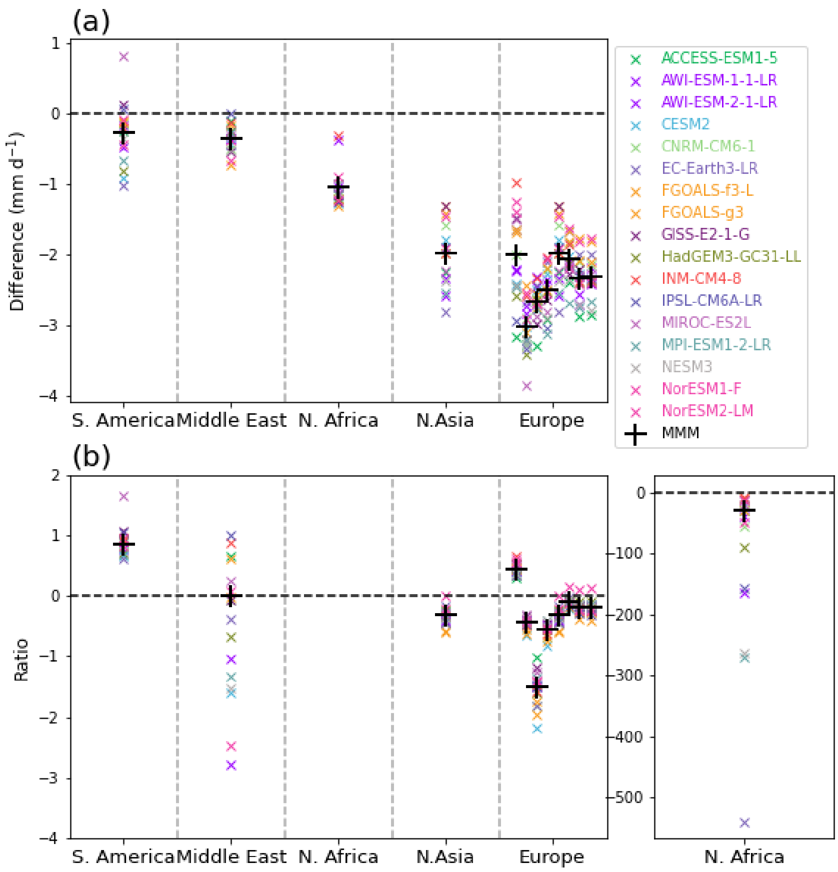

Figure 6.9: Site-level comparison between the mismatch between the simulated and reconstructed anomalies and the bias in *piControl* simulations as compared to the observation during the LIG. (a) The difference between the mismatch and the bias (mismatch - bias). (b) The ratio between the mismatch and the bias (mismatch / bias). Calculation follows the equations described in Figure 6.8 caption. See Chapter 2 for the details of the observation. See Chapter 4 for the details of the reconstruction.

ing. The PMIP4–CMIP6 models individual models do not have neither consistent cooler/warmer bias in temperature nor wetter/drier bias in precipitation across the globe. However, they are in general cooler than the observations, especially over NH land and oceans and at the poles during winter (Figures in Section 2.3.1 and Appendix A).

This suggests that models with a small bias in *piControl* do not necessarily simulate better MH and/or LIG climate. It also implies that other factors like component setup (e.g. dynamic vegetation, aerosols, and clouds) and prescribed setup (vegetation cover, aerosols) affect the regional direct and indirect response to orbital forcing. However, though AWI-ESM-1-1-LR, AWI-ESM-2-1-LR, MPI-ESM1-2-LR and NESM3 include interactive vegetation, they do not have smaller bias or produce better simulated climate change than other models. Further studies are required to explore the relationship between PI bias and simulated climate response, although it does suggest incorporating palaeoclimates in the model development of timing process might help.

Besides the uncertainty from modelling, the contribution of the uncertainties during mPWP is different to MH and LIG. The dominant forcing during mPWP is the high atmospheric CO_2 concentration. Unlike the *midHolocene* and *lig127k* experiments that prescribed many boundary conditions same as the *piControl*, the *midPliocene-eoi400* experiment (within PlioMIP2 Haywood et al., 2016b) prescribed boundary conditions (see Chapter 5) from Dowsett et al. (2016) based on mPWP proxy data PRISM4. Chronology becomes important to raise confidence in that proxy data are reconstructed at the same time slab. The reconstructed temperature anomalies during the mPWP are only available over the oceans, and with poor coverage (Foley and Dowsett, 2019; Dowsett et al., 2013). The gaps of coverage would raise difficulty in understanding the regional climate and building the pattern of change at global scale. Therefore, Dowsett et al. (2016) and Haywood et al. (2020) focused on comparison between model and data at sites. Site-level comparison is further affected by how the models could simulate regional-scale change. Haywood et al. (2020) suggest that the notable mismatch in the Benguela upwelling arises from low resolution climate models having difficulty in simulating the thermocline depth structure and cloud-surface temperature feedbacks in the region. The importance of the uncertainties varies for different periods.

Uncertainty in model structure and parameter (Figure 6.7) exists in all simulations. Though the latest state-of-art climate models are powerful tools to represent the physical, chemical and biological processes in climate system, they are still limited by the understanding of earth system and the possibility to represent the processes (Palmer and Bjorn, 2019; Bjorn and Sandrine, 2013), as well as the high computing cost (Shukla et al., 2010). Models raise uncertainty when downscaling to simulate regional response and the processes smaller than the size of a grid are parameterised. This would bring uncertainty in site-level data-model comparison, as proxy data reflect local change. The uncertainty from the design of the PMIP4 protocols and its magnitude varies across periods, but in general it depends on how the prescribed boundary conditions could represent the real condition at the time slice, which limited by our understanding of the process in the past and the quality of proxy data used as reference. For example, the data-model mismatch over the North African monsoon in the *midHolocene* and *lig127k* simulations highlighted the importance of including dynamic vegetation and the usage of MH and LIG vegetation cover. It deserves further development to appropriate schemes of dynamic vegetation in the next generation of climate models, including the use of Earth System models (ESMs), and include them in PMIP5 experiments.

Besides vegetation, aerosols such as dust is also an important factor, as shown by Chapter 5. Braconnot et al. (2021) studied the importance of dust forcing in the *midHolocene* simulations via three dust sensitivity experiments that applies no dust, the pre-industrial and the mid-Holocene dust distribution according to Albani et al. (2015). Their results highlighted the importance of dust patterns in simulating mid-Holocene climate change. The quality of proxy data is mainly limited by poor coverage and chronological uncertainty. Proxy distribution and the composition of the dataset also affects the reconstructed anomalies especially those global averaged anomalies that are computed by taking the average of site-level proxy data with the consideration of latitudial distribution.

So far, PMIP has focused on equilibrium simulations that produce global-scale spatial patterns of climate at a specific and precise time slice. However, reconstructions show the temporal evolution of climate at a sites. As discussed earlier, the difference between simulation and reconstruction raise challenge for PMIP. Transient simulations offer a chance to deal with the challenges. Though not analysed in this work, transient simulations have been completed and published in this cycle of CMIP for long-term and abrupt climate transitions. Ivanovic et al. (2021) highlight the importance and challenge in future PMIP with the development in the integration of transient simulations for addressing.

6.4 Limitations and future work

This thesis was not able to include all the analyses that were initially planned, and further work would help refine some aspects.

The ensemble mean analysis in this work was conducted by directly taking the average of all simulations in the ensemble, following the method used in earlier CMIP and PMIP analysis (e.g. Braconnot et al., 2000, 2007; Harrison et al., 2014). This computation is based on the assumptions that all models contributing to the ensemble are independent and their outputs are equally good. However, in reality, some models use the same or similar components (see Appendix A) or the simulations have differing levels of bias from observations. For example, FGOALS-f3-L and UofT-CCSM4 were developed based on CCSM4 and NorESM2-LR is built on the structure and many components of CESM2. This would rise the weight of CESM2 and its predecessors in computing the ensemble means. Touzé-Peiffer et al. (2020) questioned the ensemble analysis of CMIP outputs, as the interpretation of model results are often solely based on simulations without considering the schemes and parameterisation in models.

Combining multi-periods can help to examine whether a change is a common feature or is specific in response to the forcing driving the simulation, as demonstrated by the three warm periods analysed here. It would be possible to include additional warm periods, for example the early Eocene at roughly 50 million years ago with high atmospheric CO_2 concentration between 900 and 2500 ppmv (Lunt et al., 2012a, 2017, 2021). Burke et al. (2018) suggested that the climate under the Representative Concentration Pathway 4.5 (RCP4.5) produces the conditions similar to Pliocene by 2040s and then persists, and the climate under RCP8.5 produces the Pliocene-like conditions by 2030s and the Eocene-like by 2150s.

The analysis in this work was conducted based on monthly mean surface air temperature and precipitation rate and was focused on the changes in temperature, precipitation and monsoons characteristics. D'Agostino et al. (2019, 2020) show the benefit of more sophisticated analysis to learn the mechanisms and processes behind the changes. Future work could analyse other variables like surface wind, vertical velocity and/or latitude-averaged meridional flow over monsoon sectors, because they are important factors affecting monsoon features and/or their changes are associated with changes in monsoons. Relationships with other features such as ENSO (Brown et al., 2020) could be analysed as well.

The previous section mentioned the potential use of transient simulations. Including the published transient simulations should be really helpful to explain some data-model mismatch and expand the findings in this work (Ivanovic et al., 2021). A series of studies use transient simulations and improve our knowledge about long-term and abrupt change in the past and investigate the factor driving the change (Bader et al., 2020; Crétat et al., 2020). The well-agreed long-term cooling trend between 8 and 3 ka from marine proxies published by Marcott et al. (2013) was largely affected by the reconstructed SSTs from mid-latitudial North Atlantic Ocean. The cooling trend has been supported by proxy reconstructed GMST by Kaufman et al. (2020a) but is in contrast to the warming suggested by the surface temperature reconstructed based on pollen(Marsicek et al., 2018). Osman et al. (2021) resolve global surface temperature since 24 ka via paleoclimate data assimilation combining both climate model simulations and proxy data to produce proxy-constrained full-field reanalysis of surface temperature change that show steady warming during the Holocene contrast to Marcott et al. (2013). Bader et al. (2020) produce transient simulations covering 6ka to 1850CE via model MPI-ESM. Their results mode suggest that the cooling in Marcott et al. (2013) was biased towards the summer season as the reconstructed temperature anomaly from marine proxy is similar to the global mean temperature computed from monthly maximum instead of monthly mean. Besides investigating the reason behind data-model mismatch, transient simulations could also be used to examine which forcing the climate change is sensitive to. Braconnot et al. (2019a) characterise the multiscale variability of Indian and West African monsoon during the last 6 thousand years. Their results show that orbital forcing drove the trying in Indian and West African monsoon through the Holocene, while the Indian monsoon is more sensitive to change in GHGs. Crétat et al. (2020) studied the Indian monsoon in transient global simulations, confirmed the finding of Indian monsoon in Braconnot et al. (2019a), and suggested that ENSO and IOD drove the variability in the Indian monsoon at interannual-to-decadal scale through the Holocene.

6.5 Conclusion

This chapter brings together the analyses performed on individual periods. A comparison between the response to various orbital forcings in the *midHolocene* and *lig127k* simulations provides a chance to examine how climate would respond to two different radiative forcing changes with other forcings similar to those present. Both the *midHolocene* and *lig127k* ensembles show strong seasonal variations relative to the *piControl* in response to various orbital forcing. As expected, both ensembles produce warming in NH high latitudes during boreal summer and increased seasonality. Monsoons are enhanced in the NH and weakened in the SH in both ensembles. The magnitude of changes in *lig127k* simulations is greater that in the *midHolocene*, agreeing with the stronger orbital forcing during LIG than MH. Both ensembles produce the NAF expansion and the relationship between the poleward extension in the *lig127k* and *midHolocene* gives a linear fit.

The patterns of temperature, precipitation and monsoon response in the *midPliocene-eoi400* simulations are different to those in response to orbital forcings, showing global warming and polar amplification in both hemispheres throughout the year and enhanced regional monsoons except NAMS. All the three ensembles underestimate the polar amplification suggested by proxy data.

The contribution of different sources of uncertainty varies during different periods. The quality of the simulations in all the three experiments are influenced by the possibility of climate models to represent the processes in climate. For MH and LIG, uncertainties in prescribed boundary condition like not using appropriate vegetation dominates the uncertainty raising from modelling. Poor spatial coverage of proxy data limits the strength of the conclusion. For the mPWP, as well as these uncertainties, reconstruction chronology is also important. For this work, the assumptions applied in the ensemble analysis ignore the common history of in models. Evaluation of model performance is limited by the coverage of proxy data. The last two sections also give potential improvements, such as applying more realistic boundary condition and including dynamic vegetation in the next generation of PMIP. These two sections also highlight the benefit of involving transient simulations.

Chapter 7

Conclusion

The climate in past warm periods was different from present-day or historical period, upon which climate model are trained. This offers the chance to test the performance of climate models to the out-of-sample boundary conditions and forcings (e.g. Harrison et al., 2014, 2015; Schmidt et al., 2014a). PMIP4 is an endorsed model intercomparison project of CMIP6 that has contributed to the assessment in several chapters of the latest IPCC AR6 (IPCC, 2021d; Gulev et al., 2021; Eyring et al., 2021; Forster et al., 2021; Douville et al., 2021; Fox-Kemper et al., 2021). The previous chapters have analysed the climate response (focused on monsoons) to different forcings based on the simulations of three PMIP4 experiments – (*mid-Holocene*, *lig127k* and *midPliocene-eoi400* (also called PlioMIP2 in the literature). This chapter summarises the progress made within this dissertation.

This work applied an analysis process (Chapter 2) that can be used as a general method for ensemble analysis based on PMIP/CMIP simulations that have been uploaded onto the Earth System Grid Federation (ESGF; Balaji et al., 2018) stored in a CMIP standard format. The whole process from downloading files from the ESGF to plotting the final analysis and the relevant scripts have been published in the peer-reviewed journal Geoscientific Model Development as Zhao et al. (2022). The chapter also discussed the bias in the *piControl* simulations which indicates the challenge to sufficiently represent the climatic processes in models and how these biases could potentially explain the mismatch in the data-model comparison.

The mid-Holocene climate response to orbital forcing has been an experiment since the beginning of the PMIP (Joussaume et al., 1999) and kept contributing to the evaluation model performance in the last three major assessments of the IPCC (Jansen et al., 2007; Flato et al., 2013; Eyring et al., 2021). The results of the PMIP4-CMIP6 *midHolocene* simulations (Chapter 3) demonstrate expected response in annual and seasonal temperature and precipitation change responding to the seasonal variation in insolation anomalies induced by orbital forcing, enhanced monsoons in the Northern Hemisphere and weakened monsoons in Southern Hemisphere in both experiments, agreeing with the findings in preceding the PMIPs. However, the ensemble underestimates some climate features such as Arctic warming, the northward extension of the North African monsoon and are not able to fully reproduce the precipitation change over Europe. Mismatches between reconstructions and simulations could be explained by the inappropriate parameterisation schemes in models including vegetation, ocean circulation or melt water and/or the boundary conditions described in the protocols. As the *midHolocene* experiment has been included in the last three phases of the PMIP, it offers a good chance to evaluate the improvements between the protocols of different PMIP phases, and the generations of climate models if their previous generations have contributed to previous PMIP *midHolocene* ensembles. Chapter 3 gave a comparison between the PMIP3-CMIP5 and PMIP4-CMIP4 *midHolocene* ensembles. Results found no significant difference between the two generations. Those PMIP4-CMIP6 models having previous generations contributing to the PMIP3 (PMIP3-CMIP5 models) do not necessary perform better then the previous generations.

The PMIP4-CMIP6 *lig127k* experiment was designed to address the climate responses to a stronger orbital forcing than the *midHolocene* experiment. The results of *lig127k* simulations (Chapter 4) show strong seasonal changes in temperatures and precipitation. Monsoons are enhanced in the NH during boreal summer and weakened in the SH during austral summer, in line with the change in insolation. The patterns of change are similar but stronger than those in the *midHolocene* simulations (see Chapter 6 for a comparison). Analysis in Chapter 4 has different focus to the Chapter 3, which aimed to address how the quality of model's *lig127k* simulation relates to its climate sensitivity, and if models perform better with the inclusion of dynamic vegetation. Results show that models with a high climate sensitivity do not capture the last interglacial climate than those with low one. The four models with dynamic vegetation do not perform better than others.

The results in Chapter 5 demonstrate warming, polar amplification and reduced temperature gradients in the *midPliocene-eoi400* simulations, which also show wetter tropics, drier subtropics and an enhancement in all regional monsoons except over North America. However, the persistent mismatch between simulations and reconstructions suggests that some mechanisms behind the mPWP warming remain unknown. Idealised experiments with different aerosol scenarios demonstrate that aerosol forcing could be a source of uncertainty. Removal of aerosol effects also causes asymmetric changes in precipitation and it has a stronger effect on annual and seasonal precipitation over the tropics and subtropics than the mPWP boundary conditions. Precipitation increases over eastern and southern Asia and western Africa during monsoon seasons after removing the aerosols. Results highlight the potential importance of aerosol uncertainty in simulating the mPWP climate.

Chapter 6 discussed the climate response across different time periods firstly. The *lig127k* simulations show stronger signal than the *midHolocene*, which is in line with the stronger orbital forcing during the LIG. Response in the *midPliocene-eoi400* simulations are different to the *midHolocene* and the *lig127k* with different mechanisms. Orbital forcing change the dynamic compoent in monsoon, which high CO_2 alters thermodynamics and net flux. All the three ensembles in this work show mismatch between model and data. The contribution of different source of uncertainty varies during different periods. For MH and LIG, uncertainties in prescribed boundary condition like not using appropriate vegetation dominates the uncertainty raising from modelling. Poor spatial coverage of proxy data limits the results. For the mPWP, besides these uncertainties, reconstruction chronology is also important. Improvements in the next generation of PMIP could be done by applying more realistic boundary condition and including dynamic vegetation. Involving transient simulations could be another improvement. For this work, including more paleo periods and more variables should be able to improve the finding in this work. Despite those limitations, this thesis, for the first time, combines such a large number of PMIP4 simulations of three past warm periods to improve our understanding of palaeo-monsoons, and to evaluate the performance of current state-of-art models. It provides an integrated picture of past monsoon behaviour across these latest palaeoclimate simulations. The findings from this thesis, combined with future work, improve our understanding of monsoon forced responses and could help to ensure that the next generation of climate models provides more confident projections of future climate change.

Appendix A

Chapter 2 SI

A.1 PMIP3-CMIP5 model description

A.1.1 BCC-CSM1.1

BCC-CSM1.1 is a GCM developed by the Beijing Climate Center at China Meteorological Administration. This model uses BCC_AGCM2.1 with prescribed aerosol (Wu, 2012) as its atmospheric component with a T42 resolution with 26 vertical levels. The land surface component is BCC_AVIM1.0 (Wu, 2012), and the sea ice component uses the GFDL Sea Ice Simulator (SIS; Winton, 2000). The ocean component MOM4-L40 (Griffies et al., 2005) includes ocean biogeochemistry (BGC), and uses a tripolar grid with an 1° resolution in the meridional direction in the tropics enhanced to 1/3° at the Equator. Detailed description of the model can be found in Xin et al. (2013).

A.1.2 CCSM4

CCSM4 (Gent et al., 2011) was developed by the US National Center for Atmospheric Research (NCAR) along with contributions from the academic community. It consists of an atmospheric component, CAM4, with interactive aerosols (Neale et al., 2010), a land component, CLM4, (Oleson, 2010), the ocean component is a modified version of POP2 (Danabasoglu et al., 2012) and the sea ice component is CICE4 with modifications as well (Holland et al., 2012). CAM4 uses an atmospheric resolution of 0.9° by 1.25° with 27 vertical levels. CCSM4 has an oceanic resolution of nominal 1° (1.125° in longitude and 0.27-0.64° in latitude) with 60 vertical levels. Gent et al. (2011) provides a description of CCSM4 in detail.

A.1.3 CNRM-CM5

CNRM-CM5, developed by the CNRM-GAME and CERFACS institutes in France (Voldoire et al., 2013), consists of the ARPEGE-Climat version 5.2 with prescribed aerosol as its atmospheric component that operates on a T127 triangular truncation within the model (equivalent to 1.4° by 1.4°) with 31 levels (Voldoire et al., 2013), the SURFEX interface as the ocean-atmospheric fluxes and land surface component (ISBA scheme; Voldoire et al., 2013), TRIP as the river routing and water discharge component, NEMO v3.2 as the ocean component using a resolution of 2.1° with 42 levels (Madec, 2008) and GELATO v5 for its sea ice (Salas-Melia, 2002; Voldoire et al., 2013). Component models are coupled through OASIS v3 for every 24 hours, and a detailed description can be found in Voldoire et al. (2013).

A.1.4 CSIRO-MK3.6.0

The Queensland Climate Change Centre of Excellence and Commonwealth Scientific and Industrial Research Organisation developed CSIRO-MK3.6.0 model (Rotstayn et al., 2012). As described in Gordon et al. (2002) and Gordon et al. (2010), CSIRO-MK3.6.0 includes components of atmosphere with interactive aerosols , land surface , sea ice and a modified MOM2.2 as its ocean component. The atmospheric component uses a resolution of spectral T63 (1.875° x 1.875°) with 18 vertical levels, and the ocean component uses 0.9° x 1.875° with 31 levels.

A.1.5 CSIRO-MK3L v1.2

CSIRO-Mk3L v1.2 (Phipps et al., 2012) uses a reduced resolution of the atmosphere, land and sea ice models used by the CSIRO Mk3 coupled model, and the ocean model taken from the CSIRO Mk2 coupled model. It was developed primarily for millennial-scale climate simulation and palaeoclimate research. The atmospheric and ocean resolution are both 5.625° and $\sim$ 3.18° in horizontal direction with 18 vertical levels in the atmosphere and 21 vertical levels in the ocean.

A.1.6 EC-Earth2.2

EC-Earth was developed based on the operational seasonal forecast system of the European Centre for Medium-Range Weather Forecasts (ECMWF) (as described in detail in Hazeleger et al., 2012). The model has the IFS c31r1 atmosphere model with prescribed aerosols (Hazeleger et al., 2012). The ocean model is NEMO_ecmwf, which uses a resolution of 1° tripolar curvilinear grid with 30 vertical levels (Hazeleger et al., 2012). HTESSEL (Balsamo et al., 2009) and LIM2 (Fichefet and Maqueda, 1999) are included as the land surface and sea ice components.

A.1.7 FGOALS-g2

The Flexible Global Ocean–Atmosphere–Land System model was developed by the Institute of Atmospheric Physics at Chinese Academy of Sciences (CAS) and Tsinghua University in China. Detailed description can be found in Li et al. (2013a). This model consists of GAMIL2 (Li et al., 2013a) as the atmospheric component with a semi-interactive aerosols, CLM3 (Oleson, 2010) as the land component, the LASG/IAP Climate System Ocean Model version 2 (LICOM2; Liu et al., 2012a) as the oceanic component and CICE4-LASG (Liu, 2010) as the sea ice component. The atmospheric resolution is 2.8125° x 2.8125° with 26 layers, and the oceanic resolution is 1° refining down to 0.5° in the tropical region with 30 levels.

A.1.8 FGOALS-s2

FGOALS-s2 is the spectral version of the FGOALS model developed by the Institute of Atmospheric Physical at Chinese Academy of Sciences. Detailed description can be found in Bao et al. (2010, 2013). Its atmospheric component uses SAMIL2.4.7 with semi-interactive aerosol (Liu et al., 2013; Bao et al., 2010), and has a resolution of 2.81° lon x 1.66° lat (R42) with 26 vertical layers. This model uses the same oceanic component as FGOASL-g2 (Lin et al., 2013) but with IAP-OBM for ocean BGC (Xu et al., 2012). The sea ice component is Community Sea Ice Model version 5 (CSIM5; Briegleb et al., 2004).

A.1.9 GISS-E2-R

GISS-E2-R is one of the long running series of models developed by the NASA Goddard Institute for Space Studies in the USA (Schmidt et al., 2014b). The GISS ModelE2 version was developed from the ModelE version (Schmidt et al., 2006). Schmidt et al. (2014b) documented the changes in ModelE2 to the previous ModelE. ModelE2 has three versions of AGCMs (designed to fit the physics_index (1, 2 and 3) in the CMIP5) and two OGCMs. GISS-E2-R model is designed by ModelE2 AGCM being coupled to Russell OGCM (Schmidt et al., 2014b). The NINT model version of the AGCM, identified as *p1* (physics_index = 1) in the CMIP5 archive, has prescribed the mass of radiatively active atmospheric constituents and the magnitude of the aerosol indirect effect (Miller et al., 2014). The land surface model, consisting of soil, canopy and snowpack, was developed from Rosenzweig and Abramopoulos (1997) by applying new algorithms for the underground runoff computation, having a new vegetation canopy conductance scheme and implementing a three-layer snow model (Schmidt et al., 2014b). GISS-E2-R uses a ocean resolution of 1° lat by 1.25° lon with 32 levels, and a atmospheric resolution of 2° lat by 2.5° lon with 40 vertical levels.

A.1.10 HadGEM2-CC

HadGEM2-CC was developed by the UK Met Office Hadley Centre (Collins et al., 2011; Martin et al., 2011). The model consists of the land surface component (Essery et al., 2003), the sea ice component (McLaren et al., 2006), the atmospheric component HadGAM2 (Davies et al., 2005) with interactive aerosol (Bellouin et al., 2011) and atmospheric chemistry (Martin et al., 2011), and the oceanic component

(Johns et al., 2006) including ocean BGC (Halloran, 2012). The atmospheric resolution is N96, 1.25° x 1.875° (lat x lon) (Johns et al., 2006). Both the atmosphere and ocean models have 60 vertical levels.

A.1.11 HadGEM2-ES

HadGEM2-ES is another version of HadGEM2 (Collins et al., 2011) that has similar design as HadGEM2-CC, but it includes enhanced atmospheric chemistry as described in O'Connor et al. (2009). Both atmospheric and oceanic resolutions are also different from HadGEM2-CC. HadGEM2-ES uses the same horizontal resolution in atmosphere in HadGEM2-CC but reduces the vertical levels to 38 (Davies et al., 2005). The horizontal oceanic resolution is N180, 1° between 30° and 90°N/S and the meridional resolution is increased to 1/3° at the Equator. The number of vertical layers is 40.

A.1.12 IPSL-CM5A-LR

IPSL-CM5A-LR is the low resolution version of IPSL-CM5A developed by the Institute Pierre Simon Laplace (IPSL) in France (Dufresne et al., 2013). It includes LMDZ5A (Hourdin et al., 2013) with semi-interactive aerosol as its atmospheric component, and uses a resolution of 1.9° x 3.75°. This model also includes the land component ORCHIDEE (Krinner et al., 2005), the ocean component (Madec, 2008) using a resolution of 2 x 2-0.5° ORCA2 with 31 vertical levels with ocean BGC (PISCES; Aumont et al., 2003) and the LIM2 sea ice component (Fichefet and Maqueda, 1999) model.

A.1.13 MIROC-ESM

MIROC-ESM was developed by University of Tokyo, the National Institute for Environmental Studies, and the Japan Agency for Marine-Earth Science and Technology (Watanabe et al., 2011). It uses MIROC-AGCM as the atmospheric component (Watanabe et al., 2008) and SPRINTARS for aerosol (Takemura et al., 2005, 2009).

The land component uses MATSIRO (Takata et al., 2003). COCO3.4 (Hasumi, H., Emori, 2004) is used as the ocean and sea ice components and NPZD-type (Schmittner et al., 2005) as oceanic BGC. The atmospheric resolution uses T42 (2.8125 x 2.8125°) with 80 levels, and the oceanic resolution uses 1.4° (in zonal) x 0.5 - 1.4° (in meridional) with 44 levels.

A.1.14 MPI-ESM-P

MPI-ESM-P (Giorgetta et al., 2013) was developed by Max Planck Institute for Meteorology in Germany. This model uses ECHAM6 (Stevens et al., 2013) with prescribed aerosol as its atmosphere model, JSBACH (Reick et al., 2013) as the land surface model, MPIOM (Jungclaus et al., 2013) as the oceanic component with HAMOCC ocean BGC (Ilyina et al., 2013). Sea ice is also included (Notz et al., 2013). The atmospheric resolution is approximately 1.8° (T63) with 47 vertical levels, and the oceanic resolution is 1.5° in average (GR15) with 40 vertical levels.

A.1.15 MRI-CGCM3

MRI-CGCM3 (Yukimoto et al., 2012), developed by Meteorological Research Institute (MRI) in Japan, consists of the atmospheric component MRI-AGCM3.3 with MASINGARmk-2 scheme to capture the aerosols (Yukimoto et al., 2011), the land component HAL (Yukimoto et al., 2011), and the oceanic component MRI.COM3 (Tsujino et al., 2011) with sea ice included. This model uses a atmospheric resolution of TL159 with 48 layers and a oceanic resolution of 1x0.5 with 50 vertical levels plus a bottom boundary layer.

A.2 PMIP4-CMIP6 model description

A.2.1 ACCESS-ESM-1-5

ACCESS-ESM1.5 (Ziehn et al., 2020) is a global circulation model developed by the Bureau of Meteorology and CSIRO (CSIRO) in Australia. The atmospheric component is UM 7.3, the 7.3 version of the UK Met Office Unified Model (UM; Martin et al., 2010) with a configuration which is similar to 'GA1' (Hewitt et al., 2011). The Community Atmosphere Biosphere Land Exchange (CABLE) model version 2.4 (Kowalczyk et al., 2013) is used as the land surface model with BGC implemented by using the CASA-CNP module (Wang et al., 2010). ACCESS-ESM1.5 uses fixed vegetation with interactive LAI and prescribed aerosol. The sea ice model is CICE4.1 (Hunke and Lipscomb, 2010). The ocean model is the National Oceanic and Atmospheric Administration (NOAA)/Geophysical Fluid Dynamics Laboratory (GFDL) Modular Ocean Model (MOM), version 5 (Griffies, 2012) with Whole Ocean Model of BGC And Trophic-dynamics (WOMBAT) to simulate carbon cycle (Kowalczyk et al., 2016). The atmospheric resolution is 1.8758° by 1.258° (lon x lat) with 38 vertical levels, and the oceanic resolution is nominal 1°having higher latitudinal resolution near the Equator at 0.338° and over the Southern Ocean at $\sim$ 0.4° at 70°S with 50 layers. Notably, it uses a solar constant of 1365.65 Wm^{-2} which is different from 1360.75 Wm^{-2} prescribed in the DECK protocols (Eyring et al., 2016).

A.2.2 AWI-ESM-1-1-LR

AWI-ESM-1-1-LR is the modified low resolution version of AWI's Climate Model with dynamic vegetation (Sidorenko et al., 2015; Rackow et al., 2018) . It was developed by the Alfred Wegener Institute, Helmholtz Centre for Polar and Marine Research (AWI) who are contributing a model to CMIP for the first time. It consists of three component models: the atmosphere model, the sixth generation of ECHAM (ECHAM6; Stevens et al., 2013) developed by the Max Planck Institute for Meteorology in Hamburg; the sea-ice ocean model, the Finite Element Sea ice-Ocean

Model version 1.4 (FESOM1.4 Wang et al., 2014c), and the coupler OASIS3-MCT (Valcke, 2013) coupling FESOM and ECHAM6 for every hour. AWI-ESM-1-1-LR uses an atmospheric resolution of 1.875° with 47 levels. Its oceanic resolution uses 126859 wet nodes with 46 vertical levels instead of regular grids. Detailed description of this model can be found in Sidorenko et al. (2015) and Rackow et al. (2018).

A.2.3 AWI-ESM-2-1-LR

AWI-ESM-2-1-LR (Sidorenko et al., 2019) follows the formulation of AWI-ESM-1-1-LR (Sidorenko et al., 2015; Rackow et al., 2018) but with an updated version of the sea ice-ocean model FESOM that has been updated to version 2.4 (Scholz et al., 2019). BICUBIC option (a bicubic interpolation) in OASIS3-MCT is used in AWI-ESM-2-1-LR, which is a more expensive option of the coupler (Rackow et al., 2019). The model grids are the same between the two AWI models.

A.2.4 CESM2

The Community Earth System Model version 2 (CESM2; Danabasoglu et al., 2020) is developed by the NCAR as an updated version of CESM1 (Hurrell et al., 2013) which was developed from CCSM4 (Section 2.1.1.2). CCSM4 were developed into an ESM (CESM1; Hurrell et al., 2013) by adding capabilities related to BGC processes and aerosol effects. According to the documentation in Danabasoglu et al. (2020), the atmospheric model CAM6 in CESM2 uses the same Finite Volume dynamical core as in CESM1 and CCSM4, but its parameterisation have all been updated except the radiation model. The atmospheric resolution uses 1.25° x 0.9° (lon x lat) with 32 vertical levels. The land model has been updated to CLM5 (Lawrence et al., 2019) with notable changes and potential natural land cover. The ocean component model remains as POP2 (Smith et al., 2010) but with improvements in both the physical parameterisation and numerical methods. The sea ice model CICE has been improved to CICE5 (Hunke et al., 2015) with more new physical options. The oceanic girds have 60 vertical levels, and the horizontal resolution varies from the 0.27° at the Equator which then increases monotonically to 32°S reaching 0.53°in the SH. The horizontal oceanic resolution in the NH high latitudes is finest in the NW Atlantic Ocean at 0.38°and is coarsest in the NW Pacific Ocean at 0.64°.

A.2.5 CNRM-CM6-1

CNRM-CM6-1 is an updated version of CNRM-CM5 (Section 2.1.1.3) with major updates in atmosphere and land surface (Voldoire et al., 2019). Compared to its predecessor, the atmosphere and land surface models have been updated to ARPEGE-Climat v6.3 (Voldoire et al., 2019) and SURFEX v8.0 with fully revised physical parameterisation. Other component models have limited improvements (Voldoire et al., 2019), as updated to the most resent version with only limited changes in the choice of parameterisation. It uses NEMO3.6 (Madec and the NEMO Team, 2016) as the oceanic component and GALATO v6 as the sea ice component. Component models are coupled via OASIS3-MCT software (Craig et al., 2017). The atmospheric resolution uses Tl127 with 91 vertical levels, and the oceanic resolution is eORCA1 horizontal grid with 71 levels.

A.2.6 EC-Earth3-LR

EC-Earth3 (Döscher et al., 2021) has been developed from EC-Earth2 (Section 2.1.1.6). Compared to its predecessor, EC-Earth uses updated LIM3 as the sea ice component, NEMO3.6 as the oceanic component in which the BGC processes are provided by PISCES. The Greenland ice sheet can be modelled by the ice sheet model PISM as an option. Atmospheric and land components in EC-Earth3 are covered by ECMWF's IFS cycle 36r4. TM5 describes the processes in aerosols and chemistry. LPJ-GUESS (Smith et al., 2014) simulates land use, terrestrial BGC and dynamic vegetation. EC-Earth3-LR uses an atmospheric resolution of T159L62 (125 km) and an oceanic resolution of ORCA1L75 (1°).

A.2.7 FGOALS-f3-L

FGOALS-f3-L is the low version of finite-volume of the FGOALS model (He et al., 2020). The atmospheric component model is the Finite-volume Atmospheric Model version 2.2 (FAMILv2.2; Bao et al., 2013; Bao and Li, 2020). The oceanic model is LICOM version 3 (Liu et al., 2012a; Li et al., 2017). The land, sea ice and coupler models are CLM4.0 (Oleson, 2010), CICE4.0 (Hunke and Lipscomb, 2010) and CPL7 as used in CCSM4 (Craig et al., 2012; Gent et al., 2011). The atmospheric resolution is 1° by 1° with 32 vertical levels, and the oceanic uses a tripolar grid (1° × 1°) with 30 layers.

A.2.8 FGOALS-g3

FGOALS-g3 (Li et al., 2020) has been updated from FGOALS-g2 (Section 2.1.1.7) with a branch of improvements. As described in Li et al. (2013b), the atmosphere model has been updated from GAMIL2 to GAMIL3 with improvements in several aspects such as resolution and parameterisation schemes. Its land model uses CAS-LSM which has been developed from CLM4.5 with improvements in groundwater (Zeng et al., 2016), frozen soil parameterisation (Liu et al., 2019) and anthropogenic nitrogen discharge (Gao et al., 2016). LICOM has been updated to version 3 by adding a set of mixing-related schemes and replacing the coordinate structure by arbitrary orthogonal curvilinear coordinate. CICE4-LASG (Liu, 2010) is still used as the sea ice model. Components are coupled by CPL7 (Craig et al., 2012) and the Community Coupler Version 2 developed by Tsinghua University (C-Coupler2; Liu et al., 2018). The atmospheric resolution now has been increased to $\sim 2°$ (180×80) with 26 layers. The oceanic resolution uses a tripolar grid and has 360×218 horizontal grid points with 30 layers for the low resolution version used in CMIP6.

A.2.9 GISS-E2-1-G

As described in Kelley et al. (2020), GISS-E2-1-G has seen many changes since GISS-E2-R (Section 2.1.1.9) including fixing bugs, updating input files and replacing or structurally varying some parameterisation. In the atmosphere model, updates has been made in radiative transfer, clouds, convection, boundary layers, atmospheric composition and chemistry. The ocean model is coupling to GISS Ocean v1 (GO1) and has updates in the parameterisation of mesoscale eddies and in vertical mixing a high-order advection scheme and finer upper-ocean layering. Groundwater and vegetation structure have been updated in the land model since the last generation. Resolutions remain unchanged except the ocean layers have increased to 40 from 32.

A.2.10 HadGEM3-GC31-LL

The Global Coupled 3 (GC3) configuration of the Met Office Unified Model (HadGEM3-GC31; Williams et al., 2018) is an update version of GC2 that was developed from HadGEM2-AO. The model consists of Global Atmosphere 7 and Global Land 7 (GA2 and GL7; Walters et al., 2019), Global Ocean 6 (GO6; Storkey et al., 2018), and Global Sea Ice 8 (GIS8; Ridley et al., 2018). Compared to earlier versions, GC3 has revised all of the existing parametrisation schemes and included new models and schemes (Williams et al., 2018). Atmospheric resolution has been updated to 1.25° lat by 1.875° lon with 85 vertical levels, and the oceanic resolution has been updated to ORCA025 (0.25°) with 75 levels (Williams et al., 2018).

A.2.11 INM-CM4-8

INM-CM48 (Volodin et al., 2018) is developed by the Institute of Numerical Mathematics of the Russian Academy of Sciences in Russia. An earlier version INM-CM4.0 was included in CMIP5 (Volodin et al., 2013). INM-CM4-8 is designed for long palaeoclimate experiments, which has similar physical processes as its later version INM-CM5 (Volodin et al., 2017) but with a lower upper boundary.

Compared to INM-CM4.0, INM-CM4-8 includes an aerosol block that has the concentration and the radiative properties of 10 types of aerosol calculated interactively, and meanwhile, the large-scale condensation has been updated (Volodin et al., 2018). In the oceanic component, implicit schemes for transfer equations and the dependence of the background coefficient on depth have been improved and introduced (Volodin et al., 2018). The atmospheric resolution is 2° lon by 1.5° lat with 21 vertical levels, and the oceanic resolution is 1° lon by 0.5° lat with 40 levels. This model has the lowest climate sensitivity amongst the CMIP6 models at 2.1°C (Volodin et al., 2018, Table 2.2).

A.2.12 IPSL-CM6A-LR

IPSL-CM6A-LR (Boucher et al., 2020) is updated from IPSL-CM5A-LR (Hourdin et al., 2013). The atmosphere model has been updated to LMGZ6A with updates in convection, radiation, cloud cover and cloud water content (Boucher et al., 2020). The ocean component is NEMO v3.6 and the updates are described in Boucher et al. (2020). Major components in the ocean model include the ocean physics NEMO-OPA (Gurvan et al., 2017), the sea ice dynamics and thermodynamics NEMO-LIM3 (Rousset et al., 2015) and the ocean BGC NEMO-PISCES (Aumont et al., 2015). Carbon cycle, vegetation heterogeneity, soil freezing and soil hydrology scheme have been updated in the version 2.0 of the land model ORCHIDEE (Boucher et al., 2020). Components are coupled by OASIS3-MCT coupler. The model has an atmospheric resolution of 2.5° × 1.3° with 79 vertical layers. The oceanic resolution uses eORCA1 with 75 layers.

A.2.13 MIROC-ES2L

MIROC-ES2L (Hajima et al., 2020) is an improved version of MIROC-ESM (Section 2.1.1.13) as the Earth System version 2 for Long-term simulations, with components having been updated to later versions in which land BGC (VISIT) and oceanic BGC (OECO2) being the main modifications (Hajima et al., 2020). Improvements in BGC include explicit C-N interaction on land accounting for controlling plant growth and carbon sink, BGC cycles in ocean controlling oceanic primary productivity and N cycle coupled between land and ocean through river discharge (Hajima et al., 2020). MIROC-ES2L uses resolutions of approximately 2.8° with 40 levels in atmosphere and 1° (and becoming finer near the Equator) with 62 vertical levels in ocean.

A.2.14 MPI-ESM1.2-LR

MPI-ESM1.2 (Mauritsen et al., 2019) is updated from MPI-ESM (Section 2.1.1.14) as the component models have been updated to their last versions: ECHAM6 (Stevens et al., 2013) to ECHAM6.3, JSBACH (Reick et al., 2013) to JSBACH3.2, MPIOM (Jungclaus et al., 2013) and HAMOCC (Ilyina et al., 2013) to MPIOM1.6 and HAMOCC6, and the sea ice model being able to have fully activated melt ponds. Mauritsen et al. (2019) documents the updates in parameterisation, which are applied to resolve the bugs in MPI-ESM. Both atmospheric and oceanic resolutions remain the same as those used in MPI-ESM, i.e. approximately 1.8° with 47 levels and 1.5° with 40 levels, respectively.

A.2.15 MRI-ESM2.0

MRI-ESM2.0 (Yukimoto et al., 2019) is an update version from previous version MRI-CGCM3 (Section 2.1.1.15) and MRI-ESM1. It uses the same horizontal atmospheric resolution as MRI-CGCM3 but has increased vertical levels to 80 from 48. The oceanic resolution is nominal 1° by 0.5° (longititude by latitude) with 61 levels. Major improvements include a new stratocumulus cloud scheme being able to reduce errors in radiative properties and removing some temperature bias shown in the previous models (Yukimoto et al., 2019).

A.2.16 NESM3

NESM3 (Cao et al., 2018) is developed by Nanjing University of Information Science and Technology in China. NESM3 consists of the atmosphere component ECHAM6.3 (Stevens et al., 2013), the ocean component NEMO3.4 (Madec, 2008), the sea ice component CICE4.1 (Holland et al., 2012) and the coupler OASIS3-MCT3.0 (Craig et al., 2017). The land surface component JSBACH (Raddatz et al., 2007) interacts with the atmosphere. Detailed description and improvements since previous version can be found in Cao et al. (2018). NESM3 uses an atmospheric resolution of 1.875° with 47 levels. The oceanic resolution is 1° of longitude and a variable mesh of 13 to 1° of latitude from the Equator to pole with 46 levels.

A.2.17 NorESM1-F

NorESM1-F (Guo et al., 2019) is a fast version (2.5 times faster) of NorESM-M that participated in the CMIP5 generation. The atmospheric aerosol chemistry is prescribed, and a tripolar horizontal grid configuration of ocean–sea ice is applied to increase the ocean–sea ice component time steps (Guo et al., 2019). NorESM-M was developed based on CCSM4 Bentsen et al. (with the differences described in detail in 2013). NorESM1-F uses an atmospheric resolution of $\sim 2°$ with 26 vertical layers, and a nominal 1° with 53 vertical layers for the ocean and sea ice configuration.

A.2.18 NorESM2-LM

NorESM2 (Seland et al., 2020) is built on the structure and many components of CESM2 (Danabasoglu et al., 2020) but with several modifications especially in atmosphere and ocean models. NorESM2's atmosphere model, CAM6-Nor, has altered aerosol life cycle, altered aerosol-cloud interactions, and some modifications related to energy and flux (with details described in Seland et al., 2020). CAM-Nor uses an atmospheric resolution of $\sim$2° with 32 hybrid-pressure layers. The ocean model is BLOM , developed based on the MICOM in NorESM1, that couples iHAMOCC as the ocean carbon cycle. Parameterisation related to vertical shear-induced mixing, eddy-induced transport etc has been updated since NorESM1-M and they are described in Seland et al. (2020). The oceanic grids have 53 layers same as NorESM1, but the horizontal resolution is 1° longitude by 0.25° latitude at the Equator and gradually approaching more isotropic grid cells at higher latitudes.

A.2.19 UofT-CCSM4

UofT-CCSM4 (Chandan and Peltier, 2017) is the University of Toronto version of CCSM4, which is slightly modified from CCSM4 (Gent et al., 2011) in the ocean model by running on the displaced pole grid in which the poles of the grid are positioned over Greenland and Antarctica, and therefore the ocean does not contain any grid singularities. The initial motivation of UofT-CCSM4 having different choice of mixing schemes in ocean model was that the turbulent mixing during Pliocene was different from modern as having changes in coastlines, bathymetry and the elevations of the mid-ocean ridges that had effects on turbulent mixing (Chandan and Peltier, 2017).

A.3 Bias in the *piControl* simulations produced by individual models

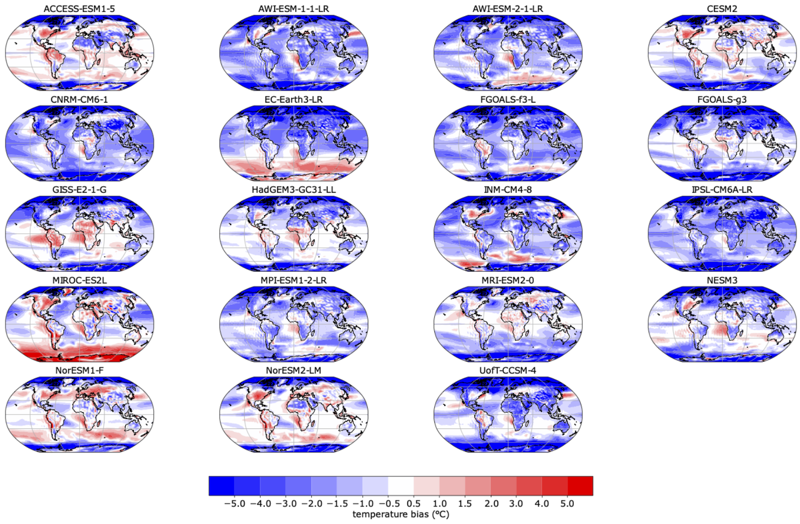

Figure A.1: Bias in annual surface temperature change (°C) by individual PMIP4-CMIP6 models.

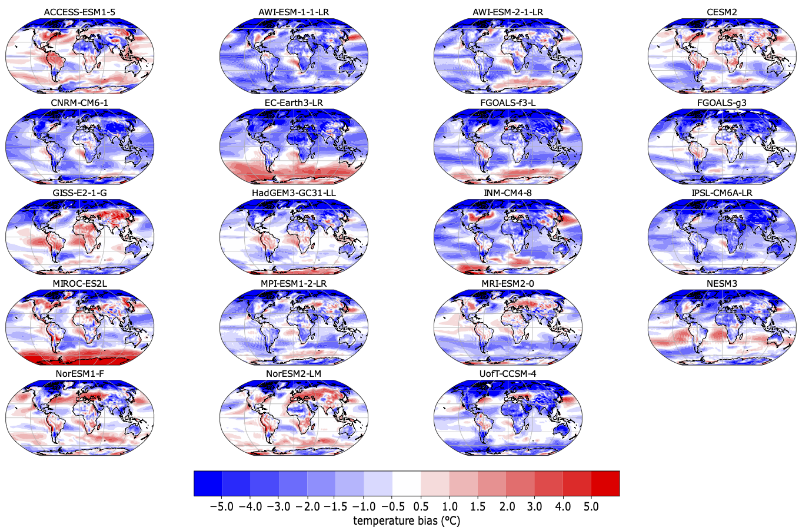

Figure A.2: Same as Figure A.1 but for DJF.

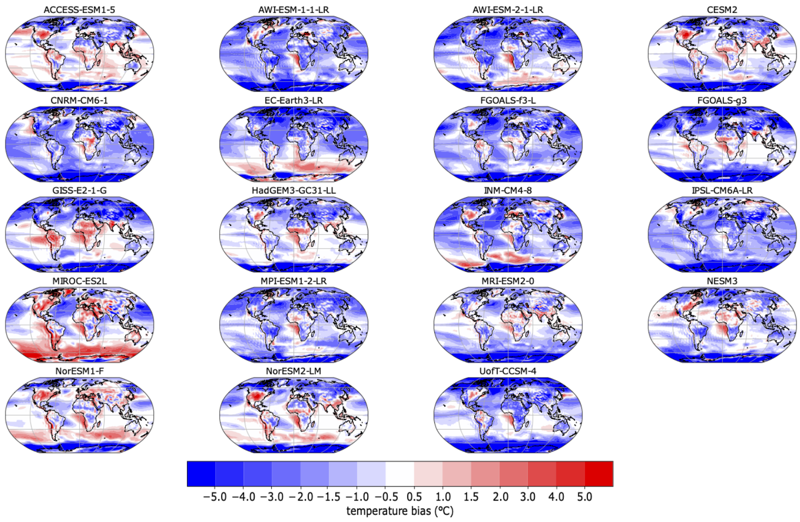

Figure A.3: Same as Figure A.1 but for JJA.

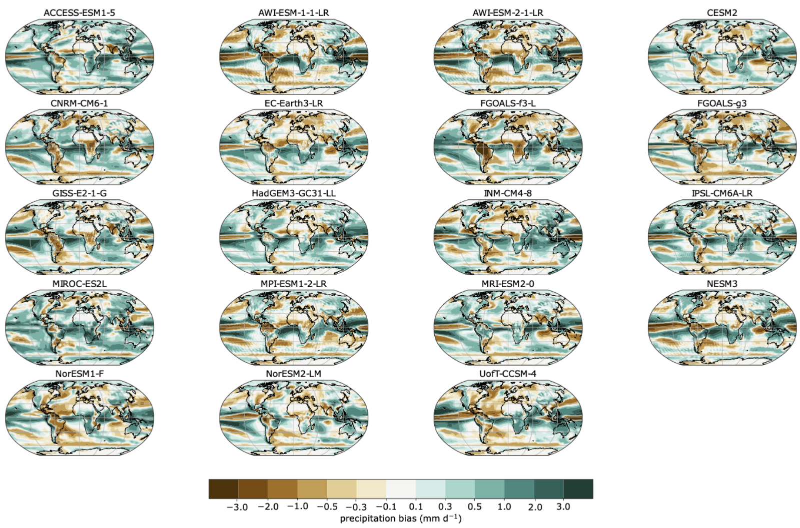

Figure A.4: Same as Figure A.1 but for precipitation in mm d^{-1}.

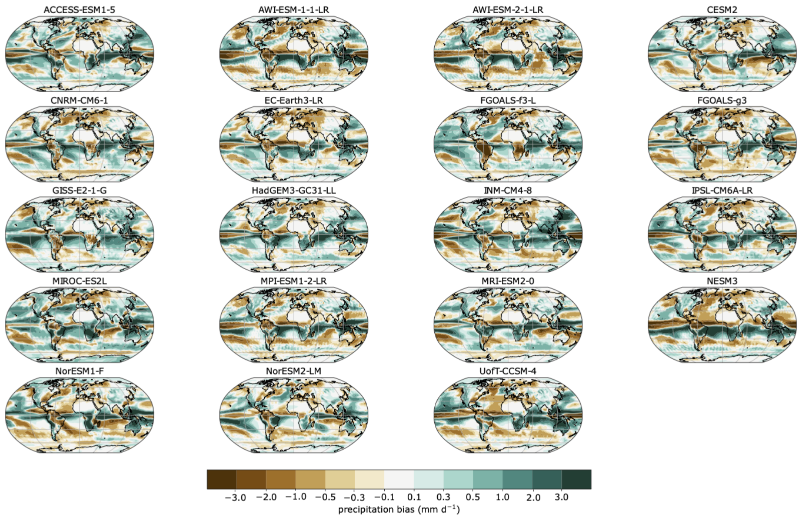

Figure A.5: Same as Figure A.1 but for DJF precipitation in mm d^{-1}.

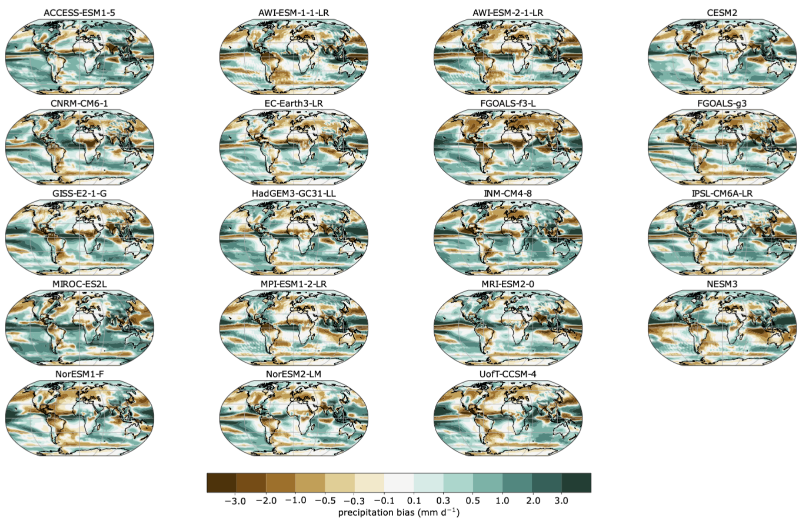

Figure A.6: Same as Figure A.1 but for JJA precipitation in mm d^{-1}.

Appendix B

Chapter 3 SI

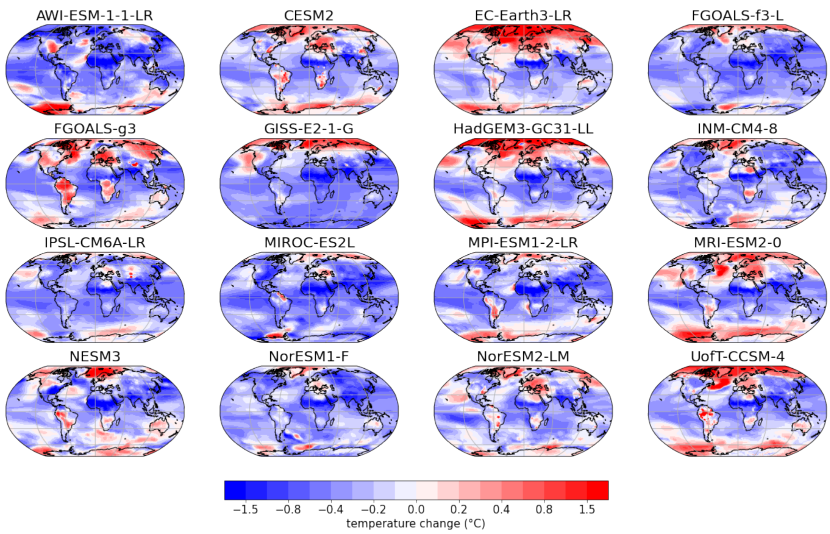

Figure B.1: Annual mean surface temperature change (°C) in the *midHolocene* as simulated by individual PMIP4-CMIP6 models.

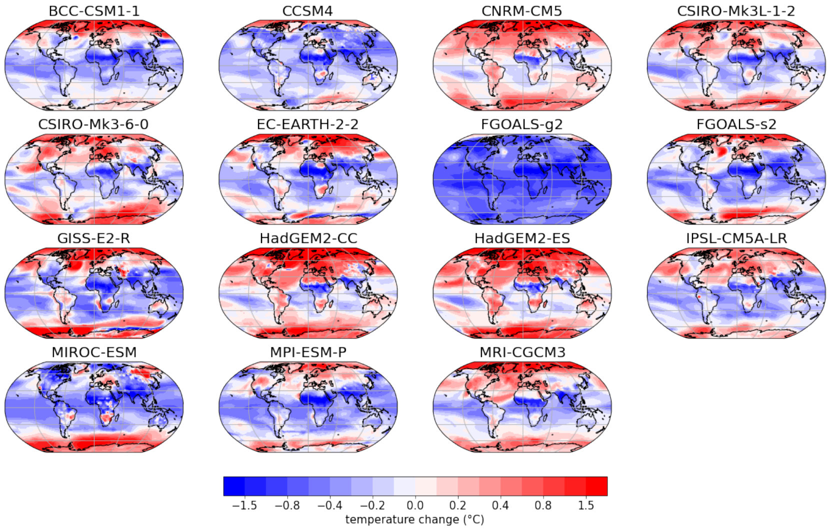

Figure B.2: Annual mean surface temperature change (°C) in the *midHolocene* as simulated by individual PMIP3-CMIP5 models.

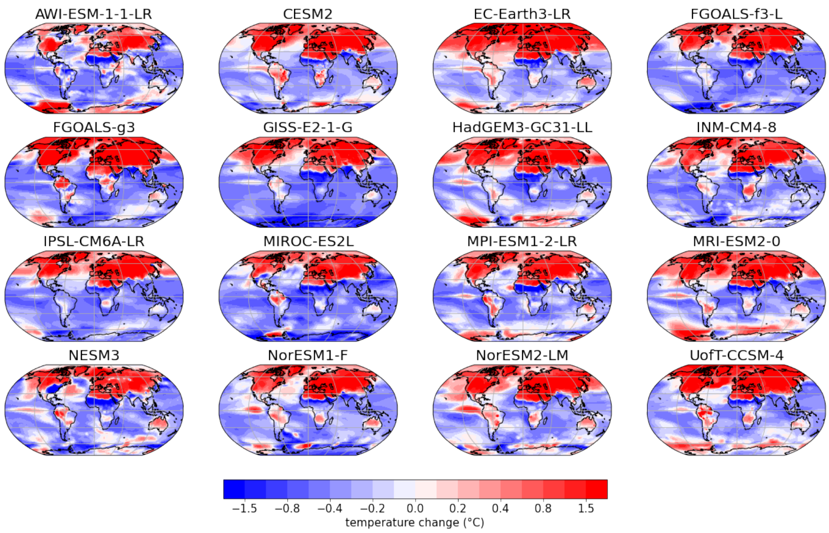

Figure B.3: JJA mean surface temperature change (°C) in the *midHolocene* as simulated by individual PMIP4-CMIP6 models.

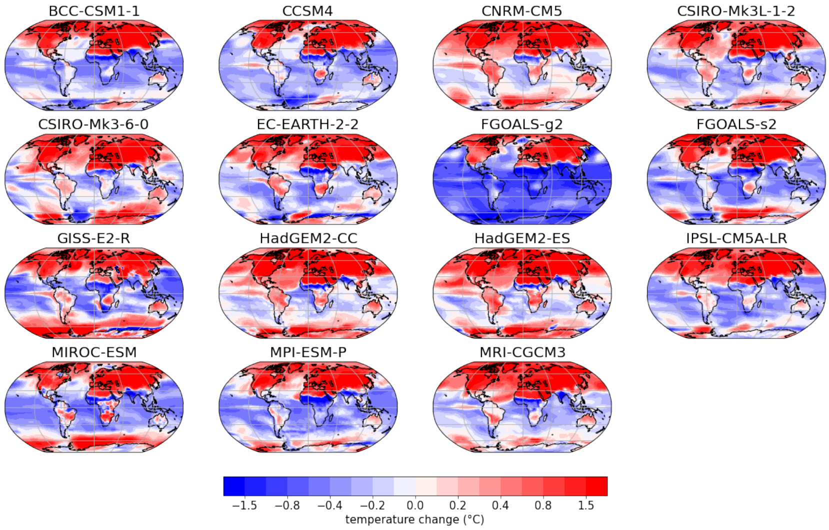

Figure B.4: JJA mean surface temperature change (°C) in the *midHolocene* as simulated by individual PMIP3-CMIP5 models.

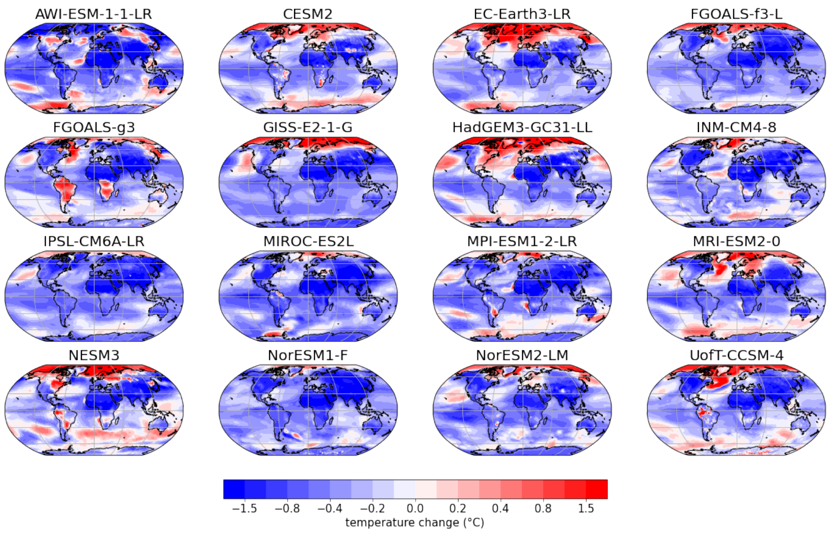

Figure B.5: DJF mean surface temperature change (°C) in the *midHolocene* as simulated by individual PMIP4-CMIP6 models.

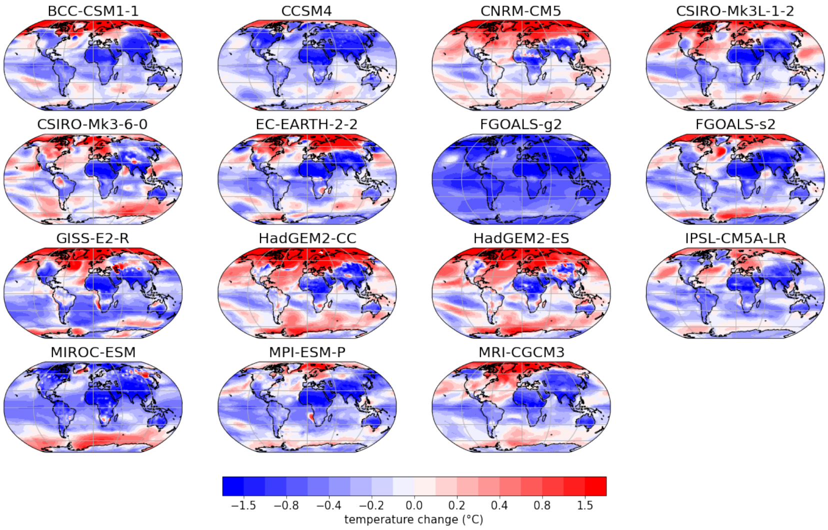

Figure B.6: DJF mean surface temperature change (°C) in the *midHolocene* as simulated by individual PMIP3-CMIP5 models.

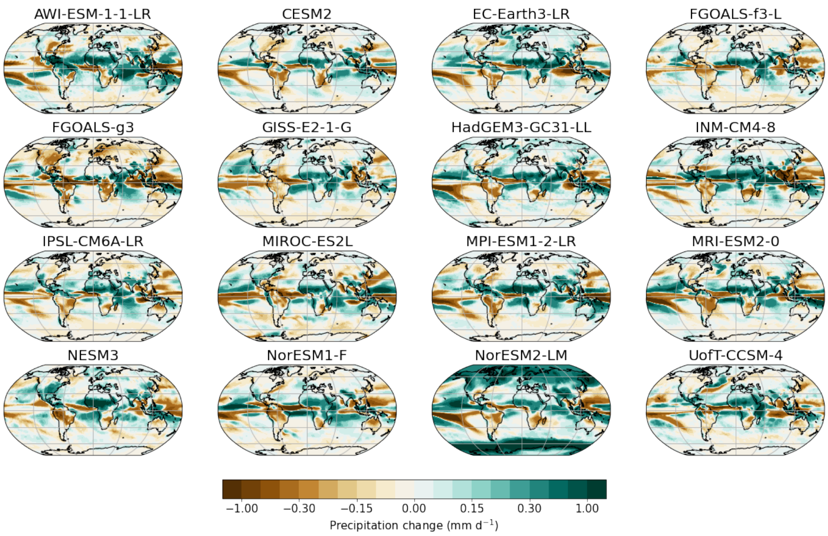

Figure B.7: Annual mean precipitation change (mm d^{-1}) in the *midHolocene* as simulated by individual PMIP4-CMIP6 models.

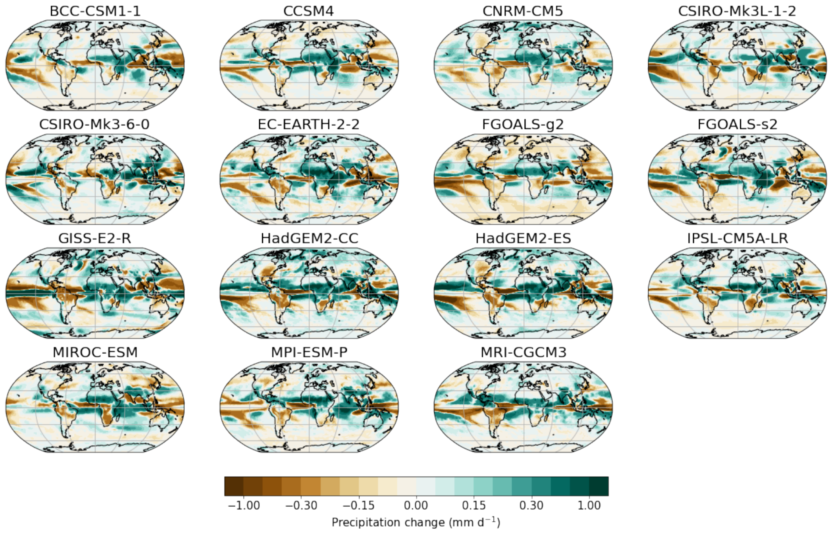

Figure B.8: Annual mean precipitation change (mm d^{-1}) in the *midHolocene* as simulated by individual PMIP3-CMIP5 models.

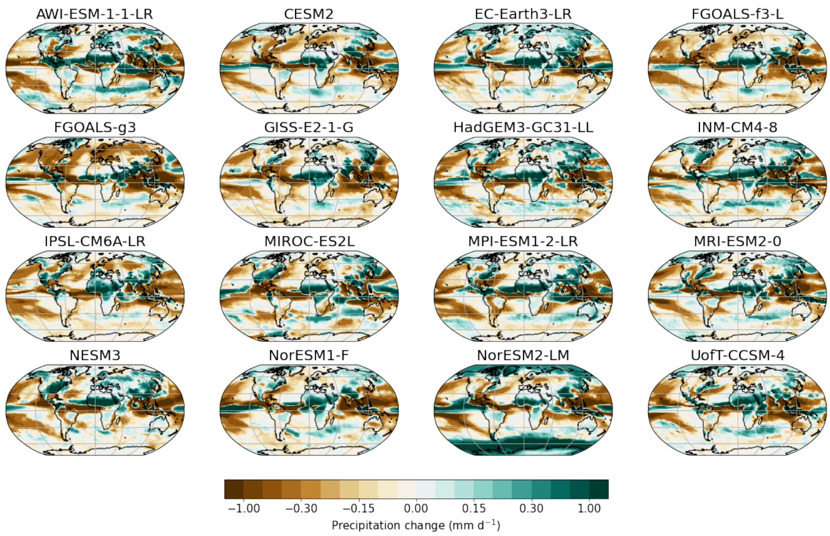

Figure B.9: JJA mean precipitation change (mm d^{-1}) in the *midHolocene* as simulated by individual PMIP4-CMIP6 models.

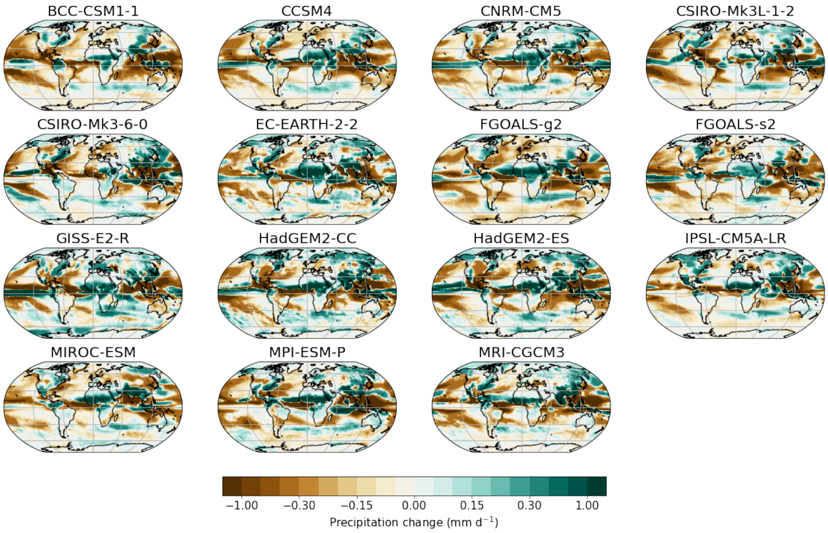

Figure B.10: JJA mean precipitation change (mm d^{-1}) in the *midHolocene* as simulated by individual PMIP3-CMIP5 models.

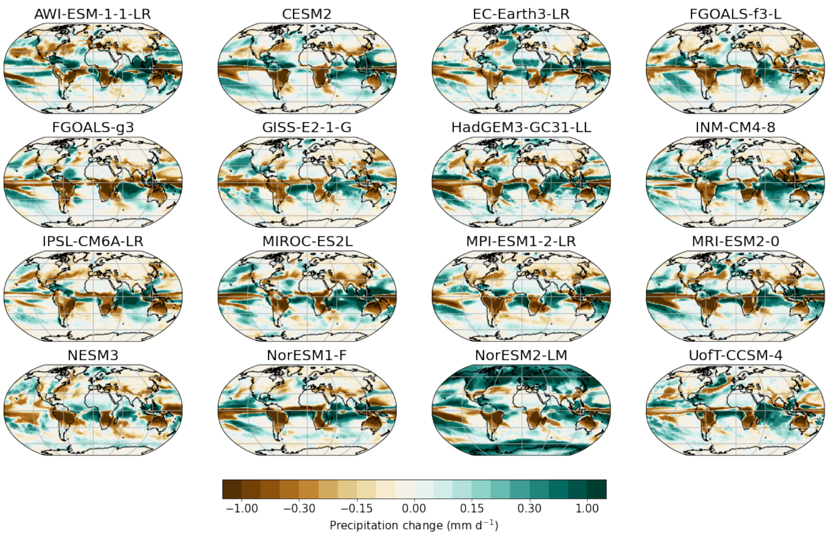

Figure B.11: DJF mean precipitation change (mm d^{-1}) in the *midHolocene* as simulated by individual PMIP4-CMIP6 models.

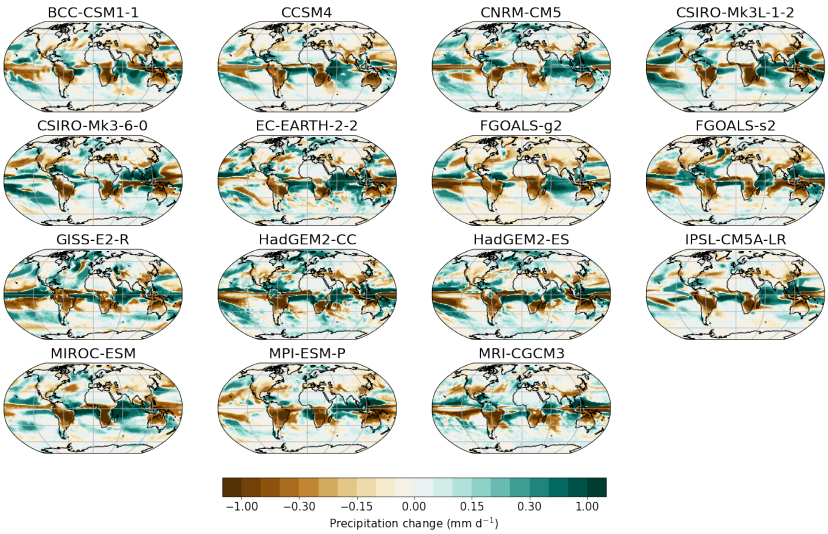

Figure B.12: DJF mean precipitation change (mm d^{-1}) in the *midHolocene* as simulated by individual PMIP3-CMIP5 models.

Appendix C

Chapter 4 SI

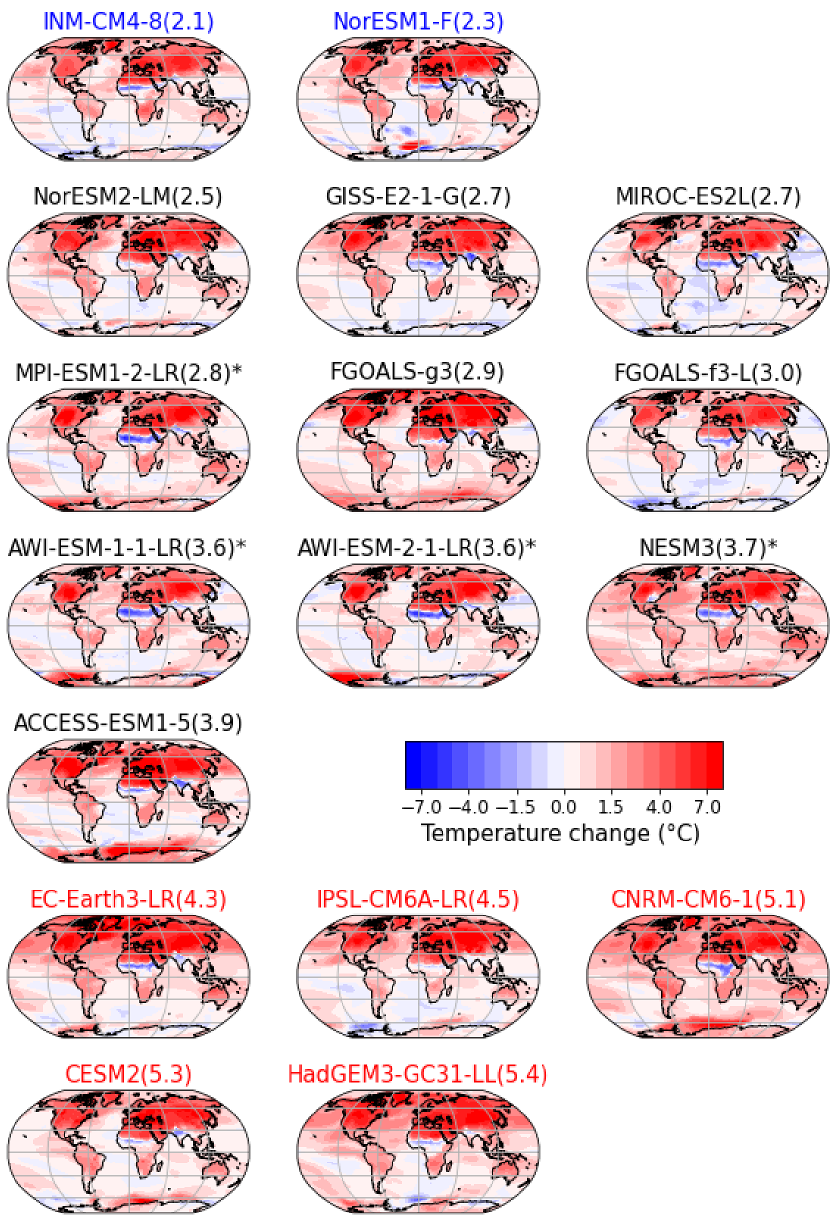

Figure C.1: JJA mean temperature (°C) change performed by individual models. Each panel title is named as the model name (ECS) and colored according to the ECS (blue for ECS $<$ 2.5°C, black for 2.5°C $<$ ECS $<$ 4.0°C and red for ECS $>$ 4.0°C.) $*$ marks the models including dynamic vegetation.

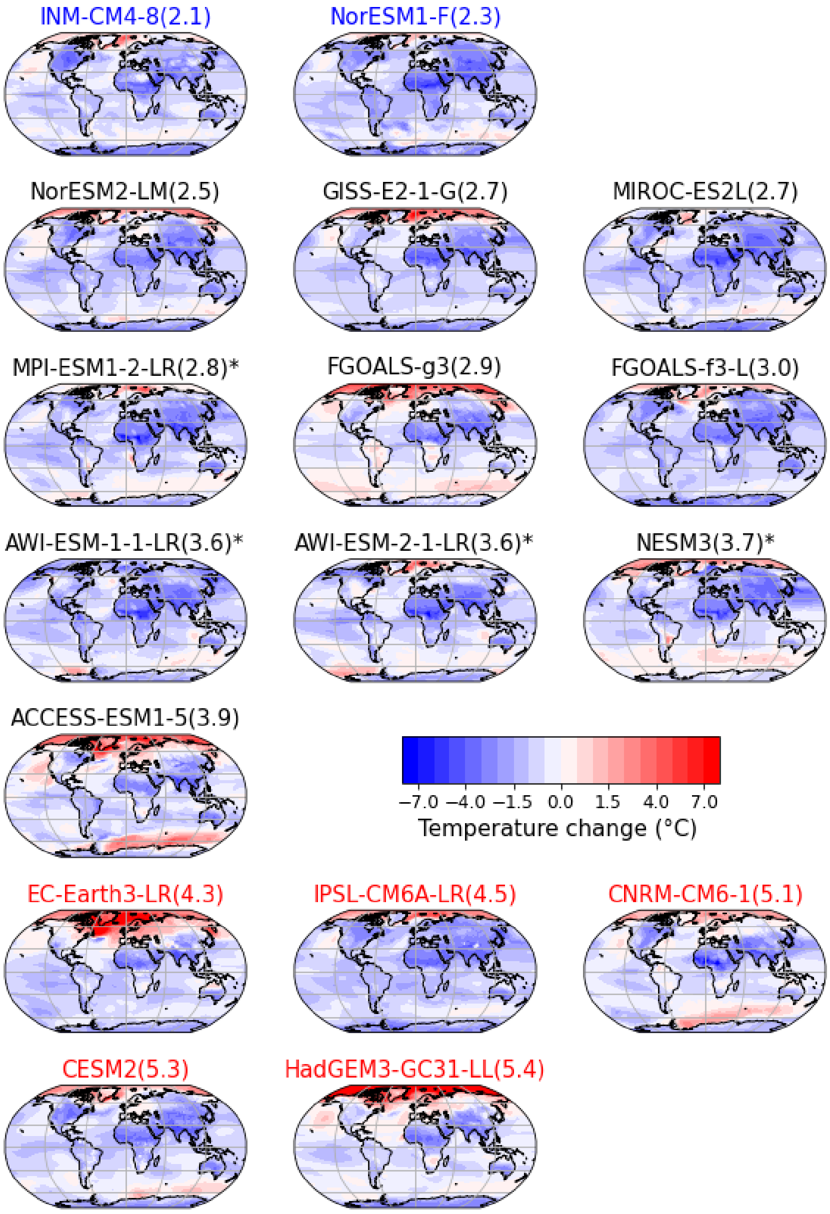

Figure C.2: Same as Figure C.1 but for DJF.

Appendix D

Chapter 5 SI

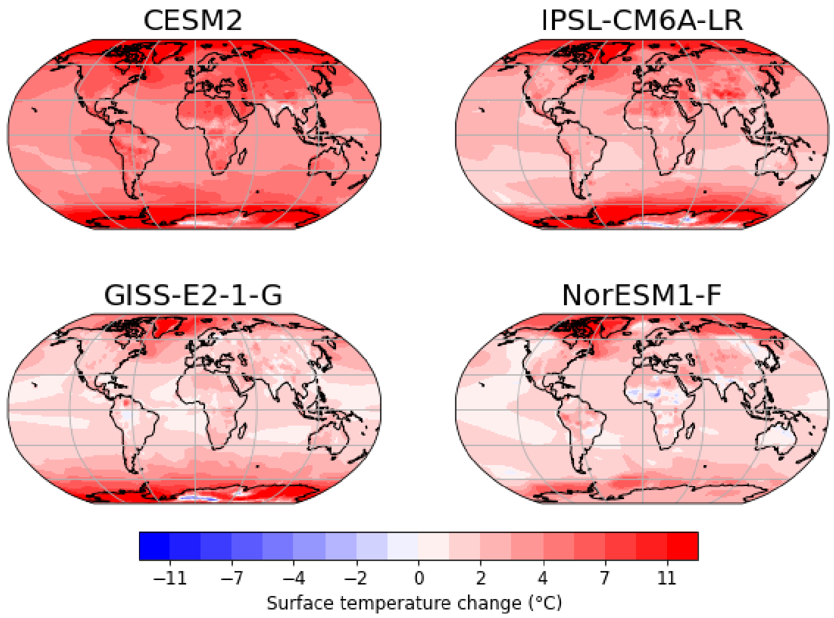

Figure D.1: ***midPliocene-eoi400*** **annual mean surface temperature change (°C) simulated by individual models.**

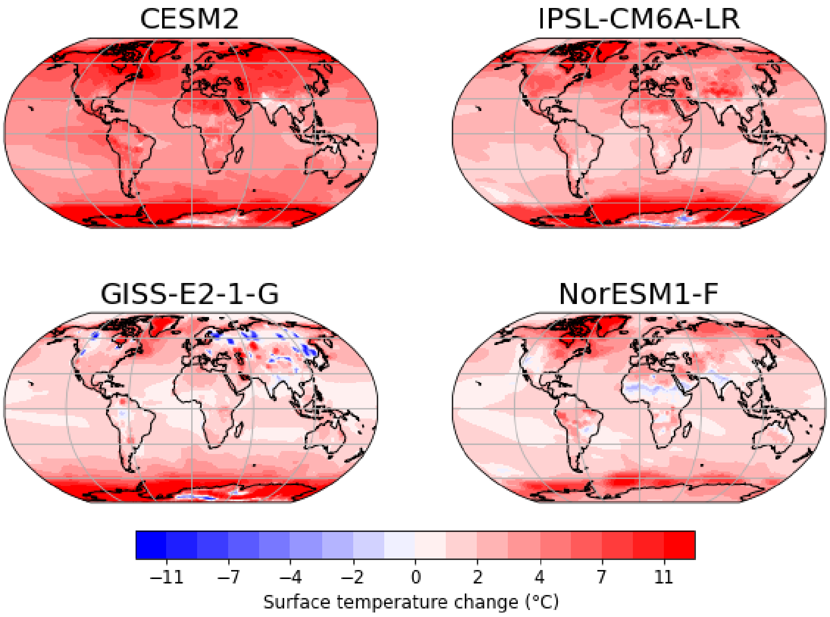

Figure D.2: Same as Figure D.1 but for JJA.

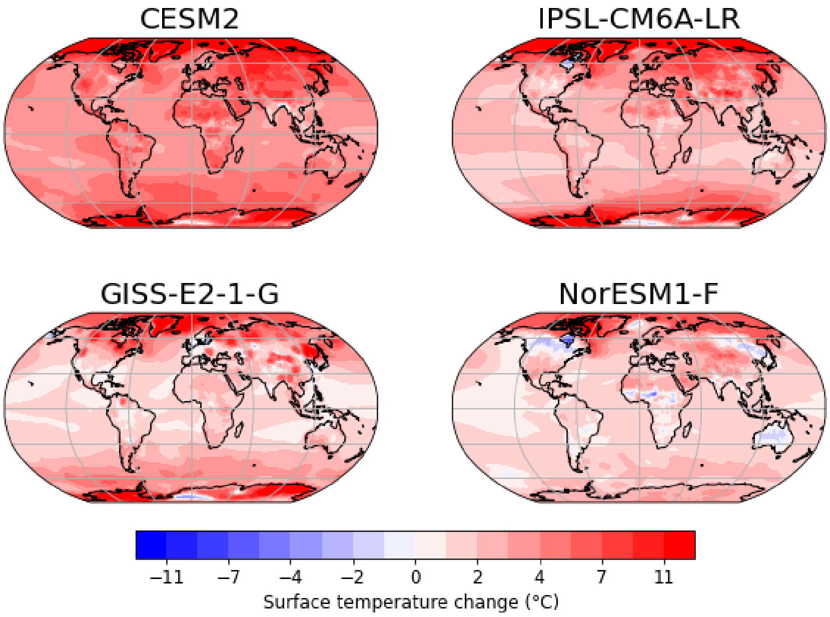

Figure D.3: Same as Figure D.1 but for DJF.

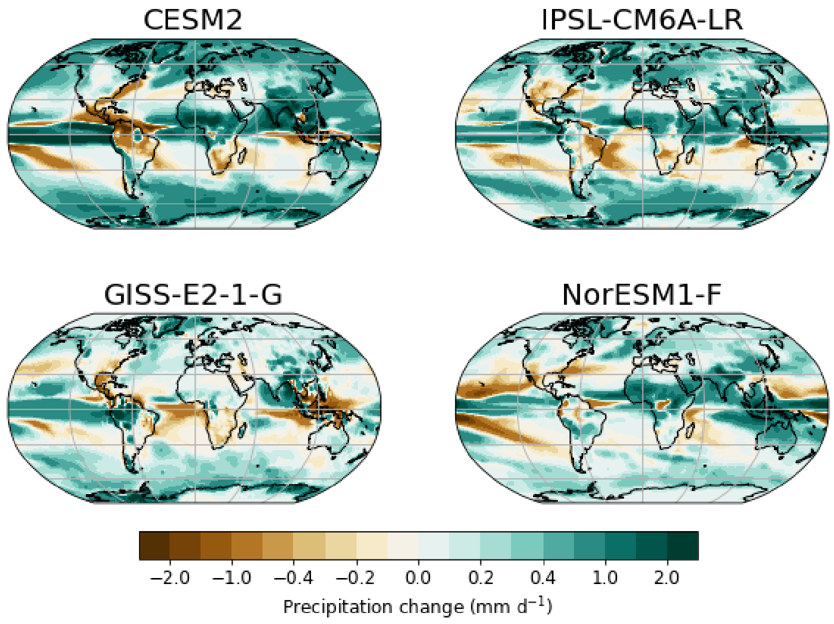

Figure D.4: *midPliocene-eoi400* annual mean surface precipitation change (mm d^{-1}) simulated by individual models.

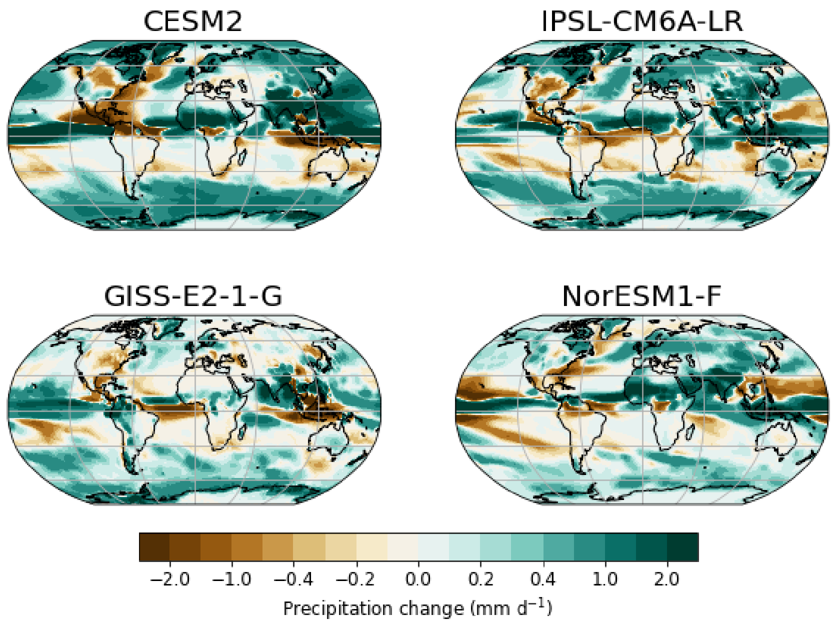

Figure D.5: Same as Figure D.4 but for JJA.

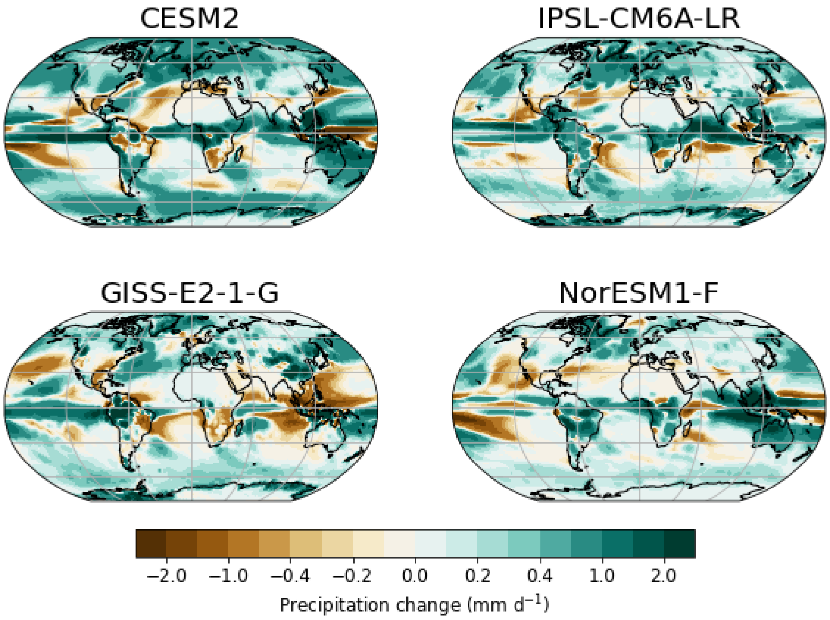

Figure D.6: Same as Figure D.4 but for DJF.

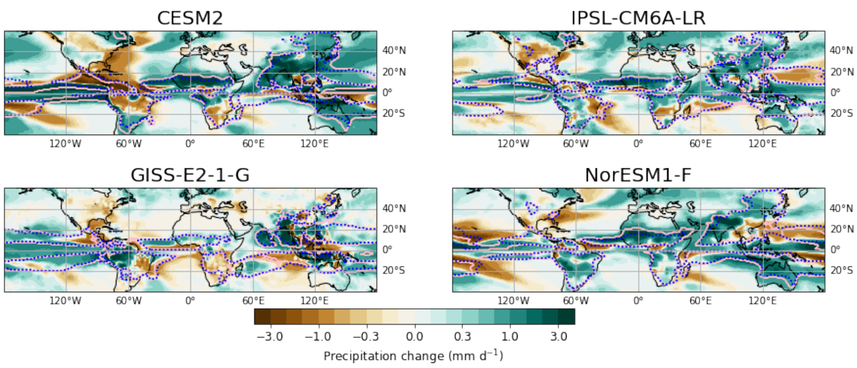

Figure D.7: *midPliocene-eoi400* global monsoon domain and change in monsoon summer rain rate (mm d^{-1})

Appendix E

Statistical comparison of individual monsoons

Table E.1: p values of comparison of individual monsoons between *experiment* and *piControl* simulations

	NAMS	NAF	EAS	SAS	SAMS	SAF	AUSMC
PMIP3 MH							
pav	0.64	0.23	0.49	0.46	0.24	0.25	0.65
psd	0.81	0.22	0.78	0.48	0.75	0.71	0.62
aav	0.41	0.00	0.11	0.38	0.52	0.27	0.39
asd	0.67	0.41	0.37	0.59	0.49	0.29	0.96
totwater	0.44	0.00	0.04	0.97	0.14	0.12	0.27
PMIP4 MH							
pav	0.74	0.03	0.70	0.45	0.35	0.47	0.71
psd	0.81	0.29	0.70	0.52	0.43	0.82	0.81
aav	0.64	0.00	0.10	0.30	0.27	0.38	0.41
asd	0.87	0.04	0.01	0.98	0.63	0.94	0.72
totwater	0.61	0.00	0.10	0.67	0.22	0.37	0.33
LIG							
pav	0.12	0.00	0.13	0.94	0.03	0.10	0.43
psd	0.52	0.01	0.56	0.99	0.36	0.16	0.21
aav	0.63	0.00	0.00	0.01	0.04	0.02	0.00
asd	0.25	0.00	0.01	0.07	0.75	0.38	0.33
totwater	0.29	0.00	0.00	0.03	0.01	0.02	0.00
mPWP							
pav	0.28	0.77	0.51	0.79	0.59	0.98	0.91
psd	0.87	0.73	0.74	0.48	0.49	0.81	0.94
aav	0.68	0.17	0.68	1.00	0.54	0.97	0.50
asd	0.52	0.07	0.59	0.69	0.97	0.88	0.94
totwater	0.50	0.26	0.31	0.74	0.52	0.97	0.50

Bibliography

Ackerley, D., Reeves, J., Barr, C., Bostock, H., Fitzsimmons, K., Fletcher, M.-S., Gouramanis, C., McGregor, H., Mooney, S., Phipps, S. J., Tibby, J., and Tyler, J. (2017). Evaluation of pmip2 and pmip3 simulations of mid-holocene climate in the indo-pacific, australasian and southern ocean regions. Climate of the Past, 13(11):1661–1684.

Adler, R. F., Huffman, G. J., Chang, A., Ferraro, R., Xie, P.-P., Janowiak, J., Rudolf, B., Schneider, U., Curtis, S., Bolvin, D., Gruber, A., Susskind, J., Arkin, P., and Nelkin, E. (2003). The version-2 global precipitation climatology project (gpcp) monthly precipitation analysis (1979–present). Journal of hydrometeorology, 4(6):1147–1167.

Albani, S., Mahowald, N. M., Winckler, G., Anderson, R. F., Bradtmiller, L. I., Delmonte, B., François, R., Goman, M., Heavens, N. G., Hesse, P. P., Hovan, S. A., Kang, S. G., Kohfeld, K. E., Lu, H., Maggi, V., Mason, J. A., Mayewski, P. A., McGee, D., Miao, X., Otto-Bliesner, B. L., Perry, A. T., Pourmand, A., Roberts, H. M., Rosenbloom, N., Stevens, T., and Sun, J. (2015). Twelve thousand years of dust: the holocene global dust cycle constrained by natural archives. Clim. Past, 11:869–903.

Albrecht, B. A. (1989). Aerosols, Cloud Microphysics, and Fractional Cloudiness. Science, 245(4923):1227–1230.

Amies, J. D., Rohling, E. J., Grant, K. M., Rodríguez-Sanz, L., and Marino, G. (2019). Quantification of african monsoon runoff during last interglacial sapropel s5. Paleoceanography and Paleoclimatology, 34(8):1487–1516.

An, Z., Kutzbach, J. E., Prell, W. L., and Porter, S. C. (2001). Evolution of asian monsoons and phased uplift of the himalaya–tibetan plateau since late miocene times. Nature, 411(6833):62–66.

Andreae, M. O. (2004). Smoking Rain Clouds over the Amazon. Science, 303(5662):1337–1342.

Andrews, T., Gregory, J. M., Webb, M. J., and Taylor, K. E. (2012). Forcing, feedbacks and climate sensitivity in cmip5 coupled atmosphere-ocean climate models. Geophysical Research Letters, 39(9).

Aumont, O., Ethé, C., Tagliabue, A., Bopp, L., and Gehlen, M. (2015). Pisces-v2: an ocean biogeochemical model for carbon and ecosystem studies. Geoscientific Model Development, 8(8):2465–2513.

Aumont, O., Maier-Reimer, E., Blain, S., and Monfray, P. (2003). An ecosystem model of the global ocean including fe, si, p colimitations. Global Biogeochemical Cycles, 17(2).

Bader, J., Jungclaus, J., Krivova, N., Lorenz, S., Maycock, A., Raddatz, T., Schmidt, H., Toohey, M., Wu, C.-J., and Claussen, M. (2020). Global temperature modes shed light on the holocene temperature conundrum. Nature Communications, 11(1):4726.

Balaji, V., Taylor, K. E., Juckes, M., Lawrence, B. N., Durack, P. J., Lautenschlager, M., Blanton, C., Cinquini, L., Denvil, S., Elkington, M., Guglielmo, F., Guilyardi, E., Hassell, D., Kharin, S., Kindermann, S., Nikonov, S., Radhakrishnan, A., Stockhause, M., Weigel, T., and Williams, D. (2018). Requirements for a global data infrastructure in support of cmip6. Geoscientific Model Development, 11(9):3659–3680.

Balsamo, G., Viterbo, P., Beijaars, A., van den Hurk, B., Hirschi, M., Betts, A. K., and Scipal, K. (2009). A revised hydrology for the ECMWF model: Verification from field site to terrestrial water storage and impact in the integrated forecast system. Journal of Hydrometeorology, 10(3):623 – 643.

Bao, Q. and Li, J. (2020). Progress in climate modeling of precipitation over the tibetan plateau. National Science Review, 7:486–687.

Bao, Q., Lin, P., Zhou, T., Liu, Y., Yu, Y., Wu, G., He, B., He, J., Li, L., Li, J., Li, C., Liu, H., Qiao, F., Song, Z., Wang, B., Wang, J., Wang, P., Wang, X., Wang, Z., Wu, B., Wu, T., Xu, Y., Yu, H., Zhao, W., Zheng, W., and Zhou, L. (2013). The flexible global ocean-atmosphere-land system model, spectral version 2: Fgoals-s2. Advances in Atmospheric Sciences, 30(3):561–576.

Bao, Q., Wu, G., Liu, Y., Yang, J., Wang, Z., and Zhou, T. (2010). An introduction to the coupled model fgoals1.1-s and its performance in east asia. Advances in Atmospheric Sciences, 27(5):1131–1142.

Barker, S., Cacho, I., Benway, H., and Tachikawa, K. (2005). Planktonic foraminiferal mg/ca as a proxy for past oceanic temperatures: a methodological overview and data compilation for the last glacial maximum. Quaternary Science Reviews, 24(7):821–834. Multiproxy Approach for the Reconstruction of the Glacial Ocean surface.

Barlow, N. L. M., McClymont, E. L., Whitehouse, P. L., Stokes, C. R., Jamieson, S. S. R., Woodroffe, S. A., Bentley, M. J., Callard, S. L., Cofaigh, C. Ó., Evans, D. J. A., Horrocks, J. R., Lloyd, J. M., Long, A. J., Margold, M., Roberts, D. H., and Sanchez-Montes, M. L. (2018). Lack of evidence for a substantial sea-level fluctuation within the last interglacial. Nature Geoscience, 11(9):627–634.

Barron, J. A., Metcalfe, S. E., and Addison, J. A. (2012). Response of the north american monsoon to regional changes in ocean surface temperature. Paleoceanography, 27(3).

Bartlein, P. J., Harrison, S., Brewer, S., Connor, S., Davis, B., Gajewski, K., Guiot, J., Harrison-Prentice, T., Henderson, A., and Peyron, O. (2011). Pollen-based continental climate reconstructions at 6 and 21 ka: a global synthesis. Climate Dynamics, 37(3-4):775–802.

Bartlein, P. J., Harrison, S. P., and Izumi, K. (2017). Underlying causes of eurasian midcontinental aridity in simulations of mid-holocene climate. Geophysical research letters, 44(17):9020–9028.

Bartlein, P. J. and Shafer, S. L. (2019). Paleo calendar-effect adjustments in time-slice and transient climate-model simulations (PaleoCalAdjust v1.0): impact and strategies for data analysis. Geoscientific Model Development, 12(9):3889–3913.

Bartoli, G., Hönisch, B., and Zeebe, R. E. (2011). Atmospheric CO 2 decline during the Pliocene intensification of Northern Hemisphere glaciations. Paleoceanography, 26(4):PA4213.

Bellouin, N., Rae, J., Jones, A., Johnson, C., Haywood, J., and Boucher, O. (2011). Aerosol forcing in the climate model intercomparison project (cmip5) simulations by hadgem2-es and the role of ammonium nitrate. Journal of Geophysical Research: Atmospheres, 116(D20):D20206.

Bentsen, M., Bethke, I., Debernard, J. B., Iversen, T., Kirkevåg, A., Seland, Ø., Drange, H., Roelandt, C., Seierstad, I. A., Hoose, C., and Kristjánsson, J. E. (2013). The norwegian earth system model, noresm1-m â part 1: Description and basic evaluation of the physical climate. Geoscientific Model Development, 6(3):687–720.

Bereiter, B., Eggleston, S., Schmitt, J., Nehrbass-Ahles, C., Stocker, T. F., Fischer, H., Kipfstuhl, S., and Chappellaz, J. (2015). Revision of the epica dome c co2 record from 800 to 600kyr before present. Geophysical Research Letters, 42(2):542–549.

Berg, P., Moseley, C., and Haerter, J. O. (2013). Strong increase in convective precipitation in response to higher temperatures. Nature Geoscience, 6:181–185.

Berger, A. and Loutre, M.-F. (1991). Insolation values for the climate of the last 10 million years. Quaternary Science Reviews, 10(4):297–317.

Berger, A. L. (1978). Long-term variations of caloric insolation resulting from the earth's orbital elements. Quaternary Res., 9:139–167.

Bhattacharya, T., Tierney, J. E., Addison, J. A., and Murray, J. W. (2018). Ice-sheet modulation of deglacial north american monsoon intensification. Nature Geoscience, 11(11):848–852.

Biasutti, M., Voigt, A., Boos, W. R., Braconnot, P., Hargreaves, J. C., Harrison, S. P., Kang, S. M., Mapes, B. E., Scheff, J., Schumacher, C., Sobel, A. H., and Xie, S.-P. (2018). Global energetics and local physics as drivers of past, present and future monsoons. Nature Geoscience, 11(6):392–400.

Bigelow, N. H., Brubaker, L. B., Edwards, M. E., Harrison, S. P., Prentice, I. C., Anderson, P. M., Andreev, A. A., Bartlein, P. J., Christensen, T. R., Cramer, W., Kaplan, J. O., Lozhkin, A. V., Matveyeva, N. V., Murray, D. F., McGuire, A. D., Razzhivin, V. Y., Ritchie, J. C., Smith, B., Walker, D. A., Gajewski, K., Wolf, V., Holmqvist, B. H., Igarashi, Y., Kremenetskii, K., Paus, A., Pisaric, M. F. J., and Volkova, V. S. (2003). Climate change and arctic ecosystems: 1. vegetation changes north of 55°n between the last glacial maximum, mid-holocene, and present. Journal of Geophysical Research: Atmospheres, 108(D19):8170.

Bird, B. W., Abbott, M. B., Rodbell, D. T., and Vuille, M. (2011). Holocene tropical south american hydroclimate revealed from a decadally resolved lake sediment 18o record. Earth and Planetary Science Letters, 310(3):192–202.

Bjorn, S. and Sandrine, B. (2013). What are climate models missing? Science, 340(6136):1053–1054.

Boucher, O., Randall, D., Artaxo, P., Bretherton, C., Feingold, G., Forster, P., Kerminen, V.-M. Kondo, Y., Liao, H., Lohmann, U., Rasch, P., Satheesh, S., Sherwood, S., Stevens, B., and Zhang, X. (2013). Clouds and Aerosols. In Stocker, T., Qin, D., Plattner, G.-K., Tignor, M., Allen, S., Boschung, J., Nauels, A., Xia, Y., Bex, V., and Midgley, P., editors, Climate Change 2013 - The Physical Science Basis, pages 571–658. Cambridge University Press.

Boucher, O., Servonnat, J., Albright, A. L., Aumont, O., Balkanski, Y., Bastrikov, V., Bekki, S., Bonnet, R., Bony, S., Bopp, L., Braconnot, P., Brockmann, P., Cadule, P., Caubel, A., Cheruy, F., Codron, F., Cozic, A., Cugnet, D., D'Andrea, F., Davini, P., Lavergne, C., Denvil, S., Deshayes, J., Devilliers, M., Ducharne, A., Dufresne, J., Dupont, E., Éthé, C., Fairhead, L., Falletti, L., Flavoni, S., Foujols, M., Gardoll, S., Gastineau, G., Ghattas, J., Grandpeix, J., Guenet, B., Guez, Lionel, E., Guilyardi, E., Guimberteau, M., Hauglustaine, D., Hourdin, F., Idelkadi, A., Joussaume, S., Kageyama, M., Khodri, M., Krinner, G., Lebas, N., Levavasseur, G., Lévy, C., Li, L., Lott, F., Lurton, T., Luyssaert, S., Madec, G., Madeleine, J., Maignan, F., Marchand, M., Marti, O., Mellul, L., Meurdesoif, Y., Mignot, J., Musat, I., Ottlé, C., Peylin, P., Planton, Y., Polcher, J., Rio, C., Rochetin, N., Rousset, C., Sepulchre, P., Sima, A., Swingedouw, D., Thiéblemont, R., Traore, A. K., Vancoppenolle, M., Vial, J., Vialard, J., Viovy, N., and Vuichard, N. (2020). Presentation and evaluation of the IPSL-CM6A-LR climate model. Journal of Advances in Modeling Earth Systems, 12:p.e2019MS002010–n/a.

Braconnot, P., Albani, S., Balkanski, Y., Cozic, A., Kageyama, M., Sima, A., Marti, O., and Peterschmitt, J.-Y. (2021). Impact of dust in pmip-cmip6 mid-holocene simulations with the ipsl model. Climate of the Past, 17(3):1091–1117.

Braconnot, P., Crétat, J., Marti, O., Balkanski, Y., Caubel, A., Cozic, A., Foujols, M. A., and Sanogo, S. (2019a). Impact of multiscale variability on last 6,000 years indian and west african monsoon rain. Geophysical Research Letters, 46(23):14021–14029.

Braconnot, P., Harrison, S. P., Kageyama, M., Bartlein, P. J., Masson-Delmotte, V., Abe-Ouchi, A., Otto-Bliesner, B., and Zhao, Y. (2012). Evaluation of climate models using palaeoclimatic data. Nature Climate Change, 2(6):417–424.

Braconnot, P., Harrison, S. P., Otto-Bliesner, B., Abe-Ouch, A., Jungclaus, J., and Peterschmitt, J.-Y. (2011). The paleoclimate modeling intercomparison project contribution to cmip5. CLIVAR Exchanges No. 56, 16(2):15–19.

Braconnot, P., Joussaume, S., de Noblet, N., and Ramstein, G. (2000). Mid-holocene and last glacial maximum african monsoon changes as simulated within the paleoclimate modelling intercomparison project. Global and planetary change, 26(1-3):51–66.

Braconnot, P., Joussaume, S., Marti, O., and de Noblet, N. (1999). Synergistic feedbacks from ocean and vegetation on the african monsoon response to mid-holocene insolation. Geophysical Research Letters, 26(16):2481–2484.

Braconnot, P., Loutre, M., Dong, B., Joussaume, S., Valdes, P., , and participating groups, P. (2002). How the simulated change in monsoon at 6 ka bp is related to the simulation of the modern climate: results from the paleoclimate modeling intercomparison project. Climate Dynamics, 19(2):107–121.

Braconnot, P., Otto-Bliesner, B., Harrison, S., Joussaume, S., Peterchmitt, J.-Y., Abe-Ouchi, A., Crucifix, M., Driesschaert, E., Fichefet, T., Hewitt, C. D., Kageyama, M., Kitoh, A., La\^\iné, A., Loutre, M.-F., Marti, O., Merkel, U., Ramstein, G., Valdes, P., Weber, S. L., Yu, Y., and Zhao, Y. (2007). Results of PMIP2 coupled simulations of the Mid-Holocene and Last Glacial Maximum – Part 1: experiments and large-scale features. Climate of the Past, 3(2):261–277.

Braconnot, P., Zhu, D., Marti, O., and Servonnat, J. (2019b). Strengths and challenges for transient mid-to late holocene simulations with dynamical vegetation. Climate of the Past, 15(3):997–1024.

Brassell, S. C., Eglinton, G., Marlowe, I. T., Pflaumann, U., and Sarnthein, M. (1986). Molecular stratigraphy: a new tool for climatic assessment. Nature, 320(6058):129–133.

Brewer, S., Guiot, J., Sánchez-Goñi, M. F., and Klotz, S. (2008). The climate in Europe during the Eemian: a multi-method approach using pollen data. Quaternary Science Reviews, 27(25):2303–2315.

Briegleb, B. P., Bitz, C. M., Hunke, E. C., Lipscomb, W. H., Holland, M., Schramm, J. L., and Moritz, R. E. (2004). Scientific Description of the Sea Ice Component in the Community Climate System Model, Version 3. Technical Report NCAR/TN-463+STR.

Brierley, C. and Wainer, I. (2018). Inter-annual variability in the tropical atlantic from the last glacial maximum into future climate projections simulated by cmip5/pmip3. Climate of the Past, 14(10):1377–1390.

Brierley, C. M. and Fedorov, A. V. (2016). Comparing the impacts of miocene–pliocene changes in inter-ocean gateways on climate: Central american seaway, bering strait, and indonesia. Earth and Planetary Science Letters, 444:116–130.

Brierley, C. M., Zhao, A., Harrison, S. P., Braconnot, P., Williams, C. J. R., Thornalley, D. J. R., Shi, X., Peterschmitt, J.-Y., Ohgaito, R., Kaufman, D. S., Kageyama, M., Hargreaves, J. C., Erb, M. P., Emile-Geay, J., D'Agostino, R., Chandan, D., Carré, M., Bartlein, P. J., Zheng, W., Zhang, Z., Zhang, Q., Yang, H., Volodin, E. M., Tomas, R. A., Routson, C., Peltier, W. R., Otto-Bliesner, B., Morozova, P. A., McKay, N. P., Lohmann, G., Legrande, A. N., Guo, C., Cao, J., Brady, E., Annan, J. D., and Abe-Ouchi, A. (2020). Large-scale features and evaluation of the pmip4-cmip6 *midHolocene* simulations. Climate of the Past, 16(5):1847–1872.

Broström, A., Coe, M., Harrison, S. P., Gallimore, R., Kutzbach, J. E., Foley, J., Prentice, I. C., and Behling, P. (1998). Land surface feedbacks and palaeomonsoons in northern africa. Geophysical Research Letters, 25(19):3615–3618.

Brown, J. R., Brierley, C. M., An, S.-I., Guarino, M.-V., Stevenson, S., Williams, C. J. R., Zhang, Q., Zhao, A., Abe-Ouchi, A., Braconnot, P., Brady, E. C., Chandan, D., D'Agostino, R., Guo, C., LeGrande, A. N., Lohmann, G., Morozova, P. A., Ohgaito, R., O'ishi, R., Otto-Bliesner, B. L., Peltier, W. R., Shi, X., Sime, L., Volodin, E. M., Zhang, Z., and Zheng, W. (2020). Comparison of past and future simulations of enso in cmip5/pmip3 and cmip6/pmip4 models. Climate of the Past, 16(5):1777–1805.

Brown, J. R., Moise, A. F., and Colman, R. A. (2013). The south pacific convergence zone in cmip5 simulations of historical and future climate. Climate dynamics, 41(7-8):2179–2197.

Burke, K. D., Williams, J. W., Chandler, M. A., Haywood, A. M., Lunt, D. J., and Otto-Bliesner, B. L. (2018). Pliocene and eocene provide best analogs for near-future climates. Proceedings of the National Academy of Sciences of the United States of America, 115(52):13288–13293.

Burls, N. J. and Fedorov, A. V. (2014). Simulating Pliocene warmth and a permanent El Niño-like state: The role of cloud albedo. Paleoceanography, 29(10):893–910.

Burls, N. J., Fedorov, A. V., Sigman, D. M., Jaccard, S. L., Tiedemann, R., and Haug, G. H. (2017). Active Pacific meridional overturning circulation (PMOC) during the warm Pliocene. Science Advances, 3(9):e1700156.

Byrne, M. P., Pendergrass, A. G., Rapp, A. D., and Wodzicki, K. R. (2018). Response of the Intertropical Convergence Zone to Climate Change: Location, Width, and Strength. Current Climate Change Reports, 4(4):355–370.

Byrne, M. P. and Schneider, T. (2016). Narrowing of the itcz in a warming climate: Physical mechanisms. Geophysical Research Letters, 43(21):11,350–11,357.

Cao, J., Wang, B., Yang, Y.-M., Ma, L., Li, J., Sun, B., Bao, Y., He, J., Zhou, X., and Wu, L. (2018). The NUIST Earth System Model (NESM) version 3: description and preliminary evaluation. Geoscientific Model Development, 11(7):2975–2993.

Capron, E., Govin, A., Feng, R., Otto-Bliesner, B., and Wolff, E. (2017). Critical evaluation of climate syntheses to benchmark cmip6/pmip4 127 ka last interglacial simulations in the high-latitude regions. Quaternary Science Reviews, 168:137 – 150.

Capron, E., Govin, A., Stone, E. J., Masson-Delmotte, V., Mulitza, S., Otto-Bliesner, B., Rasmussen, T. L., Sime, L. C., Waelbroeck, C., and Wolff, E. W. (2014). Temporal and spatial structure of multi-millennial temperature changes at high latitudes during the last interglacial. Quaternary Science Reviews, 103:116 – 133.

Carlson, A. E. and Winsor, K. (2012). Northern hemisphere ice-sheet responses to past climate warming. Nature Geoscience, 5(9):607–613.

Chandan, D. and Peltier, W. R. (2017). Regional and global climate for the mid-Pliocene using the University of Toronto version of CCSM4 and PlioMIP2 boundary conditions. Climate of the Past, 13(7):919–942.

Chandler, M., Rind, D., and Thompson, R. (1994). Joint investigations of the middle pliocene climate ii: Giss gcm northern hemisphere results. Global and Planetary Change, 9(3):197–219.

Chen, F. H., Qiang, M. R., Feng, Z. D., Wang, H. B., and Bloemendal, J. (2003). Stable east asian monsoon climate during the last interglacial (eemian) indicated by paleosol s1 in the western part of the chinese loess plateau. Global and Planetary Change, 36(3):171–179.

Cheng, F., Zhang, J., He, J., Zha, Y., Li, Q., and Li, Y. (2017). Analysis of aerosol-cloud-precipitation interactions based on modis data. Advances in Space Research, 59(1):63–73.

Cheng, H., Edwards, R. L., Broecker, W. S., Denton, G. H., Kong, X., Wang, Y., Zhang, R., and Wang, X. (2009). Ice age terminations. Science, 326(5950):248–252.

Cheng, H., Sinha, A., Wang, X., Cruz, F. W., and Edwards, R. L. (2012). The global paleomonsoon as seen through speleothem records from asia and the americas. Climate Dynamics, 39:1045+.

Chevalier, M., Brewer, S., and Chase, B. M. (2017). Qualitative assessment of pmip3 rainfall simulations across the eastern african monsoon domains during the mid-holocene and the last glacial maximum. Quaternary Science Reviews, 156:107–120.

Chevalier, M. and Chase, B. M. (2015). Southeast african records reveal a coherent shift from high- to low-latitude forcing mechanisms along the east african margin across last glacial–interglacial transition. Quaternary Science Reviews, 125:117–130.

Christensen, J., Krishna Kumar, K., Aldrian, E., An, S.-I., Cavalcanti, I., de Castro, M., Dong, W.and Goswami, P., Hall, A., Kanyanga, J., Kitoh, A., Kossin, J., Lau, N.-C., Renwick, J., Stephenson, D., Xie, S.-P., and Zhou, T. (2013). Climate phenomena and their relevance for future regional climate change. In Stocker, T., Qin, D., Plattner, G.-K., Tignor, M., Allen, S., Boschung, J., Nauels, A., Xia, Y., Bex, V., and Midgley, P., editors, Climate change 2013: the physical science basis. Contribution of Working Group I to the Fifth Assessment Report of the Intergovernmental Panel on Climate Change, pages 1217–1308. Cambridge University Press.

Collins, W., Bellouin, N., Doutriaux-Boucher, M., Gedney, N., Halloran, P., Hinton, T., Hughes, J., Jones, C., Joshi, M., Liddicoat, S., et al. (2011). Development and evaluation of an Earth-System model–HadGEM2. Geoscientific Model Development, 4(4):1051–1075.

Compo, G. P., Whitaker, J. S., Sardeshmukh, P. D., Matsui, N., Allan, R. J., Yin, X., Gleason, B. E., Vose, R. S., Rutledge, G., Bessemoulin, P., Brönnimann, S., Brunet, M., Crouthamel, R. I., Grant, A. N., Groisman, P. Y., Jones, P. D., Kruk, M. C., Kruger, A. C., Marshall, G. J., Maugeri, M., Mok, H. Y., Nordli, Ø., Ross, T. F., Trigo, R. M., Wang, X. L., Woodruff, S. D., and Worley, S. J. (2011). The twentieth century reanalysis project. Quarterly Journal of the Royal Meteorological Society, 137(654):1–28.

Conway, T., Wolff, E., Röthlisberger, R., Mulvaney, R., and Elderfield, H. (2015). Constraints on soluble aerosol iron flux to the Southern Ocean at the Last Glacial Maximum. Nature Communications, 6(1):7850.

Craig, A., Valcke, S., and Coquart, L. (2017). Development and performance of a new version of the OASIS coupler, OASIS3-MCT-3.0. Geoscientific Model Development, 10(9):3297–3308.

Craig, A. P., Vertenstein, M., and Jacob, R. (2012). A new flexible coupler for earth system modeling developed for ccsm4 and cesm1. The International Journal of High Performance Computing Applications, 26(1):31–42.

Crétat, J., Braconnot, P., Terray, P., Marti, O., and Falasca, F. (2020). Mid-holocene to present-day evolution of the indian monsoon in transient global simulations. Climate Dynamics, 55(9):2761–2784.

Crowley, T. J. (1996). Pliocene climates: the nature of the problem. Marine Micropaleontology, 27(1-4):3–12.

Curtis, H. D. (2014). Orbital position as a function of time. Elsevier, Amsterdam, the Netherlands.

D'Agostino, R., Bader, J., Bordoni, S., Ferreira, D., and Jungclaus, J. (2019). Northern hemisphere monsoon response to mid-holocene orbital forcing and greenhouse gas-induced global warming. Geophysical Research Letters, 46(3):1591–1601.

D'Agostino, R., Brown, J. R., Moise, A., Nguyen, H., Silva Dias, P. L., and Jungclaus, J. (2020). Contrasting Southern Hemisphere monsoon response: mid-Holocene orbital forcing versus future greenhouse-gas induced global warming. Journal of Climate, pages 1–56.

Danabasoglu, G., Bates, S. C., Briegleb, B. P., Jayne, S. R., Jochum, M., Large, W. G., Peacock, S., and Yeager, S. G. (2012). The CCSM4 Ocean Componen. J. Clim, 25:1361–1389.

Danabasoglu, G., Lamarque, J.-F., Bacmeister, J., Bailey, D. A., DuVivier, A. K., Edwards, J., Emmons, L. K., Fasullo, J., Garcia, R., Gettelman, A., Hannay, C., Holland, M. M., Large, W. G., Lauritzen, P. H., Lawrence, D. M., Lenaerts, J. T. M., Lindsay, K., Lipscomb, W. H., Mills, M. J., Neale, R., Oleson, K. W., Otto-Bliesner, B., Phillips, A. S., Sacks, W., Tilmes, S., van Kampenhout, L., Vertenstein, M., Bertini, A., Dennis, J., Deser, C., Fischer, C., Fox-Kemper, B., Kay, J. E., Kinnison, D., Kushner, P. J., Larson, V. E., Long, M. C., Mickelson, S., Moore, J. K., Nienhouse, E., Polvani, L., Rasch, P. J., and Strand, W. G. (2020). The community earth system model version 2 (cesm2). Journal of Advances in Modeling Earth Systems, 12(2):e2019MS001916.

Davies, T., Cullen, M. J. P., Malcolm, A. J., Mawson, M. H., Staniforth, A., White, A. A., and Wood, N. (2005). A new dynamical core for the met office's global and regional modelling of the atmosphere. Quarterly Journal of the Royal Meteorological Society, 131(608):1759–1782.

de Nooijer, W., Zhang, Q., Li, Q., Zhang, Q., Li, X., Zhang, Z., Guo, C., Nisancioglu, K. H., Haywood, A. M., Tindall, J. C., Hunter, S. J., Dowsett, H. J., Stepanek, C., Lohmann, G., Otto-Bliesner, B. L., Feng, R., Sohl, L. E., Chandler, M. A., Tan, N., Contoux, C., Ramstein, G., Baatsen, M. L. J., von der Heydt, A. S., Chandan, D., Peltier, W. R., Abe-Ouchi, A., Chan, W.-L., Kamae, Y., and Brierley, C. M. (2020). Evaluation of arctic warming in mid-pliocene climate simulations. Climate of the Past, 16(6):2325–2341.

Ding, Z. L., Derbyshire, E., Yang, S. L., Sun, J. M., and Liu, T. S. (2005). Stepwise expansion of desert environment across northern china in the past 3.5 ma and implications for monsoon evolution. Earth and Planetary Science Letters, 237(1):45–55.

Döscher, R., Acosta, M., Alessandri, A., Anthoni, P., Arneth, A., Arsouze, T., Bergmann, T., Bernadello, R., Bousetta, S., Caron, L.-P., Carver, G., Castrillo, M., Catalano, F., Cvijanovic, I., Davini, P., Dekker, E., Doblas-Reyes, F. J., Docquier, D., Echevarria, P., Fladrich, U., Fuentes-Franco, R., Gröger, M., v. Hardenberg, J., Hieronymus, J., Karami, M. P., Keskinen, J.-P., Koenigk, T., Makkonen, R., Massonnet, F., Ménégoz, M., Miller, P. A., Moreno-Chamarro, E., Nieradzik, L., van Noije, T., Nolan, P., O'Donnell, D., Ollinaho, P., van den Oord, G., Ortega, P., Prims, O. T., Ramos, A., Reerink, T., Rousset, C., Ruprich-Robert, Y., Le Sager, P., Schmith, T., Schrödner, R., Serva, F., Sicardi, V., Sloth Madsen, M., Smith, B., Tian, T., Tourigny, E., Uotila, P., Vancoppenolle, M., Wang, S., Wårlind, D., Willén, U., Wyser, K., Yang, S., Yepes-Arbós, X., and Zhang, Q. (2021). The ec-earth3 earth system model for the climate model intercomparison project 6. Geoscientific Model Development Discussions, 2021:1–90.

Douville, H., Raghavan, K., Renwick, J., Allan, R. P., Arias, P. A., Barlow, M., Cerezo-Mota, R., Cherchi, A., Gan, T. Y., Gergis, J., Jiang, D., Khan, A., Pokam Mba, W., Rosenfeld, D., Tierney, J., and Zolina, O. (2021). Water cycle changes. In Masson-Delmotte, V., Zhai, P., Pirani, A., Connors, S. L., Péan, C., Berger, S., Caud, N., Chen, Y., Goldfarb, L., Gomis, M. I., Huang, M., Leitzell, K., Lonnoy, E., Matthews, J., Maycock, T. K., Waterfield, T., Yelekçi, O., Yu, R., , and Zhou, B., editors, Climate Change 2021: The Physical Science Basis. Contribution of Working Group I to the Sixth Assessment Report of the Intergovernmental Panel on Climate Change. Cambridge University Press.

Dowsett, H. (2007). Faunal re-evaluation of Mid-Pliocene conditions in the western equatorial Pacific. Micropaleontology, 53(6):447–456.

Dowsett, H., Dolan, A., Rowley, D., Moucha, R., Forte, A. M., Mitrovica, J. X., Pound, M., Salzmann, U., Robinson, M., Chandler, M., Foley, K., and Haywood, A. (2016). The PRISM4 (mid-Piacenzian) paleoenvironmental reconstruction. Climate of the Past, 12(7):1519–1538.

Dowsett, H. and Poore, R. (1991). Pliocene sea surface temperatures of the north atlantic ocean at 3.0 Ma. Quaternary Science Reviews, 10(2-3):189–204.

Dowsett, H. J., Barron, J. A., Poore, R. Z., Thompson, R. S., Cronin, T. M., Ishman, S. E., and Willard, D. A. (1999). Middle Pliocene Paleoenvironmental Reconstruction: PRISM 2. U.S. GEOLOGICAL SURVEY OPEN FILE REPORT 99-535.

Dowsett, H. J., Foley, K. M., Stoll, D. K., Chandler, M. A., Sohl, L. E., Bentsen, M., Otto-Bliesner, B. L., Bragg, F. J., Chan, W.-L., Contoux, C., Dolan, A. M., Haywood, A. M., Jonas, J. A., Jost, A., Kamae, Y., Lohmann, G., Lunt, D. J., Nisancioglu, K. H., Abe-Ouchi, A., Ramstein, G., Riesselman, C. R., Robinson, M. M., Rosenbloom, N. A., Salzmann, U., Stepanek, C., Strother, S. L., Ueda, H., Yan, Q., and Zhang, Z. (2013). Sea Surface Temperature of the mid-Piacenzian Ocean: A Data-Model Comparison. Scientific Reports, 3(1):2013.

Dowsett, H. J., Robinson, M. M., Foley, K. M., Herbert, T. D., Otto-Bliesner, B. L., and Spivey, W. (2019). The mid-piacenzian of the north atlantic ocean. Stratigraphy, 16:119–144.

Dowsett, H. J., Robinson, M. M., Haywood, A. M., Salzmann, U., Hill, D. J., Sohl, L. E., Chandler, M. A., Williams, M., Foley, K. M., and Stoll, D. K. (2010). The PRISM3D paleoenvironmental reconstruction. Stratigraphy, 7:123–139.

Dufresne, J.-L., Foujols, M.-A., Denvil, S., Caubel, A., Marti, O., Aumont, O., Balkanski, Y., Bekki, S., Bellenger, H., Benshila, R., Bony, S., Bopp, L., Braconnot, P., Brockmann, P., Cadule, P., Cheruy, F., Codron, F., Cozic, A., Cugnet, D., de Noblet, N., Duvel, J.-P., Ethé, C., Fairhead, L., Fichefet, T., Flavoni, S., Friedlingstein, P., Grandpeix, J.-Y., Guez, L., Guilyardi, E., Hauglustaine, D., Hourdin, F., Idelkadi, A., Ghattas, J., Joussaume, S., Kageyama, M., Krinner, G., Labetoulle, S., Lahellec, A., Lefebvre, M.-P., Lefevre, F., Levy, C., Li, Z. X., Lloyd, J., Lott, F., Madec, G., Mancip, M., Marchand, M., Masson, S., Meurdesoif, Y., Mignot, J., Musat, I., Parouty, S., Polcher, J., Rio, C., Schulz, M., Swingedouw, D., Szopa, S., Talandier, C., Terray, P., Viovy, N., and Vuichard, N. (2013). Climate change projections using the IPSL-CM5 Earth System Model: from CMIP3 to CMIP5. Climate Dynamics, 40(9-10):2123–2165.

Emanuel, K. A., David Neelin, J., and Bretherton, C. S. (1994). On large-scale circulations in convecting atmospheres. Quarterly Journal of the Royal Meteorological Society, 120(519):1111–1143.

Eroglu, D., McRobie, F. H., Ozken, I., Stemler, T., Wyrwoll, K.-H., Breitenbach, S. F. M., Marwan, N., and Kurths, J. (2016). See–saw relationship of the holocene east asian–australian summer monsoon. Nature Communications, 7(1):12929.

Essery, R. L., Best, M. J., Betts, R. A., Cox, P. M., and Taylor, C. M. (01 Jun. 2003). Explicit representation of subgrid heterogeneity in a gcm land surface scheme. Journal of Hydrometeorology, 4(3):530 – 543.

Eyring, V., Bony, S., Meehl, G. A., Senior, C. A., Stevens, B., Stouffer, R. J., and Taylor, K. E. (2016). Overview of the coupled model intercomparison project phase 6 (cmip6) experimental design and organization. Geoscientific Model Development, 9(5):1937–1958.

Eyring, V., Gillett, N. P., Achuta Rao, K. M., Barimalala, R., Barreiro Parrillo, M., Bellouin, N., Cassou, C., Durack, P. J., Kosaka, Y., McGregor, S., Min, S., Morgenstern, O., and Sun, Y. (2021). Human influence on the climate system. In Masson-Delmotte, V., Zhai, P., Pirani, A., Connors, S. L., Péan, C., Berger, S., Caud, N., Chen, Y., Goldfarb, L., Gomis, M. I., Huang, M., Leitzell, K., Lonnoy, E., Matthews, J., Maycock, T. K., Waterfield, T., Yelekçi, O., Yu, R., , and Zhou, B., editors, Climate Change 2021: The Physical Science Basis. Contribution of Working Group I to the Sixth Assessment Report of the Intergovernmental Panel on Climate Change. Cambridge University Press.

Fasullo, J. (2012). A mechanism for land–ocean contrasts in global monsoon trends in a warming climate. Climate Dynamics, 39(5):1137–1147.

Fedorov, A. V., Brierley, C. M., Lawrence, K. T., Liu, Z., Dekens, P. S., and Ravelo, A. C. (2013). Patterns and mechanisms of early Pliocene warmth. Nature, 496(7443):43–49.

Feng, R., Otto-Bliesner, B. L., Xu, Y., Brady, E., Fletcher, T., and Ballantyne, A.

(2019). Contributions of aerosol-cloud interactions to mid-piacenzian seasonally sea ice-free arctic ocean. Geophysical Research Letters, 46(16):9920–9929.

Fichefet, T. and Maqueda, M. A. M. (1999). Modelling the influence of snow accumulation and snow-ice formation on the seasonal cycle of the antarctic sea-ice cover. Climate Dynamics, 15(4):251–268.

Flato, G., Marotzke, J., Abiodun, B., Braconnot, P., Chou, S. C., Collins, W., Cox, P., Driouech, F., Emori, S., Eyring, V., Forest, C., Gleckler, P., Guilyardi, E., Jakob, C., Kattsov, V., Reason, C., Rummukainen, M., AchutaRao, K., Anav, A., Andrews, T., Baehr, J., Bindoff, N. L., Bodas-Salcedo, A., Catto, J., Chambers, D., Chang, P., Dai, A., Deser, C., Doblas-Reyes, F., Durack, P. J., Eby, M., de Elia, R., Fichefet, T., Forster, P., Frame, D., Fyfe, J., Gbobaniyi, E., Gillett, N., González-Rouco, J. F., Goodess, C., Griffies, S., Hall, A., Harrison, S., Hense, A., Hunke, E., Ilyina, T., Ivanova, D., Johnson, G., Kageyama, M., Kharin, V., Klein, S. A., Knight, J., Knutti, R., Landerer, F., Lee, T., Li, H., Mahowald, N., Mears, C., Meehl, G., Morice, C., Msadek, R., Myhre, G., Neelin, J. D., Painter, J., Pavlova, T., Perlwitz, J., Peterschmitt, J.-Y., Räisänen, J., Rauser, F., Reid, J., Rodwell, M., Santer, B., Scaife, A. A., Schulz, J., Scinocca, J., Sexton, D., Shindell, D., Shiogama, H., Sillmann, J., Simmons, A., Sperber, K., Stephenson, D., Stevens, B., Stott, P., Sutton, R., Thorne, P. W., van Oldenborgh, G. J., Vecchi, G., Webb, M., Williams, K., Woollings, T., Xie, S.-P., and Zhang, J. (2013). Evaluation of climate models. In Stocker, T., Qin, D., Plattner, G.-K., Tignor, M., Allen, S., Boschung, J., Nauels, A., Xia, Y., Bex, V., and Midgley, P., editors, Climate change 2013: the physical science basis. Contribution of Working Group I to the Fifth Assessment Report of the Intergovernmental Panel on Climate Change, pages 741–866. Cambridge University Press.

Foley, K. M. and Dowsett, H. J. (2019). Community sourced mid- piacenzian sea surface temperature (sst) data. US Geological Survey data release. last access: 21 August 2021.

Folland, C. K., Karl, T. R., and Vinnikov, K. Y. (1990). Observed climate variations and change. In Houghton, J. T., Jenkins, G. J., and Ephraums, J., editors, Climate Change: The IPCC Scientific Assessment, page 195–238. Cambridge University Press.

Forster, P., Storelvmo, T., Armour, K., Collins, W., Dufresne, J., Frame, D., Lunt, D., Mauritsen, T., Palmer, M., Watanabe, M., Wild, M., and Zhang, H. (2021). The earth's energy budget, climate feedbacks, and climate sensitivity. In Masson-Delmotte, V., Zhai, P., Pirani, A., Connors, S. L., Péan, C., Berger, S., Caud, N., Chen, Y., Goldfarb, L., Gomis, M. I., Huang, M., Leitzell, K., Lonnoy, E., Matthews, J., Maycock, T. K., Waterfield, T., Yelekçi, O., Yu, R., , and Zhou, B., editors, Climate Change 2021: The Physical Science Basis. Contribution of Working Group I to the Sixth Assessment Report of the Intergovernmental Panel on Climate Change. Cambridge University Press.

Fox-Kemper, B., Hewitt, H. T., Xiao, C., Aalgeirsdóttir, G., Drijfhout, S. S., Edwards, T. L., Golledge, N. R., Hemer, M., Kopp, R. E., Krinner, G., Mix, A., Notz, D., Nowicki, S., Nurhati, I. S., Ruiz, L., Sallée, J.-B., Slangen, A. B. A., and Yu, Y. (2021). Ocean, cryosphere and sea level change. In Masson-Delmotte, V., Zhai, P., Pirani, A., Connors, S. L., Péan, C., Berger, S., Caud, N., Chen, Y., Goldfarb, L., Gomis, M. I., Huang, M., Leitzell, K., Lonnoy, E., Matthews, J., Maycock, T. K., Waterfield, T., Yelekçi, O., Yu, R., , and Zhou, B., editors, Climate Change 2021: The Physical Science Basis. Contribution of Working Group I to the Sixth Assessment Report of the Intergovernmental Panel on Climate Change. Cambridge University Press.

Gadgil, S. (2018). The monsoon system: Land–sea breeze or the itcz? Journal of Earth System Science, 127(1):1.

Gaetani, M., Messori, G., Zhang, Q., Flamant, C., and Pausata, F. S. R. (2017). Understanding the mechanisms behind the northward extension of the west african monsoon during the mid-holocene. Journal of Climate, 30(19):7621 – 7642.

Gao, J., Xie, Z., Wang, A., and Luo, Z. (2016). Numerical simulation based on two-directional freeze and thaw algorithm for thermal diffusion model. Applied Mathematics and Mechanics, 37(11):1467–1478.

Gent, P. R., Danabasoglu, G., Donner, L. J., Holland, M. M., Hunke, E. C., Jayne, S. R., Lawrence, D. M., Neale, R. B., Rasch, P. J., Vertenstein, M., Worley, P. H., Yang, Z.-L., and Zhang, M. (2011). The community climate system model version 4. Journal of Climate, 24(19):4973–4991.

Gettelman, A., Hannay, C., Bacmeister, J. T., Neale, R. B., Pendergrass, A. G., Danabasoglu, G., Lamarque, J., Fasullo, J. T., Bailey, D. A., Lawrence, D. M., and Mills, M. J. (2019). High Climate Sensitivity in the Community Earth System Model Version 2 (CESM2). Geophysical Research Letters, 46(14):8329–8337.

Gill, A. E. (1980). Some simple solutions for heat-induced tropical circulation. Quart. J. Roy. Meteorol. Soc., 106:447–462.

Giorgetta, M. A., Jungclaus, J., Reick, C. H., Legutke, S., Bader, J., Böttinger, M., Brovkin, V., Crueger, T., Esch, M., Fieg, K., Glushak, K., Gayler, V., Haak, H., Hollweg, H.-D., Ilyina, T., Kinne, S., Kornblueh, L., Matei, D., Mauritsen, T., Mikolajewicz, U., Mueller, W., Notz, D., Pithan, F., Raddatz, T., Rast, S., Redler, R., Roeckner, E., Schmidt, H., Schnur, R., Segschneider, J., Six, K. D., Stockhause, M., Timmreck, C., Wegner, J., Widmann, H., Wieners, K.-H., Claussen, M., Marotzke, J., and Stevens, B. (2013). Climate and carbon cycle changes from 1850 to 2100 in mpi-esm simulations for the coupled model intercomparison project phase 5. Journal of Advances in Modeling Earth Systems, 5(3):572–597.

Goldsmith, Y., Broecker, W. S., Xu, H., Polissar, P. J., deMenocal, P. B., Porat, N., Lan, J., Cheng, P., Zhou, W., and An, Z. (2017). Northward extent of east asian monsoon covaries with intensity on orbital and millennial timescales. Proceedings of the National Academy of Sciences, 114(8):1817–1821.

Gordon, H., Rotstayn, L., McGregor, J., Dix, M., Kowalczyk, O'Farrell, S., Waterman, L., HirstAC, Wilson, S., Collier, M., Watterson, I., and Elliott, T.

(2002). The CSIRO Mk3 climate system model. Asoendale: CSIRO Atmospheric Research Technical Paper.

Gordon, H. B., Farrell, S. O., Collier, M., Dix, M., Rotstayn, L., Kowalczyk, E., Hirst, A. C., and Watterson, I. (2010). The CSIRO Mk3.5 Climate Model. Technical report.

Govin, A., Braconnot, P., Capron, E., Cortijo, E., Duplessy, J.-C., Jansen, E., Labeyrie, L., Landais, A., Marti, O., Michel, E., Mosquet, E., Risebrobakken, B., Swingedouw, D., and Waelbroeck, C. (2012). Persistent influence of ice sheet melting on high northern latitude climate during the early last interglacial. Climate of the Past, 8(2):483–507.

Griffies, S. M. (2012). Elements of MOM5, GFDL Ocean Group Tech. Technical Report 7.

Griffies, S. M., Gnanadesikan, A., Dixon, K. W., Dunne, J. P., Gerdes, R., Harrison, M. J., Rosati, A., Russell, J. L., Samuels, B. L., Spelman, M. J., Winton, M., and Zhang, R. (2005). Formulation of an ocean model for global climate simulations. Ocean Science, 1(1):45–79.

Gulev, S. K., Thorne, P., Ahn, J., Dentener, F., Domingues, C., Gerland, S., Gong, D., Kaufman, D., Nnamchi, H., Quaas, J., Rivera, J., Sathyendranath, S., Smith, S., Trewin, B., von Shuckmann, K., and Vose, R. (2021). Changing state of the climate system. In Masson-Delmotte, V., Zhai, P., Pirani, A., Connors, S. L., Péan, C., Berger, S., Caud, N., Chen, Y., Goldfarb, L., Gomis, M. I., Huang, M., Leitzell, K., Lonnoy, E., Matthews, J., Maycock, T. K., Waterfield, T., Yelekçi, O., Yu, R., , and Zhou, B., editors, Climate Change 2021: The Physical Science Basis. Contribution of Working Group I to the Sixth Assessment Report of the Intergovernmental Panel on Climate Change. Cambridge University Press, Cambridge, United Kingdom and New York, U.S.A.

Guo, C., Bentsen, M., Bethke, I., Ilicak, M., Tjiputra, J., Toniazzo, T., Schwinger, J., and Otterå, O. H. (2019). Description and evaluation of NorESM1-F: a fast version of the Norwegian Earth System Model (NorESM). Geoscientific Model Development, 12(1):343–362.

Gurvan, M., Bourdallé-Badie, R., Bouttier, P.-A., Bricaud, C., Bruciaferri, D., Calvert, D., Chanut, J., Clementi, E., Coward, A., Delrosso, D., Ethé, C., Flavoni, S., Graham, T., Harle, J., Iovino, D., Lea, D., Lévy, C., Lovato, T., Martin, N., Masson, S., Mocavero, S., Paul, J., Rousset, C., Storkey, D., Storto, A., and Vancoppenolle, M. (2017). NEMO ocean engine.

Hadley, E. (1686). A historical account of the trade winds and monsoons observable in the seas between and near the tropics with an attempt to assign a physical cause of the said winds. Phil. Trans. Roy. Soc., 16:153–168.

Hadley, G. (1753). Concerning the cause of the general trade-winds. Phil. Trans. Roy. Soc., 39:58–62.

Hajima, T., Watanabe, M., Yamamoto, A., Tatebe, H., Noguchi, M. A., Abe, M., Ohgaito, R., Ito, A., Yamazaki, D., Okajima, H., Ito, A., Takata, K., Ogochi, K., Watanabe, S., and Kawamiya, M. (2020). Description of the miroc-es2l earth system model and evaluation of its climate–biogeochemical processes and feedbacks. Geoscientific Model Development, 13:2197–2244.

Halloran, P. R. (2012). Does atmospheric CO2 seasonality play an important role in governing the air-sea flux of CO2? Biogeosciences, 9(6):2311–2323.

Hansen, J., Sato, M., and Ruedy, R. (1997). Radiative forcing and climate response. Journal of Geophysical Research: Atmospheres, 102(D6):6831–6864.

Hargreaves, J. C., Annan, J. D., Ohgaito, R., Paul, A., and Abe-Ouchi, A. (2013). Skill and reliability of climate model ensembles at the last glacial maximum and mid-holocene. Climate of the Past, 9(2):811–823.

Harrison, S., Bartlein, P., Brewer, S., Prentice, I., Boyd, M., Hessler, I., Holmgren, K., Izumi, K., and Willis, K. (2014). Climate model benchmarking with glacial and mid-holocene climates. Climate Dynamics, 43(3-4):671–688.

Harrison, S., Braconnot, P., Hewitt, C., and Stouffer, R. J. (2002). Fourth International Workshop of the Palaeoclimate Modelling Intercomparison Project (PMIP): Launching PMIP2 Phase II. EOS, 83:447.

Harrison, S. P., Bartlein, P., Izumi, K., Li, G., Annan, J., Hargreaves, J., Braconnot, P., and Kageyama, M. (2015). Evaluation of cmip5 palaeo-simulations to improve climate projections. Nature Climate Change, 5(8):735–743.

Hasumi, H., Emori, S. (2004). K-1 Coupled GCM (MIROC) Description. Center for Climate System Research, University of Tokyo, Tokyo, Japan,. Technical report.

Haug, G. H., Hughen, K. A., Sigman, D. M., Peterson, L. C., and Röhl, U. (2001). Southward migration of the intertropical convergence zone through the holocene. Science, 293:1304–1308.

Haywood, A. M., Dowsett, H. J., and Dolan, A. M. (2016a). Integrating geological archives and climate models for the mid-Pliocene warm period. Nature Communications, 7(1):10646.

Haywood, A. M., Dowsett, H. J., Dolan, A. M., Rowley, D., Abe-Ouchi, A., Otto-Bliesner, B., Chandler, M. A., Hunter, S. J., Lunt, D. J., Pound, M., and Salzmann, U. (2016b). The Pliocene Model Intercomparison Project (PlioMIP) Phase 2: Scientific objectives and experimental design. Climate of the Past, 12(3):663–675.

Haywood, A. M., Dowsett, H. J., Otto-Bliesner, B., Chandler, M. A., Dolan, A. M., Hill, D. J., Lunt, D. J., Robinson, M. M., Rosenbloom, N., Salzmann, U., and Sohl, L. E. (2010). Pliocene Model Intercomparison Project (PlioMIP): experimental design and boundary conditions (Experiment 1). Geoscientific Model Development, 3(1):227–242.

Haywood, A. M., Dowsett, H. J., Robinson, M. M., Stoll, D. K., Dolan, A. M., Lunt, D. J., Otto-Bliesner, B., and Chandler, M. A. (2011). Pliocene Model Intercomparison Project (PlioMIP): experimental design and boundary conditions (Experiment 2). Geoscientific Model Development, 4(3):571–577.

Haywood, A. M., Hill, D. J., Dolan, A. M., Otto-Bliesner, B. L., Bragg, F., Chan, W.-L., Chandler, M. A., Contoux, C., Dowsett, H. J., Jost, A., Kamae, Y., Lohmann, G., Lunt, D. J., Abe-Ouchi, A., Pickering, S. J., Ramstein, G., Rosenbloom, N. A., Salzmann, U., Sohl, L., Stepanek, C., Ueda, H., Yan, Q., and Zhang, Z. (2013). Large-scale features of pliocene climate: results from the pliocene model intercomparison project. Climate of the Past, 9(1):191–209.

Haywood, A. M., Tindall, J. C., Dowsett, H. J., Dolan, A. M., Foley, K. M., Hunter, S. J., Hill, D. J., Chan, W.-L., Abe-Ouchi, A., Stepanek, C., Lohmann, G., Chandan, D., Peltier, W. R., Tan, N., Contoux, C., Ramstein, G., Li, X., Zhang, Z., Guo, C., Nisancioglu, K. H., Zhang, Q., Li, Q., Kamae, Y., Chandler, M. A., Sohl, L. E., Otto-Bliesner, B. L., Feng, R., Brady, E. C., von der Heydt, A. S., Baatsen, M. L. J., and Lunt, D. J. (2020). The pliocene model intercomparison project phase 2: large-scale climate features and climate sensitivity. Climate of the Past, 16(6):2095–2123.

Haywood, A. M. and Valdes, P. J. (2004). Modelling Pliocene warmth: Contribution of atmosphere, oceans and cryosphere. Earth and Planetary Science Letters, 218(3-4):363–377.

Hazeleger, W., Wang, X., Severijns, C., Ştefănescu, S., Bintanja, R., Sterl, A., Wyser, K., Semmler, T., Yang, S., Van den Hurk, B., van Noije, T., van der Linden, E., van der Wiel, K Hazeleger, W., Bintanja, R., Hazeleger, W., and Bintanja, R. (2012). Ec-earth v2. 2: description and validation of a new seamless earth system prediction model. Climate dynamics, 39(11):2611–2629.

He, B., Yu, Y., Bao, Q., Lin, P., Liu, H., Li, J., Wang, L., Liu, Y., Wu, G., Chen, K., Guo, Y., Zhao, S., Zhang, X., Song, M., and Xie, J. (2020). CAS FGOALS-f3-L Model dataset descriptions for CMIP6 DECK experiments. Atmospheric and Oceanic Science Letters, ahead-of-print:1–7.

Hewitt, H. T., Copsey, D., Culverwell, I. D., Harris, C. M., Hill, R. S. R., Keen, A. B., McLaren, A. J., and Hunke, E. C. (2011). Design and implementation of the infrastructure of hadgem3: the next-generation met office climate modelling system. Geoscientific Model Development, 4(2):223–253.

Hill, D. J., Haywood, A. M., Lunt, D. J., Hunter, S. J., Bragg, F. J., Contoux, C., Stepanek, C., Sohl, L., Rosenbloom, N. A., Chan, W. L., Kamae, Y., Zhang, Z., Abe-Ouchi, A., Chandler, M. A., Jost, A., Lohmann, G., Otto-Bliesner, B. L., Ramstein, G., and Ueda, H. (2014). Evaluating the dominant components of warming in Pliocene climate simulations. Climate of the Past, 10(1):79–90.

Hoffman, J. S., Clark, P. U., Parnell, A. C., and He, F. (2017). Regional and global sea-surface temperatures during the last interglaciation. Science, 355(6322):276–279.

Holland, M. M., Bailey, D. A., Briegleb, B. P., Light, B., and Hunke, E. (2012). Improved sea ice shortwave radiation physics in CCSM4: The impact of melt ponds and aerosols on Arctic sea ice. Journal of Climate, 25(5):1413 – 1430.

Holloway, M. D., Sime, L. C., Singarayer, J. S., Tindall, J. C., and Valdes, P. J. (2018). Simulating the 128-ka antarctic climate response to northern hemisphere ice sheet melting using the isotope-enabled hadcm3. Geophysical Research Letters, 45(21):11,921–11,929.

Hopcroft, P. O. and Valdes, P. J. (2019). On the role of dust-climate feedbacks during the mid-holocene. Geophysical Research Letters, 46(3):1612–1621.

Hopcroft, P. O., Valdes, P. J., Harper, A. B., and Beerling, D. J. (2017). Multi vegetation model evaluation of the green sahara climate regime. Geophysical Research Letters, 44(13):6804–6813.

Hourdin, F., Foujols, M. A., Codron, F., Guemas, V., Dufresne, J. L., Bony, S., Denvil, S., Guez, L., Lott, F., Ghattas, J., Braconnot, P., Marti, O., Meurdesoif, Y., and Bopp, L. (2013). Impact of the LMDZ atmospheric grid configuration on the climate and sensitivity of the IPSL-CM5A coupled model. Climate Dynamics, 40:2167–2192.

Huang, B., Thorne, P. W., Banzon, V. F., Boyer, T., Chepurin, G., Lawrimore, J. H., Menne, M. J., Smith, T. M., Vose, R. S., and Zhang, H.-M. (2017). Extended reconstructed sea surface temperature, version 5 (ersstv5): Upgrades, validations, and intercomparisons. Journal of Climate, 30(20):8179 – 8205.

Hunke, E. C. and Lipscomb, W. H. (2010). The Los Alamos Sea Ice Model, Documentation and Software User's Manual, Version 4.1, Los Alamos National Laboratory.

Hunke, E. C., Lipscomb, W. H., Turner, A. K., Jeffery, N., and Elliott, S. (2015). CICE: The Los Alamos Sea Ice Model. Documentation and Software User's Manual. Version 5.1. Technical Report Tech. Rep. LA-CC-06-012.

Hurrell, J. W., Holland, M. M., Gent, P. R., Ghan, S., Kay, J. E., Kushner, P. J., Lamarque, J.-F., Large, W. G., Lawrence, D., Lindsay, K., Lipscomb, W. H., Long, M. C., Mahowald, N., Marsh, D. R., Neale, R. B., Rasch, P., Vavrus, S., Vertenstein, M., Bader, D., Collins, W. D., Hack, J. J., Kiehl, J., and Marshall, S. (2013). The Community Earth System Model: A Framework for Collaborative Research. Bulletin of the American Meteorological Society, 94(9):1339–1360.

Hwang, Y.-T., Frierson, D. M. W., and Kang, S. M. (2013). Anthropogenic sulfate aerosol and the southward shift of tropical precipitation in the late 20th century. Geophysical Research Letters, 40(11):2845–2850.

Ibarra, D. E., Oster, J. L., Winnick, M. J., Caves Rugenstein, J. K., Byrne, M. P., and Chamberlain, C. P. (2018). Warm and cold wet states in the western United States during the Pliocene–Pleistocene. Geology, 46(4):355–358.

Ilyas, M., Brierley, C. M., and Guillas, S. (2017). Uncertainty in regional temperatures inferred from sparse global observations: Application to a probabilistic classification of el niño. Geophysical Research Letters, 44(17):9068–9074.

Ilyina, T., Six, K. D., Segschneider, J., Maier-Reimer, E., Li, H., and NÃºÃ±ez-Riboni, I. (2013). Global ocean biogeochemistry model hamocc: Model architecture and performance as component of the mpi-earth system model in different cmip5 experimental realizations. Journal of Advances in Modeling Earth Systems, 5(2):287–315.

IPCC (2007). Climate Change 2007 - The Physical Science Basis. Working Group I Contribution to the Fourth Assessment Report of the IPCC. Cambridge University Press.

IPCC (2013). Climate Change 2013: The Physical Science Basis. Working Group I Contribution to the IPCC Fifth Assessment Report. Cambridge University Press.

IPCC (2021a). Annex ii: Models [gutierrez, j.m., a-m. treguier (eds.)]. In Masson-Delmotte, V., Zhai, P., Pirani, A., Connors, S. L., Péan, C., Berger, S., Caud, N., Chen, Y., Goldfarb, L., Gomis, M. I., Huang, M., Leitzell, K., Lonnoy, E., Matthews, J., Maycock, T. K., Waterfield, T., Yelekçi, O., Yu, R., , and Zhou, B., editors, Climate Change 2021: The Physical Science Basis. Contribution of Working Group I to the Sixth Assessment Report of the Intergovernmental Panel on Climate Change. Cambridge University Press.

IPCC (2021b). Annex v: Monsoons [cherchi, a., a. turner (eds.)]. In Masson-Delmotte, V., Zhai, P., Pirani, A., Connors, S. L., Péan, C., Berger, S., Caud, N., Chen, Y., Goldfarb, L., Gomis, M. I., Huang, M., Leitzell, K., Lonnoy, E., Matthews, J., Maycock, T. K., Waterfield, T., Yelekçi, O., Yu, R., , and Zhou, B., editors, Climate Change 2021: The Physical Science Basis. Contribution of Working Group I to the Sixth Assessment Report of the Intergovernmental Panel on Climate Change. Cambridge University Press.

IPCC (2021c). Annex vii: Glossary [matthews, j. b. r., j. s. fuglestvedt, v. masson-delmotte, v. möller, c. 36 méndez, r. van diemen, a. reisinger, s. semenov (ed.)]. In Masson-Delmotte, V., Zhai, P., Pirani, A., Connors, S. L., Péan, C., Berger, S., Caud, N., Chen, Y., Goldfarb, L., Gomis, M. I., Huang, M., Leitzell, K., Lonnoy, E., Matthews, J., Maycock, T. K., Waterfield, T., Yelekçi, O., Yu, R., , and Zhou, B., editors, Climate Change 2021: The Physical Science Basis. Contribution of Working Group I to the Sixth Assessment Report of the Intergovernmental Panel on Climate Change. Cambridge University Press.

IPCC (2021d). Summary for policymakers. In Masson-Delmotte, V., Zhai, P., Pirani, A., Connors, S. L., Péan, C., Berger, S., Caud, N., Chen, Y., Goldfarb, L., Gomis, M. I., Huang, M., Leitzell, K., Lonnoy, E., Matthews, J., Maycock, T. K., Waterfield, T., Yelekçi, O., Yu, R., , and Zhou, B., editors, Climate Change 2021: The Physical Science Basis. Contribution of Working Group I to the Sixth Assessment Report of the Intergovernmental Panel on Climate Change. Cambridge University Press, Cambridge, United Kingdom and New York, U.S.A.

Ivanovic, R. F., Capron, E., and Gregoire, L. (2021). New pmip challenges: simulations of deglaciations and abrupt earth system changes. PAGES, 29(2):78–79.

Jansen, E., Overpeck, J., Briffa, K., Duplessy, J.-C., Joos, F., Masson-Delmotte, V., Olago, D., Otto-Bliesner, B., Peltier, W., Rahmstorf, S., Ramesh, R., Raynaud, D., Rind, D., Solomina, O., Villalba, R., and Zhang, D. (2007). Palaeoclimate. In Solomon, S., Qin, D., Manning, M., Chen, Z., Marquis, M., Averyt, K., Tignor, M., and Miller, H., editors, Climate Change 2007: The Physical Science Basis. Contribution of Working Group I to the Fourth Assessment Report of the Intergovernmental Panel on Climate Change. Cambridge University Press.

Jiang, D., Lang, X., Tian, Z., and Ju, L. (2013). Mid-holocene east asian summer monsoon strengthening: Insights from paleoclimate modeling intercomparison project (pmip) simulations. Palaeogeography, Palaeoclimatology, Palaeoecology, 369:422–429.

Jiang, D., Tian, Z., and Lang, X. (2015). Mid-holocene global monsoon area and precipitation from pmip simulations. Climate Dynamics, 44(9-10):2493–2512.

Jin, L., Schneider, B., Park, W., Latif, M., Khon, V., and Zhang, X. (2014). The spatial–temporal patterns of asian summer monsoon precipitation in response to holocene insolation change: a model-data synthesis. Quaternary Science Reviews, 85:47–62.

Johns, T. C., Durman, C. F., Banks, H. T., Roberts, M. J., McLaren, A. J., Ridley, J. K., Senior, C. A., Williams, K. D., Jones, A., Rickard, G. J., Cusack, S., Ingram, W. J., Crucifix, M., Sexton, D. M., Joshi, M. M., Dong, B. W., Spencer, H., Hill, R. S., Gregory, J. M., Keen, A. B., Pardaens, A. K., Lowe, J. A., Bodas-Salcedo, A., Stark, S., and Searl, Y. (2006). The new Hadley Centre Climate Model (HadGEM1): Evaluation of coupled simulations. Journal of Climate, 19(7):1327–1353.

Joussaume, S. and Braconnot, P. (1997). Sensitivity of paleoclimate simulation results to season definitions. Journal of Geophysical Research: Atmospheres, 102(D2):1943–1956.

Joussaume, S. and Taylor, K. E. (1995). Status of the Paleoclimate Modelling Intercomparison Project (PMIP).Proceedings of the first international AMIP scientific conference. pages 425–430.

Joussaume, S., Taylor, K. E., Braconnot, P., Mitchell, J. F. B., Kutzbach, J. E., Harrison, S. P., Prentice, I. C., Broccoli, A. J., Abe-Ouchi, A., Bartlein, P. J., Bonfils, C., Dong, B., Guiot, J., Herterich, K., Hewitt, C. D., Jolly, D., Kim, J. W., Kislov, A., Kitoh, A., Loutre, M. F., Masson, V., McAvaney, B., McFarlane, N., de Noblet, N., Peltier, W. R., Peterschmitt, J. Y., Pollard, D., Rind, D., Royer, J. F., Schlesinger, M. E., Syktus, J., Thompson, S., Valdes, P., Vettoretti, G., Webb, R. S., and Wyputta, U. (1999). Monsoon changes for 6000 years ago: Results of 18 simulations from the paleoclimate modeling intercomparison project (pmip). Geophysical Research Letters, 26(7):859–862.

Jouzel, J., Masson-Delmotte, V., Cattani, O., Dreyfus, G., Falourd, S., Hoffmann, G., Minster, B., Nouet, J., Barnola, J. M., Chappellaz, J., Fischer, H., Gallet, J. C., Johnsen, S., Leuenberger, M., Loulergue, L., Luethi, D., Oerter, H., Parrenin, F., Raisbeck, G., Raynaud, D., Schilt, A., Schwander, J., Selmo, E., Souchez, R., Spahni, R., Stauffer, B., Steffensen, J. P., Stenni, B., Stocker, T. F., Tison, J. L., Werner, M., and Wolff, E. W. (2007). Orbital and millennial antarctic climate variability over the past 800,000 years. Science, 317(5839):793–796.

Juckes, M., Taylor, K. E., Durack, P. J., Lawrence, B., Mizielinski, M. S., Pamment, A., Peterschmitt, J.-Y., Rien, M., and Sénési, S. (2020). The cmip6 data request (dreq, version 01.00.31). Geoscientific Model Development, 13(1):201–224.

Jungclaus, J. H., Bard, E., Baroni, M., Braconnot, P., Cao, J., Chini, L. P., Egorova, T., Evans, M., González-Rouco, J. F., Goosse, H., Hurtt, G. C., Joos, F., Kaplan, J. O., Khodri, M., Klein Goldewijk, K., Krivova, N., LeGrande, A. N., Lorenz, S. J., Luterbacher, J., Man, W., Maycock, A. C., Meinshausen, M., Moberg, A., Muscheler, R., Nehrbass-Ahles, C., Otto-Bliesner, B. I., Phipps, S. J., Pongratz, J., Rozanov, E., Schmidt, G. A., Schmidt, H., Schmutz, W., Schurer, A., Shapiro, A. I., Sigl, M., Smerdon, J. E., Solanki, S. K., Timmreck, C., Toohey, M., Usoskin, I. G., Wagner, S., Wu, C.-J., Yeo, K. L., Zanchettin, D., Zhang, Q., and Zorita, E. (2017). The pmip4 contribution to cmip6 – part 3: The last millennium, scientific objective, and experimental design for the pmip4 *past1000* simulations. Geoscientific Model Development, 10(11):4005–4033.

Jungclaus, J. H., Fischer, N., Haak, H., Lohmann, K., Marotzke, J., Matei, D., Mikolajewicz, U., Notz, D., and von Storch, J. S. (2013). Characteristics of the ocean simulations in the Max Planck Institute Ocean Model (MPIOM) the ocean component of the MPI-Earth system model. Journal of Advances in Modeling Earth Systems, 5(2):422–446.

Kageyama, M., Albani, S., Braconnot, P., Harrison, S. P., Hopcroft, P. O., Ivanovic, R. F., Lambert, F., Marti, O., Richard Peltier, W., Peterschmitt, J. Y., Roche, D. M., Tarasov, L., Zhang, X., Brady, E. C., Haywood, A. M., Legrande, A. N., Lunt, D. J., Mahowald, N. M., Mikolajewicz, U., Nisancioglu, K. H., Otto-Bliesner, B. L., Renssen, H., Tomas, R. A., Zhang, Q., Abe-Ouchi, A., Bartlein, P. J., Cao, J., Li, Q., Lohmann, G., Ohgaito, R., Shi, X., Volodin, E., Yoshida, K., Zhang, X., and Zheng, W. (2017). The PMIP4 contribution to CMIP6 - Part 4:

Scientific objectives and experimental design of the PMIP4-CMIP6 Last Glacial Maximum experiments and PMIP4 sensitivity experiments. Geoscientific Model Development, 10(11):4035–4055.

Kageyama, M., Braconnot, P., Harrison, S. P., Haywood, A. M., Jungclaus, J. H., Otto-Bliesner, B. L., Abe-Ouchi, A., Albani, S., Bartlein, P. J., and Brierley, C. (2018). The pmip4 contribution to cmip6-part 1: Overview and over-arching analysis plan. Geoscientific Model Development, 11(3):1033–1057.

Kageyama, M., Harrison, S. P., Kapsch, M.-L., Lofverstrom, M., Lora, J. M., Mikolajewicz, U., Sherriff-Tadano, S., Vadsaria, T., Abe-Ouchi, A., Bouttes, N., Chandan, D., Gregoire, L. J., Ivanovic, R. F., Izumi, K., LeGrande, A. N., Lhardy, F., Lohmann, G., Morozova, P. A., Ohgaito, R., Paul, A., Peltier, W. R., Poulsen, C. J., Quiquet, A., Roche, D. M., Shi, X., Tierney, J. E., Valdes, P. J., Volodin, E., and Zhu, J. (2021). The pmip4 last glacial maximum experiments: preliminary results and comparison with the pmip3 simulations. Climate of the Past, 17(3):1065–1089.

Karas, C., Nürnberg, D., Bahr, A., Groeneveld, J., Herrle, J. O., Tiedemann, R., and deMenocal, P. B. (2017). Pliocene oceanic seaways and global climate. Scientific Reports, 7(1):39842.

Kaufman, D., McKay, N., Routson, C., Erb, M., Dätwyler, C., Sommer, P., Heiri, O., and Davis, B. (2020a). Holocene global mean surface temperature: a multi-method reconstruction approach. Scientific Data, 7:1–13.

Kaufman, D., McKay, N., Routson, C., Erb, M., Davis, B., Heiri, O., Jaccard, S., Tierney, J., Dätwyler, C., Axford, Y., Brussel, T., Cartapanis, O., Chase, B., Dawson, A., de Vernal, A., Engels, S., Jonkers, L., Marsicek, J., Moffa-Sánchez, P., Morrill, C., Orsi, A., Rehfeld, K., Saunders, K., Sommer, P. S., Thomas, E., Tonello, M., Tóth, M., Vachula, R., Andreev, A., Bertrand, S., Biskaborn, B., Bringué, M., Brooks, S., Caniupán, M., Chevalier, M., Cwynar, L., Emile-Geay, J., Fegyveresi, J., Feurdean, A., Finsinger, W., Fortin, M.-C., Foster, L., Fox, M., Gajewski, K., Grosjean, M., Hausmann, S., Heinrichs, M., Holmes, N., Ilyashuk, B., Ilyashuk, E., Juggins, S., Khider, D., Koinig, K., Langdon, P., Larocque-Tobler, I., Li, J., Lotter, A., Luoto, T., Mackay, A., Magyari, E., Malevich, S., Mark, B., Massaferro, J., Montade, V., Nazarova, L., Novenko, E., Pařil, P., Pearson, E., Peros, M., Pienitz, R., Płóciennik, M., Porinchu, D., Potito, A., Rees, A., Reinemann, S., Roberts, S., Rolland, N., Salonen, S., Self, A., Seppa, H., Shala, S., St-Jacques, J.-M., Stenni, B., Syrykh, L., Tarrats, P., Taylor, K., van den Bos, V., Velle, G., Wahl, E., Walker, I., Wilmshurst, J., Zhang, E., and Zhilich, S. (2020b). A global database of Holocene paleo-temperature records. Scientific Data, 7(1):115.

Kelley, M., Schmidt, G. A., Nazarenko, L., Bauer, S. E., Ruedy, R., Russell, G. L., Ackerman, A. S., Aleinov, I., Bauer, M., Bleck, R., Canuto, V., Cesana, G., Cheng, Y., Clune, T. L., Cook, B. I., Cruz, C. A., Del Genio, A. D., Elsaesser, G. S., Faluvegi, G., Kiang, N. Y., Kim, D., Lacis, A. A., Leboissetier, A., LeGrande, A. N., Lo, K. K., Marshall, J., Matthews, E. E., McDermid, S., Mezuman, K., Miller, R. L., Murray, L. T., Oinas, V., Orbe, C., Pérez García-Pando, C., Perlwitz, J. P., Puma, M. J., Rind, D., Romanou, A., Shindell, D. T., Sun, S., Tausnev, N., Tsigaridis, K., Tselioudis, G., Weng, E., Wu, J., and Yao, M.-S. (2020). Giss-e2.1: Configurations and climatology. J. Adv. Model. Earth Syst., 12(8):e2019MS002025.

Khan, S., Farooqui, A., Shukla, U. K., Grøsfjeld, K., Knies, J., and Prasad, V. (2022). Late pliocene continental climate and vegetation variability in the arctic-atlantic gateway region prior to the intensification of northern hemisphere glaciations. Palaeogeography, Palaeoclimatology, Palaeoecology, 586:110746.

Kiehl, J. T. and Shields, C. A. (2013). Sensitivity of the Palaeocene-Eocene Thermal Maximum climate to cloud properties. Philosophical Transactions of the Royal Society A: Mathematical, Physical and Engineering Sciences, 371(2001):20130093–20130093.

Kim, J.-H., Schouten, S., Hopmans, E. C., Donner, B., and Sinninghe Damsté, J. S.

(2008). Global sediment core-top calibration of the tex86 paleothermometer in the ocean. Geochimica et Cosmochimica Acta, 72(4):1154–1173.

Knutti, R., Masson, D., and Gettelman, A. (2013). Climate model genealogy: Generation cmip5 and how we got there. Geophysical Research Letters, 40(6):1194–1199.

Kohfeld, K. E. and Harrison, S. P. (2000). How well can we simulate past climates? evaluating the models using global palaeoenvironmental datasets. Quaternary Science Reviews, 19(1-5):321–346.

Kou, X.-Y., Ferguson, D. K., Xu, J.-X., Wang, Y.-F., and Li, C.-S. (2006). The reconstruction of paleovegetation and paleoclimate in the late pliocene of west yunnan, china. Climatic Change, 77(3):431–448.

Kowalczyk, E. A., Stevens, L., Law, R. M., Dix, M., Wang, Y. P., Harman, I. N., Haynes, K., Srbinovsky, J., Pak, B., and Ziehn, T. (2013). The land surface model component of access: description and impact on the simulated surface climatology. Aus. Meteor. Oceanogr., 63:65—-82.

Kowalczyk, E. A., Stevens, L. E., Law, R. M., Harman, I. N., Dix, M., Franklin, C. N., and Wang, Y.-P. (2016). The impact of changing the land surface scheme in access(v1.0/1.1) on the surface climatology. Geoscientific Model Development, 9(8):2771–2791.

Krinner, G., Viovy, N., de Noblet-Ducoudré, N., Ogée, J., Polcher, J., Friedlingstein, P., Ciais, P., Sitch, S., and Prentice, I. C. (2005). A dynamic global vegetation model for studies of the coupled atmosphere-biosphere system. Global Biogeochemical Cycles, 19(1):GB1015.

Kroon, D. and Ganssen, G. (1989). Northern indian ocean upwelling cells and the stable isotope composition of living planktonic foraminifers. Deep-sea research. Part A. Oceanographic research papers, 36(8):1219–1236.

Lamarque, J. F., Bond, T. C., Eyring, V., Granier, C., Heil, A., Klimont, Z., Lee, D., Liousse, C., Mieville, A., Owen, B., Schultz, M. G., Shindell, D., Smith, S. J., Stehfest, E., Van Aardenne, J., Cooper, O. R., Kainuma, M., Mahowald, N., McConnell, J. R., Naik, V., Riahi, K., and Van Vuuren, D. P. (2010). Historical (1850-2000) gridded anthropogenic and biomass burning emissions of reactive gases and aerosols: Methodology and application. Atmospheric Chemistry and Physics, 10(15):7017–7039.

Lambert, F. and Albani, S. (2021). mineral dust in pmip simulations: a short review. PAGES, 29(2):86–87.

Lambert, F., Kug, J. S., Park, R. J., Mahowald, N., Winckler, G., Abe-Ouchi, A., O'Ishi, R., Takemura, T., and Lee, J. H. (2013). The role of mineral-dust aerosols in polar temperature amplification. Nature Climate Change, 3:487–491.

Laskar, J., Fienga, A., Gastineau, M., and Manche, H. (2011). La2010: a new orbital solution for the long-term motion of the Earth. A&A, 532:A89.

Laskar, J., Robutel, P., Joutel, F., Gastineau, M., Correia, A. C. M., and Levrard, B. (2004). A long term numerical solution for the insolation quantities of the Earth. Astronomy & Astrophysics, 428(1):261–285.

Lawrence, D. M., Fisher, R. A., Koven, C. D., Oleson, K. W., Swenson, S. C., Bonan, G., Collier, N., Ghimire, B., van Kampenhout, L., Kennedy, D., Kluzek, E., Lawrence, P. J., Li, F., Li, H., Lombardozzi, D., Riley, W. J., Sacks, W. J., Shi, M., Vertenstein, M., Wieder, W. R., Xu, C., Ali, A. A., Badger, A. M., Bisht, G., van den Broeke, M., Brunke, M. A., Burns, S. P., Buzan, J., Clark, M., Craig, A., Dahlin, K., Drewniak, B., Fisher, J. B., Flanner, M., Fox, A. M., Gentine, P., Hoffman, F., Keppel-Aleks, G., Knox, R., Kumar, S., Lenaerts, J., Leung, L. R., Lipscomb, W. H., Lu, Y., Pandey, A., Pelletier, J. D., Perket, J., Randerson, J. T., Ricciuto, D. M., Sanderson, B. M., Slater, A., Subin, Z. M., Tang, J., Thomas, R. Q., Val Martin, M., and Zeng, X. (2019). The community land model version

5: Description of new features, benchmarking, and impact of forcing uncertainty. Journal of Advances in Modeling Earth Systems, 11(12):4245–4287.

Lee, J. Y., Marotzke, J., Bala, G., Cao, L., Corti, S., Dunne, J., Engelbrecht, F., Fischer, E., Fyfe, J., Jones, C., Maycock, A., Mutemi, J., Ndiaye, O., Panickal, S., and Zhou, T. (2021). Future global climate: Scenario-based projections and near-term information. In Masson-Delmotte, V., Zhai, P., Pirani, A., Connors, S. L., Péan, C., Berger, S., Caud, N., Chen, Y., Goldfarb, L., Gomis, M. I., Huang, M., Leitzell, K., Lonnoy, E., Matthews, J., Maycock, T. K., Waterfield, T., Yelekçi, O., Yu, R., , and Zhou, B., editors, Climate Change 2021: The Physical Science Basis. Contribution of Working Group I to the Sixth Assessment Report of the Intergovernmental Panel on Climate Change. Cambridge University Press.

Levis, S., Bonan, G. B., and Bonfiles, C. (2004). Soil feedback drives the mid-holocene north african monsoon northward in fully coupled ccsm2 simulations with a dynamic vegetation model. Clim. Dynam., 23:791–802.

Li, L., Lin, P., Yu, Y., Wang, B., Zhou, T., Liu, L., Liu, J., Bao, Q., Xu, S., Huang, W., Xia, K., Pu, Y., Dong, L., Shen, S., Liu, Y., Hu, N., Liu, M., Sun, W., Shi, X., Zheng, W., Wu, B., Song, M., Liu, H., Zhang, X., Wu, G., Xue, W., Huang, X., Yang, G., Song, Z., and Qiao, F. (2013a). The flexible global ocean-atmosphere-land system model, grid-point version 2: Fgoals-g2. Advances in Atmospheric Sciences, 30(3):543–560.

Li, L., Wang, B., Dong, L., Liu, L., Shen, S., Hu, N., Sun, W., Wang, Y., Huang, W., Shi, X., Pu, Y., and Yang, G. (2013b). Evaluation of grid-point atmospheric model of iap lasg version 2 (gamil2). Advances in Atmospheric Sciences, 30(3):855–867.

Li, L., Yu, Y., Tang, Y., Lin, P., Xie, J., Song, M., Dong, L., Zhou, T., Liu, L., Wang, L., Pu, Y., Chen, X., Chen, L., Xie, Z., Liu, H., Zhang, L., Huang, X., Feng, T., Zheng, W., Xia, K., Liu, H., Liu, J., Wang, Y., Wang, L., Jia, B., Xie, F., Wang, B., Zhao, S., Yu, Z., Zhao, B., and Wei, J. (2020). The flexible global ocean-atmosphere-land system model grid-point version 3 (fgoals-g3): Description and evaluation. Journal of Advances in Modeling Earth Systems, 12(9):e2019MS002012.

Li, X., Jiang, D., Tian, Z., and Yang, Y. (2018). Mid-pliocene global land monsoon from pliomip1 simulations. Palaeogeography, Palaeoclimatology, Palaeoecology, 512:56–70.

Li, X., Yu, Y., Liu, H., and Lin, P. (2017). Sensitivity of atlantic meridional overturning circulation to the dynamical framework in an ocean general circulation model. Journal of Meteorological Research, 31(3):490–501.

Lin, P., Yu, Y., and Liu, H. (2013). Long-term stability and oceanic mean state simulated by the coupled model fgoals-s2. Advances in Atmospheric Sciences, 30(1):175–192.

Lisiecki, L. E. and Raymo, M. E. (2005). A Pliocene-Pleistocene stack of 57 globally distributed benthic δ 18O records. Paleoceanography, 20(1):1–17.

Liu, H., Lin, P., Yu, Y., and Zhang, X. (2012a). The baseline evaluation of lasg/iap climate system ocean model (licom) version 2. Acta Meteorologica Sinica, 26(3):318–329.

Liu, J. (2010). Sensitivity of sea ice and ocean simulations to sea ice salinity in a coupled global climate model. Science China Earth Sci., 53:911–918.

Liu, J., Chen, J., Zhang, X., Li, Y., Rao, Z., and Chen, F. (2015). Holocene east asian summer monsoon records in northern china and their inconsistency with chinese stalagmite 18o records. Earth-Science Reviews, 148:194–208.

Liu, J., Ning, L., Yan, M., Sun, W., Chen, K., and Qin, Y. (2021). Paleomonsoon modeling within pmip: recent progress and future directions. PAGES, 29(96–97).

Liu, L., Zhang, C., Li, R., Wang, B., and Yang, G. (2018). C-coupler2: a flexible and user-friendly community coupler for model coupling and nesting. Geoscientific Model Development, 11(9):3557–3586.

Liu, S., Xie, Z., Zeng, Y., Liu, B., Li, R., Wang, Y., Wang, L., Qin, P., Jia, B., and Xie, J. (2019). Effects of anthropogenic nitrogen discharge on dissolved inorganic nitrogen transport in global rivers. Global Change Biology, 25(4):1493–1513.

Liu, X., Easter, R. C., Ghan, S. J., Zaveri, R., Rasch, P., Shi, X., Lamarque, J. F., Gettelman, A., Morrison, H., Vitt, F., Conley, A., Park, S., Neale, R., Hannay, C., Ekman, A. M., Hess, P., Mahowald, N., Collins, W., Iacono, M. J., Bretherton, C. S., Flanner, M. G., and Mitchell, D. (2012b). Toward a minimal representation of aerosols in climate models: Description and evaluation in the Community Atmosphere Model CAM5. Geoscientific Model Development, 5(3):709–739.

Liu, Y., Hu, J., He, B., Bao, Q., Duan, A., and Wu, G. (2013). Seasonal evolution of subtropical anticyclones in the climate system model fgoals-s2. Advances in Atmospheric Sciences, 30(3):593–606.

Liu, Z., Harrison, S. P., Kutzbach, J., and Otto-Bliesner, B. (2004). Global monsoons in the mid-holocene and oceanic feedback. Climate Dynamics, 22(2):157–182.

Liu, Z., Zhu, J., Rosenthal, Y., Zhang, X., Otto-Bliesner, B. L., Timmermann, A., Smith, R. S., Lohmann, G., Zheng, W., and Elison, T. O. (2014). The holocene temperature conundrum. Proceedings of the National Academy of Sciences, 111(34):E3501–E3505.

Loulergue, L., Schilt, A., Spahni, R., Masson-Delmotte, V., Blunier, T., Lemieux, B., Barnola, J.-M., Raynaud, D., Stocker, T. F., and Chappellaz, J. (2008). Orbital and millennial-scale features of atmospheric ch4 over the past 800,000 years. Nature, 453(7193):383–386.

Lu, Z., Miller, P. A., Zhang, Q., Zhang, Q., Wårlind, D., Nieradzik, L., Sjolte, J., and Smith, B. (2018). Dynamic vegetation simulations of the mid-holocene green sahara. Geophysical Research Letters, 45(16):8294–8303.

Lunt, D. J., Abe-Ouchi, A., Bakker, P., Berger, A., Braconnot, P., Charbit, S., Fischer, N., Herold, N., Jungclaus, J. H., Khon, V. C., Krebs-Kanzow, U., Langebroek, P. M., Lohmann, G., Nisancioglu, K. H., Otto-Bliesner, B. L., Park, W., Pfeiffer, M., Phipps, S. J., Prange, M., Rachmayani, R., Renssen, H., Rosenbloom, N., Schneider, B., Stone, E. J., Takahashi, K., Wei, W., Yin, Q., and Zhang, Z. S. (2013). A multi-model assessment of last interglacial temperatures. Climate of the Past, 9(2):699–717.

Lunt, D. J., Bragg, F., Chan, W.-L., Hutchinson, D. K., Ladant, J.-B., Morozova, P., Niezgodzki, I., Steinig, S., Zhang, Z., Zhu, J., Abe-Ouchi, A., Anagnostou, E., de Boer, A. M., Coxall, H. K., Donnadieu, Y., Foster, G., Inglis, G. N., Knorr, G., Langebroek, P. M., Lear, C. H., Lohmann, G., Poulsen, C. J., Sepulchre, P., Tierney, J. E., Valdes, P. J., Volodin, E. M., Dunkley Jones, T., Hollis, C. J., Huber, M., and Otto-Bliesner, B. L. (2021). Deepmip: model intercomparison of early eocene climatic optimum (eeco) large-scale climate features and comparison with proxy data. Climate of the Past, 17(1):203–227.

Lunt, D. J., Dunkley Jones, T., Heinemann, M., Huber, M., LeGrande, A., Winguth, A., Loptson, C., Marotzke, J., Roberts, C. D., Tindall, J., Valdes, P., and Winguth, C. (2012a). A model–data comparison for a multi-model ensemble of early eocene atmosphere–ocean simulations: Eomip. Climate of the Past, 8(5):1717–1736.

Lunt, D. J., Haywood, A. M., Schmidt, G. A., Salzmann, U., Valdes, P. J., Dowsett, H. J., and Loptson, C. A. (2012b). On the causes of mid-Pliocene warmth and polar amplification. Earth and Planetary Science Letters, 321-322:128–138.

Lunt, D. J., Huber, M., Anagnostou, E., Baatsen, M. L., Caballero, R., DeConto, R., Dijkstra, H. A., Donnadieu, Y., Evans, D., Feng, R., Foster, G. L., Gasson, E., Von Der Heydt, A. S., Hollis, C. J., Inglis, G. N., Jones, S. M., Kiehl, J., Turner, S. K., Korty, R. L., Kozdon, R., Krishnan, S., Ladant, J. B., Langebroek, P., Lear, C. H., LeGrande, A. N., Littler, K., Markwick, P., Otto-Bliesner, B., Pearson, P., Poulsen, C. J., Salzmann, U., Shields, C., Snell, K., Stärz, M., Super, J., Tabor, C., Tierney, J. E., Tourte, G. J., Tripati, A., Upchurch, G. R., Wade, B. S., Wing, S. L., Winguth, A. M., Wright, N. M., Zachos, J. C., and Zeebe, R. E. (2017). The DeepMIP contribution to PMIP4: Experimental design for model simulations of the EECO, PETM, and pre-PETM (version 1.0). Geoscientific Model Development, 10(2):889–901.

Madec, G. (2008). NEMO ocean engine, Technical Note, IPSL. Technical report.

Madec, G. and the NEMO Team (2016). NEMO ocean engine. Note du Pôle de modélisation.

Magiera, M., Lechleitner, F. A., Erhardt, A. M., Hartland, A., Kwiecien, O., Cheng, H., Bradbury, H. J., Turchyn, A. V., Riechelmann, S., Edwards, L., and Breitenbach, S. F. M. (2019). Local and regional indian summer monsoon precipitation dynamics during termination ii and the last interglacial. Geophysical Research Letters, 46(21):12454–12463.

Marcott, S. A., Shakun, J. D., Clark, P. U., and Mix, A. C. (2013). A reconstruction of regional and global temperature for the past 11,300 years. science, 339(6124):1198–1201.

Marino, G., Rohling, E. J., Rodríguez-Sanz, L., Grant, K. M., Heslop, D., Roberts, A. P., Stanford, J. D., and Yu, J. (2015). Bipolar seesaw control on last interglacial sea level. Nature, 522(7555):197–201.

Marsicek, J., Shuman, B. N., Bartlein, P. J., Shafer, S. L., and Brewer, S. (2018). Reconciling divergent trends and millennial variations in holocene temperatures. Nature, 554(7690):92–96.

Martin, G. M., Milton, S. F., Senior, C. A., Brooks, M. E., Ineson, S., Reichler, T., and Kim, J. (2010). Analysis and reduction of systematic errors through a seamless approach to modeling weather and climate. Journal of Climate, 23(22):5933 – 5957.

Martin, T. H. D. T. G. M., Bellouin, N., Collins, W. J., Culverwell, I. D., Halloran, P. R., Hardiman, S. C., Hinton, T. J., Jones, C. D., McDonald, R. E., McLaren, A. J., O'Connor, F. M., Roberts, M. J., Rodriguez, J. M., Woodward, S., Best, M. J., Brooks, M. E., Brown, A. R., Butchart, N., Dearden, C., Derbyshire, S. H., Dharssi, I., Doutriaux-Boucher, M., Edwards, J. M., Falloon, P. D., Gedney, N., Gray, L. J., Hewitt, H. T., Hobson, M., Huddleston, M. R., Hughes, J., Ineson, S., Ingram, W. J., James, P. M., Johns, T. C., Johnson, C. E., Jones, A., Jones, C. P., Joshi, M. M., Keen, A. B., Liddicoat, S., Lock, A. P., Maidens, A. V., Manners, J. C., Milton, S. F., Rae, J. G. L., Ridley, J. K., Sellar, A., Senior, C. A., Totterdell, I. J., Verhoef, A., Vidale, P. L., and Wiltshire, A. (2011). The hadgem2 family of met office unified model climate configurations. Geoscientific Model Development, 4(3):723–757.

Martinez, J. M. (2012). Managing scientific uncertainty in medical decision making: the case of the advisory committee on immunization practices. The Journal of medicine and philosophy, 37(1):6–27.

Martínez-Botí, M. A., Foster, G. L., Chalk, T. B., Rohling, E. J., Sexton, P. F., Lunt, D. J., Pancost, R. D., Badger, M. P. S., and Schmidt, D. N. (2015). Plio-pleistocene climate sensitivity evaluated using high-resolution co2 records. Nature, 518(7537):49–54.

Masson, D. and Knutti, R. (2011). Climate model genealogy. Geophysical Research Letters, 38(8):L08703.

Masson-Delmotte, V., Schulz, M., Abe-Ouchi, A., Beer, J., Ganopolski, A., González Rouco, J., Jansen, E., Lambeck, K., Luterbacher, J., Naish, T., Osborn, T., Otto-Bliesner, B., Quinn, T., Ramesh, R., Rojas, M., Shao, X., and Timmermann, A. (2013). Information from paleoclimate archives. In Stocker, T., Qin, D., Plattner, G.-K., Tignor, M., Allen, S., Boschung, J., Nauels, A., Xia, Y., Bex, V., and Midgley, P., editors, Climate Change 2013: The Physical Science Basis. Contribution of Working Group I to the Fifth Assessment Report of the Intergovernmental Panel on Climate Change, pages 383–464. Cambridge University Press.

Mauritsen, T., Bader, J., Becker, T., Behrens, J., Bittner, M., Brokopf, R., Brovkin, V., Claussen, M., Crueger, T., Esch, M., Fast, I., Fiedler, S., Fläschner, D., Gayler, V., Giorgetta, M., Goll, D. S., Haak, H., Hagemann, S., Hedemann, C., Hohenegger, C., Ilyina, T., Jahns, T., Jimenéz-de-la Cuesta, D., Jungclaus, J., Kleinen, T., Kloster, S., Kracher, D., Kinne, S., Kleberg, D., Lasslop, G., Kornblueh, L., Marotzke, J., Matei, D., Meraner, K., Mikolajewicz, U., Modali, K., Möbis, B., Müller, W. A., Nabel, J. E. M. S., Nam, C. C. W., Notz, D., Nyawira, S.-S., Paulsen, H., Peters, K., Pincus, R., Pohlmann, H., Pongratz, J., Popp, M., Raddatz, T. J., Rast, S., Redler, R., Reick, C. H., Rohrschneider, T., Schemann, V., Schmidt, H., Schnur, R., Schulzweida, U., Six, K. D., Stein, L., Stemmler, I., Stevens, B., von Storch, J.-S., Tian, F., Voigt, A., Vrese, P., Wieners, K.-H., Wilkenskjeld, S., Winkler, A., and Roeckner, E. (2019). Developments in the mpi-m earth system model version 1.2 (mpi-esm1.2) and its response to increasing co2. Journal of Advances in Modeling Earth Systems, 11(4):998–1038.

McLaren, A. J., Banks, H. T., Durham, C. F., Gregory, J. M., Johns, T. C., Keen, A. B., Ridley, J. K., Roberts, M. J., Lipscomb, W. H., Connolley, W. M., and Laxon, S. W. (2006). Evaluation of the sea ice simulation in a new coupled atmosphere-ocean climate model (HadGEM1). Journal of Geophysical Research: Oceans, 111:C12014. 17.

Meehl, G. A. (1992). Effect of tropical topography on global climate. Annual Review of Earth and Planetary Sciences, 20(1):85–112.

Meehl, G. A., Boer, G. J., Covey, C., Latif, M., and Stouffer, R. J. (1997). Intercomparison makes for a better climate model. Eos, 78:445–451.

Meehl, G. A., Boer, G. J., Covey, C., Latif, M., and Stouffer, R. J. (2000). The coupled model intercomparison project (cmip). B. Am. Meteorol. Soc., 81:313–318.

Meehl, G. A., Covey, C., Delworth, T., Latif, M., McAvaney, B., Mitchell, J. F. B., Stouffer, R. J., and Taylor, K. E. (2007). The wcrp cmip3 multimodel dataset: A new era in climate change research. Bulletin of the American Meteorological Society, 88(9):1383 – 1394.

Meehl, G. A., Senior, C. A., Eyring, V., Flato, G., Lamarque, J.-F., Stouffer, R. J., Taylor, K. E., and Schlund, M. (2020). Context for interpreting equilibrium climate sensitivity and transient climate response from the cmip6 earth system models. Science Advances, 6(26):eaba1981.

Meehl, G. A., Washington, W. M., Arblaster, J. M., Hu, A., Teng, H., Kay, J. E., Gettelman, A., Lawrence, D. M., Sanderson, B. M., and Strand, W. G. (2013). Climate change projections in CESM1(CAM5) compared to CCSM4. Journal of Climate, 26(17):6287–6308.

Messori, G., Gaetani, M., Zhang, Q., Zhang, Q., and Pausata, F. S. R. (2019). The water cycle of the mid-holocene west african monsoon: The role of vegetation and dust emission changes. International Journal of Climatology, 39(4):1927–1939.

Metcalfe, S. E., Barron, J. A., and Davies, S. J. (2015). The holocene history of the north american monsoon: 'known knowns'and 'known unknowns' in understanding its spatial and temporal complexity. Quaternary Science Reviews, 120:1–27.

Milankovitch, M. (1941). Kanon der erdbestrahlung und seine anwendung auf das eiszeitenproblem. Spec. Acad. R. Serbe, Belgrade.

Miller, R. L., Schmidt, G. A., Nazarenko, L. S., Tausnev, N., Bauer, S. E., DelGenio, A. D., Kelley, M., Lo, K. K., Ruedy, R., Shindell, D. T., Aleinov, I., Bauer, M., Bleck, R., Canuto, V., Chen, Y., Cheng, Y., Clune, T. L., Faluvegi, G., Hansen, J. E., Healy, R. J., Kiang, N. Y., Koch, D., Lacis, A. A., LeGrande, A. N., Lerner, J., Menon, S., Oinas, V., Pérez García-Pando, C., Perlwitz, J. P., Puma, M. J., Rind, D., Romanou, A., Russell, G. L., Sato, M., Sun, S., Tsigaridis, K., Unger, N., Voulgarakis, A., Yao, M.-S., and Zhang, J. (2014). Cmip5 historical simulations (1850–2012) with giss modele2. Journal of Advances in Modeling Earth Systems, 6(2):441–478.

Mohtadi, M., Prange, M., and Steinke, S. (2016). Palaeoclimatic insights into forcing and response of monsoon rainfall. Nature, 533(7602):191–199.

Mollier-Vogel, E., Leduc, G., Böschen, T., Martinez, P., and Schneider, R. R. (2013). Rainfall response to orbital and millennial forcing in northern peru over the last 18 ka. Quaternary Science Reviews, 76:29–38.

Monnin, E., Steig, E. J., Siegenthaler, U., Kawamura, K., Schwander, J., Stauffer, B., Stocker, T. F., Morse, D. L., Barnola, J.-M., Bellier, B., Raynaud, D., and Fischer, H. (2004). Evidence for substantial accumulation rate variability in antarctica during the holocene, through synchronization of co2 in the taylor dome, dome c and dml ice cores. Earth and Planetary Science Letters, 224(1):45–54.

Morice, C. P., Kennedy, J. J., Rayner, N. A., and Jones, P. D. (2012). Quantifying uncertainties in global and regional temperature change using an ensemble of observational estimates: The hadcrut4 data set. Journal of Geophysical Research: Atmospheres, 117(D8):p.n/a.

Neale, R. B., Richter, J. H., Conley, A. J., Park, S., Lauritzen, P. H., Gettelman, A., and Williamson, D. L. (2010). Description of the NCAR Community Atmosphere Model (CAM 4.0). Ncar/Tn-485+Str.

Nie, J., Boos, W. R., and Kuang, Z. (2010). Observational evaluation of a convective quasi-equilibrium view of monsoons. Journal of Climate, 23(16):4416 – 4428.

Nie, J., Stevens, T., Song, Y., King, J. W., Zhang, R., Ji, S., Gong, L., and Cares, D. (2014). Pacific freshening drives pliocene cooling and asian monsoon intensification. Scientific Reports, 4(1):5474.

Notz, D., Haumann, F. A., Haak, H., Jungclaus, J. H., and Marotzke, J. (2013). Arctic sea-ice evolution as modeled by Max Planck Institute for Meteorology's Earth system model. Journal of Advances in Modeling Earth Systems, 5(2):173–194.

O'Brien, C. L., Foster, G. L., Martínez-Botí, M. A., Abell, R., Rae, J. W., and Pancost, R. D. (2014). High sea surface temperatures in tropical warm pools during the Pliocene. Nature Geoscience, 7(8):606–611.

O'Connor, F. M., Johnson, C. E., Morgenstern, O., and Collins, W. J. (2009). Interactions between tropospheric chemistry and climate model temperature and humidity biases. Geophysical Research Letters, 36(16):L16801.

Ohgaito, R. and Abe-Ouchi, A. (2009). The effect of sea surface temperature bias in the pmip2 aogcms on mid-holocene asian monsoon enhancement. Climate dynamics, 33(7-8):975–983.

O'ishi, R. and Abe-Ouchi, A. (2011). Polar amplification in the mid-holocene derived from dynamical vegetation change with a gcm. Geophysical Research Letters, 38(14):L14702.

O'ishi, R., Chan, W.-L., Abe-Ouchi, A., Sherriff-Tadano, S., Ohgaito, R., and Yoshimori, M. (2021). Pmip4/cmip6 last interglacial simulations using three different versions of miroc: importance of vegetation. Climate of the Past, 17(1):21–36.

Oleson, K. (2010). Technical description of the community land model (clm). NCAR Technical Note, TN-478+STR.

Orland, I. J., He, F., Bar-Matthews, M., Chen, G., Ayalon, A., and Kutzbach, J. E. (2019). Resolving seasonal rainfall changes in the middle east during the last interglacial period. Proceedings of the National Academy of Sciences, 116(50):24985–24990.

Osman, M. B., Tierney, J. E., Zhu, J., Tardif, R., Hakim, G. J., King, J., and Poulsen, C. J. (2021). Globally resolved surface temperatures since the last glacial maximum. Nature, 599(7884):239–244.

Otto-Bliesner, B. L., Braconnot, P., Harrison, S. P., Lunt, D. J., Abe-Ouchi, A., Albani, S., Bartlein, P. J., Capron, E., Carlson, A. E., Dutton, A., et al. (2017a). The pmip4 contribution to cmip6–part 2: Two interglacials, scientific objective and experimental design for holocene and last interglacial simulations. Geoscientific Model Development, 10(11):3979–4003.

Otto-Bliesner, B. L., Brady, E. C., Tomas, R. A., Albani, S., Bartlein, P. J., Mahowald, N. M., Shafer, S. L., Kluzek, E., Lawrence, P. J., Leguy, G., Rothstein, M., and Sommers, A. (2020). A comparison of the cmip6 midholocene and lig127k simulations in cesm2. Paleoceanography and Paleoclimatology, 35(11):e2020PA003957.

Otto-Bliesner, B. L., Brady, E. C., Zhao, A., Brierley, C. M., Axford, Y., Capron, E., Govin, A., Hoffman, J. S., Isaacs, E., Kageyama, M., Scussolini, P., Tzedakis, P. C., Williams, C. J. R., Wolff, E., Abe-Ouchi, A., Braconnot, P., Ramos Buarque, S., Cao, J., de Vernal, A., Guarino, M. V., Guo, C., LeGrande, A. N., Lohmann, G., Meissner, K. J., Menviel, L., Morozova, P. A., Nisancioglu, K. H., O'ishi, R., Salas y Mélia, D., Shi, X., Sicard, M., Sime, L., Stepanek, C., Tomas, R., Volodin, E., Yeung, N. K. H., Zhang, Q., Zhang, Z., and Zheng, W. (2021). Large-scale features of last interglacial climate: results from evaluating the *lig127k* simulations for the coupled model intercomparison project (cmip6)–paleoclimate modeling intercomparison project (pmip4). Climate of the Past, 17(1):63–94.

Otto-Bliesner, B. L., Jahn, A., Feng, R., Brady, E. C., Hu, A., and Löfverström, M. (2017b). Amplified North Atlantic warming in the late Pliocene by changes in Arctic gateways. Geophysical Research Letters, 44(2):957–964.

Otto-Bliesner, B. L., Rosenbloom, N., Stone, E. J., McKay, N. P., Lunt, D. J., Brady,

E. C., and Overpeck, J. T. (2013). How warm was the last interglacial? new model–data comparisons. Philosophical Transactions of the Royal Society A: Mathematical, Physical and Engineering Sciences, 371(2001):20130097.

Pagani, M., Liu, Z., Lariviere, J., and Ravelo, A. C. (2010). High Earth-system climate sensitivity determined from Pliocene carbon dioxide concentrations. Nature Geoscience, 3(1):27–30.

Palmer, T. and Bjorn, S. (2019). The scientific challenge of understanding and estimating climate change. Proceedings of the National Academy of Sciences, 116(49):24390–24395.

Park, H.-S., Kim, S.-J., Seo, K.-H., Stewart, A. L., Kim, S.-Y., and Son, S.-W. (2018). The impact of arctic sea ice loss on mid-holocene climate. Nature communications, 9(1):1–9.

Pausata, F. S., Messori, G., and Zhang, Q. (2016). Impacts of dust reduction on the northward expansion of the african monsoon during the green sahara period. Earth and Planetary Science Letters, 434:298–307.

Perez-Sanz, A., Li, G., González-Sampériz, P., and Harrison, S. P. (2014). Evaluation of modern and mid-holocene seasonal precipitation of the mediterranean and northern africa in the cmip5 simulations. Climate of the Past, 10(2):551–568.

Petit, J. R., Mourner, L., Jouzel, J., Korotkevich, Y. S., Kotlyakov, V. I., and Lorius, C. (1990). Palaeoclimatological and chronological implications of the vostok core dust record. Nature, 343(6253):56–58.

Peyron, O., Guiot, J., Cheddadi, R., Tarasov, P., Reille, M., de Beaulieu, J.-L., Bottema, S., and Andrieu, V. (1998). Climatic reconstruction in europe for 18,000 yr b.p. from pollen data. Quaternary Research, 49(2):183–196.

Phillips, A. S., Deser, C., and Fasullo, J. (2014). Evaluating modes of variability in climate models. Eos, Transactions American Geophysical Union, 95(49):453–455.

Phipps, S., Rotstayn, L., Gordon, H., Roberts, J., Hirst, A., and Budd, W. (2012). The csiro mk3l climate system model version 1.0–part 2: Response to external forcings. Geoscientific Model Development, 5(3):649–682.

Piao, J., Chen, W., Wang, L., Pausata, F. S. R., and Zhang, Q. (2020). Northward extension of the east asian summer monsoon during the mid-holocene. Global and Planetary Change, 184:103046.

Pontes, G. M., Wainer, I., Taschetto, A. S., Sen Gupta, A., Abe-Ouchi, A., Brady, E. C., Chan, W.-L., Chandan, D., Contoux, C., Feng, R., Hunter, S. J., Kame, Y., Lohmann, G., Otto-Bliesner, B. L., Peltier, W. R., Stepanek, C., Tindall, J., Tan, N., Zhang, Q., and Zhang, Z. (2020). Drier tropical and subtropical southern hemisphere in the mid-pliocene warm period. Scientific Reports, 10(1):13458.

Prado, L. F., Wainer, I., and Chiessi, C. M. (2013a). Mid-holocene pmip3/cmip5 model results: Intercomparison for the south american monsoon system. The Holocene, 23(12):1915–1920.

Prado, L. F., Wainer, I., Chiessi, C. M., Ledru, M.-P., and Turcq, B. (2013b). A mid-holocene climate reconstruction for eastern south america. Climate of the Past, 9(5):2117–2133.

Prahl, F. G. and Wakeham, S. G. (1987). Calibration of unsaturation patterns in long-chain ketone compositions for palaeotemperature assessment. Nature, 330(6146):367–369.

Prentice, C., Guiot, J., Huntley, B., Jolly, D., and Cheddadi, R. (1996). Reconstructing biomes from palaeoecological data: a general method and its application to european pollen data at 0 and 6 ka. Climate Dynamics, 12(3):185–194.

Prentice, I. C., Jolly, D., and participants , B. . (2000). Mid-holocene and glacial-maximum vegetation geography of the northern continents and africa. Journal of Biogeography, 27(3):507–519.

Prentice, I. C. and Webb III, T. (1998). Biome 6000: reconstructing global mid-holocene vegetation patterns from palaeoecological records. Journal of Biogeography, 25(6):997–1005.

Qin, B., Harrison, S. P., and Kutzbach, J. E. (1998). Evaluation of modelled regional water balance using lake status data: a comparison of 6ka simulations with the ncar ccm. Quaternary Science Reviews, 17(6):535–548.

Rackow, T., Goessling, H. F., Jung, T., Sidorenko, D., Semmler, T., Barbi, D., and Handorf, D. (2018). Towards multi-resolution global climate modeling with ECHAM6-FESOM. Part II: climate variability. Climate Dynamics, 50(7-8):2369–2394.

Rackow, T., Sein, D. V., Semmler, T., Danilov, S., Koldunov, N. V., Sidorenko, D., Wang, Q., and Jung, T. (2019). Sensitivity of deep ocean biases to horizontal resolution in prototype cmip6 simulations with awi-cm1.0. Geoscientific Model Development, 12(7):2635–2656.

Raddatz, T. J., Reick, C. H., Knorr, W., Kattge, J., Roeckner, E., Schnur, R., Schnitzler, K.-G., Wetzel, P., and Jungclaus, J. (2007). Will the tropical land biosphere dominate the climate?carbon cycle feedback during the twenty-first century? Climate Dynamics, 29(6):565–574.

Ramage, C. S. (1971). In Monsoon Meteorology, page pp296. Academic Press.

Raymo, M. E. and Nisancioglu, K. H. (2003). The 41 kyr world: Milankovitch's other unsolved mystery. Paleoceanography, 18(1):1011.

Reed, K. A., Bacmeister, J. T., Huff, J. J. A., Wu, X., Bates, S. C., and Rosenbloom, N. A. (2019). Exploring the Impact of Dust on North Atlantic Hurricanes in a High-Resolution Climate Model. Geophysical Research Letters, 46(2):1105–1112.

Reick, C. H., Raddatz, T., Brovkin, V., and Gayler, V. (2013). Representation of natural and anthropogenic land cover change in mpi-esm. Journal of Advances in Modeling Earth Systems, 5(3):459–482.

Renoult, M., Annan, J. D., Hargreaves, J. C., Sagoo, N., Flynn, C., Kapsch, M.-L., Li, Q., Lohmann, G., Mikolajewicz, U., Ohgaito, R., Shi, X., Zhang, Q., and Mauritsen, T. (2020). A bayesian framework for emergent constraints: case studies of climate sensitivity with pmip. Climate of the Past, 16(5):1715–1735.

Ridley, H. E., Asmerom, Y., Baldini, J. U., Breitenbach, S. F., Aquino, V. V., Prufer, K. M., Culleton, B. J., Polyak, V., Lechleitner, F. A., Kennett, D. J., Zhang, M., Marwan, N., Macpherson, C. G., Baldini, L. M., Xiao, T., Peterkin, J. L., Awe, J., and Haug, G. H. (2015). Aerosol forcing of the position of the intertropical convergence zone since ad 1550. Nature Geoscience, 8:195–200.

Ridley, J. K., Blockley, E. W., Keen, A. B., Rae, J. G. L., West, A. E., and Schroeder, D. (2018). The sea ice model component of hadgem3-gc3.1. Geoscientific Model Development, 11(2):713–723.

Rosenbloom, N. A., Otto-Bliesner, B. L., Brady, E. C., and Lawrence, P. J. (2013). Simulating the mid-Pliocene Warm Period with the CCSM4 model. Geoscientific Model Development, 6(2):549–561.

Rosenfeld, D., Rudich, Y., and Lahav, R. (2001). Desert dust suppressing precipitation: A possible desertification feedback loop. Proceedings of the National Academy of Sciences, 98(11):5975–5980.

Rosenzweig, C. and Abramopoulos, F. (1997). Land-surface model development for the giss gcm. Journal of Climate, 10(8):2040 – 2054.

Rostek, F., Ruhlandt, G., Bassinot, F. C., Muller, P. J., Labeyrie, L. D., Lancelot, Y., and Bard, E. (1993). Reconstructing sea surface temperature and salinity using 18o and alkenone records. Nature, 364(6435):319–321.

Rotstayn, L. D., Collier, M. A., Mitchell, R. M., Qin, Y., Campbell, S. K., and Dravitzki, S. M. (2011). Simulated enhancement of enso-related rainfall variability due to australian dust. Atmospheric Chemistry and Physics, 11(13):6575–6592.

Rotstayn, L. D., Jeffrey, S. J., Collier, M. A., Dravitzki, S. M., Hirst, A. C., Syktus, J. I., and Wong, K. K. (2012). Aerosol- and greenhouse gas-induced changes in summer rainfall and circulation in the australasian region: a study using single-forcing climate simulations. Atmospheric Chemistry and Physics, 12(14):6377–6404.

Rousset, C., Vancoppenolle, M., Madec, G., Fichefet, T., Flavoni, S., Barthélemy, A., Benshila, R., Chanut, J., Levy, C., Masson, S., and Vivier, F. (2015). The louvain-la-neuve sea ice model lim3.6: global and regional capabilities. Geoscientific Model Development, 8(10):2991–3005.

Sagoo, N. and Storelvmo, T. (2017). Testing the sensitivity of past climates to the indirect effects of dust. Geophysical Research Letters, 44:5807–5817.

Salas-Melia, D. (2002). A global coupled sea ice-ocean model. Ocean Model., 4:137–172.

Salzmann, U., Haywood, A. M., Lunt, D. J., Valdes, P. J., and Hill, D. J. (2008). A new global biome reconstruction and data-model comparison for the Middle Pliocene. Global Ecology and Biogeography, 17(3):432–447.

Samset, B. H., Sand, M., Smith, C. J., Bauer, S. E., Forster, P. M., Fuglestvedt, J. S., Osprey, S., and Schleussner, C. F. (2018). Climate Impacts From a Removal of Anthropogenic Aerosol Emissions. Geophysical Research Letters, 45:1020–1029.

Sarnthein, M., Tetzlaff, G., Koopmann, B., Wolter, K., and Pflaumann, U. (1981). Glacial and interglacial wind regimes over the eastern subtropical atlantic and north-west africa. Nature (London), 293(5829):193–196.

Schmidt, G. A., Annan, J. D., Bartlein, P. J., Cook, B. I., Guilyardi, E., Hargreaves, J. C., Harrison, S. P., Kageyama, M., LeGrande, A. N., Konecky, B., Lovejoy, S., Mann, M. E., Masson-Delmotte, V., Risi, C., Thompson, D., Timmermann, A., Tremblay, L.-B., and Yiou, P. (2014a). Using palaeo-climate comparisons to constrain future projections in cmip5. Climate of the Past, 10(1):221–250.

Schmidt, G. A., Kelley, M., Nazarenko, L., Ruedy, R., Russell, G. L., Aleinov, I., Bauer, M., Bauer, S. E., Bhat, M. K., Bleck, R., Canuto, V., Chen, Y.-H., Cheng, Y., Clune, T. L., Del Genio, A., de Fainchtein, R., Faluvegi, G., Hansen, J. E., Healy, R. J., Kiang, N. Y., Koch, D., Lacis, A. A., LeGrande, A. N., Lerner, J., Lo, K. K., Matthews, E. E., Menon, S., Miller, R. L., Oinas, V., Oloso, A. O., Perlwitz, J. P., Puma, M. J., Putman, W. M., Rind, D., Romanou, A., Sato, M., Shindell, D. T., Sun, S., Syed, R. A., Tausnev, N., Tsigaridis, K., Unger, N., Voulgarakis, A., Yao, M.-S., and Zhang, J. (2014b). Configuration and assessment of the giss modele2 contributions to the cmip5 archive. Journal of Advances in Modeling Earth Systems, 6(1):141–184.

Schmidt, G. A., Ruedy, R., Hansen, J. E., Aleinov, I., Bell, N., Bauer, M., Bauer, S., Cairns, B., Canuto, V., Cheng, Y., Del Genio, A., Faluvegi, G., Friend, A. D., Hall, T. M., Hu, Y., Kelley, M., Kiang, N. Y., Koch, D., Lacis, A. A., Lerner, J., Lo, K. K., Miller, R. L., Nazarenko, L., Oinas, V., Perlwitz, J., Perlwitz, J., Rind, D., Romanou, A., Russell, G. L., Sato, M., Shindell, D. T., Stone, P. H., Sun, S., Tausnev, N., Thresher, D., and Yao, M. S. (2006). Present-day atmospheric simulations using giss modele: Comparison to in situ, satellite, and reanalysis data. Journal of Climate, 19(2):153–192.

Schmittner, A., Oschlies, A., Giraud, X., Eby, M., and Simmons, H. L. (2005). A global model of the marine ecosystem for long-term simulations: Sensitivity to ocean mixing, buoyancy forcing, particle sinking, and dissolved organic matter cycling. Global Biogeochemical Cycles, 19:GB3004.

Schneider, T., Bischoff, T., and Haug, G. H. (2014). Migrations and dynamics of the intertropical convergence zone. Nature, 513(7516):45–53.

Scholz, P., Sidorenko, D., Gurses, O., Danilov, S., Koldunov, N., Wang, Q., Sein, D., Smolentseva, M., Rakowsky, N., and Jung, T. (2019). Assessment of the finite-volume sea ice-ocean model (fesom2.0) – part 1: Description of selected key model elements and comparison to its predecessor version. Geoscientific Model Development, 12(11):4875–4899.

Scussolini, P., Bakker, P., Guo, C., Stepanek, C., Zhang, Q., Braconnot, P., Cao, J., Guarino, M.-V., Coumou, D., Prange, M., Ward, P. J., Renssen, H., Kageyama, M., Otto-Bliesner, B., and Aerts, J. C. J. H. (2019). Agreement between reconstructed and modeled boreal precipitation of the last interglacial. Science advances, 5(11):eaax7047.

Seland, Ø., Bentsen, M., Seland Graff, L., Olivié, D., Toniazzo, T., Gjermundsen, A., Debernard, J. B., Gupta, A. K., He, Y., Kirkevåg, A., Schwinger, J., Tjiputra, J., Schancke Aas, K., Bethke, I., Fan, Y., Griesfeller, J., Grini, A., Guo, C., Ilicak, M., Hafsahl Karset, I. H., Landgren, O., Liakka, J., Onsum Moseid, K., Nummelin, A., Spensberger, C., Tang, H., Zhang, Z., Heinze, C., Iverson, T., and Schulz, M. (2020). The norwegian earth system model, noresm2 – evaluation of thecmip6 deck and historical simulations. Geoscientific Model Development Discussions, 2020:1–68.

Selvaraj, K., Chen, C. T. A., and Lou, J.-Y. (2007). Holocene east asian monsoon variability: Links to solar and tropical pacific forcing. Geophysical Research Letters, 34(1):L01703.

Serreze, M. C. and Barry, R. G. (2011). Processes and impacts of arctic amplification: A research synthesis. Global and Planetary Change, 77(1):85–96.

Shukla, J., Palmer, T. N., Hagedorn, R., Hoskins, B., Kinter, J., Marotzke, J., Miller, M., and Slingo, J. (2010). Toward a new generation of world climate research and computing facilities. Bulletin of the American Meteorological Society, 91(10):1407 – 1412.

Sidorenko, D., Goessling, H., Koldunov, N., Scholz, P., Danilov, S., Barbi, D., Cabos, W., Gurses, O., Harig, S., Hinrichs, C., Juricke, S., Lohmann, G., Losch, M., Mu, L., Rackow, T., Rakowsky, N., Sein, D., Semmler, T., Shi, X., Stepanek, C., Streffing, J., Wang, Q., Wekerle, C., Yang, H., and Jung, T. (2019). Evaluation of fesom2.0 coupled to echam6.3: Preindustrial and highresmip simulations. Journal of Advances in Modeling Earth Systems, 11(11):3794–3815.

Sidorenko, D., Rackow, T., Jung, T., Semmler, T., Barbi, D., Danilov, S., Dethloff, K., Dorn, W., Fieg, K., Goessling, H. F., Handorf, D., Harig, S., Hiller, W., Juricke, S., Losch, M., Schröter, J., Sein, D. V., and Wang, Q. (2015). Towards multi-resolution global climate modeling with ECHAM6?FESOM. Part I: model formulation and mean climate. Climate Dynamics, 44(3-4):757–780.

Smith, B., Wårlind, D., Arneth, A., Hickler, T., Leadley, P., Siltberg, J., and Zaehle, S. (2014). Implications of incorporating n cycling and n limitations on primary production in an individual-based dynamic vegetation model. Biogeosciences, 11(7):2027–2054.

Smith, R., Jones, P., Briegleb, B., Bryan, F., Danabasoglu, G., Dennis, J., Dukowicz, J., Eden, C., Fox-Kemper, B., Gent, P., Hecht, M., Jayne, S., Jochum, M., Large, W., Lindsay, K., Maltrud, M., Norton, N., Peacock, S., Vertenstein, M., and Yeager, S. (2010). The Parallel Ocean Program (POP) reference manual: Ocean component of the Community Climate System Model (CCSM). Los Alamos National Laboratory Tech. Rep. LAUR-10-01853.

Spahni, R., Chappellaz, J., Stocker, T. F., Loulergue, L., Hausammann, G., Kawamura, K., Flückiger, J., Schwander, J., Raynaud, D., Masson-Delmotte, V., and Jouzel, J. (2005). Atmospheric methane and nitrous oxide of the late pleistocene from antarctic ice cores. Science, 310(5752):1317–1321.

Steinke, S., Mohtadi, M., Prange, M., Varma, V., Pittauerova, D., and Fischer, H. W. (2014). Mid- to late-holocene australian–indonesian summer monsoon variability. Quaternary Science Reviews, 93:142–154.

Stevens, B., Giorgetta, M., Esch, M., Mauritsen, T., Crueger, T., Rast, S., Salzmann, M., Schmidt, H., Bader, J., Block, K., Brokopf, R., Fast, I., Kinne, S., Kornblueh, L., Lohmann, U., Pincus, R., Reichler, T., and Roeckner, E. (2013). Atmospheric component of the mpi-m earth system model: Echam6. Journal of Advances in Modeling Earth Systems, 5(2):146–172.

Stone, E. J., Capron, E., Lunt, D. J., Payne, A. J., Singarayer, J. S., Valdes, P. J., and Wolff, E. W. (2016). Impact of meltwater on high-latitude early last interglacial climate. Climate of the Past, 12(9):1919–1932.

Storkey, D., Blaker, A. T., Mathiot, P., Megann, A., Aksenov, Y., Blockley, E. W., Calvert, D., Graham, T., Hewitt, H. T., Hyder, P., Kuhlbrodt, T., Rae, J. G. L., and Sinha, B. (2018). Uk global ocean go6 and go7: a traceable hierarchy of model resolutions. Geoscientific Model Development, 11(8):3187–3213.

Sueyoshi, T., Ohgaito, R., Yamamoto, A., Chikamoto, M. O., Hajima, T., Okajima, H., Yoshimori, M., Abe, M., O'ishi, R., Saito, F., Watanabe, S., Kawamiya, M., and Abe-Ouchi, A. (2013). Set-up of the pmip3 paleoclimate experiments conducted using an earth system model, miroc-esm. Geoscientific Model Development, 6(3):819–836.

Sun, W., Wang, B., Zhang, Q., Pausata, F. S. R., Chen, D., Lu, G., Yan, M., Ning, L., and Liu, J. (2019). Northern hemisphere land monsoon precipitation increased by the green sahara during middle holocene. Geophysical Research Letters, 46(16):9870–9879.

Swann, A., Fung, I., Liu, Y., and Chiang, J. (2014a). Remote vegetation feedbacks and the mid-holocene green sahara. Journal of Climate, 27:4857–4870.

Swann, A. L., Fung, I. Y., Liu, Y., and Chiang, J. C. (2014b). Remote vegetation feedbacks and the mid-holocene green sahara. Journal of Climate, 27:4857–4870.

Takata, K., Emori, S., and Watanabe, T. (2003). Development of the minimal advanced treatments of surface interaction and runoff. Global and Planetary Change, 38(1):209–222.

Takemura, T., Egashira, M., Matsuzawa, K., Ichijo, H., O'ishi, R., and Abe-Ouchi, A. (2009). A simulation of the global distribution and radiative forcing of soil dust aerosols at the last glacial maximum. Atmospheric Chemistry and Physics, 9(9):3061–3073.

Takemura, T., Nozawa, T., Emori, S., Nakajima, T. Y., and Nakajima, T. (2005). Simulation of climate response to aerosol direct and indirect effects with aerosol transport-radiation model. Journal of Geophysical Research: Atmospheres, 110(D2).

Taylor, K. E., Stouffer, R. J., and Meehl, G. A. (2012). An Overview of CMIP5 and the Experiment Design. Bulletin of the American Meteorological Society, 93(4):485–498.

Tebaldi, C. and Knutti, R. (2007). The use of the multi-model ensemble in probabilistic climate projections.

Thompson, A. J., Skinner, C. B., Poulsen, C. J., and Zhu, J. (2019). Modulation of mid-holocene african rainfall by dust aerosol direct and indirect effects. Geophysical Research Letters, 46(7):3917–3926.

Tierney, J. E., Pausata, F. S., and deMenocal, P. B. (2017). Rainfall regimes of the green sahara. Science advances, 3(1):e1601503.

Touzé-Peiffer, L., Barberousse, A., and Le Treut, H. (2020). The coupled model intercomparison project: History, uses, and structural effects on climate research. WIREs Climate Change, 11(4):e648.

Tsujino, H., Hirabara, M., Nakano, H., Yasuda, T., Motoi, T., and Yamanaka, G. (2011). Simulating present climate of the global ocean–ice system using the meteorological research institute community ocean model (mri.com): simulation characteristics and variability in the pacific sector. Journal of Oceanography, 67(4):449–479.

Twomey, S. (1977). The Influence of Pollution on the Shortwave Albedo of Clouds. Journal of the Atmospheric Sciences, 34:1149–1152.

Unger, N. and Yue, X. (2014). Strong chemistry-climate feedbacks in the Pliocene. Geophysical Research Letters, 41(2):527–533.

Valcke, S. (2013). The oasis3 coupler: a european climate modelling community software. Geoscientific Model Development, 6(2):373–388.

Voigt, A., Pincus, R., Stevens, B., Bony, S., Boucher, O., Bellouin, N., Lewinschal, A., Medeiros, B., Wang, Z., and Zhang, H. (2017). Fast and slow shifts of the zonal-mean intertropical convergence zone in response to an idealized anthropogenic aerosol. Journal of Advances in Modeling Earth Systems, 9:870–892.

Voldoire, A., Saint-Martin, D., Sénési, S., Decharme, B., Alias, A., Chevallier, M., Colin, J., Guérémy, J., Michou, M., Moine, M., Nabat, P., Roehrig, R., Salas y Mélia, D., Séférian, R., Valcke, S., Beau, I., Belamari, S., Berthet, S., Cassou, C., Cattiaux, J., Deshayes, J., Douville, H., Ethé, C., Franchistéguy, L., Geoffroy, O., Lévy, C., Madec, G., Meurdesoif, Y., Msadek, R., Ribes, A., Sanchez?Gomez, E., Terray, L., and Waldman, R. (2019). Evaluation of CMIP6 DECK Experiments With CNRM-CM6-1. Journal of Advances in Modeling Earth Systems, 11(7):2177–2213.

Voldoire, A., Sanchez-Gomez, E., y Mélia, D. S., Decharme, B., Cassou, C., Sénési, S., Valcke, S., Beau, I., Alias, A., Chevallier, M., Déqué, M., Deshayes, J., Douville, H., Fernandez, E., Madec, G., Maisonnave, E., Moine, M.-P., Planton, S., Saint-Martin, D., Szopa, S., Tyteca, S., Alkama, R., Belamari, S., Braun, A., Coquart, L., and Chauvin, F. (2013). The cnrm-cm5. 1 global climate model: description and basic evaluation. Climate Dynamics, 40(9-10):2091–2121.

Volodin, E. M., Diansky, N. A., and Gusev, A. V. (2013). Simulation and prediction of climate changes in the 19th to 21st centuries with the Institute of Numerical Mathematics, Russian Academy of Sciences, model of the Earth's climate system. Izvestiya, Atmospheric and Oceanic Physics, 49(4):347–366.

Volodin, E. M., Mortikov, E. V., Kostrykin, S. V., Galin, V. Y., Lykossov, V. N., Gritsun, A. S., Diansky, N. A., Gusev, A. V., and Iakovlev, N. G. (2017). Simulation of the present-day climate with the climate model INMCM5. Climate Dynamics, 49(11-12):3715–3734.

Volodin, E. M., Mortikov, E. V., Kostrykin, S. V., Galin, V. Y., Lykossov, V. N., Gritsun, A. S., Diansky, N. A., Gusev, A. V., Iakovlev, N. G., Shestakova, A. A., and Emelina, S. V. (2018). Simulation of the modern climate using the INM-CM48 climate model. Russian Journal of Numerical Analysis and Mathematical Modelling, 33(6):367–374.

von Gunten, L., D'Andrea, W. J., Bradley, R. S., and Huang, Y. (2012). Proxy-to-proxy calibration: Increasing the temporal resolution of quantitative climate reconstructions. Scientific Reports, 2(1):609.

Walker, M., Johnsen, S., Rasmussen, S. O., Popp, T., Steffensen, J.-P., Gibbard, P., Hoek, W., Lowe, J., Andrews, J., BjÃ¶rck, S., Cwynar, L. C., Hughen, K., Kershaw, P., Kromer, B., Litt, T., Lowe, D. J., Nakagawa, T., Newnham, R., and Schwander, J. (2009). Formal definition and dating of the gssp (global stratotype section and point) for the base of the holocene using the greenland ngrip ice core, and selected auxiliary records. Journal of Quaternary Science, 24(1):3–17.

Walters, D., Baran, A. J., Boutle, I., Brooks, M., Earnshaw, P., Edwards, J., Furtado, K., Hill, P., Lock, A., Manners, J., Morcrette, C., Mulcahy, J., Sanchez, C., Smith, C., Stratton, R., Tennant, W., Tomassini, L., Van Weverberg, K., Vosper, S., Willett, M., Browse, J., Bushell, A., Carslaw, K., Dalvi, M., Essery, R., Gedney, N., Hardiman, S., Johnson, B., Johnson, C., Jones, A., Jones, C., Mann, G., Milton, S., Rumbold, H., Sellar, A., Ujiie, M., Whitall, M., Williams, K., and Zerroukat, M. (2019). The met office unified model global atmosphere 7.0 7.1 and jules global land 7.0 configurations. Geoscientific Model Development, 12(5):1909–1963.

Wang, B. and Ding, Q. (2008). Global monsoon: Dominant mode of annual variation in the tropics. Dynamics of Atmospheres and Oceans, 44(3):165–183.

Wang, C., W.L., L., and Chou, C. (2019a). Climate effects of anthropogenic aerosol forcing on tropical precipitation and circulations. Journal of Climate, 32(16):5275 – 5287.

Wang, H., Chen, J., Zhang, X., and Chen, F. (2014a). Palaeosol development in the chinese loess plateau as an indicator of the strength of the east asian summer monsoon: Evidence for a mid-holocene maximum. Quaternary International, 334-335:155–164.

Wang, H., Lu, H., Zhao, L., Zhang, H., Lei, F., and Wang, Y. (2019b). Asian monsoon rainfall variation during the pliocene forced by global temperature change. Nature Communications, 10(1):5272.

Wang, K., Lu, H., Garzione, C. N., Zhao, L., Liang, C., Li, S., Breecker, D. O., Lei, F., and Zhang, H. (2022a). Enhanced soil respiration, vegetation and monsoon precipitation at lantian, east asia during pliocene warmth. Climate Dynamics, 59:2683–2697.

Wang, P. X., Wang, B., Cheng, H., Fasullo, J., Guo, Z., Kiefer, T., and Liu, Z. (2017). The global monsoon across time scales: Mechanisms and outstanding issues. Earth-Science Reviews, 174:84–121.

Wang, P. X., Wang, B., Cheng, H., Fasullo, J., Guo, Z. T., Kiefer, T., and Liu, Z. Y. (2014b). The global monsoon across timescales: coherent variability of regional monsoons. Climate of the Past, 10(6):2007–2052.

Wang, Q., Danilov, S., Sidorenko, D., Timmermann, R., Wekerle, C., Wang, X., Jung, T., and Schröter, J. (2014c). The Finite Element Sea Ice-Ocean Model (FESOM) v.1.4: formulation of an ocean general circulation model. Geoscientific Model Development, 7(2):663–693.

Wang, Y. J., Cheng, H., Edwards, R. L., An, Z. S., Wu, J. Y., Shen, C.-C., and Dorale, J. A. (2001). A high-resolution absolute-dated late pleistocene monsoon record from hulu cave, china. Science, 294(5550):2345–2348.

Wang, Y. P., Law, R. M., and Pak, B. (2010). A global model of carbon, nitrogen and phosphorus cycles for the terrestrial biosphere. Biogeosciences, 7(7):2261–2282.

Wang, Y. V., Larsen, T., Lauterbach, S., Andersen, N., Blanz, T., Krebs-Kanzow, U., Gierz, P., and Schneider, R. R. (2022b). Higher sea surface temperature in the indian ocean during the last interglacial weakened the south asian monsoon. Proceedings of the National Academy of Sciences, 119(10):e2107720119.

Wara, M. W. (2005). Permanent El Nino-Like Conditions During the Pliocene Warm Period. Science, 309(5735):758–761.

Watanabe, M., Chikira, M., Imada, Y., and Kimoto, M. (2011). Convective control of ENSO simulated in MIROC. Journal of Climate, 24(2):543 – 562.

Watanabe, S., Kawatani, Y., Tomikawa, Y., Miyazaki, K., Takahashi, M., and Sato, K. (2008). General aspects of a t213l256 middle atmosphere general circulation model. Journal of Geophysical Research: Atmospheres, 113(D12).

Webster, P. J. (1972). Response of the tropical atmosphere to local, steady forcing. Month. Weather Rev., 100:518–541.

Webster, P. J., Magaña, V. O., Palmer, T. N., Shukla, J., Tomas, R. A., Yanai, M., and Yasunari, T. (1998). Monsoons: Processes, predictability, and the prospects for prediction. Journal of Geophysical Research: Oceans, 103(C7):14451–14510.

Weldeab, S., Lea, D. W., Schneider, R. R., and Andersen, N. (2007). 155,000 years of west african monsoon and ocean thermal evolution. Science, 316:1303–1307.

Wilcox, L. J., Liu, Z., Samset, B. H., Hawkins, E., Lund, M. T., Nordling, K., Undorf, S., Bollasina, M., Ekman, A. M. L., Krishnan, S., Merikanto, J., and Turner,

A. G. (2020). Accelerated increases in global and asian summer monsoon precipitation from future aerosol reductions. Atmospheric Chemistry and Physics, 20(20):11955–11977.

Wilks, D. (2006). On "field significance" and the false discovery rate. Journal of applied meteorology and climatology, 45(9):1181–1189.

Wilks, D. S. (2011). Statistical methods in the atmospheric sciences, volume 100. Academic press.

Williams, C. J. R., Guarino, M.-V., Capron, E., Malmierca-Vallet, I., Singarayer, J. S., Sime, L. C., Lunt, D. J., and Valdes, P. J. (2020). Cmip6/pmip4 simulations of the mid-holocene and last interglacial using hadgem3: comparison to the pre-industrial era, previous model versions and proxy data. Climate of the Past, 16(4):1429–1450.

Williams, K. D., Copsey, D., Blockley, E. W., Bodas-Salcedo, A., Calvert, D., Comer, R., Davis, P., Graham, T., Hewitt, H. T., Hill, R., Hyder, P., Ineson, S., Johns, T. C., Keen, A. B., Lee, R. W., Megann, A., Milton, S. F., Rae, J. G. L., Roberts, M. J., Scaife, A. A., Schiemann, R., Storkey, D., Thorpe, L., Watterson, I. G., Walters, D. N., West, A., Wood, R. A., Woollings, T., and Xavier, P. K. (2018). The met office global coupled model 3.0 and 3.1 (gc3.0 and gc3.1) configurations. Journal of Advances in Modeling Earth Systems, 10(2):357–380.

Winton, M. (2000). A reformulated three-layer sea ice model. Journal of Atmospheric and Oceanic Technology, 17(4):525 – 531.

Wood, R., Mechoso, C. R., Bretherton, C. S., Weller, R. A., Huebert, B., Straneo, F., Albrecht, B. A., Coe, H., Allen, G., Vaughan, G., Daum, P., Fairall, C., Chand, D., Gallardo Klenner, L., Garreaud, R., Grados, C., Covert, D. S., Bates, T. S., Krejci, R., Russell, L. M., de Szoeke, S., Brewer, A., Yuter, S. E., Springston, S. R., Chaigneau, A., Toniazzo, T., Minnis, P., Palikonda, R., Abel, S. J., Brown, W. O. J., Williams, S., Fochesatto, J., Brioude, J., and Bower,

K. N. (2011). The VAMOS Ocean-Cloud-Atmosphere-Land Study Regional Experiment (VOCALS-REx): goals, platforms, and field operations. Atmospheric Chemistry and Physics, 11(2):627–654.

Woodward, F. (1987). In Climate and plant distribution. Cambridge University Press.

Wu, T. (2012). A mass-flux cumulus parameterization scheme for large-scale models: description and test with observations. Climate Dynamics, 38(3):725–744.

Xin, X., Wu, T., Li, J., Wang, Z., Li, W., and Wu, F. (2013). How Well does BCC_CSM1.1 Reproduce the 20th Century Climate Change over China? Atmospheric and Oceanic Science Letters, 6(1):21–26.

Xiong, S., Ding, Z., Zhu, Y., Zhou, R., and Lu, H. (2010). A 6ma chemical weathering history, the grain size dependence of chemical weathering intensity, and its implications for provenance change of the chinese loess–red clay deposit. Quaternary Science Reviews, 29(15):1911–1922.

Xu, Y., Huang, Y., and Li, Y. (2012). Summary of recent cimate change studies on the carbon and nitrogen cycles in the terrestrial ecosystem and ocean in china. Advances in Atmospheric Sciences, 29(5):1027–1047.

Yan, Q., Wei, T., Korty, R. L., Kossin, J. P., Zhang, Z., and Wang, H. (2016). Enhanced intensity of global tropical cyclones during the mid-Pliocene warm period. Proceedings of the National Academy of Sciences, 113(46):12963–12967.

Yokohata, T., Annan, J. D., Collins, M., Jackson, C. S., Tobis, M., Webb, M. J., and Hargreaves, J. C. (2012). Reliability of multi-model and structurally different single-model ensembles. Climate Dynamics, 39(3):599–616.

Yoshimori, M. and Suzuki, M. (2019). The relevance of mid-holocene arctic warming to the future. Climate of the Past, 15(4):1375–1394.

Yuan, D., Cheng, H., Edwards, R., Dykoski, C., Kelly, M., Zhang, M., Qing, J., Lin, Y., Wang, Y., Wu, J., Dorale, J. A., An, Z., and Cai, Y. (2004). Timing, duration, and transitions of the last interglacial asian monsoon. Science, 304(5670):575–578.

Yukimoto, S., Adachi, Y., Hosaka, M., Sakami, T., Yoshimura, H., Hirabara, M., Tanaka, T. Y., Shindo, E., Tsujino, H., Deushi, M., Mizuta, R., Yabu, S., Obata, A., Nakano, H., Koshiro, T., Ose, T., and Kitoh, A. (2012). A new global climate model of the meteorological research institute: Mri-cgcm3—model description and basic performance. Journal of the Meteorological Society of Japan. Ser. II, 90:23–64.

Yukimoto, S., Kawai, H., Koshiro, T., Oshima, N., Yoshida, K., Urakawa, S., Tsujino, H., Deushi, M., Tanaka, T., Hosaka, M., Yabu, S., Yoshimura, H., Shindo, E., Mizuta, R., Obata, A., Adachi, Y., and Ishii, M. (2019). The meteorological research institute earth system model version 2.0, mri-esm2. 0: Description and basic evaluation of the physical component. Journal of the Meteorological Society of Japan. Ser. II, 97(5):931–965.

Yukimoto, S., Yoshimura, H., and Hosaka, M. (2011). Meteorological Research Institute-Earth System Model v1 (MRI-ESM1)?Model Description. Technical Report of MRI. Ibaraki, Japan. Technical report.

Zelinka, M. D., Myers, T. A., McCoy, D. T., Po-Chedley, S., Caldwell, P. M., Ceppi, P., Klein, S. A., and Taylor, K. E. (2020). Causes of higher climate sensitivity in cmip6 models. Geophysical Research Letters, 47(1):e2019GL085782.

Zeng, Y. J., Xie, Z. H., Yu, Y., Liu, S., Wang, L. Y., Zou, J., Qin, P., and Jia, B. (2016). Effects of anthropogenic water regulation and groundwater lateral flow on land processes. Journal of Advances in Modeling Earth Systems, 8:1106–1131.

Zhang, W., Zhang, Z., Liao, Z., Wang, Y., Chen, S., Shao, Q., and Wang, Y. (2019). Changes in the asian monsoon climate during the late last interglacial recorded in oxygen isotopes of a stalagmite from the yongxing cave, central china. Journal of Asian Earth Sciences, 179:211–218.

Zhang, Y. G., Pagani, M., and Liu, Z. (2014). A 12-Million-Year Temperature History of the Tropical Pacific Ocean. Science, 344(6179):84–87.

Zhao, A., Brierley, C. M., Jiang, Z., Eyles, R., Oyarzún, D., and Gomez-Dans, J. (2022). Analysing the pmip4-cmip6 collection: a workflow and tool (pmip_p2fvar_analyzer v1). Geoscientific Model Development, 15(6):2475–2488.

Zhao, Y., Braconnot, P., Marti, O., Harrison, S. P., Hewitt, C., Kitoh, A., Liu, Z., Mikolajewicz, U., Otto-Bliesner, B., and Weber, S. L. (2005). A multi-model analysis of the role of the ocean on the african and indian monsoon during the mid-holocene. Climate Dynamics, 25(7):777–800.

Zhao, Y. and Harrison, S. P. (2012). Mid-holocene monsoons: a multi-model analysis of the inter-hemispheric differences in the responses to orbital forcing and ocean feedbacks. Climate Dynamics, 39(6):1457–1487.

Zheng, J., Zhang, Q., Li, Q., Zhang, Q., and Cai, M. (2019). Contribution of sea ice albedo and insulation effects to arctic amplification in the ec-earth pliocene simulation. Climate of the Past, 15(1):291–305.

Ziehn, T., Chamberlain, Matthew A.and Law, R. M., Lenton, A., Bodman, R. W., Dix, M., Stevens, L., Wang, Y.-P., and Srbinovsky, J. (2020). The australian earth system model: Access-esm1.5. Journal of Southern Hemisphere Earth Systems Science, 70:193–216.

Zubakov, V. and Borzenkova, I. (1988). Pliocene palaeoclimates: Past climates as possible analogues of mid-twenty-first century climate. Palaeogeography, Palaeoclimatology, Palaeoecology, 65(1):35–49.